Modelling and optimisation of bistable composite laminates

Betts, David

Award date:
2012

Awarding institution:
University of Bath

MODELLING AND OPTIMISATION OF BISTABLE COMPOSITE LAMINATES

David Betts

A thesis submitted for the degree of Doctor of Philosophy
University of Bath
Department of Mechanical Engineering

January 2012

COPYRIGHT

David Betts

Abstract

Asymmetric composite laminates can have a bistable response to loading. The potentially large structural deformations which can be achieved during snap-through from one stable state to another with small and removable energy input make them of interest for a wide range of engineering applications. After 30 years of research effort the shapes and response to applied loads of laminates of general layup can be quantitatively predicted. With attention switching to the incorporation of bistable laminates for practical applications, tools for the design and optimisation of actuated bistable devices are desirable.

This thesis describes the analytical and experimental studies undertaken to develop novel modelling and optimisation techniques for the design of actuated asymmetric bistable laminates. These structures are investigated for practical application to morphing structures and the developing technology of piezoelectric energy harvesting.

Existing analytical models are limited by the need for a numerical solver to determine stable laminate shapes. As the problem has multiple equilibria, convergence to the desired solution cannot be guaranteed and multiple initial guesses are required to identify all possible solutions. The approach developed in this work allows the efficient and reliable prediction of the stable shapes of laminates with off-axis ply orientations in a closed form manner. This model is validated against experimental data and finite element predictions, with an extensive sensitivity study presented to demonstrate the effect of uncertainty and imperfections in the laminate composition.

This closed-form solution enables detailed optimisation studies to tailor the design of bistable devices for a range of applications. The first study considers tailoring of the directional stiffness properties of bistable laminates to provide resistance to externally applied loads while allowing low energy actuation. The optimisation formulation is constrained to guarantee bistability and to ensure a useful level of deformation. It is demonstrated that 'cross-symmetric' layups can provide stiffness in an arbitrary loading direction which is five times greater than in a chosen actuation direction.

The optimisation formulation is extended to include a method of actuation, with a series of experimental and modelling studies presented to assess mechanical and smart actuators. Orthogonal piezoelectric macro-fibre composite actuators are identified as the most suitable method for both modelling and experimental actuation. The analytical model is extended to include piezoelectric loading in such a way as to maintain the reliable prediction of all loaded laminate shapes. Using this formulation piezo-laminate structures are identified which provide resistance to operating loads while still maintaining a useful structural deformation which is achievable within recommended operating voltage limits. A secondary study demonstrates that required actuation voltages can be reduced by up to 33% through the simultaneous use of the positive and negative voltage range of two oppositely oriented piezoelectric layers.

Finally, the modelling and optimisation methods are applied to study piezoelectric composite laminates for electrical energy harvesting from ambient mechanical vibrations. The novel formulation aims to maximise the electrical energy output in an arrangement of piezoelectric layers excited by the alternating stress due to repeated mechanical actuation. Due to the complex mechanical-electrical coupling and the highly nonlinear behaviour, existing studies are limited to experimental demonstration with scope for improving designs for broadband harvesting identified. Enabled by the modelling formulation developed in this work, optimisation of the piezo-laminate structure demonstrates improved electrical energy generation. Through variation in laminate geometry, arbitrary stacking sequences and piezoelectric configurations, optimum designs are presented which differ from those considered experimentally, identifying wide scope for improvement of this developing technology.

Acknowledgements

I would like to thank the Engineering and Physical Sciences Research Council for sponsoring my time as a PhD student.

The work presented in this thesis owes a great deal to the knowledge passed down by Peter Giddings who provided much technical knowledge and answered my many, many questions in the early months of my PhD.

For their academic input and knowledgeable support I am very grateful to both Giles Hunt and Richard Butler. I would also like to thank Aki Salo and Nick Gathercole for their technical know-how and assistance with experimental testing, and Chris Bowen for collaborating on much of my work and for providing a great deal of teaching and guidance.

Finally, I would like to express my sincere gratitude to my academic supervisor Alicia Kim who has been a supportive mentor throughout my studentship. Thank you for guiding me in all the right directions and allowing me the freedom to go off on a tangent to develop my own ideas.

Contents

List of Figures

List of Tables

Nomenclature

a, b, c	out-of-plane displacement coefficients
A	surface area
A_{s0}, A_{f0}	start and finish martensite transition temperatures
A_{ij}, B_{ij}, D_{ij}	in-plane, coupling and flexural stiffness terms
c_{ijkl}	elastic constants
C	capacitance
C_i	non-uniform ply thickness factor
d_{1-11}, e_{1-8}	in-plane displacement coefficients
d_{ij}	effective piezoelectric strain constant
E	electric field
E_{11}, E_{22}	longitudinal and transverse Young's moduli
E_A, E_M	pure austenite and martensite Young's moduli
E_f, E_m	fibre and matrix Young's moduli
E_i	ply thickness factor for out-of-plane location
F	applied force
f_i	energy equilibrium equation
g_{ij}	effective piezoelectric voltage constant
G_{12}	shear modulus
G_f, G_m	fibre and matrix shear moduli
h_c	convection heat transfer coefficient
H	total laminate thickness
J	Jacobian matrix
l_w	SMA wire length
L, L_x, L_y	laminate edge lengths
$N_{x,y,xy}, M_{x,y,xy}$	externally applied forces and moments
$N^T_{x,y,xy}, M^T_{x,y,xy}$	thermally induced forces and moments
$N^P_{x,y,xy}, M^P_{x,y,xy}$	piezoelectrically induced forces and moments
Q	charge
Q_{ij}	stiffness matrix term

$\bar{Q}_{ij}$	transformed stiffness matrix term
S	SMA wire surface area
t_i	thickness of the i-th ply
t_p	piezoelectric layer thickness
T_s	austenite to martensite transition temperature
T_∞	SMA zero-volt temperature
u^0, v^0	in-plane displacements in x and y
U	electrical energy
U_{1-5}	stiffness invariants
$V_{1-4}^{A,B,D}$	lamination parameters
w	out-of-plane displacement
w_{def}	deflection between stable states
W	total laminate strain energy
X_s	bistability safety factor
$Z_{1-4}^{A,B,D}$	ply orientation components of lamination parameters
α_1, α_2	thermal expansions coefficients in ply coordinates
α_A, α_M	pure austenite and martensite thermal expansion coefficients
α_f, α_m	fibre and matrix thermal expansion coefficients
$\hat{\alpha}_{ij}$	constants related to thermal expansion coefficients
$\alpha_x, \alpha_y, \alpha_{xy}$	thermal expansion coefficients in global coordinates
β_1, β_2	piezoelectric coefficients in ply coordinates
$\hat{\beta}_{ij}$	constants related to piezoelectric coefficients
$\beta_x, \beta_y, \beta_{xy}$	piezoelectric coefficients in global coordinates
ΔT	temperature change from cure
ΔV	change in applied voltage
$\epsilon_x, \epsilon_y, \epsilon_{xy}$	total strains
$\epsilon_x^0, \epsilon_y^0, \epsilon_{xy}^0$	midplane strains
ζ	martensite volume fraction
θ, θ_p	ply and piezoelectric orientation relative to x axis
$\kappa_x, \kappa_y, \kappa_{xy}$	curvatures
ν_{12}, ν_{21}	major and minor Poisson's ratio
ν_f, ν_m	fibre and matrix Poisson's ratio
ρ	electrical resistivity
σ	stress
ϕ_1, ϕ_2	snap-through and loading direction
ψ_f, ψ_m	fibre and matrix volume fraction
ω	strain energy density

List of Matrices

$\boldsymbol{A}$	extensional stiffness matrix
$\boldsymbol{B}$	coupling stiffness matrix
$\boldsymbol{D}$	bending stiffness matrix
$\boldsymbol{K}$	laminate thermal expansion properties
$\boldsymbol{K_p}$	piezoelectric thermal expansion properties
$\boldsymbol{L}$	laminate edge length terms
$\boldsymbol{Q}$	material stiffnesses for stiffness invariants
$\boldsymbol{Q_{coef}}$	coefficients for stiffness invariants
$\boldsymbol{T}$	ply thickness terms
$\boldsymbol{T_p}$	piezoelectric thickness terms
$\boldsymbol{T_\phi}$	coordinate transformation matrix
$\boldsymbol{U}$	laminate stiffness invariants
$\boldsymbol{U_p}$	piezoelectric stiffness invariants
$\boldsymbol{V}^{A,B,D}$	lamination parameters
$\boldsymbol{X}$	shape coefficient terms
$\boldsymbol{Z}$	ply orienatation terms
$\boldsymbol{Z_p}$	piezoelectric orienatation terms
$\boldsymbol{Z}^{A,B,D}$	orientation dependent terms of lamination parameters

List of Acronyms

CLT	Clasical Laminated Plate Theory
FEA	Finite Element Analysis
FOM	Figure of Merit
MFC	Macro-Fibre Composite
RMS	Root Mean Square
SMA	Shape Memory Alloy
SMAPAS	Shape Memory Alloy - Piezoelectric Active Structure
SQP	Sequential Quadratic Programming

Chapter 1

Introduction

In recent years there has been increasing interest in morphing structures which are capable of significant shape change, with the development of smart materials reinvigorating the field in the past decade. A structure which has the ability to change its configuration or adapt to specific design requirements has obvious appeal, notably in the aerospace industry. An example of this is the trailing edge of a commercial aircraft. Currently, discrete sections move relative to one another to achieve changes in aerodynamic performance. These surfaces are designed to operate optimally at design conditions with a significant drop in performance as conditions change. In order to expand the operational range a morphing structure may be deployed to dynamically adapt to current flight conditions. This may be through fine shape control, or through exploiting bistability to achieve large-scale deformation.

A bistable structure is one that has two stable configurations when unloaded. Once such a structure exists in one of these configurations it remains there until enough energy is applied for it to climb out of an energy well and 'snap' into the second configuration. As an example, a typical load-displacement diagram for a bistable structure is shown in Fig. 1.1 where points C and G correspond to two stable configurations. A load-cycle may begin with the structure in its original configuration, point C. When positive load is applied the structure will approach the critical point at D where the snap occurs. The structure then follows the path C-D-H-I, bypassing the unstable path D-E-F-G-H. Upon removal of all load the structure will settle into its second stable configuration, point G. Significantly, the potentially large structural deformation between points C and G can be achieved through relatively small and removable energy input.

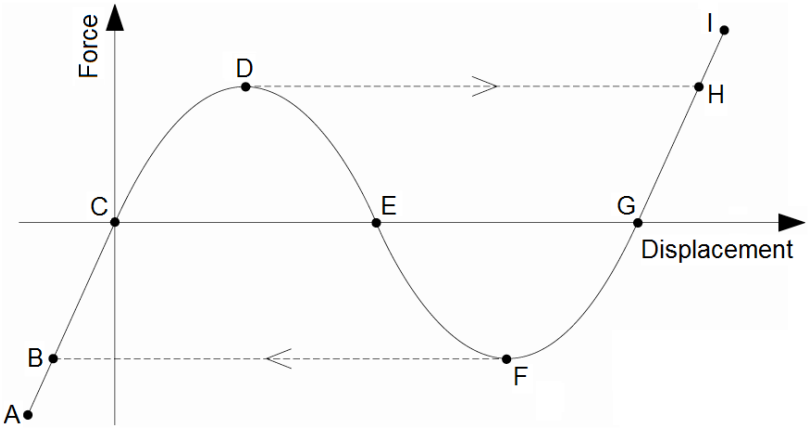

Figure 1.1: Example load-displacement behaviour for a bistable structure.

There exist a number of material and structural configurations exhibiting bistability in which continuous energy input is not required to maintain the structural deformation. One such structure is composite laminates of asymmetric layup. It is well known that laminates with an asymmetric layup may exhibit twisted or deformed shapes [54], and under certain geometric conditions two stable configurations. This warping is due to the anisotropic response to the elevated temperatures experienced during the manufacturing process resulting in thermal residual stresses. For many years these deformed shapes were regarded as undesirable and often countered by the addition of extra plies to make the laminate symmetric, or to reduce the global effect of the thermal stresses. More recently these properties have been exploited, making use of the large deflections between the different configurations. Figure 1.2 shows a range of samples of asymmetric laminates demonstrating deformed room-temperature shapes.

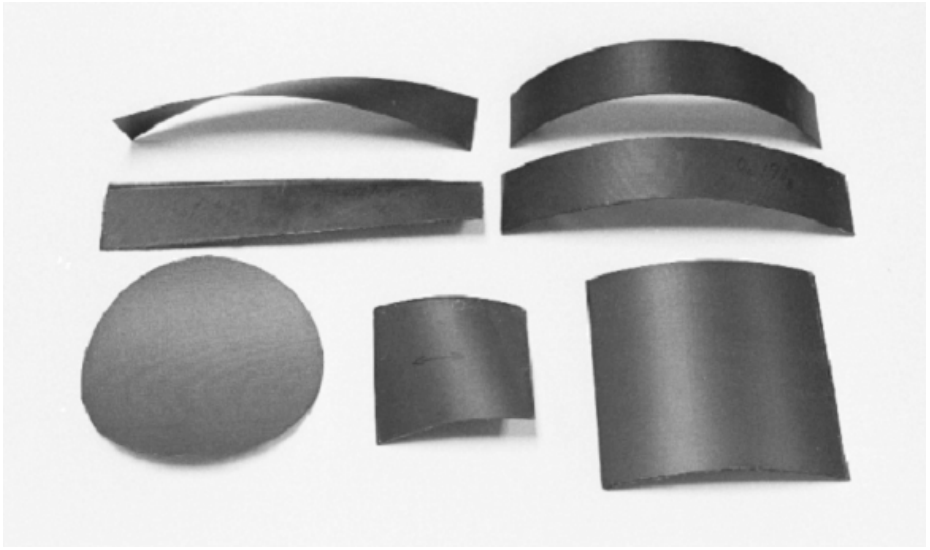

Figure 1.2: Curved shapes of asymmetric laminates, from [54].

The bistable behaviour exhibited by some asymmetric laminates clearly offers a great potential for morphing applications. An example demonstrating how this behaviour can be exploited is illustrated in Fig. 1.3. Figure 1.3a shows a possible wing trailing edge arrangement with both an adaptive local spoiler bump and variable trailing edge flap requiring no cumbersome internal mechanism. The behaviour of this variable flap can be mimicked by the structural changes of a bistable laminate cantilever controlled by a small piezoelectric patch shown in Fig. 1.3b. Initially in a raised position, the cantilever can be finely controlled by applying an electric field to the piezoelectric patch, inducing small downward displacements. At a critical point the structure 'snaps' to a second stable configuration of significantly greater deflection, much like the change in flap angle required in changing flight conditions. Similarly, the adaptive spoiler bump could utilise a bistable laminate with small energy input to induce the necessary aerodynamic change.

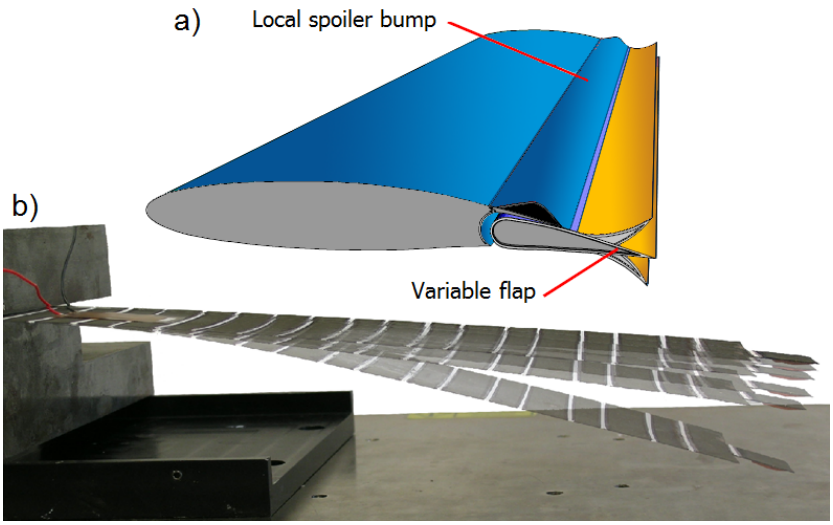

Figure 1.3: a) An adaptive trailing edge system proposed by Bein [7] and b) a bistable laminate mimicking the trailing edge deflection.

To date there have been numerous attempts to analytically model the stable shapes of asymmetric laminates [16, 22, 24, 60, 75]. However, the complexity of the modelling increases greatly when considering laminates of general layup and numerical solution procedures are typically required. Furthermore, the success of these methods is dependent on some prior knowledge of the shapes to provide multiple reasonable initial guesses to identify all possible solutions. Convergence to the desired solution therefore cannot be guaranteed. Limited closed-form approaches have been presented [53, 95] but these require simplifications which severely limit the potential design space. Finite element approaches [39, 89, 90] have also been considered but typically require imperfections to be introduced to 'force' the capture of both stable shapes. These techniques are considered to be useful analysis tools but poorly suited as design tools.

The nature of a multimodal problem where the number of solutions is dependent on the laminate design presents difficulties. Combined with the lack of an efficient and robust method of capturing the multiple stable shapes, optimisation of the design of bistable laminates is particularly limited. The full potential of bistable laminate structures has therefore not been exploited in existing research.

Clearly, with the ability to exploit the directional stiffness properties of composite materials, and tailoring of the structural shape, there is a scope for improving the useful application of bistable laminates for morphing, and other applications. The work presented in this thesis represents the research effort towards the development of optimisation of bistable laminates through novel modelling and optimisation methods. This work highlights interesting solutions to existing practical problems which have not previously been obvious in the field.

Chapter 2

Thesis Scope

The aim of this work is to develop optimisation techniques for the design of bistable asymmetric laminates. The underlying modelling for curved laminate shapes must be flexible enough to allow off-axis curvatures and non-uniform geometries to fully exploit the directional stiffness properties of composite materials. The stable shapes of such laminates must be predicted without the need for any prior knowledge of the solutions with all shapes captured in a reliable manner so as to enable iteration based optimisation. Beyond this static modelling, a method of actuating the laminates to achieve large structural deformation is to be identified and incorporated. Experimental validation of the modelling is to be conducted with recommendations made about any observed limitations or sensitivities.

The validated model is to form the basis of an optimisation formulation, limited in existing literature by the lack of an explicit solution to modelling. This optimisation formulation is to be applied to a number of practical design problems to be identified in existing literature relating to morphing structures and other actuated laminate applications. Given the inherently discontinuous nature of the design space when considering structures with multiple stable states, the problem formulation must include understanding of when bistability is present. To the author's knowledge no method of ensuring bistability for fully general cases is presented in existing literature. It is intended that this formulation will identify novel solutions to well documented design problems which may not be obvious in existing work.

2.1 Objectives

In order to fulfil the scope of this work the following objectives are to be met.

1. To identify the 'state of the art' model for the shapes of bistable laminates of general layup, appropriate for optimisation studies.
2. To assess the accuracy and sensitivity of the chosen modelling technique through experimental and analytical studies.
3. To develop an optimisation technique suitable for the design of bistable asymmetric laminates. This is to include overcoming the issues associated with having multiple solutions within the problem formulation.
4. To identify problems in existing literature suitable to test the optimisation methods.
5. To identify the most suitable method for actuation of bistable laminates from both a practical and modelling viewpoint. The validity of a number of possible methods are to be assessed experimentally.
6. To extend the modelling techniques and optimisation formulation to include the chosen method of actuation.
7. To apply the extended formulation to one or more practical applications and identify novel solutions to existing problems.

2.2 Thesis Overview

This section summarises the technical content of each chapter and details the structure of this work to aid the reader in finding information of specific interest. The work presented in Chapters 4 - 10 forms the research effort aimed at developing optimisation methods for the design of bistable composite laminates. Each chapter addresses a key objective for the incremental development of this design tool. Roman numerals denote journal publications or conference presentations in which the relevant work has been published, a list of which can be found in Section 2.3.

Chapter 3 - Literature Review

Chapter 3 gives motivation for the work and highlights the selection of research objectives based on a literature survey of bistable morphing research. The review is split into three main areas; bistability of composite structures including composite plate and bistable shell theories; actuation of bistable laminates including both mechanical and smart actuation methods; and optimisation of the design of bistable laminates. This chapter provides much of the necessary background information to allow specific discussion in the subsequent chapters.

Chapter 4 - Modelling of Bistable Laminate Shapes

Chapter 4 contains a detailed description of the derivation of a new modelling formulation for prediction of the shapes of bistable laminates of arbitrary layup. The existing 'state of the art' analytical model is outlined with its applicability to design optimisation critically assessed. A new closed-form solution to this modelling is developed for a laminate geometry which reduces the size of the problem using knowledge of design space, [ii] and [x]. Finally, a brief discussion of how this modelling technique can be extended for a fully general design case is discussed.

Chapter 5 - Experimental Shape Characterisation

Chapter 5 outlines an experimental study and modelling sensitivity analysis to investigate the validity of the model presented in the previous chapter for predicting asymmetric laminate shapes. The first half of the chapter outlines the methodology and results of an experimental study to capture the stable shapes of a family of laminates using a 3D motion analysis technique. The results are compared with modelling predictions and potential sources of observed discrepancies are discussed, [vii] and [xiii]. The second half of the chapter presents a sensitivity study highlighting the dependence of the modelling accuracy on the material and geometric properties.

Chapter 6 - Optimisation of Bistable Laminates

Chapter 6 presents a preliminary optimisation study for bistable laminate design, [ii] and [x], enabled by the closed-form modelling solution outlined in Chapter 4. The optimisation formulation maximises the bending stiffness in a direction of known loading condition whilst the bending stiffness in the direction of actuation is minimised. A deflection requirement is applied as a constraint. The feasibility of designing a bistable composite needing a low actuation energy while still providing a reasonable stiffness to resist operating loads is demonstrated.

Chapter 7 - Analysis of Actuation Methods

Based on the findings of Chapter 6 various actuation methods are described and analysed in Chapter 7 with a view to incorporating actuation within the optimisation formulation. Firstly, an extension to the existing modelling to include an externally applied mechanical force is presented. Secondly, a piezoelectric macro-fibre composite (MFC) actuator is added to the model with an experimental study to assess the validity of this extension [iv]. Thirdly, an experimental study using shape memory alloy (SMA) wires is presented [xiv]. Finally, reversible actuation using combinations of MFCs and SMA is considered, [viii]. It is concluded that the reversible actuation using two MFCs of orthogonal alignment is the most appropriate method.

Chapter 8 - Optimisation of Actuated Bistable Laminates

Chapter 8 presents an optimisation study for the design of bistable laminates for reversible actuation, [iii] and [xi], enabled by two orthogonal piezoelectric layers. The formulation optimises the load carrying capability of the structure subject to deflection and actuation limits through variation in ply orientations and laminate geometry. A secondary study demonstrates that reduction in total actuation voltage can be achieved through the simultaneous use of the positive and negative working ranges of the two piezoelectric layers.

Chapter 9 - Optimisation for Piezoelectric Energy Harvesting

In Chapter 9 many of the methods developed in this work are combined in a study of a bistable piezoelectric energy harvester to convert mechanical motion into electrical energy by exploiting ambient vibrations. The aim is to utilise the novel techniques developed to investigate optimisation of an existing technology. Due to the complex nature of existing modelling techniques optimisation of the design of such structures is limited in published literature. Here an existing experimental study is considered as an example problem, with optimum solutions investigated for changing aspect ratio,

thickness, stacking sequence, and piezoelectric patch size, [i], [v] and [ix]. Increased electrical output is demonstrated for geometries and piezoelectric configurations which are not intuitively obvious and which have not been investigated by other authors.

Chapter 10 - Conclusions

Finally, Chapter 10 summarises the main conclusions of this work and highlights the novel findings which are of interest in the field of morphing laminate structures. Specifically the success of the presented work with reference to the key objectives outlined in Section 2.1 is discussed. This section also includes discussion on a number of potential paths for future work.

2.3 List of Publications

This section lists the peer reviewed journal publications and conference presentations completed as part of the work outlined in this thesis.

Award

Best Student Paper in Composites Award by American Society for Composites, "Optimization of Bistable Composite Laminates with Actuated State-Change," *52nd AIAA/ASME/ASCE/AHS/ASC Structures, Structural Dynamics and Materials Conference*, Denver, CO USA, 2011.

Journal Publications

[i] DN Betts, HA Kim, CR Bowen and DJ Inman, "Optimal configuration of bistable piezo-composites for energy harvesting," *Applied Physics Letters*, Accepted, 2012.

[ii] DN Betts, HA Kim and CR Bowen, "Optimization of stiffness characteristics for the design of bistable composite laminates," *AIAA Journal*, Accepted, 2012.

[iii] DN Betts, HA Kim and CR Bowen, "Modeling and optimization of bistable composite laminates for piezoelectric actuation," *Journal of Intelligent Material Systems and Structures*, 22(18), 2011, pp. 2186-2196, doi: 10.1177/1045389X11427478.

[iv] CR Bowen, DN Betts, PF Giddings, AIT Salo and HA Kim, "A study of bistable laminates of generic lay-up for adaptive structures," *Strain*, Accepted, 2011, doi:10.1111/j.1475-1305.2011.00817.x.

[v] DN Betts, HA Kim and CR Bowen, "Preliminary study of optimum piezoelectric cross-ply composites for energy harvesting," Special Issue on Smart Composite Materials, *Smart Materials Research*, Accepted, 2011.

[vi] PF Giddings, CR Bowen, HA Kim, AIT Salo and DN Betts, "Snap-through of piezoelectrically actuated bistable composite laminates - A couple field finite element model," *IEEE Transactions on Ultrasonic, Ferroelectric and Frequency Control Society*, Accepted, 2011.

[vii] DN Betts, AIT Salo, CR Bowen and HA Kim, "Characterisation and modelling of the cured shapes of arbitrary layup bistable composite laminates," *Composite Structures*, 92(7), 2010, pp. 1694-1700, doi: 10.1016/j.compstruct.2009.12.005.

[viii] HA Kim, DN Betts, AIT Salo and CR Bowen, "Shape memory alloy - piezoelectric active structures for reversible actuation of bistable composites," *AIAA Journal*, 48(6), 2010, pp. 1265-1268, doi: 10.2514/1.J050100.

Conference Proceedings and Presentations

[ix] DN Betts, HA Kim and CR Bowen, "Optimization of bistable composite laminates for piezoelectric energy harvesting," *53rd AIAA/ASME/ASCE/ AHS/ASC Structures, Structural Dynamics and Materials Conference* (Accepted), Honolulu, HI USA, 2012.

[x] DN Betts, HA Kim and CR Bowen, "Design optimization of stiffness characteristics for bistable composite laminates," *52nd AIAA/ASME/ASCE/AHS/ASC Structures, Structural Dynamics and Materials Conference*, Denver, CO USA, 2011.

[xi] DN Betts, HA Kim and CR Bowen, "Optimization of bistable composite laminates with actuated state-change," *52nd AIAA/ASME/ASCE/AHS/ASC Structures, Structural Dynamics and Materials Conference*, Denver, CO USA, 2011.

[xii] HA Kim and DN Betts, "Design Studies of Bistable Composites," *9th WCCM/4th APCOM International Conference*, Sydney, Australia, 2010.

[xiii] DN Betts, AIT Salo, CR Bowen and HA Kim, "Characterisation and modelling of arbitrary layup bistable composite laminates," *15th International Conference on Composite Structures*, Porto, Portugal, 2009.

[xiv] HA Kim, DN Betts, AIT Salo and CR Bowen, "Shape memory alloy actuation for asymmetric bistable composites," *17th International Conference on Composites or Nano Engineering*, Honolulu, HI USA, 2009.

[xv] DN Betts, HA Kim and T Fong, "Towards the optimisation of the design of bistable composites," *7th ASMO-UK/ISSMO International Conference on Engineering Design Optimisation*, Bath, UK, 2008.

Chapter 3

Literature Review

This chapter presents a comprehensive review of published work relevant to the development of optimisation techniques for bistable laminates. The aim of the literature review is to give motivation for the work presented in this thesis by demonstrating the current state of the field, highlighting where new work fits into the existing research and identifying areas of novelty. The review is split into three main areas:

Section 3.1 - Bistability of Asymmetric Composite Structures
A review of existing analytical studies for the shapes of unloaded bistable composite structures is presented. This section is further split into composite plate theories, bistable shell theories and a brief discussion on modelling of edge effects. This section is intended to provide a background to the development of modelling techniques, identifying the most appropriate method for optimisation studies.

Section 3.2 - Modelling of Bistable Laminate Actuation
In order to induce the structural deformation discussed in Section 3.1 some method of actuating bistable laminates must be included. A review of attempts to include an actuation method using both mechanical and smart actuators is presented. This review of analytical and experimental studies is intended to identify issues associated with the modelling and practical application of various actuation methods.

Section 3.3 - Optimisation of Bistable Laminate Design
Finally, existing optimisation studies for the design of bistable laminate structures are discussed. As becomes evident in Sections 3.1 and 3.2, this area is extremely limited and represents the main area of novelty of the work presented in this thesis.

3.1 Bistability of Asymmetric Composite Structures

When a composite laminate has an asymmetric stacking sequence the resulting mismatch in thermal properties through-thickness results in thermally induced strain. This leads to a curved deformation. Under certain geometric conditions the thermal warping can lead to two stable states, resulting in a large deflection which does not require continuous energy input to be maintained. Figure 3.1 shows this behaviour for an example square $[0/90]_{\mathrm{T}}$ laminate. For a low ratio of edge length to thickness only a single stable state is observed, point A, with x- and y-curvatures of equal magnitude in opposite out-of-plane directions. As the ratio increases the solution bifurcates, point B. Beyond this point two approximately cylindrical stable states are observed, points C and D, while the saddle state becomes unstable (dashed line).

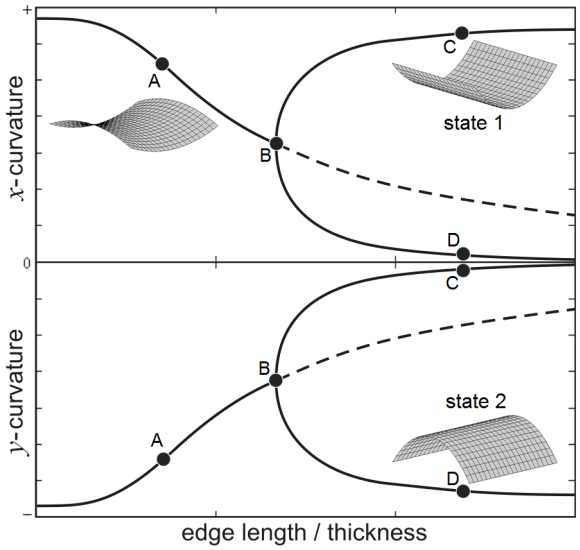

Figure 3.1: Stable (solid) and unstable (dashed) shapes of a $[0/90]_{\mathrm{T}}$ laminate.

Over the past 30 years extensive studies have been conducted on modelling of two particular bistable structures; asymmetric laminated rectangular plates, and bistable cylindrical shells. In this section a comprehensive review of the existing literature in these areas is presented.

3.1.1 Asymmetric Composite Laminate Theories

In general the response of composite laminates to loading can be analysed using linear calculations based on classical laminated plate theory (CLT) [3]. This theory is based on a number of assumptions:

1. Displacements are continuous throughout the laminate.
2. Kirchhoff hypothesis is valid.
3. Strain-displacement relationships are linear.
4. The material is linearly elastic.
5. Through-thickness stresses are small in comparison to in-plane stresses.

This theory smears the properties of the individual lamina to give overall laminate properties defined by the in-plane ($\boldsymbol{A}$), coupling ($\boldsymbol{B}$) and flexural ($\boldsymbol{D}$) stiffness matrices. While CLT is capable of accurately predicting static deflections, natural vibration frequencies and mode shapes, buckling loads and mode shapes, and thermal expansion properties, there are cases where the theory fails to capture the correct behaviour. Two notable situations are the response of thicker laminates as studied by [105] and [106], and the local behaviour near laminate edges, discussed later in this chapter.

A third situation in which CLT fails to predict the physical reality was observed by Hyer [54]. CLT predicts all asymmetric laminates to have a single stable state of anticlastic or 'saddle' curvature. Hyer [54] documented the room-temperature shapes of a number of thin asymmetric laminates and found that some exhibit approximately cylindrical shape. Furthermore, in some cases two stable states of opposing cylindrical curvature were observed. This contrast to the predictions of CLT was observed for a four-ply $[0_2/90_2]_\mathrm{T}$ laminate. However, when the thickness of the laminate was doubled to $[0_4/90_4]_\mathrm{T}$, the observed shapes conformed to the theoretical predictions.

The first attempt to model this behaviour of thin asymmetric laminates was presented by Hyer [53]. It was assumed that nonlinearity would be required in order to capture the two room-temperature shapes. Given that the out-of-plane displacements observed in [54] were many laminate thicknesses in magniutude, geometric nonlinearity was considered. Therefore, nonlinear terms were added to the typical strain-displacement relations of CLT of the following form,

$$\begin{aligned}
\epsilon_x^0 &= \frac{\partial u^0}{\partial x} + \frac{1}{2}\left(\frac{\partial w}{\partial x}\right)^2 \\
\epsilon_y^0 &= \frac{\partial v^0}{\partial y} + \frac{1}{2}\left(\frac{\partial w}{\partial y}\right)^2 \\
\epsilon_{xy}^0 &= \frac{\partial u^0}{\partial y} + \frac{\partial v^0}{\partial x} + \frac{\partial w}{\partial x}\frac{\partial w}{\partial y}
\end{aligned} \tag{3.1}$$

where ϵ_x^0, ϵ_y^0 and ϵ_{xy}^0 are the midplane strains, u^0 and v^0 are the in-plane displacments in the x- and y-directions respectively and w is the out-of-plane displacement. This theory was used to predict the shapes of cross-ply laminates of the $[0_n/90_n]_\mathrm{T}$ family through

a Rayleigh-Ritz minimisation of total strain energy. A quadratic approximation to the out-of-plane displacements of the following form was assumed,

$$w(x,y) = \frac{1}{2}(ax^2 + by^2) \tag{3.2}$$

allowing both the saddle shape, $a = -b$, and cylindrcal shapes, $a \approx 0$, $b \neq 0$ and $a \neq 0$, $b \approx 0$, to be captured. It was further assumed that midplane shear strain ϵ^0_{xy}, is negligible and therefore neglected. For this simple model, requiring just four coefficients to approximate the laminate shape, an analytical solution was derived to define the minimum energy stable shapes. The model was found to capture the bifurcation behaviour associated with the disappearance of a saddle shape to be replaced by two cylindrical shapes with varying geometry. However, with very limited experimental data the quantitative accuracy of the model was not assessed.

This same model was used by Hamamoto and Hyer [45] to investigate the change in laminate curvature with change in temperature. Results predicted that laminates which exhibit multiple stable states at room temperature will revert back to a single saddle shape as the ambient temperature increases, tending towards a flat laminate at the cure temperature. Full experimental comparison confirmed this behaviour but with large discrepancies in the observed curvatures. It was assumed that imperfections were responsible for much of the error, with modelling of imperfect ply thicknesses used to demonstrate the sensitivity of the model.

The cross-ply theory was later developed by Hyer [55] to consider all possible combinations of asymmetric, four-ply stacking sequence consisting of 0° and 90° orientations: $[0/0/0/90]_T$, $[0/0/90/0]_T$, $[0/90/0/90]_T$, and $[0/0/90/90]_T$. In order to model this extended problem two additional shape coefficients were introduced to the formulation of [53] to capture the in-plane displacements more accurately. This resulted in minimisation of the total strain energy with respect to six coefficients. With this increased complexity a Rayleigh-Ritz minimisation of the total strain energy was solved using a Newton-Raphson style numerical technique as no analytical solution could be derived. Unlike in [53] two different forms of bifurcation behaviour were observed. Firstly, the ideal bifurcation behaviour of $[0/90/0/90]_T$ and $[0/0/90/90]_T$ where a bifurcation point is seen, Fig. 3.2a. Secondly, a disjoint solution for the $[0/0/0/90]_T$ and $[0/0/90/0]_T$ laminates, with a limit point observed, Fig. 3.2b. No experimental results were presented to validate the theoretical predictions.

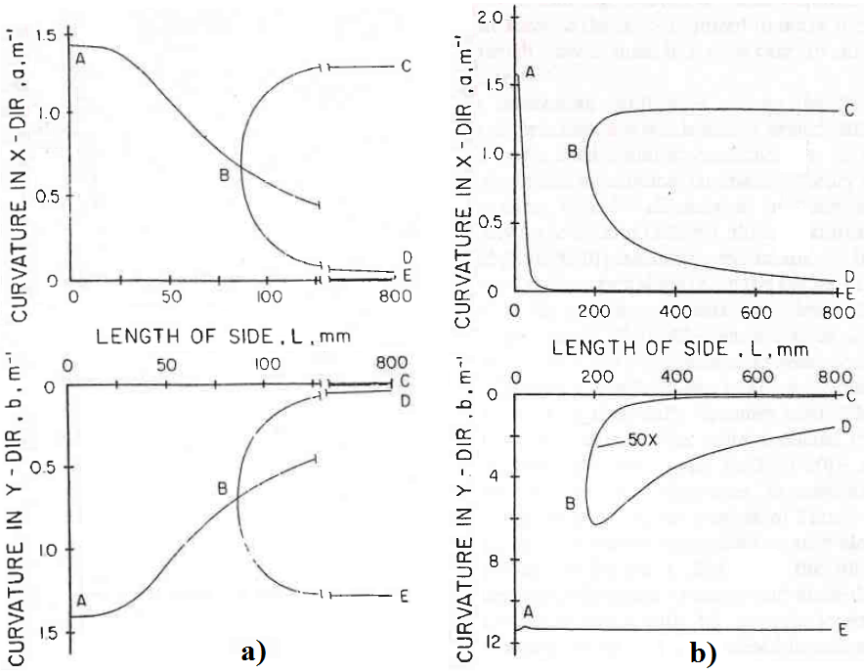

Figure 3.2: Room temperature shapes of sqaure a) $[0/90/0/90]_{\mathrm{T}}$ and b) $[0/0/0/90]_{\mathrm{T}}$ laminates, adapted from [55].

Jun and Hong [58] built on the work of Hyer [55] by considering more general cases of laminate geometry but presented no extensions to existing modelling theory. The study focussed on the general trends of the bifurcation point of laminates with $[0_n/90_n]_{\mathrm{T}}$ and $[0/90]_{n\mathrm{T}}$ layup of varying size, aspect ratio and number of plies. They demonstrated that the edge length to thickness ratio defining the bifurcation point decreases with an increase in aspect ratio, but that it is not sensitive to number of plies.

All models outlined to this point maintain Hyer's [53] assumption that thermal residual shear strain is negligible and can be neglected. Jun and Hong [59] noted that residual shear strains generally do exist in asymmetric laminates and extended Hyer's general cross-ply model [55] to include such terms. Numerical results were presented to demonstrate the effect of these additonal terms when compared with the zero shear results previously published [58]. Figure 3.3 shows a comparison of the bifurcation behaviour using the two different approaches for a $[0_2/90_2]_{\mathrm{T}}$ laminate. It was found that for a low edge to thickness ratio ($\leq$30) and for a high edge to thickness ratio ($\geq$130) the results validated the theory that the shear strain effect is negligible. However, close to the bifurcation point the difference in predicted curvature is significant, and the inclusion of shear strain for asymmetric laminates is recommended.

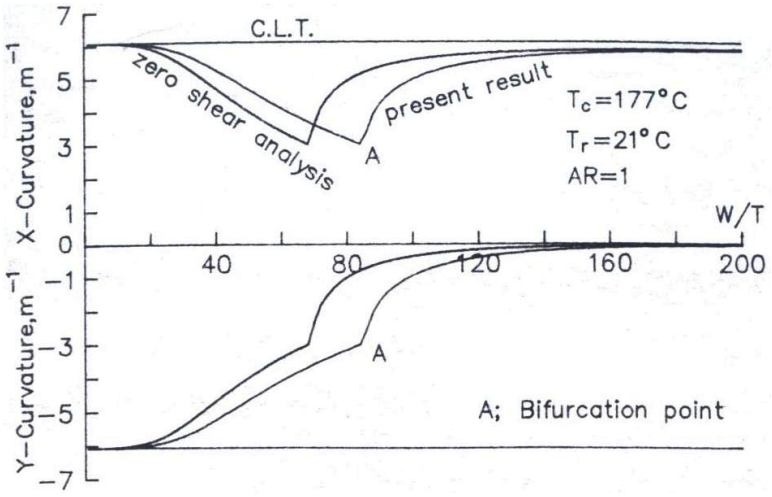

Figure 3.3: The effect of residual thermal shear strain on the curvatures of a square $[0_2/90_2]_T$ laminate, from [59].

Ren et al. [86] extended the existing cross-ply work to consider a different problem. Knowing that a laminate which is cured flat may result in cylindrical curvature at room-temperature, it was considered whether an asymmetric laminate may be manufactured to be flat at room-temperature by introducing some level of curvature during the curing process. The nonlinear extension to CLT was extended further to the following form,

$$\begin{aligned}
\epsilon_x^0 &= \frac{\partial u^0}{\partial x} + \frac{1}{2}\left(\frac{\partial w}{\partial x}\right)^2 \\
\epsilon_y^0 &= \frac{\partial v^0}{\partial y} + \frac{1}{2}\left(\frac{\partial w}{\partial y}\right)^2 - \frac{w}{R} \\
\epsilon_{xy}^0 &= \frac{\partial u^0}{\partial y} + \frac{\partial v^0}{\partial x} + \frac{\partial w}{\partial x}\frac{\partial w}{\partial y}
\end{aligned} \tag{3.3}$$

where R is the radius of the mold on which the laminate is cured. This additional term results in more complex strain and displacement expressions. Results demonstrated that, although the laminates could not be made flat, the magnitude of curvature could be reduced. Furthermore, for small values of R the bistable behaviour of the laminates studied in [55] could be suppressed. For large values of R the results tended towards those presented in [55] for the flat curing process. While only limited experimental comparison with the analytical model was presented, some additional finite element predictions were included showing good agreement.

Dang and Tang [22] presented a reformulation of Hyer's cross-ply model [55] to predict the shapes of asymmetric laminates with stacking sequences not limited to 0° and 90°. They made the observation that in a certain coordinate system an asymmetric laminate will have two perpendicular principal curvatures. Using this as a starting point they restated the model in terms of the principal curvature coordinate system,

with a transformation used to obtain the shapes in the structural coordinate system. Experimental comparisons showed reasonable agreement. However, the displacement functions were not correctly defined and the system could only be solved for the sum of two of the displacment coefficients, rather than considering each independently.

Jun and Hong [60] modified Dang and Tang's [22] approach by adding additional terms to the displacement functions. The resulting generalised expressions were more complex, requiring several combinations of variables to be redefined to obtain simpler expressions. In this form it is difficult to visualise or give meaning to the set of shape coefficients. This method, like that of Dang and Tang [22], makes it particularly difficult to provide a good approximate 'guess' for the laminate shape, required for iterative solution of the minimum energy system. However, good agreement was demonstrated between experimental results and theoretical predictions for the angle of principal curvature. No results were presented to validate the magnitude of curvature.

Peeters et al. [74] developed a theory for arbitrary layup laminates with square edge length based on the work by Jun and Hong [60]. The displacement functions were approximated using a more complete third order polynomial. The complexity of the modelling was reduced by assuming that the angle of principal curvature is at 45° to the laminate edge length for all laminates as predicted by CLT. Furthermore, the elongation strains in the principal curvature coordinate system were assumed to be independent of orientation, treating the laminate as if it was square in the principal curvature coordinate system. This model is therefore restrictive in the set of laminates which can be analysed. For the very limited experimental comparison presented, with a number of uncertainties in manufacturing stated, the accuracy of the model was shown to be reasonable.

Theories developed to this point for the shapes of arbitrary layup laminates used the same method of approximating the displacements with varying polynomial forms. Dano and Hyer [24] noted that this approach leads to expressions for the strains which are unnecessarily complex. For the prediciton of the unloaded deformation behaviour the displacement functions are only used to obtain expressions for strains required in computation of the total laminate strain energy. Thus, rather than approximating the displacements, direct approximations for strains were presented. Initially, complete third order polynomials were used to approximate the midplane strains.

$$\begin{aligned}\epsilon_x^0 &= c_{00} + c_{10}x + c_{01}y + c_{20}x^2 + c_{11}xy + c_{02}y^2 + c_{30}x^3 + c_{21}x^2y + c_{12}xy^2 + c_{03}y^3 \\ \epsilon_y^0 &= d_{00} + d_{10}x + d_{01}y + d_{20}x^2 + d_{11}xy + d_{02}y^2 + d_{30}x^3 + d_{21}x^2y + d_{12}xy^2 + d_{03}y^3\end{aligned} \tag{3.4}$$

This method resulted in 28 coefficients to be determined to define the laminate shapes. Using a Rayleigh-Ritz minimisation of the total strain energy it was noted that the

resulting 28 equilibrium equations could be reorganised to a set of three nonlinear equations to be solved numerically,

$$f_a(a,b,c,\Delta T)=0 \quad f_b(a,b,c,\Delta T)=0 \quad f_c(a,b,c,\Delta T)=0 \tag{3.5}$$

where a, b and c define the out-of-plane displacements and ΔT is the temperature change from cure. Results obtained for all laminates studied showed that a number of the coefficients always appeared to be zero. It was concluded that only the terms with powers of x and y that sum to an odd number needed to be included. Therefore the model was reduced to 14 unknown coefficients by introducing the following simplified strain expressions.

$$\begin{aligned}\epsilon_x^0 &= c_{00}+c_{20}x^2+c_{11}xy+c_{02}y^2\\ \epsilon_y^0 &= d_{00}+d_{20}x^2+d_{11}xy+d_{02}y^2\end{aligned} \tag{3.6}$$

Results were presented comparing this 14 coefficient model with those of Jun and Hong [60] and with finite element analysis (FEA) results. It was found that the method outlined by Dano and Hyer [24] showed greater agreement with FEA, particularly around the bifurcation point. Small discrepancies in displacement at the laminate corners were noted, attributed to the simple quadratic approximation of the out-of-plane displacement not capturing free edge behaviour. Further analysis of the direction of prinicipal curvature was presented to compare with the assumption made by Peeters et al. [74] that the angle of prinicipal curvature could be fixed to 45° relative to the laminate edge for all laminates. This assumption was shown to be incorrect.

While the model presented by Dano and Hyer [24] is widely considered to be the 'state of the art' analytical model, a number of interesting studies have been performed using variations of the models described in this section. Gigliotti et al. [40] investigated the location of the bifurcation point to develop a method for predicting the presence of bistability. The study was limited to $[0/90]_{\mathrm{T}}$ laminates using Hyer's original model [53], but some interesting observations were made. The problem is non-dimensionalised using the following definitions,

$$a^*=\frac{aL^2}{t}, \quad b^*=\frac{bL^2}{t}, \quad L^*=\frac{\alpha\Delta TL^2}{t^2} \tag{3.7}$$

where L is the square edge length, t is the single ply thickness, a^* and b^* are the non-dimensional curvatures, L^* is non-dimensional length and α is the difference between the longitudinal and transverse coefficients of thermal expansion. This non-dimensionalised form allows two conditions relating to the bifurcation point to be identified. Firstly, the range of non-dimensional lengths for which unique solutions are found increases as the ratio of 0° and 90° ply thickness (t_0/t_{90}) decreases by the following relationship,

$$(L^*_{tr})\cdot(t_0/t_{90})^3=\text{constant} \tag{3.8}$$

where L^*_{tr} is the non-dimensional length at the bifurcation point. Secondly, the aspect ratio at the bifurcation point, AR_{tr} for any length follows the relationship,

$$\frac{L^*}{AR_{tr}} = \text{constant} \tag{3.9}$$

allowing transition from saddle to cylindrical shapes to be established from known reference values. These relationships are very useful in defining the range of bistaility. It is anticipated that similar rules applying to fully general laminates may allow a wider design space to be constrained such that bistability is ensured.

Limited extensions to modelling to include certain environmental factors have also been presented. Cho and Roh [17] considered a known manufacturing issue related to the interaction between the tool plate and the laminate, referred to as the slippage effect. An extension to Hamamoto and Hyer's model [45] was presented to modify the displacement field giving a monotonically varying transverse shear stress profile. The effect was found to vary the location of the bifurcation point due to the reduced overall curvature induced by the shear stress. However, the greatly increased complexity of the model results in very small variations.

Finally, it is important to note that while environmental factors such as moisture absorption are often noted, examples of modelling including such effects are sparse [34, 76]. One notable study by Portela et al. [76] considered the combined effects of thermal and moisture expansion on bistable laminate shapes. Moisture absorption creates a stress field which can be conveniently treated in much the same way as thermal stresses. Portela et al. [76] considered the following form of combined coefficients α^*_{ij} to consider this dual issue,

$$\left(\alpha_{ij} + \lambda_{ij}\frac{\Delta M}{\Delta T}\right)\Delta T = \alpha^*_{ij}\Delta T \tag{3.10}$$

where α_{ij}'s are the thermal expansion coefficients, λ_{ij}'s are the moiture expansion coefficients, ΔM is the percent weight gained through moisture absorption and ΔT is temperature change. These coefficients were added to an FEA model to predict the moisture absorption influence on the shape and the snap-through behaviour of bistable laminates. It was demonstrated that the moisture absorption effect acts to relax the thermal stresses and thus reduce the laminate curvatures.

Edge effects

Earlier observations by Hyer [55] and Potter et al. [77] have highlighted areas of locally reversed curvature along the free edges of bistable laminates, and in particular at the free corners. This phenomena is not captured by the CLT based analytical models. Furthermore, these deviations from the approximately constant curvature are too great to be explained by the well known anticlastic curvature caused by the Poisson's ratio effects. Figure 3.4 shows a $[-30/60]_T$ laminate which exhibits this phenomena, along with an FEA prediction of the shape deviation presented by Giddings et al. [39].

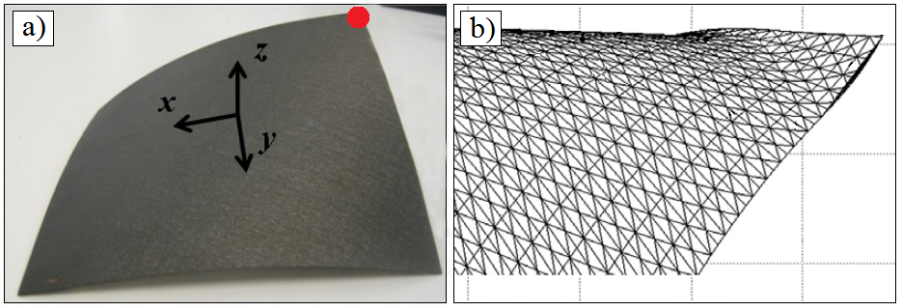

Figure 3.4: a) $[-30/60]_T$ laminate exhibiting free corner deflection, and b) FEA prediction of reversed curvature, adapted from [39].

This phenomena, classically referred to as the free-edge effect, occurs due to the conditions for equilibrium along the boundaries. A clear description of the stress mechanism is provided by Mittelstedt and Becker [68] and summarised here. The classically considered case is that of a symmetric four-ply laminate under uniaxial extension, ϵ_{11}. The stresses within the system are then the intralaminar stresses σ_{11}, σ_{22} and σ_{12}, as predcited by CLT, and the interlaminar stresses σ_{13}, σ_{23} and σ_{33} which are not considered by CLT. Figure 3.5 shows an example $[0/90/90/0]_T$ laminate which is assumed to be sufficiently long in the x_1 direction that the strains, stresses, and the transverse displacements become independent of the x_1 axis.

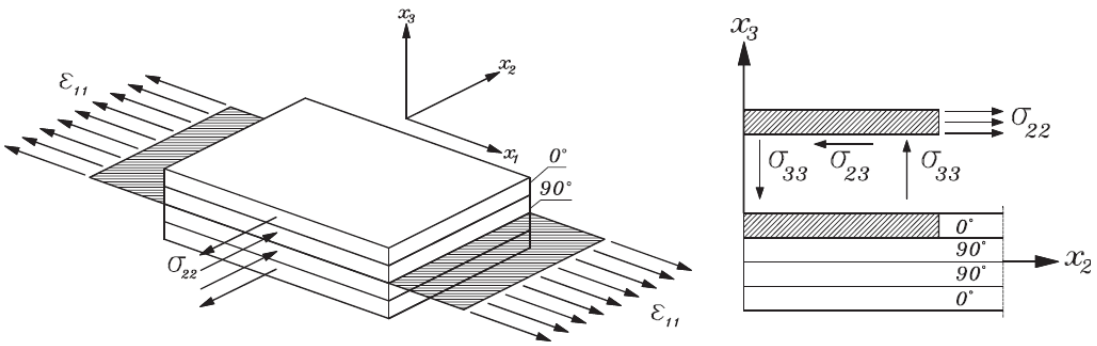

Figure 3.5: The free-edge effect in a $[0/90/90/0]_T$ laminate under uniaxial extension, from [68].

When a constant strain is applied in the x_1 direction the outer 0° plies will want to strain more than the inner 90° plies due to the differing contraction behaviour of the two layers. Hence according to CLT intralaminar normal stress σ_{22} must arise for equilibrium. The absolute values of σ_{22} will be identical in the 0° (tensile) and 90° (compressive) plies, ensuring zero resultant. Furthermore, σ_{22} must be zero at the free-edges of the laminate to conserve equilibrium in the horizontal direction. Therforefore interlaminar shear stresses σ_{23} must arise, which in turn leads to the presence of σ_{33}, or peeling stress, to maintain equilibrium of moments. In order to maintain equilibrium of forces in the x_3 direction, σ_{33} must switch sign at least once along the x_2 direction. Figure 3.6 shows typical stress distributions near the free-edge for this example where zero is considered the free-edge and d is the total laminate thickness.

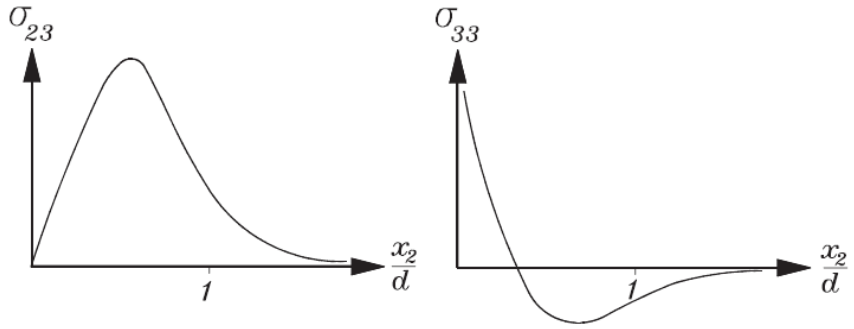

Figure 3.6: Stress distribution near the free-edge in a $[0/90/90/0]_T$ laminate under uniaxial extension, adapted from [68].

Figure 3.6 shows that large concentrations of stress are common at the free-edge, considered as the predominant reason for the onset and propagation of delaminations in this type of laminate. This becomes more prominent at the free corners of such laminates where the condition may be considered as a superposition of two adjacent edge effects. In asymmetric laminates the mismatch in thermal properties between plies induces this same mechanism and explains the localised deformations observed in Fig. 3.4.

Attempts to model this inherently localised three-dimensional field, which is naturally not predictable by CLT, are numerous and may be considered a research field in their own right. This work is therefore not detailed here but is well reviewed by Kant and Swaminathan [61], Mittelstedt and Becker [68] and Nosier and Maleki [71].

3.1.2 Bistability of Cylindrical Shells

In this section a family of thin shell structures having bistable characteristics is discussed. These structures behave much like a standard, steel tape measure in that they have a strain-free stable configuration which is straight in the longitudinal direction with a curved cross-section. By specifying certain relative stiffnesses, for example using composite materials, the structures can exhibit a second stable configuration which is highly strained but energy minimising. By providing enough external energy to climb over the 'energy threshold' between the two solutions it is possible to actuate the shell structure. An example of these configurations is shown in Fig. 3.7, taken from [43].

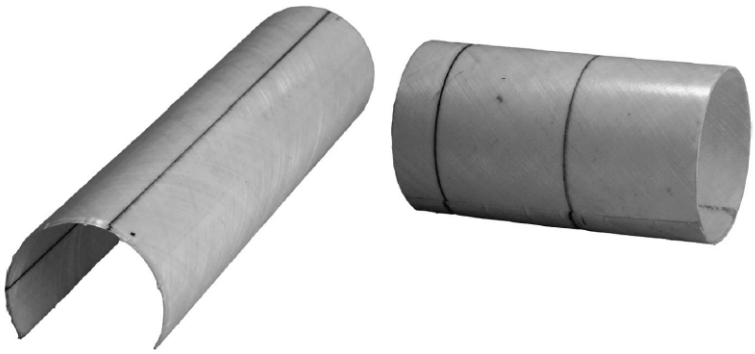

Figure 3.7: Bistable cylindrical shell with extended and coiled configurations [43].

Iqbal and Pellegrino [56] and Iqbal [57] presented a simple extensional model to capture this behaviour, able to describe both the straight and coiled configurations of a shell made of composite materials. The model considers a uniform longitudinal curvature κ_x and transverse curvature κ_y, with zero twisting, i.e. $\kappa_{xy} = 0$ everywhere. Additionally the stretching-bending coupling of the structure is omitted, i.e. it is assumed $\boldsymbol{B} = 0$. Stable shapes are then found by minimising the total energy of the shell, considered to be the sum of the bending (U_b) and stretching (U_s) energies, with respect to the two curvatures.

$$\begin{aligned} U_b &= \frac{1}{2}\beta R\left[D_{11}\kappa_x^2 + 2D_{12}\kappa_x\left(\kappa_y - \frac{1}{R}\right) + D_{22}\left(\kappa_y - \frac{1}{R}\right)^2\right] \\ U_s &= \frac{1}{2}A_{11}\left[\frac{\beta R}{2}\frac{\kappa_x^2}{\kappa_y^2} + \frac{\sin(\beta R\kappa_y)}{2}\frac{\kappa_x^2}{\kappa_y^3} - \frac{4\sin^2(\beta R\kappa_y/2)}{\beta R}\frac{\kappa_x^2}{\kappa_y^4}\right] \end{aligned} \tag{3.11}$$

where β is the angle subtending the cross-section arc and R is the radius of the cross-section. As an exmaple, this model is used to describe the anti-symmetric 45° layup defined in Table 3.1. The associated energy contour plot is shown in Fig. 3.8. The two energy minima corresponding to the cylindrical configurations are marked with crosses along with an additional unstable saddle point. While the general behaviour is captured the authors [56] note that the model does not correlate well with FEA results,

citing the assumption that the deformations are assumed to be uniform as the main source of error.

Table 3.1: $\boldsymbol{A}$, $\boldsymbol{B}$ and $\boldsymbol{D}$ matrices for anti-symmetric and symmetric 45° layups.

Antisymmetric 45° layup, $[45/\text{-}45/0/45/\text{-}45]_T$

$$\left[\begin{array}{ccc|ccc} 13.32 & 6.06 & 0 & 0 & 0 & 0.550 \\ 6.06 & 8.05 & 0 & 0 & 0 & 0.550 \\ 0 & 0 & 6.23 & 0.550 & 0.550 & 0 \\ \hline 0 & 0 & 0.550 & 0.868 & 0.665 & 0 \\ 0 & 0 & 0.550 & 0.665 & 0.848 & 0 \\ 0.550 & 0.550 & 0 & 0 & 0 & 0.681 \end{array}\right]$$

Symmetric 45° layup, $[45/\text{-}45/0/\text{-}45/45]_T$

$$\left[\begin{array}{ccc|ccc} 13.32 & 6.06 & 0 & 0 & 0 & 0 \\ 6.06 & 8.05 & 0 & 0 & 0 & 0 \\ 0 & 0 & 6.23 & 0 & 0 & 0 \\ \hline 0 & 0 & 0 & 0.868 & 0.665 & 0.345 \\ 0 & 0 & 0 & 0.665 & 0.848 & 0.345 \\ 0 & 0 & 0 & 0.345 & 0.345 & 0.681 \end{array}\right]$$

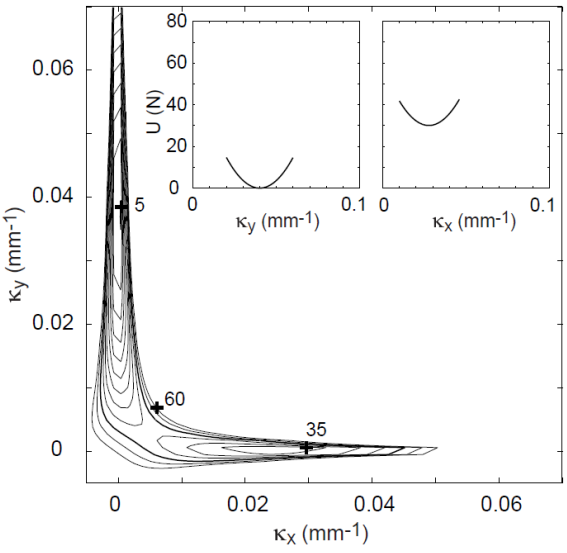

Figure 3.8: Energy contour plot for an anti-symmetric 45° layup (minima marked by crosses), from [56].

It is also noted that to avoid twisting as stated above, bending-twisting coupling has to be decoupled in this model, i.e. D_{16} and D_{26} are both zero. This means that Eq. 3.11 describes the energy of an anti-symmetric laminate. This assumption is extremely restrictive for composite laminates and cannot be justified for more general stacking sequences. For example, if this model were used to describe a symmetric 45° laminate

as defined in Table 3.1, exactly the same plot as for the anti-symmetric 45° layup would be obtained, with twisted configurations excluded.

Murphey and Pellegrino [69] extended this modelling to include the effects of pre-stressing the layers in a study of neutrally stable tape-springs. This simplistic model was compared to experimental data for cross-ply laminates with limited success. While the two stable states were predicted the magnitude of curvature was overestimated by 26%. Given the difficulties associated with manufacture and the sensitive nature of the process, these errors are unsurprising and a more indepth assessment of the problem is required.

A different approach to prestress is taken by Kebadze et al. [62]. An appropriate distribution of residual stresses to induce bistability is generated through a specified forming process for beryllium copper cylindrical shells, equivalent to the thermal stresses associated with composite laminated plates. Experimental comparison with predictions shows good agreemet with errors of around 10%. Away from bistable composites, this approach could form an interesting future study.

Galletly and Guest [35] extended the model of Iqbal and Pellegrino [56] to include twist, and thus allow a distinction to be made between symmetric and anti-symmetric layups. The assumption of uniform curvature was maintained with the structure modelled as an exact cylindrical section. However, non-zero twist κ_{xy} was allowed with a variable radius of curvature. This radius of curvature was later removed in a subsequent paper, discussed below [36], with the structure considered as a beam here and a shell in the later work. The results presented show that the model is able to capture the unstable nature of the coiled configuration for unstressed, isotropic shells. Additionally, the dependence of bistability of symmetric layups on the initial twisting is demonstrated. Results compare favourably with FEA results but show larger discrepancies when compared with experimental results. The authors attribute this disparity to phenomena not modelled by either the analytical or FEA models, such as the viscoelastic behaviour of the matrix material. Finally, it is noted that this model is relatively complex when compared wih Iqbal and Pellegrino [56], primarily due to the introduction of an additional variable to define the twist.

Later work by Galletly and Guest [36] removed the constraint on the circular arc of curvature defining the transverse shape. Instead a differential equation was introduced to describe the transverse shape. However, the model maintains the assumption that the shell is longitudinally uniform and therefore makes no attempt to model the shape transition, but does give a more detailed analysis of the stable equilibria. The calculation of the transverse shape is based on the following governing equation,

$$\frac{d^4w}{dy^4} + \frac{4}{\mu^4}w(y) = -a\left(\frac{4}{\mu^4}\right)\left(\frac{\Phi^2}{2}\left(y^2 - \frac{l^2}{12}\right)\right) \tag{3.12}$$

where w is outward displacement of the cross-section, y is the reference coordinate along the width l, Φ is the twist, a is the radius of the coiled configuration, and μ is a function of a and the stiffness properties. Equation 3.12 is an extension of the well-known 'beam on elastic foundation' of Calladine [15]. Calladine's equation is for an untwisted isotropic shell. Mansfield [64] extended the equation for isotropic shells including twist. When isotropic properties are substituted into Eq. 3.12 it reduces to that presented by Mansfield. Results presented by Galletly and Guest [36] demonstrate the differences between this and the beam model [35]. Figure 3.9 shows a comparison of the two models for an anti-symmetric 45° layup for different values of initial cross-sectional angle, characterised by α.

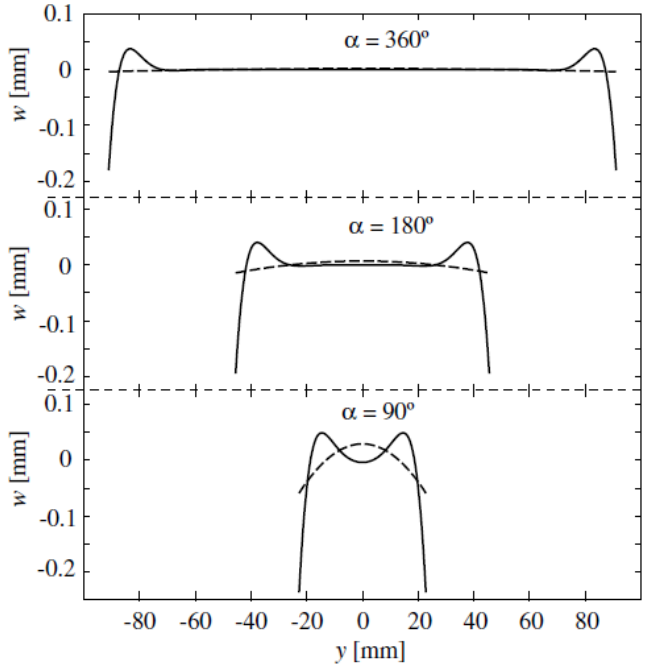

Figure 3.9: Cross-sectional shape in coiled configuration for an anti-symmetric 45° layup. Solid lines represent the shell model [36] and dashed lines the beam model [35].

A boundary layer effect is noticeable on the edge of the structure for all values of α, although the effect is far more prominent for the smaller angle. This difference between the models is noted to affect the location of equilibrium, in particular for small α. In some cases even the existence of the second configuration can be affected.

While the results presented by Galletly and Guest [36] are of real interest, the modelling is far more complex than that of [35]. Guest and Pellegrino [43] introduced a model which although less general and accurate than the one by Galletly and Guest [36], is much simpler. Importantly the simplistic nature of the model is the result of an

observation of the plot shown in Fig. 3.8, and not an arbitrary simplifiaction to reduce the complexity. Considered the 'state of the art' model of its type, it is outlined at length here.

Guest and Pellegrino [43] highlight that there is a severe penalty associated with stretching rather bending the midsurface and hence the interesting behaviour in Fig. 3.8 is concentrated around $\hat{\kappa}_x\hat{\kappa}_y \approx 0$. It is therefore possible to make the assumption that the deformation will be inextensional with a good degree of accuracy. It is then assumed that the shell can be fitted to the surface of a cylinder. Thus, the problem can be reduced to two variables defining the structural configurations, namely the radius $1/C$ of the underlying cylinder and the orientation θ of the shell relative to the cylinder, Fig. 3.10.

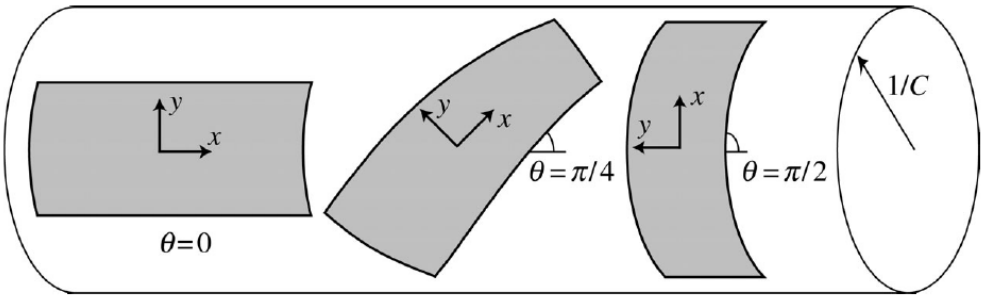

Figure 3.10: Coordinate system defining shell configurations on an underlying cylinder of radius $1/C$, from [43].

For any combination of C and θ, the curvature of the shell can be defined using a Mohr's circle as in Fig. 3.11.

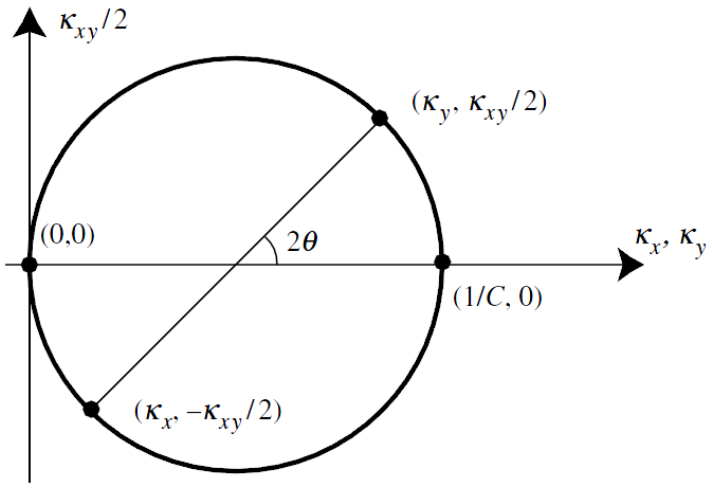

Figure 3.11: Mohr's circle of curvature for the configurations of Fig. 3.10, from [43].

In the inital configuration ($\theta = 0$), $\kappa_x = 0$, $\kappa_y = 1/R$ and $\kappa_{xy} = 0$. In the final

configuration $\kappa_x = (C/2)(1-\cos 2\theta)$, $\kappa_y = (C/2)(1+\cos 2\theta)$ and $\kappa_{xy} = C\sin 2\theta$. Thus the changes in curvature are defined by,

$$\Delta \begin{bmatrix} \kappa_x \\ \kappa_y \\ \kappa_{xy} \end{bmatrix} = \frac{C}{2} \begin{bmatrix} 1-\cos 2\theta \\ \cos 2\theta + 1 \\ 2\sin 2\theta \end{bmatrix} - \begin{bmatrix} 0 \\ 1/R \\ 0 \end{bmatrix} \tag{3.13}$$

The bending strain energy per unit area $\hat{U}$ (Eq. 3.15) can be written in terms of the following non-dimensional (written with a hat) variables,

$$\hat{U} = \frac{UR^2}{D_{11}}, \quad \hat{\boldsymbol{D}} = \frac{\boldsymbol{D}}{D_{11}}, \quad \hat{\boldsymbol{k}} = R\boldsymbol{k} = \frac{CR}{2} \begin{bmatrix} 1-\cos 2\theta \\ \cos 2\theta + 1 - 2/RC \\ 2\sin 2\theta \end{bmatrix}, \quad \hat{C} = CR \tag{3.14}$$

$$\hat{U} = \frac{1}{2}\hat{\boldsymbol{k}}^{\mathrm{T}}\hat{\boldsymbol{D}}\hat{\boldsymbol{k}} \tag{3.15}$$

where $\boldsymbol{k}$ is the matrix of curvatures. To find energy minimising equilibria the variation of $\hat{U}$ is considered with respect to the two variables defining the shell configurations.

$$\frac{\partial \hat{U}}{\partial \theta} = \hat{\boldsymbol{k}}^{\mathrm{T}}\hat{\boldsymbol{D}}\frac{\partial \hat{\boldsymbol{k}}}{\partial \theta} = 0, \quad \frac{\partial \hat{U}}{\partial \hat{C}} = \hat{\boldsymbol{k}}^{\mathrm{T}}\hat{\boldsymbol{D}}\frac{\partial \hat{\boldsymbol{k}}}{\partial \hat{C}} = 0, \tag{3.16}$$

Solution of Eq. 3.16 defines the equilibria, where the stability of solutions is checked by considering the Jacobian matrix. Two examples of this system are outlined to highlight the key points of the model, the first an isotropic example and the second an antisymmetric 45° layup, with the non-dimensional properties shown in Table 3.2.

Table 3.2: Non-dimensional $\hat{\boldsymbol{D}}$ matrices for two example shells.

Isotropic example	Antisymmetric 45° layup
$\hat{\boldsymbol{D}} = \begin{bmatrix} 1 & 0.3 & 0 \\ 0.3 & 1 & 0 \\ 0 & 0 & 0.35 \end{bmatrix}$	$\hat{\boldsymbol{D}} = \begin{bmatrix} 1 & 0.766 & 0 \\ 0.766 & 0.977 & 0 \\ 0 & 0 & 0.785 \end{bmatrix}$

The non-dimensional energy plot associated with the isotropic shell is shown in polar form in Fig. 3.12a. Two equilibrium positions are found, labelled M and N. Point M represents the original configuration and is an energy minimum. Point N is at $\theta = \pi/2$ and $\hat{C} = 0.3$ and is a saddle point. By considering the Jacobian matrix is can be confirmed that this is indeed an unstable solution, and the shell is monostable.

For the antisymmetric 45° layup $[45/\text{-}45/0/45/\text{-}45]_{\mathrm{T}}$ the associated non-dimensional energy plot is shown in Fig. 3.12b. Due to the antisymmetry of the layup there is no coupling between bending and twisting, $\hat{D}_{16} = \hat{D}_{26} = 0$ as with the isotropic example. However, the coupling between bending in x and y, $\hat{D}_{12}$, and the relative twisting stiffness $\hat{D}_{66}$ are approximately double that of the isotropic example. With these different

properties four equilibrium positions are found, labelled M, N, P and Q in Fig. 3.12b. Point M is again the initial configuration and is an energy minimum. Point N is at $\theta = \pi/2$ and $\hat{C} = 0.77$ and is a second stable energy minimum. Points P and Q at $\theta = \pm 0.3\pi/2$ and $\hat{C} = 0.52$ are saddle points. This layup is therefore found to be bistable.

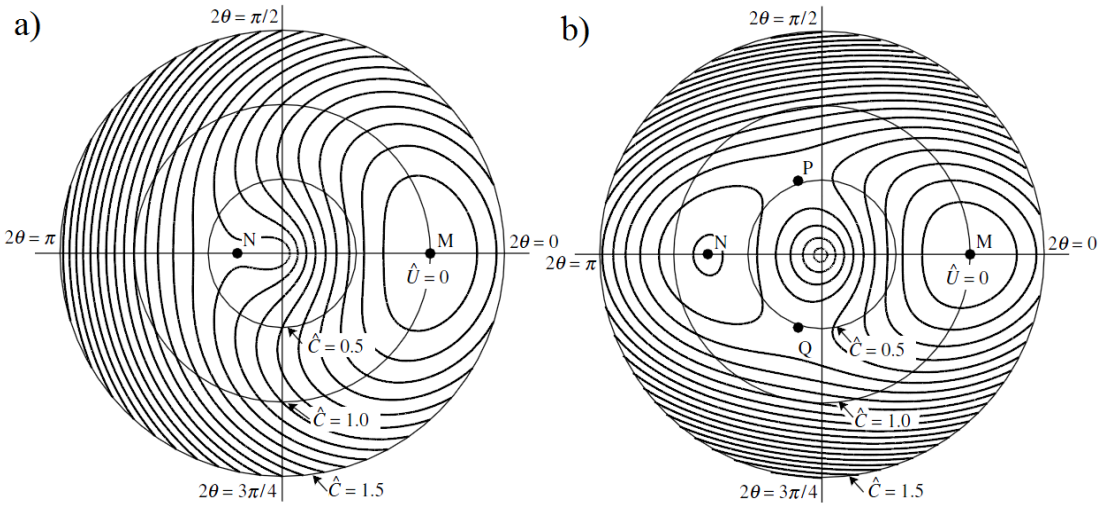

Figure 3.12: Polar plot of non-dimensional energy for a) an isotropic shell and b) an antisymmetric 45° layup, from [43]. Contours are plotted at $\hat{U} = 0.05, 0.1, 0.15$.

This model is in qualitative agreement with earlier models in that isotropic shells are found to be monostable while simple antisymmetric laminates can exhibit bistability. Furthermore, Guest and Pellegrino [43] demonstrate quantitative agreement with the more complex models of Iqbal and Pellegrino [56] and Galletly and Guest [35, 36], particularly as angle subtended by the shell in its initial state becomes large.

Comparing this model [43] with the work of Dano and Hyer [24] some important observations can be made. Dano and Hyer considered a simple out-of-plane displacement field and a second order strain formulation. By contrast, Guest and Pellegrino [43] consider the modelling in terms of curvatures which allows a linear kinematic model. This approach is clearly far simpler and more computationally manageable but does come at the expense of generality.

More recently, Seffen [94] considered the equilibrium states of extensible isotropic and orthotropic elliptical shells deforming without initial prestress. A strain energy formulation is used to derive a concise set of governing equations of deformation, which notably can be solved in a closed form manner for some isotropic cases. This particularly compact form gives rise to a search for *multi*-stability solutions, but only bistable forms are obtained. In the case of orthotropic behaviour solutions require numerical techniques. The developed technique is used to investigate the important role of ge-

ometry and initial curvature on the presence of bistability. Figure 3.13 shows example plots illustrating where bistability occurs (shaded regions) depending on initial x- and y- curvatures, $\hat{\kappa}_{x0}$ and $\hat{\kappa}_{y0}$, and initial twist $\hat{\kappa}_{xy0}$.

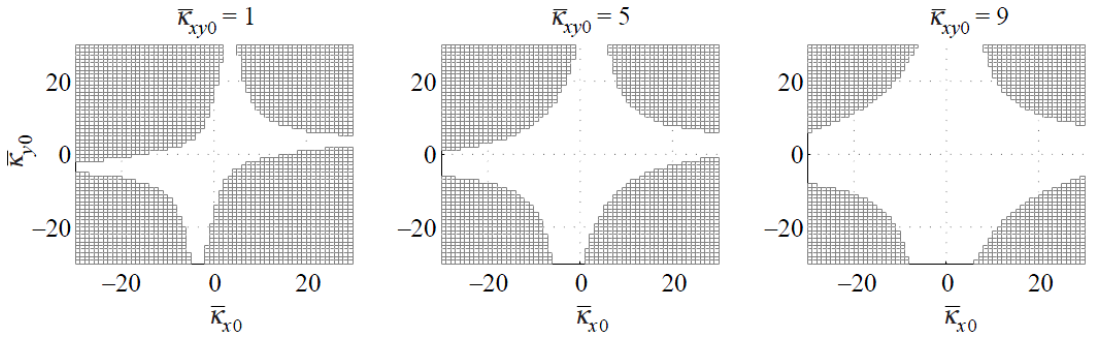

Figure 3.13: Regions of bistable configurations (shaded) for an extensible orthotropic elliptical shell with initial curvatures $\hat{\kappa}_{x0}$ and $\hat{\kappa}_{y0}$ with increasing initial twist $\hat{\kappa}_{xy0}$, unshaded regions are monostable, from [94].

Figure 3.13 shows that adding initial twist detracts from the bistability. Interestingly it is observed that isotropic shells can also be bistable given no initial twist and sufficient initial curvature in both x and y.

Vidoli and Maurini [103] extended Seffen's work [94] to demonstrate cases where particular material parameters and initial curvatures lead to apparent tristability. The modelling presented follows the same approach as Seffen [94] in order to make direct comparisons of results. Figure 3.14 shows a plot of multistable regions which has equivalent material properties to those used in Fig. 3.13 with zero initial twist. However, the plot in Fig. 3.14 considers a wider range of initial curvatures, essentially extending the bounds of Fig. 3.13. For low initial curvatures Fig. 3.14 is consistent with the patterns in Fig. 3.13. However, for large initial curvatures, H_x and H_y in this case, overlapping regions of tristability (darker grey) are reported.

Points A, B, C and D mark initial curvatures which lead to four different cases; (A) an initially flat monostable shell, (B) a bistable cup-like shell, (C) a bistable saddle-like shell and (D) a tristable shell. The behaviour of these cases for changing curvatures K_x and K_y are shown in Fig. 3.15.

Combinations of material and geometric parameters which encourage tristability are discussed but application of this theory to asymmetric laminates is difficult. As the modelling formulation does not include terms due to coupling between extension and bending (found in most asymmetric laminates), direct comparison of results with laminate plate theories cannot be performed to investigate tristability of composites.

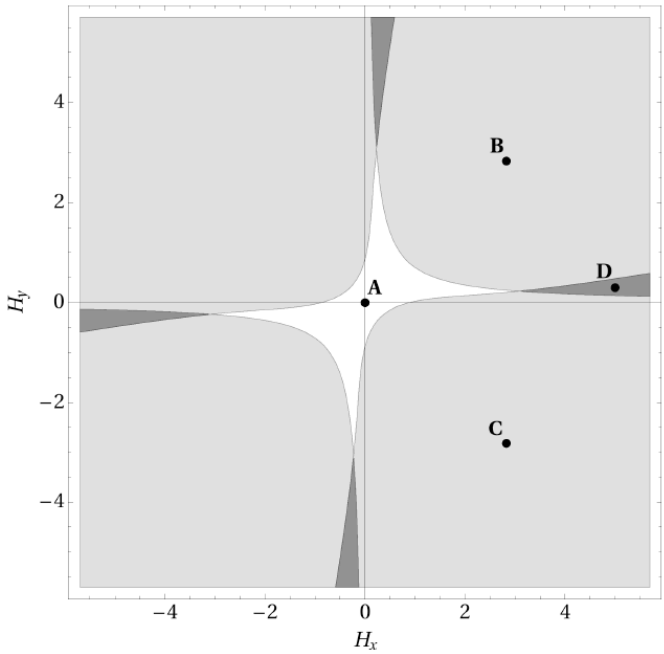

Figure 3.14: Regions of tristable solutions (dark grey) for an extensible orthotropic shell with initial curvatures H_x and H_y and zero initial twist. Light grey regions are bistable, white regions are monostable and points A-D are investigated in Fig. 3.15

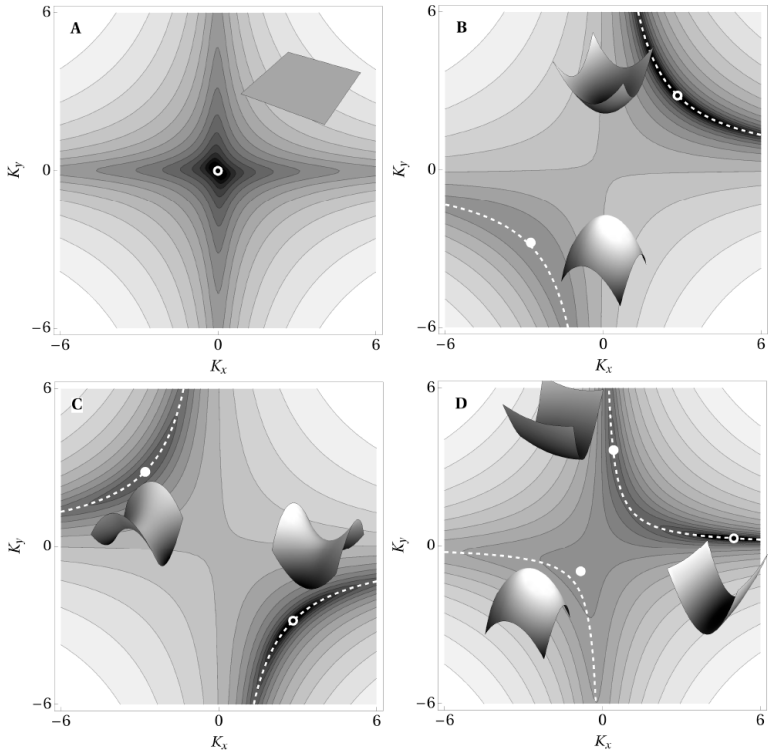

Figure 3.15: Equilibria for the four initial curvatures (a) A, (b) B, (c) C and (d) D marked in Fig. 3.14. White circles denote the minima and white−black circles denote the natural configuration and the initial curvature.

Seffen [95] later extended the earlier formulation [94] including pre-stressing by creating residual stresses. Any initial curvature is assumed to be stress-free. For simplicity the pre-stress is assumed to create residual bending stresses only, uniformly distributed throughout the shell. It is noted that the formulation could be extended to include coupling between bending and stretching, but that the formulation becomes disproportionately large for the sake of a few specialised materials. With this assumption the formulation is stated in a very elegant way, with closed form equations defining the deformations. However, these 'specialised' materials include composite laminates. The assumption of zero bending-extension coupling (zero $\boldsymbol{B}$ matrix in composite notation) would prove particularly restrictive for the studies proposed in this thesis.

While composite laminates do not necessarily exhibit bending-extension coupling, the design space for those which don't is extremely limited. Typically symmetric stacking sequences are used to avoid coupling but this is clearly not an option for bistable laminate studies. The problem of uncoupled laminates has been considered extensively in literature, a good example being a study by York [108] to characterise fully orthotropic laminate stacking sequences of discrete ply orientations. Additionally, a short study of continuous ply orientations for fully general stacking sequences in presented in Appendix A to identify a small subset of asymmetric laminates which exhibit zero bending-extension coupling.

3.2 Modelling of Bistable Laminate Actuation

The previous section has extensively outlined the existing literature for the prediction of the multiple shapes of asymmetric laminates, and therefore the potential structural deformation which can be achieved. If this structural deformation is to be realised in practical applications some method of actuating the laminate must be included in the structure and accurately modelled.

There have been numerous experimental and analytical studies in this area which can be classified as either mechanical or 'smart' actuation. This section provides an overview of the existing literature in these areas, focussing particularly on piezoelectric and shape memeory alloy (SMA) smart materials.

3.2.1 Mechanical Actuation

There have been a small number of studies considering actuation of bistable laminates using a simply applied mechanical force to provide the necessary energy input. Due to the practical limitations of requiring some external mechanism to provide the mechanical force these studies are typically presented as a proof of concept, discussed as a first step towards understanding smart actuation.

The first notable study in this area was presented by Dano and Hyer [23] in which the authors considered the response of simple cross-ply laminates of $[0_n/90_n]_{\mathrm{T}}$ layup to a force applied in the in-plane direction. This work builds on Hyer's original model for static shapes [53] by including the energy contribution due to a force applied at the end of a set of supports attached to the laminate surface. By this method a moment is generated about the geometric centre of the laminate to shallow the major curvtaure and eventually induce snap-through. The modelling formulation is then solved for incremental increases in the applied force until a state change is observed. This simplistic modelling approach, requiring just four coefficients to define the laminate shapes, showed very reasonable correlation with presented experimental data. Some divergence was observed close to the actuation point due to the limitations of the model as outlined in Section 3.1.1. Furthermore, the arrangement for actuation, stated as being designed with SMA actuation in mind, is cumbersome and impractical.

Dano and Hyer [25] later extended the formulation to general layups and off-axis force application by extending the advanced modelling approach of [24]. Figure 3.16a shows the mechanical arrangement considered, while Fig. 3.16b shows the laminate displacement under the applied force. The modelling approach is very similar to that in [23],

looking to minimise the total energy of the laminate including the contribution due to the applied force. However, the shape functions used to define the laminate deformations are necessarily more complex. Experimental results presented for three specific families of laminates showed very good agreement with modelling predictions for actuation forces. However, it is noted that the transition phase between stable states is not accurately predicted by this static approach as the transformation is a dynamic one.

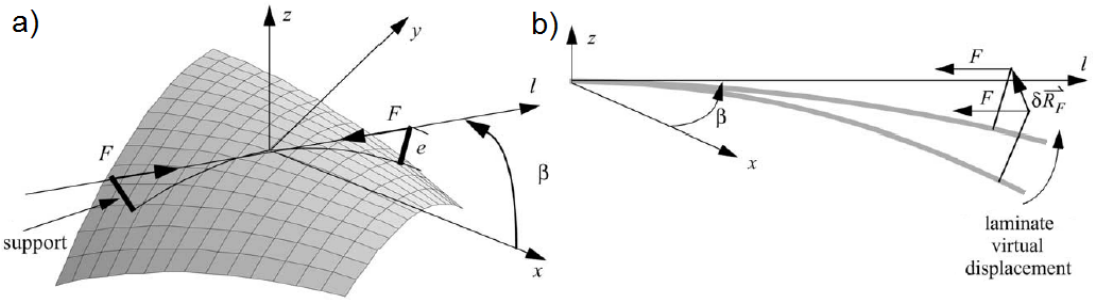

Figure 3.16: a) Geometry for actuation and b) deflection under applied force F, [25].

An alternative approach to predict the mechanical force required for actuation was presented by Schlecht and Schulte [89] using FEA. The method, suitable for laminates of fully general composition, initially captures one of the two stable states. The node at the geometric centre of the laminate is then fixed and the four corners of the laminate forced in the direction of the assumed second stable state. The peak reaction force measured at the centre node during the transition is then used to represent the actuation force. It was shown that for $[0_2/\theta_2]_\mathrm{T}$ laminates the force required to actuate increases monotonically with θ. While the stable shapes were compared to analytical modelling predictions for some laminates [55], no validation of the actuation forces was presented.

From a modelling viewpoint, and with optimisation in mind, mechanical force represents a simple mechanism which can build on existing static analysis. However, the need for external mechanisms or additional support structures is not practically ideal and perhaps does not fit the ethos of morphing/smart structures.

3.2.2 Smart Actuation

The use of smart material based actuation methods has grown significantly in recent years, and has reinvigorated research in the field of morphing structures. Chopra [18] cites five distinct reasons for this increased interest:

1. Availability of smart materials commercially.
2. Ease of embedding devices in laminated structures.

3. Exploitation of material couplings such as mechanical and electrical properties.
4. Potential of a substantial increase in performance at a small price (weight penalty).
5. Advances in microelectronics, information processing, and sensor technology.

In this section a number of existing analytical and experimental studies are described, primarily focussing on smart actuators based on piezoelectric and SMA materials.

Piezoelectric Macro-Fibre Composite Actuators

One example of smart materials being utilised for actuation is macro-fibre composite (MFC) actuators. These consist of piezoceramic fibres embedded in an epoxy matrix, sandwiched between thin layers of polymer film with interdigitated electrodes attached to the top and bottom surfaces, see Fig. 3.17. The piezoceramic fibres are typically lead zirconate titanate (PZT), often PZT-5A. This relatively soft material exhibits high piezoelectric coefficients and can therefore generate high strain per unit electric field.

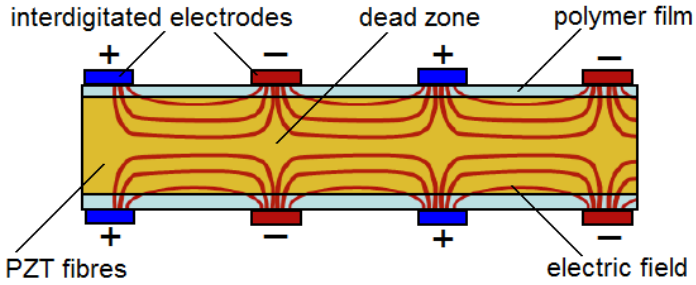

Figure 3.17: Electric field lines generated in an MFC showing variability in field directions and dead zones, adapted from [37].

To generate the maximum strain per unit electric field the poling direction of the piezoceramic is aligned with the long axis of the fibres and electric field is applied parallel to the poling direction. By aligning the poling and field directions in this manner the actuation strain is generated via the d_{33} piezoelectric coefficient (elongation), typically twice the magnitude of the transverse d_{31} coefficient.

Figure 3.17 shows the electric field directions within an MFC. The applied field is only well aligned with the fibre direction in limited regions between the interdigitated nodes, with dead areas not exposed to significant electric field highlighted in the figure. The resulting complex three-dimensional field presents a modelling challenge to capture the actuation behaviour of such a device. Existing studies using both FEA [11, 73] and analytical techniques [13, 27, 63] have been presented with limited success. While these studies do help to understand the underlying physics the inherent complexity and

computational time are far from ideal. Therefore in this section the review focusses on studies which look to represent the behaviour of MFC's based on constitutive layer properties, ideal for integration within a laminate model.

Giddings et al. [38] presented an experimental study to characterise the actuator properties of a bistable composite laminate with an MFC bonded to its upper surface. The piezo-laminate combination was evaluated in terms of its blocking force (maximum force exerted by an actuator when placed in a perfectly unyielding clamp), free displacement and load-displacement characteristics. Linear relationships were identified between blocking force and free displacement with applied voltage when the laminate was actuated in a single stable state, correlating well with the analytical studies presented in this section. The load-displacement characteristics indicated significant control of the actuation force could be achieved by the application MFC voltage.

Bowen et al. [12] presented two experimental studies to demonstrate the capability of MFC's for bistable laminate actuation. A square $[0/90]_{\mathrm{T}}$ laminate and rectangular $[0/0/90/90]_{\mathrm{T}}$ cantilever were manufactured with MFC's attached to the top surfaces. The focus of the study was to investigate the coupled behaviour between piezoelectric loading and simple mechanical loading to induce state-changes. Both structures were singly actuated in one direction only under the influence of the MFC. However, it was demonstrated that reversible actuation could be achieved by using small mechanical loads to aid a single MFC, and that these forces could be tailored by considering variation in the applied volatges. Modelling of such behaviour would require capture of nonlinear behaviour at both material and structural levels.

The first notable attempt to analytically model MFC actuation of a bistable laminate was presented by Schultz and Hyer [91]. The modelling considers minimisation of the total strain energy of the piezo-laminate structure with an applied electric field to define the shallowing shapes during actuation. The model considered cross-ply laminates only and was an extension of the unloaded model presented by Hyer [55]. The extension here was to consider the manufacture of the laminate alone as a first contribution to the strain energy, with the contributions due to attachement of the MFC and the subsequent application of an electric field as the second and third steps. These steps were treated independently as in practical experiments. It was noted that areas of locally reversed curvature exist outside the bounds of the MFC (smaller than the laminate planform), not captured by modelling due to the simplistic assumed form for the displacements. A secondary study was presented with a higher order out-of-plane displacement function,

$$w = \frac{1}{2}(c_1 x^2 + c_2 y^2) + \frac{1}{6}(c_3 x^3 + c_4 y^3) \tag{3.17}$$

It is noted that in order to apply this cubic polynomial to define the laminate profile a quarter symmetry rule was introduced (only one quadrant considered in the modelling). This higher order model was found to reduce the errors in the predicted shape but actuation voltage predictions underestimated the required voltage by around 25%. It was also noted that reversible actuation may be achievable using a second MFC attached to the opposite surface.

Schultz and Hyer [92] later validated the earlier model [91] using FEA. A number of variations of the analytical model using different levels of complexity in the shape functions were compared to FEA predictions of piezoelectrically induced shapes. The polynomial considered in [91] was found to predict the actuation voltage most accurately but still represented a large underestimation. Overall shape predictions were very good but localised phenomena such as edge effects and local deformation in regions of changing stiffness (i.e. MFC bounds) were noted.

Ren and Parvizi-Majidi [83, 85] treated the integration of an MFC within the laminate model slightly differently. It was noted that the approach of Schultz and Hyer [91, 92] to breakdown the modelling into distinct thermal and piezoelectric steps was unnecessary as the thermal loads and piezoelectric loads are mathematically similar. Where the thermal load is calculated by a temerature change and thermal expansion coefficient, the piezoelectric load is calculated by a voltage change and piezoelectric coefficient. Conceptually the laminate is considered to be manufactured in a single step with the MFC assumed to not experience the temperatue changes associated with the cure process. To validate this approach for cross-ply laminates [83] and shells with an initial pre-curvature [85], finite element results were presented for a series of laminates. Results demonstrated very close correlation of shapes and highlighted the potential for fine shape control within each stable shape. In the case of introducing some pre-curvature it was noted that if carefully designed, laminated structures could be tailored to require less external field to induce large shape deformation.

Ren [84] later extended the single step modelling approach to arbitrary layup laminates by ammending the modelling approach of Dano and Hyer [24] to include the effects of piezoelectric loads. Once again results were validated against finite element results showing very close correlation for both the direction and magnitude of principal curvature. This approach was applied to an interesting study to investigate how the shape of laminates could be finely adjusted, demonstrating how the angle of prinicipal curvature could be adjusted by applying an electric field. Potential for improving aerodynamic efficieny of aircarft wings without the large structural deformation which is typically associated with bistable laminates was highlighted.

All studies discussed to this point have been concerned with the single actuation of bistable laminates. There has been little work directed at developing mechanisms for reversible actuation between states. One study by Portela et al. [76] considered reversible actuation using a single MFC. They demonstrated that this could not be achieved without external weights to aid snap-through, citing the influence of the attached MFC on the two stable shapes. When the MFC is attached to one surface the resulting two stable shapes have different curvatures and stiffnesses. These differences and the poor alignment of the piezoelectric effect make the reverse actuation more difficult and impossible with the MFC actuator.

Schultz et al. [93] demonstrated a novel study for self-resetting laminates through the combined use of two piezoelectric MFCs attached orthogonally on opposite laminate surfaces, Fig. 3.18. A number of interesting phenomena were observed including the successful reversible actuation of a cross-ply laminate. However, the voltages required to induce the state-change were considerably higher than those predicted analytically and importantly were outside the recommended operating voltage range of the MFCs. This was partly attributed to the nature of the actuation which was not observed to be a single instantaneuous transition as predicted, but rather a multiple stage transition with individual corners of the laminate deforming prior to the global shape change. The use of MFCs which cover more of the laminate surface may overcome the problems of high required actuation voltages, time-dependent snap-through and local deformation.

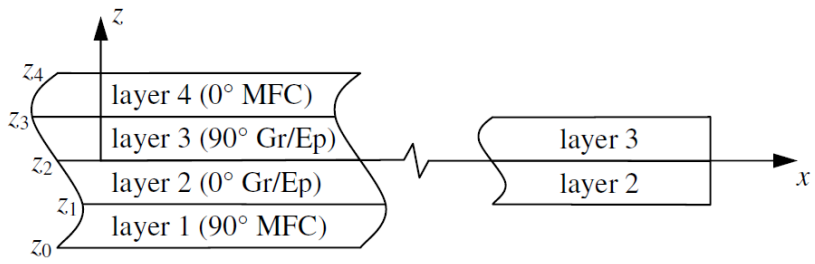

Figure 3.18: Geometry of a self-resetting cross-ply laminate, from [93].

The concept of controlling aerodynamic properties through fine piezoelectric shape control of bistable laminates was further investigated by Giddings [37]. A local spoiler bump was manufactured by integrating an elliptical bistable section within a unidirectional composite plate, actuated by an MFC attached to the top surface, Fig. 3.19. This structure was modelled using FEA to predict the raising and shallowing bump profile under an applied electric field. Excellent correlation between experimental and predicted displacements was observed although large variation in actuation voltages was stated. Despite this discrepancy, attributed to a number of manufacturing issues, this study demonstrated a novel morphing concept which demonstrates the potential for fine piezoelectric control.

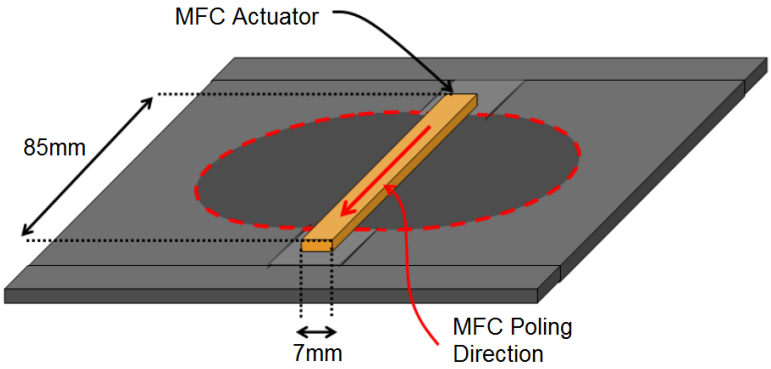

Figure 3.19: Elliptical bistable region (dark grey) within a unidirectional laminate (light grey) with an MFC actuator located on the top surface, adapted from [37].

Shape Memory Alloy Actuation

One major limitation of piezoelectric materials is that they are capable of only a relatively low strain (approx. 0.1%). While this has been demonstrated as suitable for a single actuation of a bistable laminate, the reverse or 'resetting' actuation proves more difficult, requiring multiple MFC's which can reduce the laminate curvatures.

An alternative actuation mechanism is shape memory alloy (SMA) wires which are able to induce high force and high strain (approx. 8%). The mechanism of actuation in SMA is a temperature-induced phase change (martensite to austenite) which produces a significant shear strain on heating above the transformation temperature. Typically in the form of wires for actuation, electrical resistance can be used to induce the necessary heating. A comprehensive review of the selection of SMA over alternative mechanisms is presented by Huber et al. [50]. Additionally, a limited number of analytical and experimental studies have been conducted to investigate SMA actuation of bistable laminates, briefly outlined in this section.

Dano and Hyer [26] extended their earlier mechanical actuation study [25] to include the effects of a series of SMA wires. Using a system of supports attached to the laminate surface, as described in Section 3.2.1, SMA wires were positioned above the laminate surface. In this way electrical heating of the SMA could induce a moment intended to shallow the major curvature of the laminate and eventually induce a state change. The modelling formulation was very similar to that in [25], the extension being the prediction of the SMA induced in-plane force due to heating of the SMA wires. The transition from the pure martensite to pure austenite phase was modelled as a linear variation in stress between the start and finish transition temperatures. It was demonstrated that a single SMA actuation of an arbitrary layup laminate is achievable with good correlation between predicted and experimentally observed shapes and actuation

voltages. However, no mechanism for reversing the actuation is discussed. Furthermore, as stated for the mechanical actuation, the obtrusive arrangement of supports required on the laminate surface is practically prohibitive.

Ryu et al. [87] presented an experimental and finite element study of actuation of cross-ply laminates using SMA spring (coiled SMA wire) actuators. The proposed advantage of this technology is that the spring offers multiple design parameters (number of coils, coil diameter, wire diameter etc.) which can be tailored to suit specific actuation requirements. To further investigate scope for modifying the actuation charactersitics, laminates with differing levels of intial pre-cure curvature were manufactured by laying cross-ply stacking sequences on curved metallic plates of radius of curvature between 70 and 300mm. The springs were attached to supports on the laminate surface as shown in Fig. 3.20.

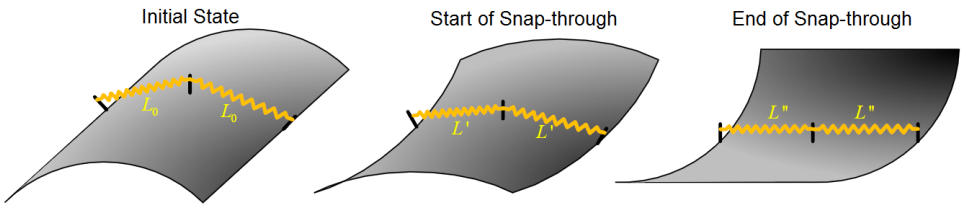

Figure 3.20: SMA spring induced actuation states for a cross-ply laminate, from [87].

Using finite element simulations the required actuation forces are determined. The design of the SMA springs are then chosen to provide the necessary force. The designed device was manufactured and tested experimentally, demonstrating the feasibility of SMA spring actuation of bistable laminates. No discussion of modelling accuracy was presented.

SMA actuation has received considerably less interest than piezoelectric actuation due to its slow response time and low bandwidth [107]. Maximum operating frequencies are lower than 10Hz for SMA compared with over 10kHz for piezoelectrics [50]. Coupled with the lack of fine control (transition occurs within a very narrow band of electrical heating), application of SMA is perhaps limited to situations requiring particularly high strain. Furthermore, SMA wires are less easily integrated into existing modelling techniques than MFCs, particularly with respect to the layer-like nature of MFCs.

3.3 Optimisation of Bistable Laminate Design

The review of existing literature on bistability of composite structures has demonstrated why optimisation of such structures presents a challenge. Unless restrictive simplifications are made, such as limiting to cross-ply laminates, ignoring coupled behaviour, or considering square laminates only, existing modelling techniques become highly complex. Furthermore, when actuation methods are included the governing equations grow further. Existing studies considering optimisation of bistable laminates are therefore extremely limited. A brief summary of work in this area is presented in this section.

Hufenbach et al. [52] considered optimisation of bistable laminate curvature through a genetic algorithm approach. The modelling was limited to cross-ply layups but required numerical solution methods to obtain the stable laminate shapes, thus ruling out gradient based optimisation technqiues. The objective of the study was to maximise the major curvature in a single stable state, or to meet a specific target curvature. The solution was not guaranteed to be bistable and the deflection between two states was not considered. Optimum solutions for maximum curvature are presented for a number of different materials with solutions differing from typical balanced thickness cross-ply laminates. Optimum curvatures were found for stacking sequences dominated by either a 0° or a 90° ply with the optimum balance of ply thicknesses found to be dependent on the material type.

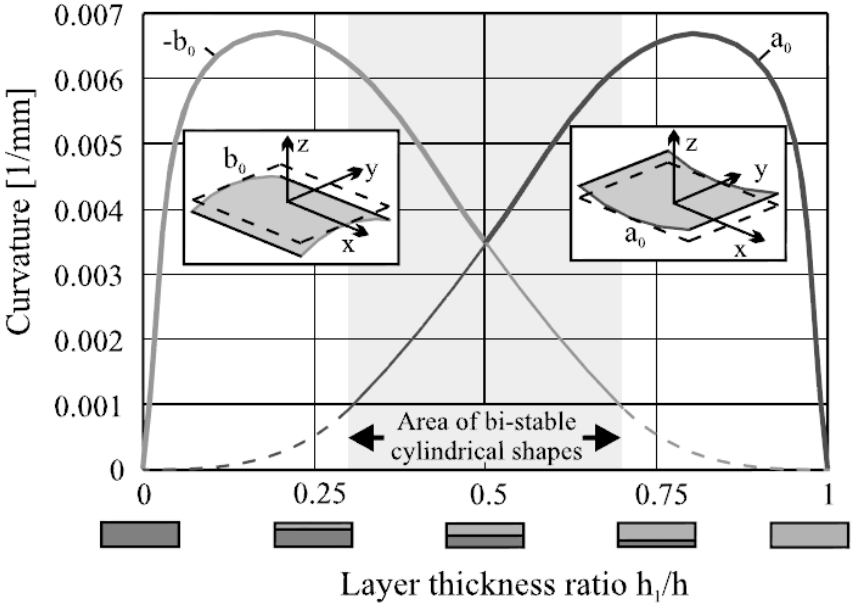

Figure 3.21: Curvature of a two-ply CFRP laminate with variable thickness ratio. Note: laminate size 300 × 300mm, total thickness h of 1mm, top layer thickness of h_1, from [52].

This study [52] was later extended by Hufenbach and Gude [51] to include failure modes of composite materials as constraints in the optimisation, found to be inactive. This work also presented a more detailed summary of the ply thicknesses for maximum curvature. A two-ply example is shown in Fig. 3.21 demonstrating the curvature in a single state with all combinations of relative ply thickness for a $[0/90]_{\mathrm{T}}$ laminate. The bistable region is shaded grey, the bounds of which define the thicknesses for maximum curvature.

A more detailed study of optimisation for a target curvature was also presented. The genetic algorithm was capable of identifying multiple solutions of differing combinations of 0° and 90° plies (variation in number and thickness of plies) to meet a target curvature in a single state within a specified tolerance. Although a primary advantage of bistable composites is the large achievable deflection between states, this example highlights the difficulty in building an understanding of both states into an iterative optimisation scheme.

On a larger scale, Panesar and Weaver [72] considered optimisation of a blended bistable laminate for a morphing flap application. In contrast to all previous studies discussed in this chapter this work presented the design of a tow-steered laminate with distinct ply orientations for each planform section. Given the complexity of this structure the design was limited to discrete ply orientations at 30° intervals. The method used FEA to assess the structural deformations and feedback information at each iteration of an ant colony optimisation routine. Designs were obtained for both maximised angle of attack and maximum out-of-plane deformation.

A number of optimisation studies have also been presented based on piezoelectrically controlled adaptive composite structures [19, 20, 21, 97]. These studies consider optimisation of piezoelectric size and location on an underlying composite structure for buckling and deformation control. These studies are of interest here as they present interesting discussion on optimisation of the piezoelectric configurations. However, the composite structures are not bistable and therefore no techniques for dealing with multiple stable states are presented.

3.4 Concluding Remarks

Modelling of Bistable Composite Plates

Analytical modelling of the thermally-induced shapes of asymmetric composite laminates has received a great deal of interest in the past few decades. This existing research appears to be split into two distinct areas; simplified modelling which allows efficient calculation of laminate shapes at the expense of greatly reducing the design space; and more complex modelling requiring numerical solution methods which allow more general application. The compromise between these two areas represents one of the main focusses of the work presented in this thesis. In order to enable optimisation studies for the design of bistable laminates the stable shapes need to be calculated at many design iterations. This requires a fast and robust modelling technique which does not currently exist for general laminate composition.

Modelling of Actuation

The requirement for an efficient modelling technique becomes even more significant when the complexity of a method of actuation is introduced. Once again, there appears to be a compromise between the simple approach of using mechanical actuation and the more complex modelling of smart actuators which offer practical advantages. Developing a modelling approach to incorporate a suitable actuation method while maintaining robustness and computational speed represents another major challenge in this work.

Optimisation of Bistable Laminate Design

The main novelty of the work undertaken in this thesis lies in the development of optimisation techniques for bistable laminate design. The modelling complexities highlighted in this chapter demonstrate why only very limited work has been conducted in this area. Development of a novel modelling formulation, coupled with identifying suitable methods to deal with the multiple equilibria inherent in this type of system, are intended to enable optimisation. Successful completion of these tasks will allow optimisation of existing technologies with the aim to identify novel solutions not considered in existing literature.

Chapter 4

Modelling of Bistable Laminate Shapes

In this chapter the analytical modelling work conducted for the static shapes of bistable laminates is described. The aim of this modelling work is to enable optimisation of bistable laminate design by removing the need for the slow numerical techniques typically required to define the shapes of arbitrary layup laminates. This includes eliminating the need for a close estimate of the shapes to reliably capture the multiple solutions.

Section 4.1 outlines the existing analytical model for the stable shapes of fully general asymmetric layups based on a constant curvature approximation. The limitations of this model from the viewpoint of optimisation are highlighted, which leads to a discussion of a simplified geometry in Section 4.2. The simplifications which can be made to the existing model due to the simplified geometry are then outlined in Section 4.3. The lamination parameter method is used to separate the model into its constitutive parts (i.e. stiffness properties, laminate geometry etc.) resulting in a matrix formulation of the governing equations. This simplified modelling formulation enables the derivation of an analytical solution, outlined in Section 4.4, with explicit expressions for each of the coefficients defining the laminate profile.

Finally, some concluding remarks discuss the application of the derived analytical method to optimisation, including consideration of how the model can be extended to more varied configurations for actuation.

4.1 Existing Model for Bistable Laminate Shapes

The existing analytical model to calculate the shapes of asymmetric laminates used as the basis for this work was first introduced by Dano and Hyer [24], and has been verified against experimental and FEA results [24, 26, 84]. The model is used to predict the shapes of laminates of general layup, referred to in this work as having an arbitrary layup. For example, Fig. 4.1 shows the shapes of a $[-30/60]_T$ laminate. Two cylindrical room-temperature shapes are observed, Figs. 4.1a and b, with equal and opposite curvatures in the x- and y-directions. A saddle shape, Fig. 4.1c, is also indicated by modelling but can be shown to be unstable.

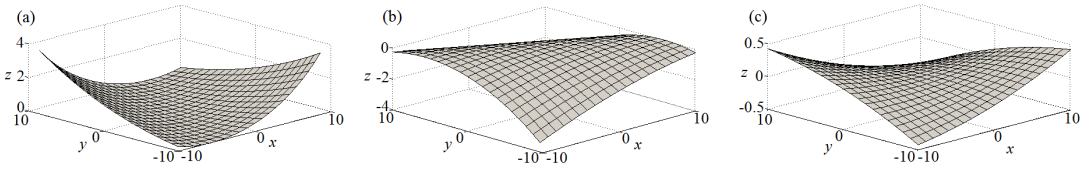

Figure 4.1: Room-temperature shapes of a square $[-30/60]_T$ laminate: (a) stable cylindrical shape, (b) opposite cylindrical shape, and (c) unstable saddle shape.

The model to predict these shapes is based on a nonlinear extension to classical laminated plate theory (CLT) [65] with approximated midplane strain functions and non-zero in-plane shear strain. A Rayleigh-Ritz method of minimisation of the total strain energy of the laminate is used to obtain information defining the room-temperature shapes.

The coordinate system used is that defined in Fig. 4.1. The origin sits at the geometric centre of the laminate and plies are defined in order starting from the negative out-of-plane surface. The out-of-plane displacement in the z-direction, w, is assumed to be of the form,

$$w = 0.5\left(ax^2 + by^2 + cxy\right) \tag{4.1}$$

where the coefficients a, b and c relate to the plate curvatures κ's as follows.

$$\begin{aligned} \kappa_x &= -\frac{\partial^2 w}{\partial x^2} = -a \\ \kappa_y &= -\frac{\partial^2 w}{\partial y^2} = -b \\ \kappa_{xy} &= -2\frac{\partial^2 w}{\partial x \partial y} = -c \end{aligned} \tag{4.2}$$

The midplane strains including geometrical nonlinearity according to the von Karman hypothesis are defined as,

$$\begin{aligned}
\epsilon_x^0 &= \frac{\partial u^0}{\partial x} + \frac{1}{2}\left(\frac{\partial w}{\partial x}\right)^2 \\
\epsilon_y^0 &= \frac{\partial v^0}{\partial y} + \frac{1}{2}\left(\frac{\partial w}{\partial y}\right)^2 \\
\epsilon_{xy}^0 &= \frac{\partial u^0}{\partial y} + \frac{\partial v^0}{\partial x} + \frac{\partial w}{\partial x}\frac{\partial w}{\partial y}
\end{aligned} \tag{4.3}$$

where u^0 and v^0 are the in-plane displacements in the x- and y-directions respectively. The midplane strains are approximated by third order polynomials. Dano and Hyer [24] considered the complete third order polynomials and found that the coefficients of the terms with powers of x and y that sum to an odd number were always zero. Therefore the form of the midplane strains can be reduced to the polynomials of Eq. 4.4.

$$\begin{aligned}
\epsilon_x^0 &= d_1 + d_2x^2 + d_3xy + d_4y^2 \\
\epsilon_y^0 &= d_5 + d_6x^2 + d_7xy + d_8y^2 \\
\epsilon_{xy}^0 &= 2d_9 + \left(ab - \frac{c^2}{4} + 2d_4 + 2d_6\right)xy \\
&\quad + \left(\frac{1}{2}\left(\frac{ac}{2} + d_3\right) + d_{10}\right)x^2 + \left(\frac{1}{2}\left(\frac{bc}{2} + d_7\right) + d_{11}\right)y^2
\end{aligned} \tag{4.4}$$

Using Eqs. 4.1 - 4.4 the in-plane displacements u^0 and v^0 can be determined.

$$\begin{aligned}
u^0 =& d_1x + d_9y + \frac{1}{2}\left(d_3 - \frac{1}{2}ac\right)x^2y + \left(d_4 - \frac{c^2}{8}\right)xy^2 + \frac{1}{3}\left(d_2 - \frac{1}{2}a^2\right)x^3 + \frac{1}{3}d_{11}y^3 \\
v^0 =& d_9x + d_5y + \frac{1}{2}\left(d_7 - \frac{1}{2}bc\right)xy^2 + \left(d_6 - \frac{c^2}{8}\right)x^2y + \frac{1}{3}\left(d_8 - \frac{1}{2}b^2\right)y^3 + \frac{1}{3}d_{10}x^3
\end{aligned} \tag{4.5}$$

The total strain energy of the laminate W can then be expressed as

$$W = \int_{vol}(\omega)\mathrm{d}vol \tag{4.6}$$

where the strain energy density ω is integrated over the volume of the laminate,

$$\omega = \frac{1}{2}c_{ijkl}\epsilon_{ij}\epsilon_{kl} - \hat{\alpha}_{ij}\epsilon_{ij}\Delta T \tag{4.7}$$

c_{ijkl}'s are elastic constants, ϵ_{ij}'s and ϵ_{kl}'s are the total strains, $\hat{\alpha}_{ij}$'s are constants related to the thermal expansion coefficients and ΔT is the change in temperature from cure. CLT follows the assumption that through-thickness stresses are small in comparison to in-plane stresses. In assuming a state of plane stress, the normal stress in the z-direction and out-of-plane shear stresses are assumed to be zero, and expansion of Eq. 4.6 leads to an expression for the total energy as a function of material and geometric properties, the temperature change and the total strains,

$$W = \int_{-L_x/2}^{L_x/2}\int_{-L_y/2}^{L_y/2}\int_{-H/2}^{H/2}\Big(\frac{1}{2}\bar{Q}_{11}\epsilon_x^2 + \bar{Q}_{12}\epsilon_x\epsilon_y + \bar{Q}_{16}\epsilon_{xy}\epsilon_x + \frac{1}{2}\bar{Q}_{22}\epsilon_y^2 + \bar{Q}_{26}\epsilon_{xy}\epsilon_y + \frac{1}{2}\bar{Q}_{66}\epsilon_{xy}^2 - \left(\bar{Q}_{11}\alpha_x + \bar{Q}_{12}\alpha_y + \bar{Q}_{16}\alpha_{xy}\right)\epsilon_x\Delta T - \left(\bar{Q}_{12}\alpha_x + \bar{Q}_{22}\alpha_y + \bar{Q}_{26}\alpha_{xy}\right)\epsilon_y\Delta T - \left(\bar{Q}_{16}\alpha_x + \bar{Q}_{26}\alpha_y + \bar{Q}_{66}\alpha_{xy}\right)\epsilon_{xy}\Delta T\Big)\mathrm{d}x\mathrm{d}y\mathrm{d}z \tag{4.8}$$

where the $\bar{Q}_{ij}$'s are the symmetric transformed stiffness matrices [65] of the individual layers, L_x and L_y are the planform side lengths of the laminate, H is the total laminate thickness and the total strains are defined as

$$\begin{aligned}\epsilon_x &= \epsilon_x^0 - za\\ \epsilon_y &= \epsilon_y^0 - zb\\ \epsilon_{xy} &= \epsilon_{xy}^0 - zc\end{aligned} \tag{4.9}$$

Substituting Eq. 4.9 into 4.8 and performing the spatial integrations results in an expression for the total energy of the laminate of the form

$$W = W\left(a, b, c, d_1, d_2, d_3, d_4, d_5, d_6, d_7, d_8, d_9, d_{10}, d_{11}\right) \tag{4.10}$$

To find the minimum energy states it is required that

$$\delta W = \sum_{i=1}^{14}\frac{\partial W}{\partial p_i}\delta p_i = 0 \tag{4.11}$$

where p_i's are a, b, c, d_1, ... , d_{11}. To meet this requirement it is necessary to have

$$f_i = \frac{\partial W}{\partial p_i} = 0; \quad i = 1, 2, ..., 14 \tag{4.12}$$

This results in 14 highly nonlinear equations to be solved to find the stable room-temperature shapes defined by the 14 shape coefficients p_i. To be a stable solution the Jacobian matrix, Eq. 4.13, must also be positive definite.

$$J = \frac{\partial\left(f_1, f_2, ..., f_{14}\right)}{\partial\left(a, b, c, d_1, ..., d_{11}\right)} \tag{4.13}$$

Symbolic computing is used to generate the 14 equilibrium equations due to the complex nature of the strain energy density function. A Newton-Raphson approach is then typically used to solve the system of equations and find the room-temperature shapes. The success of this method is highly dependent on the initial guess and convergence to a solution can be slow. Furthermore, as the problem has multiple equilibria, convergence to the desired solution can not be guaranteed and multiple initial guesses are required to identify all possible solutions.

The main aim of this work is the development of optimisation for the design of bistable laminates. With this in mind the computational issues associated with this method present a challenge. While the technique is well suited to the analysis of a single laminate the problem is not well formed for optimisation where a fast and robust method is required for the calculation of bistable laminate characteristics at every design iteration.

In this work an alternative approach to solving Eq. 4.12 is taken. By considering a simplified laminate geometry, constrained to ensure two stable states of equal and opposite curvature, an analytical solution to Eq. 4.12 is derived. This ideal laminate geometry is detailed in the next section, followed by full derivation of the simplified modelling formulation and the analytical solution.

4.2 Ideal Laminate Geometry

In the past, attempts to derive an explicit set of equations to define the stable shapes of bistable laminates have relied on assumptions or simplifications which restrict the general design space. The first work in this field by Hyer [53] was limited to cross-ply designs consisting of 0° and 90° plies. Due to the reduced number of shape coefficients required to model the problem the governing system of equilibrium equations was sufficiently simple that an analytical solution could be easily derived. By introducing arbitrary layup angles, as in this work, the number of equilibrium equations increases from 4 to 14 and the complexity of these equations increases greatly. In this case an analytical solution cannot be found.

An alternative formulation proposed by Seffen [95] outlines the governing equations of deformation for multistable shells, not limited to composite laminates. However, in order to derive the governing equations the coupling between bending and stretching is omitted. This simplification is made as the formulation becomes disproportionately large for the sake of dealing with a small set of specialised materials. However, with very few exceptions [108], composite laminates do exhibit coupling betwen bending and stretching. This point is demonstrated by a short study presented in Appendix A.

The simplifications made in both of the above cases are made for the sole purpose of reducing the complexity of the modelling. In this work the problem is considered from a practical design viewpoint and simplifications are made based on knowledge of the design space. Fully arbitrary layup is unnecessary for bistable laminate design. By focussing on geometries which will exhibit specific bistable behaviour the modelling complexity of Section 4.1 can be greatly reduced.

4.2.1 Ideal Laminate Characteristics

When designing a bistable laminate there are two main areas of concern. Firstly, the useful range of displacement between stable states. For designs requiring a high snap-through displacement the plies are positioned perpendicular to one another. For a low snap-through displacement the ply angles can either be moved closer together, which will tend towards monostability, or additional plies can be added to the structure to reduce the curvature. Secondly, we are interested in how the laminate responds to externally applied loads. It is therefore desirable to be able to tailor the directional stiffness properties of the laminate.

4.2.2 Simplified Laminate Geometry

The requirements for the simplified ideal laminate design are achieved by imposing the following set of four design rules:

1. Even number of plies with pairs of plies about the laminate midplane 90° apart.
2. Square laminate edge lengths, L.
3. Equal ply thicknesses about the laminate midplane, t_1, t_2, ... , t_n.
4. Each ply is made from the same material.

These design rules also have the property that the two stable shapes will have equal magnitude of curvature in opposite out-of-plane directions. By positioning pairs of plies at 90° to one another the laminate can exhibit maximum out-of-plane deflection. However, the scope for variation in ply orientations through-thickness means the design is not limited to maximum deflection, cross-ply designs. This simplified laminate geometry is illustrated in Fig. 4.2.

Outlined in the following sections are the modelling simplifications associated with this simplified design with pairs of orthogonal plies. For brevity this stacking sequence is referred to as cross-symmetric from here onwards. For simplicity and to reduce the length of the derivations the following sections focus on a two-ply example of the design rules. However, all of the work is easily extended to the full n-ply design case with different individual ply thicknesses. This is demonstrated in Section 4.3.3.

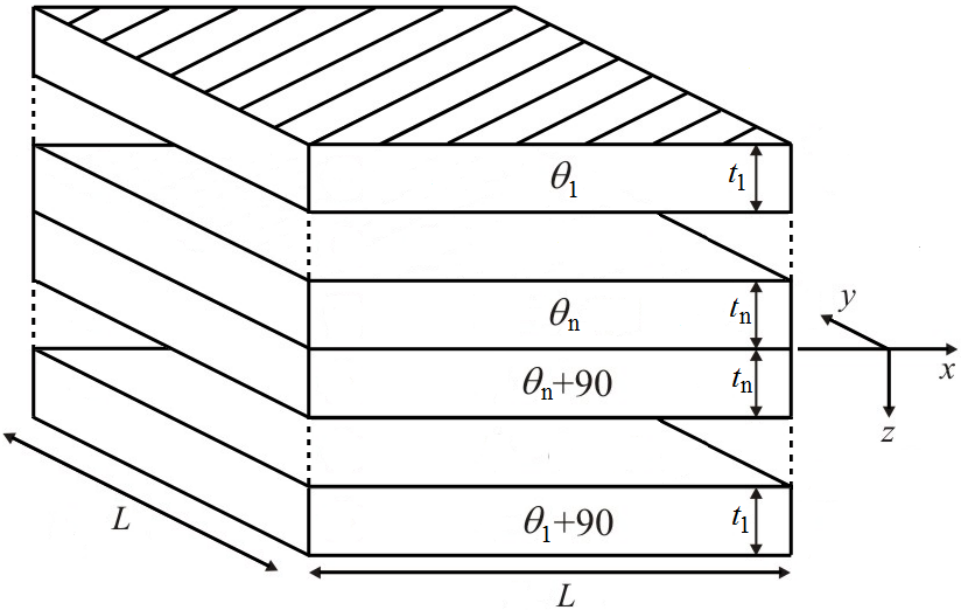

Figure 4.2: n-ply laminate geometry ensuring curvatures of equal magnitude and opposite direction.

4.3 Modelling Simplifications for an Ideal Geometry

The system of energy equilibrium equations to be solved to find the stable laminate shapes, Eq. 4.12, is a function of material stiffness terms, thermal forces and moments, and a set of shape coefficients used to define the in-plane and out-of-plane deflections. With the simplifications made to the laminate geometry in Section 4.2 a number of simplifications to the modelling can be made, reducing the system to a more manageable size in order to find an analytical solution. In this section the simplifications which can be made in each of these areas are outlined.

4.3.1 Simplified Stiffness Matrices

The expression for the total strain energy of a laminate, Eq. 4.10, is a function of the in-plane ($\boldsymbol{A}$), coupling ($\boldsymbol{B}$), and flexural ($\boldsymbol{D}$) stiffness matrices [65]. These stiffness terms are classically evaluated by performing the following integrations:

$$[A_{ij}, B_{ij}, D_{ij}] = \int_{-H/2}^{H/2} \bar{Q}_{ij} \left[1, z, z^2\right] \mathrm{d}z \tag{4.14}$$

where H is the total laminate thickness and the $\bar{Q}_{ij}$'s are the transformed stiffnesses defined as follows,

$$\begin{aligned}
\bar{Q}_{11} &= Q_{11}m^4 + 2(Q_{12} + 2Q_{66})n^2m^2 + Q_{22}n^4 \\
\bar{Q}_{22} &= Q_{11}n^4 + 2(Q_{12} + 2Q_{66})n^2m^2 + Q_{22}m^4 \\
\bar{Q}_{12} &= (Q_{11} + Q_{22} - 4Q_{66})n^2m^2 + Q_{12}(m^4 + n^4) \\
\bar{Q}_{66} &= (Q_{11} + Q_{22} - 2Q_{12} - 2Q_{66})n^2m^2 + Q_{66}(m^4 + n^4) \\
\bar{Q}_{16} &= (Q_{11} - Q_{12} - 2Q_{66})nm^3 + (Q_{12} - Q_{22} + 2Q_{66})n^3m \\
\bar{Q}_{26} &= (Q_{11} - Q_{12} - 2Q_{66})n^3m + (Q_{12} - Q_{22} + 2Q_{66})nm^3
\end{aligned} \tag{4.15}$$

where m and n are the trigonometric functions $\cos\theta$ and $\sin\theta$ respectively, θ is the ply orientation, and the Q's are the classically defined terms of the stiffness matrix,

$$\begin{aligned}
Q_{11} &= \frac{E_{11}}{1 - \nu_{12}\nu_{21}} \\
Q_{22} &= \frac{E_{22}}{1 - \nu_{12}\nu_{21}} \\
Q_{12} &= \frac{E_{11}\nu_{21}}{1 - \nu_{12}\nu_{21}} \\
Q_{66} &= G_{12}
\end{aligned} \tag{4.16}$$

where E_{11} is the longitudinal Young's modulus, E_{22} is the transverse Young's modulus, G_{12} is the shear modulus, ν_{12} is the major Poisson's ratio, and the minor Poisson's ratio ν_{21} is defined as,

$$\nu_{21} = \nu_{12}\frac{E_{22}}{E_{11}} \tag{4.17}$$

For off-axis ply orientations the expressions for the $\boldsymbol{A}$, $\boldsymbol{B}$ and $\boldsymbol{D}$ matrices are complex in nature, referring in particular to the trigonometric functions of Eq. 4.15. In order to more easily allow the ply angle θ to be a variable in a later optimisation formulation an alternative method of evaluating the $\boldsymbol{A}$, $\boldsymbol{B}$ and $\boldsymbol{D}$ matrices is introduced, replacing the trigonometric power functions with multiple-angle functions as follows [100],

$$\begin{aligned}
m^4 &= \frac{1}{8}(3 + 4\cos 2\theta + \cos 4\theta) \\
n^4 &= \frac{1}{8}(3 - 4\cos 2\theta + \cos 4\theta) \\
m^2n^2 &= \frac{1}{8}(1 - \cos 4\theta) \\
m^3n &= \frac{1}{8}(2\sin 2\theta + \sin 4\theta) \\
mn^3 &= \frac{1}{8}(2\sin 2\theta - \sin 4\theta)
\end{aligned} \tag{4.18}$$

Substitution of Eq. 4.18 into each of the components of Eq. 4.15 results in the following simplified expressions for the transformed stiffness terms. Full derivations of these

expressions can be found in Appendix B.1.

$$\begin{aligned}
\bar{Q}_{11} &= U_1 + U_2\cos 2\theta + U_3\cos 4\theta \\
\bar{Q}_{22} &= U_1 - U_2\cos 2\theta + U_3\cos 4\theta \\
\bar{Q}_{12} &= U_4 - U_3\cos 4\theta \\
\bar{Q}_{66} &= U_5 - U_3\cos 4\theta \\
\bar{Q}_{16} &= \frac{1}{2}U_2\sin 2\theta + U_3\sin 4\theta \\
\bar{Q}_{26} &= \frac{1}{2}U_2\sin 2\theta - U_3\sin 4\theta
\end{aligned} \tag{4.19}$$

where U_{1-5} are the linear combinations of single ply stiffness properties of Eq. 4.20, referred to as the stiffness invariants, and are independent of laminate geometry and ply orientations.

$$\begin{aligned}
U_1 &= \frac{1}{8}(3Q_{11} + 3Q_{22} + 2Q_{12} + 4Q_{66}) \\
U_2 &= \frac{1}{2}(Q_{11} - Q_{22}) \\
U_3 &= \frac{1}{8}(Q_{11} + Q_{22} - 2Q_{12} - 4Q_{66}) \\
U_4 &= \frac{1}{8}(Q_{11} + Q_{22} + 6Q_{12} - 4Q_{66}) \\
U_5 &= \frac{1}{8}(Q_{11} + Q_{22} - 2Q_{12} + 4Q_{66})
\end{aligned} \tag{4.20}$$

Equation 4.20 can be further simplified by separating the material properties and coefficients as follows,

$$[\boldsymbol{U}] = [U_1 \;\; U_2 \;\; U_3 \;\; U_4 \;\; U_5] = [\boldsymbol{Q}][\boldsymbol{Q}_{coef}] \tag{4.21}$$

where $\boldsymbol{Q}$ is the matrix of stiffness terms,

$$[\boldsymbol{Q}] = \begin{bmatrix} Q_{11} & Q_{22} & Q_{12} & Q_{66} \end{bmatrix} \tag{4.22}$$

and $\boldsymbol{Q}_{coef}$ is the matrix of associated coefficients.

$$[\boldsymbol{Q}_{coef}] = \begin{bmatrix}
\frac{3}{8} & \frac{1}{2} & \frac{1}{8} & \frac{1}{8} & \frac{1}{8} \\
\frac{3}{8} & -\frac{1}{2} & \frac{1}{8} & \frac{1}{8} & \frac{1}{8} \\
\frac{1}{4} & 0 & -\frac{1}{4} & \frac{3}{4} & -\frac{1}{4} \\
\frac{1}{2} & 0 & -\frac{1}{2} & -\frac{1}{2} & \frac{1}{2}
\end{bmatrix} \tag{4.23}$$

Equation 4.19 is then substituted into Eq. 4.14, resulting in the following expressions for all terms of the $\boldsymbol{A}$, $\boldsymbol{B}$ and $\boldsymbol{D}$ matrices. Full derivations of these expressions can be found in Appendix B.2.

$$
\begin{aligned}
[A_{11}, B_{11}, D_{11}] &= U_1 \int_{-H/2}^{H/2} \left[1, z, z^2\right] \mathrm{d}z + U_2 \int_{-H/2}^{H/2} \cos 2\theta \left[1, z, z^2\right] \mathrm{d}z \\
&\quad + U_3 \int_{-H/2}^{H/2} \cos 4\theta \left[1, z, z^2\right] \mathrm{d}z \\
[A_{22}, B_{22}, D_{22}] &= U_1 \int_{-H/2}^{H/2} \left[1, z, z^2\right] \mathrm{d}z - U_2 \int_{-H/2}^{H/2} \cos 2\theta \left[1, z, z^2\right] \mathrm{d}z \\
&\quad + U_3 \int_{-H/2}^{H/2} \cos 4\theta \left[1, z, z^2\right] \mathrm{d}z \\
[A_{12}, B_{12}, D_{12}] &= U_4 \int_{-H/2}^{H/2} \left[1, z, z^2\right] \mathrm{d}z - U_3 \int_{-H/2}^{H/2} \cos 4\theta \left[1, z, z^2\right] \mathrm{d}z \\
[A_{66}, B_{66}, D_{66}] &= U_5 \int_{-H/2}^{H/2} \left[1, z, z^2\right] \mathrm{d}z - U_3 \int_{-H/2}^{H/2} \cos 4\theta \left[1, z, z^2\right] \mathrm{d}z \\
[A_{16}, B_{16}, D_{16}] &= \frac{1}{2} U_2 \int_{-H/2}^{H/2} \sin 2\theta \left[1, z, z^2\right] \mathrm{d}z + U_3 \int_{-H/2}^{H/2} \sin 4\theta \left[1, z, z^2\right] \mathrm{d}z \\
[A_{26}, B_{26}, D_{26}] &= \frac{1}{2} U_2 \int_{-H/2}^{H/2} \sin 2\theta \left[1, z, z^2\right] \mathrm{d}z - U_3 \int_{-H/2}^{H/2} \sin 4\theta \left[1, z, z^2\right] \mathrm{d}z
\end{aligned}
\tag{4.24}
$$

The remaining trigonometric integrals of Eq. 4.24 are known as the lamination parameters and are defined below.

$$
\begin{aligned}
V_1^A &= \int_{-H/2}^{H/2} \cos 2\theta \mathrm{d}z, \quad V_1^B = \int_{-H/2}^{H/2} \cos 2\theta \mathrm{d}z, \quad V_1^D = \int_{-H/2}^{H/2} \cos 2\theta z^2 \mathrm{d}z \\
V_2^A &= \int_{-H/2}^{H/2} \cos 4\theta \mathrm{d}z, \quad V_2^B = \int_{-H/2}^{H/2} \cos 4\theta \mathrm{d}z, \quad V_2^D = \int_{-H/2}^{H/2} \cos 4\theta z^2 \mathrm{d}z \\
V_3^A &= \int_{-H/2}^{H/2} \sin 2\theta \mathrm{d}z, \quad V_3^B = \int_{-H/2}^{H/2} \sin 2\theta \mathrm{d}z, \quad V_3^D = \int_{-H/2}^{H/2} \sin 2\theta z^2 \mathrm{d}z \\
V_4^A &= \int_{-H/2}^{H/2} \sin 4\theta \mathrm{d}z, \quad V_4^B = \int_{-H/2}^{H/2} \sin 4\theta \mathrm{d}z, \quad V_4^D = \int_{-H/2}^{H/2} \sin 4\theta z^2 \mathrm{d}z
\end{aligned}
\tag{4.25}
$$

Substitution of Eq. 4.25 into Eq. 4.24 results in the following simplified form of the $\boldsymbol{A}$, $\boldsymbol{B}$ and $\boldsymbol{D}$ matrices.

$$
\begin{aligned}
[A_{11}, B_{11}, D_{11}] &= U_1 \left[H, 0, H^3/12\right] + U_2 \left[V_1^A, V_1^B, V_1^D\right] + U_3 \left[V_2^A, V_2^B, V_2^D\right] \\
[A_{22}, B_{22}, D_{22}] &= U_1 \left[H, 0, H^3/12\right] - U_2 \left[V_1^A, V_1^B, V_1^D\right] + U_3 \left[V_2^A, V_2^B, V_2^D\right] \\
[A_{12}, B_{12}, D_{12}] &= U_4 \left[H, 0, H^3/12\right] - U_3 \left[V_2^A, V_2^B, V_2^D\right] \\
[A_{66}, B_{66}, D_{66}] &= U_5 \left[H, 0, H^3/12\right] - U_3 \left[V_2^A, V_2^B, V_2^D\right] \\
[A_{16}, B_{16}, D_{16}] &= (1/2)\, U_2 \left[V_3^A, V_3^B, V_3^D\right] + U_3 \left[V_4^A, V_4^B, V_4^D\right] \\
[A_{26}, B_{26}, D_{26}] &= (1/2)\, U_2 \left[V_3^A, V_3^B, V_3^D\right] - U_3 \left[V_4^A, V_4^B, V_4^D\right]
\end{aligned}
\tag{4.26}
$$

For design rules 1 and 3, and for a two-ply example, the lamination parameters of Eq. 4.25 can be evaluated in terms of first ply angle and single ply thickness only. Derivation of these expressions can be found in Appendix B.3 and are expressed in

their simplest form below.

$$\begin{aligned}\boldsymbol{V}^A &= 2t\begin{bmatrix}0 & \cos 4\theta_1 & 0 & \sin 4\theta_1\end{bmatrix}\\ \boldsymbol{V}^B &= -t^2\begin{bmatrix}\cos 2\theta_1 & 0 & \sin 2\theta_1 & 0\end{bmatrix}\\ \boldsymbol{V}^D &= \frac{2t^3}{3}\begin{bmatrix}0 & \cos 4\theta_1 & 0 & \sin 4\theta_1\end{bmatrix}\end{aligned} \tag{4.27}$$

Noting that half of the terms of Eq. 4.27 are zero, Eq. 4.26 can be reduced to the following form

$$\begin{aligned}[A_{11}, B_{11}, D_{11}] &= U_1\left[H, 0, H^3/12\right] + U_2\left[0, V_1^B, 0\right] + U_3\left[V_2^A, 0, V_2^D\right]\\ [A_{22}, B_{22}, D_{22}] &= U_1\left[H, 0, H^3/12\right] - U_2\left[0, V_1^B, 0\right] + U_3\left[V_2^A, 0, V_2^D\right]\\ [A_{12}, B_{12}, D_{12}] &= U_4\left[H, 0, H^3/12\right] - U_3\left[V_2^A, 0, V_2^D\right]\\ [A_{66}, B_{66}, D_{66}] &= U_5\left[H, 0, H^3/12\right] - U_3\left[V_2^A, 0, V_2^D\right]\\ [A_{16}, B_{16}, D_{16}] &= (1/2)\,U_2\left[0, V_3^B, 0\right] + U_3\left[V_4^A, 0, V_4^D\right]\\ [A_{26}, B_{26}, D_{26}] &= (1/2)\,U_2\left[0, V_3^B, 0\right] - U_3\left[V_4^A, 0, V_4^D\right]\end{aligned} \tag{4.28}$$

Inspection of Eq. 4.28 reveals that certain terms of the $\boldsymbol{A}$, $\boldsymbol{B}$ and $\boldsymbol{D}$ matrices are equal to each other for this design case. The matrices can therefore be expressed in the following simplified form, which reduces the complexity of Eq. 4.10.

$$\boldsymbol{A} = \begin{bmatrix}A_{11} & A_{12} & A_{16}\\ A_{12} & A_{11} & -A_{16}\\ A_{16} & -A_{16} & A_{66}\end{bmatrix}, \boldsymbol{B} = \begin{bmatrix}B_{11} & 0 & B_{16}\\ 0 & -B_{11} & B_{16}\\ B_{16} & B_{16} & 0\end{bmatrix}, \boldsymbol{D} = \begin{bmatrix}D_{11} & D_{12} & D_{16}\\ D_{12} & D_{11} & -D_{16}\\ D_{16} & -D_{16} & D_{66}\end{bmatrix} \tag{4.29}$$

Combining Eqs. 4.27 and 4.28, the remaining terms of Eq. 4.29 can be expressed as

$$[A_{11}\ A_{12}\ A_{16}\ A_{66}\ B_{11}\ B_{16}\ D_{11}\ D_{12}\ D_{16}\ D_{66}] = [\boldsymbol{U}]\,[\boldsymbol{Z}]\,[\boldsymbol{T}] \tag{4.30}$$

where $\boldsymbol{U}$ is defined by Eq. 4.21, $\boldsymbol{Z}$ is the matrix of ply orientation dependent components of the lamination parameters,

$$[\boldsymbol{Z}] = \begin{bmatrix}1 & 0 & 0 & 0 & 0 & 0 & 1 & 0 & 0 & 0\\ 0 & 0 & 0 & 0 & Z_1^B & Z_3^B/2 & 0 & 0 & 0 & 0\\ Z_2^A & -Z_2^A & Z_4^A & -Z_2^A & 0 & 0 & Z_2^D & -Z_2^D & Z_4^D & -Z_2^D\\ 0 & 1 & 0 & 0 & 0 & 0 & 0 & 1 & 0 & 0\\ 0 & 0 & 0 & 1 & 0 & 0 & 0 & 0 & 0 & 1\end{bmatrix} \tag{4.31}$$

where $\boldsymbol{Z}$ terms are defined as

$$\boldsymbol{Z}^A = \frac{\boldsymbol{V}^A}{2t}, \quad \boldsymbol{Z}^B = \frac{\boldsymbol{V}^B}{-t^2}, \quad \boldsymbol{Z}^D = \frac{\boldsymbol{V}^D}{\frac{2}{3}t^3} \tag{4.32}$$

and $\boldsymbol{T}$ is the diagonal matrix of ply thickness dependent components of the lamination parameters.

$$[\boldsymbol{T}] = \text{diag}\left[2t \quad 2t \quad 2t \quad 2t \quad -t^2 \quad -t^2 \quad \tfrac{2}{3}t^3 \quad \tfrac{2}{3}t^3 \quad \tfrac{2}{3}t^3 \quad \tfrac{2}{3}t^3\right] \tag{4.33}$$

4.3.2 Simplified Thermal Forces and Moments

The stiffness invariants and lamination parameters can also be applied to thermal forces and moments, as considered by Diaconu and Sekine [28] and corrected in [29]. Expansion of Eq. 4.8 results in consideration of the thermally induced forces, N_x^T, N_y^T and N_{xy}^T, and moments, M_x^T, M_y^T and M_{xy}^T, defined as

$$\begin{aligned}
[N_x^T, M_x^T] &= \int_{-H/2}^{H/2} (\bar{Q}_{11}\alpha_x + \bar{Q}_{12}\alpha_y + \bar{Q}_{16}\alpha_{xy})\Delta T[1, z]\mathrm{d}z \\
[N_y^T, M_y^T] &= \int_{-H/2}^{H/2} (\bar{Q}_{12}\alpha_x + \bar{Q}_{22}\alpha_y + \bar{Q}_{26}\alpha_{xy})\Delta T[1, z]\mathrm{d}z \\
[N_{xy}^T, M_{xy}^T] &= \int_{-H/2}^{H/2} (\bar{Q}_{16}\alpha_x + \bar{Q}_{26}\alpha_y + \bar{Q}_{66}\alpha_{xy})\Delta T[1, z]\mathrm{d}z
\end{aligned} \tag{4.34}$$

where α's are the thermal expansion coefficients in the x-y plane and are defined as

$$\begin{aligned}
\alpha_x &= \alpha_1 \cos^2\theta + \alpha_2 \sin^2\theta = \alpha_1\left(\frac{1}{2} + \frac{1}{2}\cos 2\theta\right) + \alpha_2\left(\frac{1}{2} - \frac{1}{2}\cos 2\theta\right) \\
&= \frac{1}{2}(\alpha_1 + \alpha_2) + \frac{1}{2}\cos 2\theta(\alpha_1 - \alpha_2) \\
\alpha_y &= \alpha_1 \sin^2\theta + \alpha_2 \cos^2\theta = \alpha_1\left(\frac{1}{2} - \frac{1}{2}\cos 2\theta\right) + \alpha_2\left(\frac{1}{2} + \frac{1}{2}\cos 2\theta\right) \\
&= \frac{1}{2}(\alpha_1 + \alpha_2) + \frac{1}{2}\cos 2\theta(\alpha_2 - \alpha_1) \\
\alpha_{xy} &= 2(\alpha_1 - \alpha_2)\cos\theta\sin\theta = (\alpha_1 - \alpha_2)\sin 2\theta
\end{aligned} \tag{4.35}$$

where α_1 and α_2 are the material thermal expansion coefficients in the fibre and transverse directions respectively. For a two-ply stacking sequence following the layup definition of design rule 1, the global thermal coefficients of each ply become,

$$\begin{aligned}
\alpha_{x,1} &= \frac{1}{2}(\alpha_1 + \alpha_2) + \frac{1}{2}\cos 2\theta_1(\alpha_1 - \alpha_2) \\
\alpha_{y,1} &= \frac{1}{2}(\alpha_1 + \alpha_2) + \frac{1}{2}\cos 2\theta_1(\alpha_2 - \alpha_1) \\
\alpha_{xy,1} &= (\alpha_1 - \alpha_2)\sin 2\theta_1
\end{aligned} \tag{4.36}$$

$$\begin{aligned}
\alpha_{x,2} &= \frac{1}{2}(\alpha_1 + \alpha_2) + \frac{1}{2}\cos(2\theta_1 + 180)(\alpha_1 - \alpha_2) \\
&= \frac{1}{2}(\alpha_1 + \alpha_2) - \frac{1}{2}\cos 2\theta_1(\alpha_1 - \alpha_2) \\
\alpha_{y,2} &= \frac{1}{2}(\alpha_1 + \alpha_2) + \frac{1}{2}\cos(2\theta_1 + 180)(\alpha_2 - \alpha_1) \\
&= \frac{1}{2}(\alpha_1 + \alpha_2) - \frac{1}{2}\cos 2\theta_1(\alpha_2 - \alpha_1) \\
\alpha_{xy,2} &= (\alpha_1 - \alpha_2)\sin(2\theta_1 + 180) \\
&= -(\alpha_1 - \alpha_2)\sin 2\theta_1
\end{aligned} \tag{4.37}$$

where the additional subscript denotes the ply number. Equations 4.36 and 4.37 demonstrate that the following relationships exist for the layup sequence $[\theta_1, \theta_1 + 90]_{\mathrm{T}}$.

$$\alpha_{x,2} = \alpha_{y,1}, \quad \alpha_{y,2} = \alpha_{x,1}, \quad \alpha_{xy,2} = -\alpha_{xy,1} \tag{4.38}$$

Thermal Forces

The thermal forces are first considered. Expansion of Eq. 4.34 for the two-ply design case leads to the following sums for N_x^T, N_y^T and N_{xy}^T.

$$\begin{aligned}
N_x^T &= t\Delta T\left(\bar{Q}_{11,1}\alpha_{x,1} + \bar{Q}_{12,1}\alpha_{y,1} + \bar{Q}_{16,1}\alpha_{xy,1} + \bar{Q}_{11,2}\alpha_{x,2} + \bar{Q}_{12,2}\alpha_{y,2} + \bar{Q}_{16,2}\alpha_{xy,2}\right) \\
N_y^T &= t\Delta T\left(\bar{Q}_{12,1}\alpha_{x,1} + \bar{Q}_{22,1}\alpha_{y,1} + \bar{Q}_{26,1}\alpha_{xy,1} + \bar{Q}_{12,2}\alpha_{x,2} + \bar{Q}_{22,2}\alpha_{y,2} + \bar{Q}_{26,2}\alpha_{xy,2}\right) \\
N_{xy}^T &= t\Delta T\left(\bar{Q}_{16,1}\alpha_{x,1} + \bar{Q}_{26,1}\alpha_{y,1} + \bar{Q}_{66,1}\alpha_{xy,1} + \bar{Q}_{16,2}\alpha_{x,2} + \bar{Q}_{26,2}\alpha_{y,2} + \bar{Q}_{66,2}\alpha_{xy,2}\right)
\end{aligned} \tag{4.39}$$

Substitution of Eq. 4.38 in to Eq. 4.39 results in the following simplified form.

$$\begin{aligned}
N_x^T &= t\Delta T\left[\alpha_{x,1}\left(\bar{Q}_{11,1} + \bar{Q}_{12,2}\right) + \alpha_{y,1}\left(\bar{Q}_{12,1} + \bar{Q}_{11,2}\right) + \alpha_{xy,1}\left(\bar{Q}_{16,1} - \bar{Q}_{16,2}\right)\right] \\
N_y^T &= t\Delta T\left[\alpha_{x,1}\left(\bar{Q}_{12,1} + \bar{Q}_{22,2}\right) + \alpha_{y,1}\left(\bar{Q}_{22,1} + \bar{Q}_{12,2}\right) + \alpha_{xy,1}\left(\bar{Q}_{26,1} - \bar{Q}_{26,2}\right)\right] \\
N_{xy}^T &= t\Delta T\left[\alpha_{x,1}(\bar{Q}_{16,1} + \bar{Q}_{26,2}) + \alpha_{y,1}(\bar{Q}_{26,1} + \bar{Q}_{16,2}) + \alpha_{xy,1}(\bar{Q}_{66,1} - \bar{Q}_{66,2})\right]
\end{aligned} \tag{4.40}$$

The stiffness invariants are then introduced by substituting Eq. 4.19 into Eq. 4.40.

$$\begin{aligned}
N_x^T &= t\Delta T[\alpha_{x,1}\left(U_1 + U_4 + U_2\cos 2\theta_1\right) + \alpha_{y,1}\left(U_1 + U_4 - U_2\cos 2\theta_1\right) \\
&\quad + \alpha_{xy,1}\left(U_2\sin 2\theta_1\right)] \\
N_y^T &= t\Delta T[\alpha_{x,1}\left(U_1 + U_4 + U_2\cos 2\theta_1\right) + \alpha_{y,1}\left(U_1 + U_4 - U_2\cos 2\theta_1\right) \\
&\quad + \alpha_{xy,1}\left(U_2\sin 2\theta_1\right)] \\
N_{xy}^T &= 0
\end{aligned} \tag{4.41}$$

The resulting expressions demonstrate that $N_x^T = N_y^T$ and $N_{xy}^T = 0$ for this design case. The simplified expressions for the thermal expansion coefficients of Eqs. 4.36 and 4.37 are then substituted into Eq. 4.41 resulting in the following expression in terms of the thermal expansion coefficients in the fibre and transverse directions, α_1 and α_2.

$$N_x^T = N_y^T = t\Delta T[U_1\left(\alpha_1 + \alpha_2\right) + U_4\left(\alpha_1 + \alpha_2\right) + U_2\left(\alpha_1 - \alpha_2\right)] \tag{4.42}$$

For simplicity, two linear combinations of the thermal expansion coefficients are then defined.

$$\alpha_A = \frac{1}{2}\left(\alpha_1 + \alpha_2\right)\Delta T, \quad \alpha_B = \frac{1}{2}\left(\alpha_1 - \alpha_2\right)\Delta T \tag{4.43}$$

Finally, substitution of Eq. 4.43 into Eq. 4.42 results in an expression for the thermally induced forces in terms of ply thickness, stiffness invariants and thermal expansion properties only.

$$N_x^T = N_y^T = 2t\left[U_1\alpha_A + U_4\alpha_A + U_2\alpha_B\right] \tag{4.44}$$

Thermal Moments

This same method can be applied to the thermally induced moments M_x^T, M_y^T and M_{xy}^T to develop simplified expressions using stiffness invariants and lamination parameters. Expansion of Eq. 4.34 for the two-ply design leads to the following sums for M_x^T, M_y^T and M_{xy}^T.

$$\begin{aligned}
M_x^T =& \frac{1}{2}\Delta T(\bar{Q}_{11,1}\alpha_{x,1} + \bar{Q}_{12,1}\alpha_{y,1} + \bar{Q}_{16,1}\alpha_{xy,1})(0^2 - (-t)^2) \\
&+ \frac{1}{2}\Delta T(\bar{Q}_{11,2}\alpha_{x,2} + \bar{Q}_{12,2}\alpha_{y,2} + \bar{Q}_{16,2}\alpha_{xy,2})(t^2 - 0^2) \\
M_y^T =& \frac{1}{2}\Delta T(\bar{Q}_{12,1}\alpha_{x,1} + \bar{Q}_{22,1}\alpha_{y,1} + \bar{Q}_{26,1}\alpha_{xy,1})(0^2 - (-t)^2) \\
&+ \frac{1}{2}\Delta T(\bar{Q}_{12,2}\alpha_{x,2} + \bar{Q}_{22,2}\alpha_{y,2} + \bar{Q}_{26,2}\alpha_{xy,2})(t^2 - 0^2) \\
M_{xy}^T =& \frac{1}{2}\Delta T(\bar{Q}_{16,1}\alpha_{x,1} + \bar{Q}_{26,1}\alpha_{y,1} + \bar{Q}_{66,1}\alpha_{xy,1})(0^2 - (-t)^2) \\
&+ \frac{1}{2}\Delta T(\bar{Q}_{16,2}\alpha_{x,2} + \bar{Q}_{26,2}\alpha_{y,2} + \bar{Q}_{66,2}\alpha_{xy,2})(t^2 - 0^2)
\end{aligned} \tag{4.45}$$

Substitution of Eq. 4.38 into Eq. 4.45 results in the following simplified form.

$$\begin{aligned}
M_x^T &= \frac{t^2}{2}\Delta T\left[\alpha_{x,1}(\bar{Q}_{12,2} - \bar{Q}_{11,1}) + \alpha_{y,1}(\bar{Q}_{11,2} - \bar{Q}_{12,1}) - \alpha_{xy,1}(\bar{Q}_{16,1} + \bar{Q}_{16,2})\right] \\
M_y^T &= \frac{t^2}{2}\Delta T\left[\alpha_{x,1}(\bar{Q}_{22,2} - \bar{Q}_{12,1}) + \alpha_{y,1}(\bar{Q}_{12,2} - \bar{Q}_{22,1}) - \alpha_{xy,1}(\bar{Q}_{26,1} + \bar{Q}_{26,2})\right] \\
M_{xy}^T &= \frac{t^2}{2}\Delta T\left[\alpha_{x,1}(\bar{Q}_{26,2} - \bar{Q}_{16,1}) + \alpha_{y,1}(\bar{Q}_{16,2} - \bar{Q}_{26,1}) - \alpha_{xy,1}(\bar{Q}_{66,1} + \bar{Q}_{66,2})\right]
\end{aligned} \tag{4.46}$$

The stiffness invariants are then introduced by substituting Eq. 4.19 into Eq. 4.46.

$$\begin{aligned}
M_x^T &= \frac{t^2}{2}\Delta T[\alpha_{x,1}\left(U_4 - U_1 - U_2\cos 2\theta_1 - 2U_3\cos 4\theta_1\right) \\
&\quad + \alpha_{y,1}\left(U_1 - U_4 - U_2\cos 2\theta_1 + 2U_3\cos 4\theta_1\right) + \alpha_{xy,1}\left(2U_3\sin 4\theta_1\right)] \\
M_y^T &= \frac{t^2}{2}\Delta T[-\alpha_{x,1}\left(U_4 - U_1 - U_2\cos 2\theta_1 - 2U_3\cos 4\theta_1\right) \\
&\quad - \alpha_{y,1}\left(U_1 - U_4 - U_2\cos 2\theta_1 + 2U_3\cos 4\theta_1\right) - \alpha_{xy,1}\left(2U_3\sin 4\theta_1\right)] \\
M_{xy}^T &= \frac{t^2}{2}\Delta T[\alpha_{x,1}(-U_2\sin 2\theta_1 - 2U_3\sin 4\theta_1) + \alpha_{y,1}(-U_2\sin 2\theta_1 + 2U_3\sin 4\theta_1) \\
&\quad - \alpha_{xy,1}(2U_5 - 2U_3\cos 4\theta_1)]
\end{aligned} \tag{4.47}$$

This demonstrates that $M_x^T = -M_y^T$ for this design case. Equations 4.36 and 4.37 are then substituted into Eq. 4.47 resulting in the following expressions in terms of α_1 and α_2.

$$\begin{aligned}
M_x^T &= \frac{t^2}{2}\Delta T[U_1\cos 2\theta_1\left(\alpha_2 - \alpha_1\right) + U_4\cos 2\theta_1\left(\alpha_1 - \alpha_2\right) - U_2\cos 2\theta_1\left(\alpha_1 + \alpha_2\right) \\
&\quad + 2U_3\cos 2\theta_1\cos 4\theta_1\left(\alpha_2 - \alpha_1\right) - 2U_3\sin 2\theta_1\sin 4\theta_1\left(\alpha_1 - \alpha_2\right)] = -M_y^T \\
M_{xy}^T &= \frac{t^2}{2}\Delta T[2U_3\cos 2\theta_1\sin 4\theta_1(\alpha_2 - \alpha_1) - U_2\sin 2\theta_1(\alpha_1 + \alpha_2) \\
&\quad + 2U_3\sin 2\theta_1\cos 4\theta_1(\alpha_1 - \alpha_2) - 2U_5\sin 2\theta_1(\alpha_1 - \alpha_2)]
\end{aligned} \tag{4.48}$$

Finally, substitution of Eq. 4.43 into Eq. 4.48 results in expressions for the thermally induced moments in terms of ply thickness, stiffness invariants, lamination parameters and thermal expansion properties.

$$\begin{aligned}
M_x^T &= t^2\left[U_4\cos 2\theta_1\alpha_B - U_1\cos 2\theta_1\alpha_B - U_2\cos 2\theta_1\alpha_A - 2U_3\cos 2\theta_1\alpha_B\right] \\
&= t^2\left[U_4 Z_1^B\alpha_B - U_1 Z_1^B\alpha_B - U_2 Z_1^B\alpha_A - 2U_3 Z_1^B\alpha_B\right] = -M_y^T \\
M_{xy}^T &= t^2[-U_2\sin 2\theta_1\alpha_A - 2U_3\sin 2\theta_1\alpha_B - 2U_5\sin 2\theta_1\alpha_B] \\
&= t^2[-U_2 Z_3^B\alpha_A - 2U_3 Z_3^B\alpha_B - 2U_5 Z_3^B\alpha_B]
\end{aligned} \tag{4.49}$$

Combining Thermal Forces and Moments with Stiffness Matrices

Having demonstrated that only N_x^T, M_x^T and M_{xy}^T need to be calculated to model the thermal properties for this design case, and with expressions developed in terms of the ply thickness, stiffness invariants, lamination parameters and thermal expansion coefficients, the three terms can be added to Eq. 4.30 in the same format.

$$\left[A_{11}\ A_{12}\ A_{16}\ A_{66}\ B_{11}\ B_{16}\ D_{11}\ D_{12}\ D_{16}\ D_{66}\ N_x^T\ M_x^T\ M_{xy}^T\right] = [\boldsymbol{U}]\,[\boldsymbol{Z}]\,[\boldsymbol{K}]\,[\boldsymbol{T}] \tag{4.50}$$

where the additional matrix $\boldsymbol{K}$ is added containing the thermal expansion coefficient terms of Eqs. 4.44 and 4.49,

$$[\boldsymbol{K}] = \begin{bmatrix} [I_{10\times10}] & & [0_{3\times10}] & \\ & \alpha_A & 0 & 0 \\ & \alpha_B & 0 & 0 \\ [0_{10\times6}] & 0 & \alpha_A & 0 \\ & 0 & \alpha_B & 0 \\ & 0 & 0 & \alpha_A \\ & 0 & 0 & \alpha_B \end{bmatrix} \tag{4.51}$$

the $\boldsymbol{Z}$ matrix is extended to contain the lamination parameter components of Eqs. 4.44 and 4.49,

$$[\boldsymbol{Z}] = \begin{bmatrix} 1 & 0 & 0 & 0 & 0 & 0 & 1 & 0 & 0 & 0 & 2\,0 & 0 & -2Z_1^B & 0 & 0 \\ 0 & 0 & 0 & 0 & Z_1^B & Z_3^B/2 & 0 & 0 & 0 & 0 & 0\,2 & -2Z_1^B & 0 & -2Z_3^B & 0 \\ Z_2^A & -Z_2^A & Z_4^A & -Z_2^A & 0 & 0 & Z_2^D & -Z_2^D & Z_4^D & -Z_2^D & 0\,0 & 0 & -4Z_1^B & 0 & -4Z_3^B \\ 0 & 1 & 0 & 0 & 0 & 0 & 0 & 1 & 0 & 0 & 2\,0 & 0 & 2Z_1^B & 0 & 0 \\ 0 & 0 & 0 & 1 & 0 & 0 & 0 & 0 & 0 & 1 & 0\,0 & 0 & 0 & 0 & -4Z_3^B \end{bmatrix} \tag{4.52}$$

and the $\boldsymbol{T}$ matrix is extended for the ply thickness components of Eqs. 4.44 and 4.49.

$$[\boldsymbol{T}] = \text{diag}\left[2t \quad 2t \quad 2t \quad 2t \quad -t^2 \quad -t^2 \quad \tfrac{2}{3}t^3 \quad \tfrac{2}{3}t^3 \quad \tfrac{2}{3}t^3 \quad \tfrac{2}{3}t^3 \quad t \quad \tfrac{1}{2}t^2 \quad \tfrac{1}{2}t^2\right] \tag{4.53}$$

4.3.3 Extension to the n-ply Design Case

This section extends the modelling of the two-ply layup considered so far to any number of plies, and to nonuniform thicknesses between plies. The full geometry considered in this section is shown in Fig. 4.3 where there are n plies in the top half of the laminate mirrored about the midplane as defined by the design rules of Section 4.2.2.

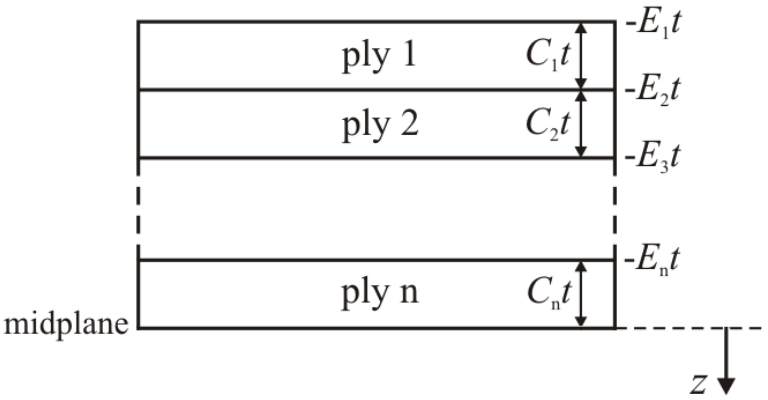

Figure 4.3: n-ply laminate geometry with variable ply thickness.

Each ply is defined in terms of a single ply thickness t with a factor C_i for each ply used to introduce nonuniform thickness. The out-of-plane distance to the top of the i-th ply from the midplane is denoted $E_i t$.

Of the matrices $\boldsymbol{U}$, $\boldsymbol{Z}$, $\boldsymbol{K}$ and $\boldsymbol{T}$ of Eq. 4.50, only the matrices $\boldsymbol{Z}$ and $\boldsymbol{T}$ vary as $\boldsymbol{U}$ and $\boldsymbol{K}$ are composed of stiffness and thermal properties which are material dependent only. For the matrix $\boldsymbol{Z}$ the lamination parameters must be evaluated for the laminate geometry of Fig. 4.3. Derivation of those terms known to be non-zero for this cross-symmetric case can be found in Appendix B.4, and are expressed in their simplest form below.

$$\begin{aligned}
\boldsymbol{V}^A &= 2t \begin{bmatrix} 0 & \sum_{i=1}^{n}(E_i - E_{i+1})\cos 4\theta_i & 0 & \sum_{i=1}^{n}(E_i - E_{i+1})\sin 4\theta_i \end{bmatrix} \\
\boldsymbol{V}^B &= -t^2 \begin{bmatrix} \sum_{i=1}^{n}(E_i^2 - E_{i+1}^2)\cos 2\theta_i & 0 & \sum_{i=1}^{n}(E_i^2 - E_{i+1}^2)\sin 2\theta_i & 0 \end{bmatrix} \\
\boldsymbol{V}^D &= \frac{2t^3}{3} \begin{bmatrix} 0 & \sum_{i=1}^{n}(E_i^3 - E_{i+1}^3)\cos 4\theta_i & 0 & \sum_{i=1}^{n}(E_i^3 - E_{i+1}^3)\sin 4\theta_i \end{bmatrix}
\end{aligned} \tag{4.54}$$

At this point it is noted that, due to the way the ply thicknesses have been defined, the ply thickness terms in Eq. 4.54 are the same as those in Eq. 4.27 for the two-ply case. The thickness factors are therefore taken out in exactly the same way as for Eq. 4.32, and the matrix $\boldsymbol{T}$ remains unchanged for this n-ply case.

$$\boldsymbol{Z}^A = \frac{\boldsymbol{V}^A}{2t}, \quad \boldsymbol{Z}^B = \frac{\boldsymbol{V}^B}{-t^2}, \quad \boldsymbol{Z}^D = \frac{\boldsymbol{V}^D}{\frac{2}{3}t^3} \tag{4.55}$$

These lamination parameters are then substituted into the matrix $\boldsymbol{Z}$, replacing the equivalent two-ply terms. The final step is to address the 1's and 2's in the $\boldsymbol{Z}$ matrix. With reference to Eqs. 4.28 and 4.44 these terms represent the total thickness terms, H, H^3 and $2H$. Following the geometry of Fig. 4.3, these terms are replaced by E_1, E_1^3 and $2E_1$ to give the following final form.

$$[\boldsymbol{Z}] = \begin{bmatrix}
E_1 & 0 & 0 & 0 & 0 & 0 & E_1^3 & 0 & 0 & 0 & 2E_1 & 0 & 0 & -2Z_1^B & 0 & 0 \\
0 & 0 & 0 & 0 & Z_1^B & Z_3^B/2 & 0 & 0 & 0 & 0 & 0 & 2E_1 & -2Z_1^B & 0 & -2Z_3^B & 0 \\
Z_2^A & -Z_2^A & Z_4^A & -Z_2^A & 0 & 0 & Z_2^D & -Z_2^D & Z_4^D & -Z_2^D & 0 & 0 & 0 & -4Z_1^B & 0 & -4Z_3^B \\
0 & E_1 & 0 & 0 & 0 & 0 & 0 & E_1^3 & 0 & 0 & 2E_1 & 0 & 0 & 2Z_1^B & 0 & 0 \\
0 & 0 & 0 & E_1 & 0 & 0 & 0 & 0 & 0 & E_1^3 & 0 & 0 & 0 & 0 & 0 & -4Z_3^B
\end{bmatrix} \tag{4.56}$$

Using this n-ply version of the $\boldsymbol{Z}$ matrix, Eq. 4.50 is now valid for calculating the $\boldsymbol{A}$, $\boldsymbol{B}$, $\boldsymbol{D}$ terms and thermal forces and moments N_x^T, M_x^T and M_{xy}^T for this extended case.

4.3.4 Reduced Number of Displacement Coefficients

For a laminate with two stable shapes of equal and opposite magnitude the number of shape coefficients used to define the strains of Eq. 4.4, and subsequently the displacements of Eq. 4.5, is unnecessarily high. By considering the rotational symmetry of the two shapes it can be shown that they can be defined in terms of a single set of coefficients, and that this set can be reduced to 11 unique terms from the existing 14.

Defining the Second Stable State in Terms of the First

Figure 4.4 shows the two stable shapes of a $[\text{-}30/60]_{\text{T}}$ laminate adhering to the design rules. The two shapes have curvatures and displacements of equal magnitude at differing orientations. By rotating the first shape (a) by 90° in the x-y plane and inverting the out-of-plane displacements, the second shape (b) is obtained. We can therefore make comparisons between the displacements in each stable state at positions 90° apart.

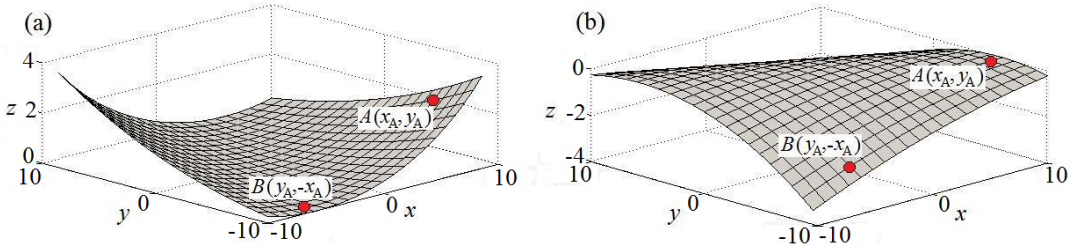

Figure 4.4: Two room-temperature shapes of a square $[\text{-}30/60]_{\text{T}}$ laminate; (a) state 1 and (b) state 2.

The magnitude of out-of-plane displacement at some arbitrary point A in state 1 must be equal to the magnitude of out-of-plane displacement (with opposite out-of-plane direction) at a point B in state 2, rotated by 90° from point A.

$$w_{1,A} = -w_{2,B} \tag{4.57}$$

where the subscript number denotes the associated state and the letter denotes the spatial location. If point A is at a position $x = x_A$, $y = y_A$ then point B is at a position $x = y_A$, $y = -x_A$. Substitution of these values and the displacement relationship of Eq. 4.1 into Eq. 4.57 results in the following expression,

$$\frac{1}{2}\left(a_1 x_A^2 + b_1 y_A^2 + c_1 x_A y_A\right) = -\frac{1}{2}\left(a_2 y_A^2 + b_2 x_A^2 - c_2 x_A y_A\right) \tag{4.58}$$

This relationship must be true for all values of x and y. This requires that each

spatially dependent component of Eq. 4.58 must be equivalent. Therefore, the following relationships can be stated.

$$a_1 = -b_2, \quad b_1 = -a_2, \quad c_1 = c_2 \tag{4.59}$$

Similarly, the in-plane displacements can be compared at points A and B. Due to the rotational symmetry between the two shapes, the displacement in the x-direction, u^0, at point A in state 1 must be equal in magnitude (with opposite sign) to the displacement in the y-direction, v^0, at point B in state 2. Equally, u^0 at point A in state 1 must be equal in magnitude (with same sign) to u^0 at point B in state 2.

$$\begin{aligned} u^0_{1,A} &= -v^0_{2,B} \\ v^0_{1,A} &= u^0_{2,B} \end{aligned} \tag{4.60}$$

Substituting the displacement expressions of Eq. 4.5 and the shape coefficient relationships of Eq. 4.59 into Eq. 4.60 results in the following expressions,

$$\begin{aligned} &d_{1,1}x_A + d_{9,1}y_A + \frac{1}{2}\left(d_{3,1} - \frac{1}{2}a_1c_1\right)x_A^2y_A + \left(d_{4,1} - \frac{c_1^2}{8}\right)x_Ay_A^2 \\ &\quad + \frac{1}{3}\left(d_{2,1} - \frac{1}{2}a_1^2\right)x_A^3 + \frac{1}{3}d_{11,1}y_A^3 \\ =&-\left(d_{9,2}y_A - d_{5,2}x_A + \frac{1}{2}\left(d_{7,2} + \frac{1}{2}a_1c_1\right)y_Ax_A^2 - \left(d_{6,2} - \frac{c_1^2}{8}\right)y_A^2x_A \right. \\ &\quad \left. - \frac{1}{3}\left(d_{8,2} - \frac{1}{2}a_1^2\right)x_A^3 + \frac{1}{3}d_{10,2}y_A^3\right) \end{aligned} \tag{4.61}$$

$$\begin{aligned} &d_{9,1}x_A + d_{5,1}y_A + \frac{1}{2}\left(d_{7,1} - \frac{1}{2}b_1c_1\right)x_Ay_A^2 + \left(d_{6,1} - \frac{c_1^2}{8}\right)x_A^2y_A \\ &\quad + \frac{1}{3}\left(d_{8,1} - \frac{1}{2}b_1^2\right)y_A^3 + \frac{1}{3}d_{10,1}x_A^3 \\ =&d_{1,2}y_A - d_{9,2}x_A - \frac{1}{2}\left(d_{3,2} + \frac{1}{2}b_1c_1\right)y_A^2x_A + \left(d_{4,2} - \frac{c_1^2}{8}\right)y_Ax_A^2 \\ &\quad + \frac{1}{3}\left(d_{2,2} - \frac{1}{2}b_1^2\right)y_A^3 - \frac{1}{3}d_{11,2}x_A^3 \end{aligned} \tag{4.62}$$

These relationships must be true for all values of x and y. This requires that each spatially dependent component of Eq. 4.61 and of Eq. 4.62 must be equivalent. Therefore, the following relationships can be stated.

$$\begin{aligned} &d_{1,1} = d_{5,2}, \quad d_{2,1} = d_{8,2}, \quad d_{3,1} = -d_{7,2}, \quad d_{4,1} = d_{6,2} \\ &d_{5,1} = d_{1,2}, \quad d_{6,1} = d_{4,2}, \quad d_{7,1} = -d_{3,2}, \quad d_{8,1} = d_{2,2} \\ &d_{9,1} = -d_{9,2}, \quad d_{10,1} = -d_{11,2}, \quad d_{11,1} = -d_{10,2}, \end{aligned} \tag{4.63}$$

From Eqs. 4.59 and 4.63, it follows that the second stable shape can be defined entirely in terms of the shape coefficients used to define the first stable shape. This property

means that only a single solution needs to be extracted from Eq. 4.12 to define the two cylindrical shapes.

Reduced Set of Coefficients to Define a Single Shape

Extensive modelling of the family of laminates described in this chapter has highlighted that the number of shape coefficients used to define a single stable shape is unnecessarily high. To demonstrate that the number of unique coefficients can be reduced, a second condition for the laminate shown in Fig. 4.4 is considered. Due to the rotational symmetry of the laminate it is clear that the change in u^0 between states 1 and 2 at point A must be equal in magnitude to the change in v^0 between states 2 and 1 at point B. Similarly, the change in v^0 between states 1 and 2 at point A must be equal in magnitude to the change in u^0 between states 2 and 1 at point B:

$$\begin{aligned} u^0_{1,A} - u^0_{2,A} &= v^0_{2,B} - v^0_{1,B} \\ v^0_{1,A} - v^0_{2,A} &= u^0_{2,B} - u^0_{1,B} \end{aligned} \tag{4.64}$$

Substitution of Eq. 4.5 into Eq. 4.64, using the relationships found in Eq. 4.63, results in expressions in terms of state 1 shape coefficients only. For this expression to be true for all values of x and y, defining the position of point A, the following equalities must be true for both stable states:

$$d_2 = d_8, \quad d_4 = d_6, \quad d_3 = -d_7 \tag{4.65}$$

Substitution of Eq. 4.65 into Eq. 4.4 results in the following simplified form for the midplane strains:

$$\begin{aligned} \epsilon^0_x &= d_1 + d_2x^2 + d_3xy + d_4y^2 \\ \epsilon^0_y &= d_5 + d_4x^2 - d_3xy + d_2y^2 \end{aligned} \tag{4.66}$$

Significantly, this reduction in the number of required displacement coefficients reduces the number of unknowns in Eq. 4.12 from the existing 14 to 11. This reduction in the complexity of the system of equations simplifies the derivation of an analytical solution outlined in the following sections.

4.3.5 Simplified Total Strain Energy Equation

With the simplifications outlined in Sections 4.3.1 - 4.3.4, the complexity of the total strain energy equation, obtained by expansion of Eq. 4.10, can be greatly reduced. Substitution of the reduced form of the $\boldsymbol{A}$, $\boldsymbol{B}$ and $\boldsymbol{D}$ matrices of Eq. 4.29, the reduced number of thermal terms of Eqs. 4.44 and 4.49, and the reduced number of shape coef-

ficients of Eq. 4.66 into Eq. 4.10 results in the simplified form of W shown in Appendix B.5.

Each term of the reduced energy equation of Appendix B.5 contains either stiffness matrix terms or thermal force or moment terms which have previously been defined in matrix form in Eq. 4.50. Furthermore, each of these terms appears linearly and independently, with only the shape coefficients appearing nonlinearly. Given this form of the energy equation it is a simple extension to the matrix formulation to express W in the following form

$$W = [\boldsymbol{U}][\boldsymbol{Z}][\boldsymbol{K}][\boldsymbol{T}][\boldsymbol{X}][\boldsymbol{L}] \tag{4.67}$$

where $\boldsymbol{X}$ is the matrix containing all of the shape coefficient terms of Eq. B.31, and can be found in full in Appendix B.6, and $\boldsymbol{L}$ contains the different edge length terms seen in Eq. B.31.

$$[\boldsymbol{L}] = \begin{bmatrix} L^2 \\ L^4 \\ L^6 \end{bmatrix} \tag{4.68}$$

4.4 An Analytical Solution for Bistable Laminate Shapes

With the total strain energy equation in the reduced form of Eq. 4.67 a simplified set of equilibrium equations can be derived. This is done by differentiating the matrix $\boldsymbol{X}$ with respect to each of the remaining shape coefficients resulting in the following system of equations,

$$f_i = [\boldsymbol{U}]\,[\boldsymbol{Z}]\,[\boldsymbol{K}]\,[\boldsymbol{T}]\,[\boldsymbol{X}]_i\,[\boldsymbol{L}]\,, \quad i = 1...11 \tag{4.69}$$

where the subscript i denotes the i-th equation of the system. The full form of these equations can be found in Appendix B.7.

Prior to attempting to find an analytical solution to the set of equations, two oberservations are made. Firstly, the matrices $\boldsymbol{U}$, $\boldsymbol{Z}$, $\boldsymbol{K}$, $\boldsymbol{T}$ and $\boldsymbol{L}$ are identical for all 11 equations. Only the matrices of shape coefficients $\boldsymbol{X}_i$ vary. Secondly, regarding the form of the equations f_i of Eq. B.33, there are many repeated terms common to more than one equation. For example there are many terms common to both f_5 and f_7. With these two observations it is simple to take advantage of the matrix formulation of the equations and greatly reduce the length of the set of equations by Gaussian elimination. As the matrices $\boldsymbol{U}$, $\boldsymbol{Z}$, $\boldsymbol{K}$, $\boldsymbol{T}$ and $\boldsymbol{L}$ are based entirely on fixed values defining the laminate composition we do not need to worry about simplifying them. The aim is to make the matrices $\boldsymbol{X}_i$ as simple as possible to allow an analytical solution

to be derived. By adding and subtracting multiples of different rows of Eq. 4.69 to each other a greatly reduced form of the 11 equations is obtained, resulting in a much more manageable system to solve. This reduced system can be found in Appendix B.8.

With the equations in this simpler form a third observation is made. The shape coefficients $d_{1,2,3,4,5,9,10,11}$ (redefined as e_{1-8} in Appendix B for convenience) which define the in-plane displacements appear independently of each other throughout the 11 equations and only ever appear as linear terms. However, the equations are not linear with respect to the remaining shape coefficients a-c which define the out-of-plane displacement, Eq. 4.1. As the equations are linear with respect to all but 3 of the shape coefficients it is possible to reduce the system to just 3 equations and 3 unknowns, a, b and c. This is done by first rearranging one of the equations in terms of e_1 and substituting it into the remaining 10 equations. This process is repeated until three equations in terms of a, b and c remain. These final three equilibrium equations, denoted f_{a-c}, can be found in Appendix B.9.

The remaining three equations are nonlinear and this leads to multiple solutions hence the bistability. The involved process of solving the nonlinear system is performed using symbolic computing for all possible solutions. By rearranging f_c into an expression for c in terms of a and b, two solutions are identified which correspond to the two cylindrical configurations. These expressions are then substituted into f_b and the process is repeated to obtain expressions for b in terms of a. Finally, the expressions for both b and c are substituted into f_a and two possible expressions for a are obtained in terms of $\boldsymbol{U}$, $\boldsymbol{Z}$, $\boldsymbol{K}$, $\boldsymbol{T}$ and $\boldsymbol{L}$ only. The final expressions for each of the out-of-plane displacement coefficients can be found in Appendix B.10. In-plane displacement coefficients are not stated in full here but can easily be computed by substituting the expressions for a, b and c into Eq. 4.69.

4.5 Application to General Cases

The analytical solution to the existing modelling formulation presented in this chapter provides a fast and robust method of calculating bistable laminate shapes, ideal for optimisation of the design where shapes must be evaluated at many iterations. However, this solution is only applicable to laminates adhering to the design rules outlined in Section 4.2.2. While this simplified geometry was selected based on knowledge of the bistable design space, it is acknowledged that this will not cover all laminate configurations which may be considered for practical applications. For example, rectangular laminates may be desirable in certain cases, and no method of actuation has been considered to this point. Despite these cases having not been considered in this chapter

the new modelling formulation does go a long way towards solving these problems. As stated earlier, the primary concern with solving the existing modelling formulation is the difficulty in obtaining a suitable initial guess, resulting in slow convergence to a solution or failure to capture the stable shapes. With the exact analytical solution derived in this chapter, a method of finding a close initial guess by considering a similar design case has been developed. For example, to calculate the shapes of a rectangular laminate which adheres to the remaining 3 design rules of Section 4.2.2, it is convenient to obtain an exact solution for the equivalent square case and use it as a very close initial guess for the rectangular case. An iterative method can then be employed to obtain the exact solution. This concept will be discussed further where appropriate later in this work.

4.6 Concluding Remarks

This chapter has outlined the derivation of a novel modelling formulation to calculate the stable shapes of bistable laminates with cross-symmetric layups. This work is based on an existing model [24] which deals with fully general stacking sequences. While the model is successful in capturing the multiple equilibria within the system, the complexity of the governing equations requires an iterative solution method to identify these solutions. Having identified that the fully general layup is not necessary for bistable design, a simplified laminate configuration has been proposed which allows many modelling simplifications to be made. With these simplifications, an analytical solution to the existing modelling case has been derived.

The derivation of an analytical solution to modelling has provided an analysis tool which is ideal for optimisation of laminate composition. With a fast and robust method of identifying all stable solutions, the model can be used to evaluate the characteristics of a laminate at many design iterations. Furthermore, with explicit equations defining the laminate displacements, no initial guess is required removing the need for prior knowledge of the solution. For analysis of a single laminate design the need for a reasonable approximation of the laminate shape is not a significant issue as an intuitive estimate can be used to iterate towards the exact solution. However, in an optimisation routine where the design is constantly being updated, obtaining a close approximation of the shape is more difficult. Furthermore, when analysing many hundreds of designs within a single optimisation routine the computation time is vastly reduced by having an explicit set of equations to define the shapes. It has also been observed that when a laminate of this family is bistable one stable shape can be defined entirely in terms of the coefficients used to define the opposite stable shape, meaning only a single solution needs to be extracted to model the bistable behaviour.

While the simplifications made to the laminate composition have been selected to enhance the bistable characteristics and to avoid restricting the desgin space in a prohibitive way, it has been acknowledged that this modelling formulation will not cover all laminate designs which may be considered. For example no actuation methods have been considered to this point. However, for such extended cases this modelling formulation does overcome the main hurdle which is obtaining a close initial guess.

The modelling outlined in this chapter has met the objective of providing a design tool which is suitable for use in an optimisation methodology. However, further analysis of the model is proposed before applying it to a design problem. It has been stated that the accuracy of the existing model has been examined experimentally and using FEA [24, 26, 84]. However, the sensitivity of the model to changes in the many design variables has not been characterised in existing literature.

Chapter 5

Experimental Shape Characterisation and Modelling Uncertainty

In this chapter the sensitivity of the derived model to imperfections and uncertainties is investigated via experimental and analytical studies. Section 5.1 details an experimental study to map the surface profiles of a series of arbitrary layup laminates using a three-dimensional motion analysis technique. Results are presented to compare the experimentally observed shapes with those predicted using the analytical model, including a quantitative discussion of the observed errors in thermally induced displacements.

Section 5.2 presents a discussion on sources of uncertainty within the model, including material and geometric properties, manufacturing accuracy, and environmental conditions. Limitations of the model related to free edge characteristics are also discussed.

Sources of uncertainty which cannot be controlled via improved manufacturing processes are identified and examined further in Section 5.3 in an analytical study of the modelling sensitivities. It is concluded that while the existing modelling technique is successful in accurately predicting room-temperature shapes, the sensitivity of solutions to imperfections is significant.

5.1 Experimental Characterisation of Laminate Shapes

This section outlines the experimental work conducted with the aim of characterising the shapes of a series of bistable asymmetric laminates with arbitrary layup for comparison with shapes predicted by the analytical modelling methods. This was achieved through a three-dimensional motion analysis technique [70] to map the surface profiles.

5.1.1 Laminate Manufacture

The experimental study considered five carbon fibre/epoxy composite laminates of differing asymmetric layup: $[\text{-}45/45]_\text{T}$, $[\text{-}30/60]_\text{T}$, $[\text{-}15/75]_\text{T}$, $[30/60]_\text{T}$, and $[45/90]_\text{T}$, the first three of which meet the design rules of Section 4.2.2, while the remaining two require the iterative modelling approach of Section 4.1. These layups were chosen to provide a range of laminate shapes with differing magnitudes of displacement and angle of principal curvature. All laminates consisted of two plies, each with a thickness of 0.25mm and a square edge length of 150mm. The manufacturing process was a standard layup procedure using M21/T800 carbon fibre prepreg sheet, Table 5.1.

Table 5.1: M21/T800 prepreg sheet properties [47].

Property	Value
Longitudinal Young's modulus, E_{11} (GPa)	157.0
Transverse Young's modulus, E_{22} (GPa)	8.5
Poisson's ratio, ν_{12}	0.35
Shear modulus, G_{12} (GPa)	4.5
Longitudinal thermal expansion coefficient, α_1 ($\times 10^{-6}/^\circ$C)	-0.09
Transverse thermal expansion coefficient, α_2 ($\times 10^{-6}/^\circ$C)	30.0

The laminates were run through a standard autoclave cure cycle with a maximum cure temperature of 180°C and a pressure of 0.69MPa. Upon cooling to room-temperature, all five manufactured laminates were observed to have two stable states of curvature. Since the laminate is placed on a flat metallic surface within the autoclave, the side in contact with the surface has a smooth finish while the opposite side has a thin layer of resin which bleeds from the top ply and cures on the surface. Cylindrical shapes with this rough resin layer on the concave surface are denoted as state I while those with the resin layer on the outside convex surface of the cylinder are denoted state II. The effect of this resin layer is discussed later.

5.1.2 Displacement Characterisation

Experimental analysis of the two stable shapes of each of the five laminates was performed to measure the out-of-plane displacement of the laminates. This was carried out using standard three-dimensional motion analysis techniques to gain a map of coordinates distributed on the laminate surfaces. Each laminate had 145 round coloured labels of 8mm diameter attached to one surface, see Fig. 5.1a.

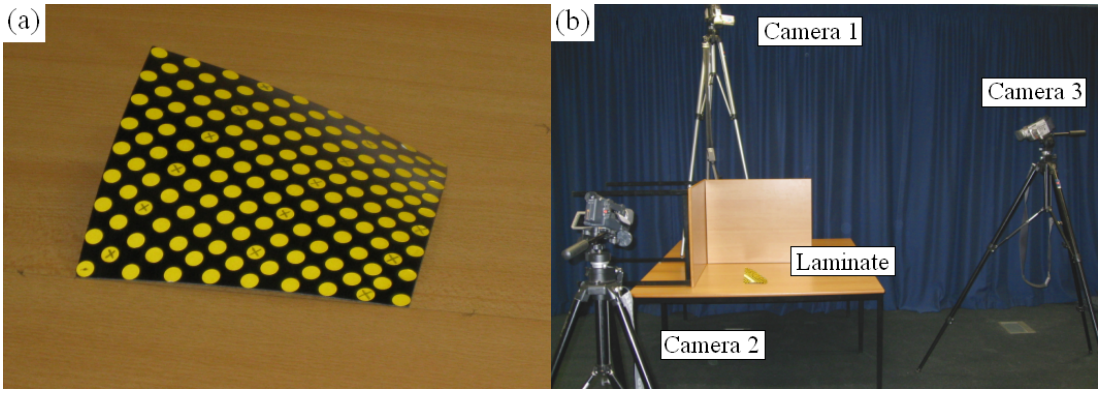

Figure 5.1: (a) Round labels distributed on the surface of a square $[45/90]_T$ laminate and (b) an example of the experimental camera setup.

Three digital video camera recorders (Sony DCR-TRV 900E, Sony Corporation, Japan) operating at 50 fields per second were set up in an umbrella configuration [70] around the experimental area. Camera 1, Fig. 5.1b, was always positioned to view this area from a high position (the centre of the lens positioned 2.19m away from the origin of the experimental area at a height of 1.86m). Due to differences in the shapes of the laminates, the other two cameras were moved such that the best possible viewing angle was always achieved without compromising the umbrella configuration. In total, six different camera setups were required to capture the 10 different laminate shapes. The other two cameras had the centre of lens ranging from 1.63 to 2.71m away from the origin in different setups with the height ranging from 0.51 to 1.32m above the experimental area. The height and locations of cameras varied in such a way that the cameras were not all in the same plane in accordance to recommendations by Nigg et al. [70]. The angle between the cameras ranged from 55 to 105° with a mean angle between the three cameras varying from 77 to 92° in different setups.

The laminates were positioned within the experimental volume, which was calibrated with a 20×20×10mm wire frame. The camera views were restricted to a volume just slightly larger than the calibration frame. The wire frame was videotaped in each camera setup before it was removed and the laminate was positioned within this calibrated volume. Following this, the laminates were videotaped simultaneously by the three video cameras.

Mapping of the surface coordinates was carried out using PeakMotus motion analysis system (v. 8.5, Vicon, USA). First, the eight corners of the calibration wire frame were manually digitised from each camera view (and for each camera setup). Then, the centre of each of the 145 round labels and the 4 corners of the each laminate were manually digitised from all three camera views using a round cursor matching the size of the round labels. The digitised area was 1440×1152 pixels.

Due to the curved shape of the laminates, it was not always possible to see every label or corner point of the laminate from all cameras. The minimum requirement to get a three dimensional coordinate is that the point is visible for at least two cameras, which was the case for all points. For most laminates, all the points were visible for all three cameras. In those occasions when all points were not visible, the maximum number of non-visible points was five in one view. The digitised pixel information from each camera view was combined with the calibration information to transform these to Cartesian co-ordinates of the laminate surfaces using Direct Linear Transformation method [1]. The mean of the root mean square (RMS) error of six different setups between the known eight calibration coordinates and the respective digitised points was 0.2mm for each coordinate direction.

5.1.3 Results

The measured Cartesian coordinates of each of the ten laminate shapes were three-dimensionally rotated to match the coordinate system defined for the analytical model using Matlab. This was because the experiments were set up in such a way to capture the most data points of laminates, each of which has different three-dimensional curvatures. The centre of both laminates was then set to [0,0,0] such that the z-coordinates of the experimental points represent the out-of-plane displacements of the laminate and the lines of symmetry in the curvatures were aligned to determine the angle of rotation about each of the three axes. Surface fitting was applied to the transformed data using the method outlined in [88]. This spline interpolation method fits a surface of the form $z = f(x, y)$ to the nonuniformly spaced data and interpolates this surface at the uniformly specified mesh grid points. The fitted surface is then plotted alongside the shape predicted by the analytical model. An example plot of state I of the $[-45/45]_{\mathrm{T}}$ laminate is shown in Fig. 5.2, including both the mesh fit and individual data points. The surface generated using the experimental data is offset for illustrative purposes.

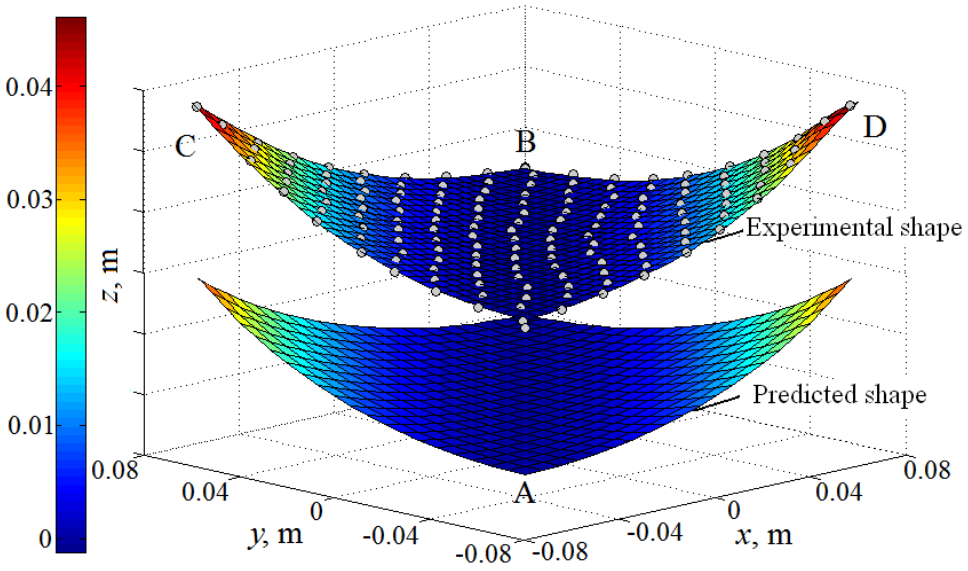

Figure 5.2: Predicted room-temperature state I shape and experimental data with spline fitted surface for a square $[-45/45]_T$ laminate. Experimental data offset.

The analytical models of the $[0\pm\theta/90\pm\theta]_T$ laminate family have two stable shapes of equal and opposite curvature. For square laminates of this type, if the laminate is inverted it can be oriented in the x-y plane such that the layup definition remains unchanged. This results in the prediction of two identical shapes of different global orientation. Such behaviour is observed for the $[-45/45]_T$, $[-30/60]_T$, $[-15/75]_T$ and $[30/60]_T$ laminates. However, this is not the case for the $[45/90]_T$ laminate where two stable shapes of both different angle of principal curvature and magnitude of curvature are observed. The two observed shapes, and those predicted by modelling, are shown in Figs. 5.3 and 5.4. Experimental data is again offset.

The analytical model and experimental shapes generally show good agreements for all laminates studied. The $[-45/45]_T$ laminate is used as a demonstrative example (Fig. 5.2) and is more closely examined in Figs. 5.5 and 5.6 where the curvature profiles in the major and minor axes, C-D and A-B respectively, are plotted. These profiles are selected as the errors at the corners are at their maximum, as shown in Table 5.2. As the reference point for the comparison is set at the centre of the laminates, the error at the centre is zero. The profiles in the major axis shown in Fig. 5.5 illustrate that the profiles for both states are smooth and the curvature deviation increases smoothly towards the corners of the laminates. The discrepancies in the curvatures between states are also noticeable which the analytical model does not account for.

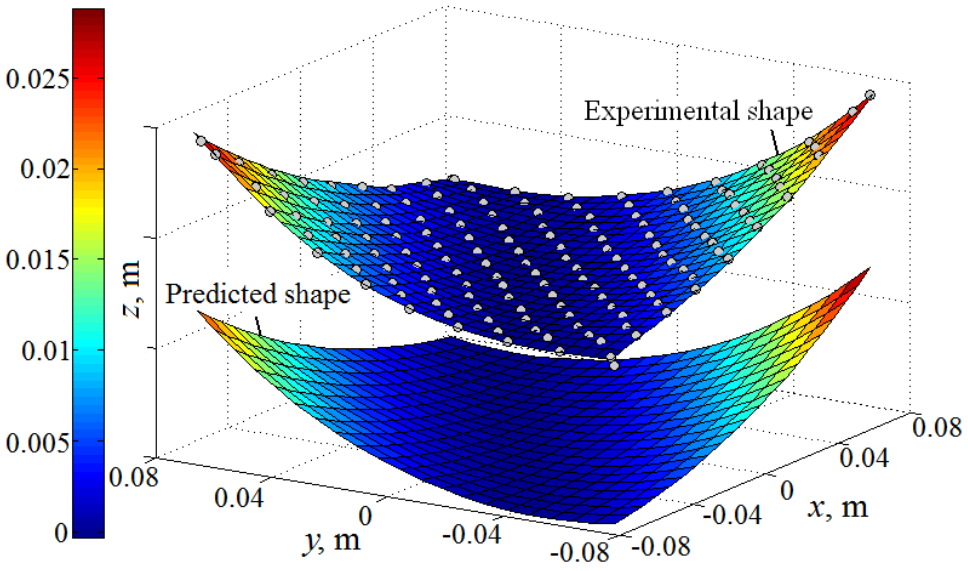

Figure 5.3: Predicted shapes and offset experimental data for state I shape for a square $[45/90]_{\mathrm{T}}$ laminate.

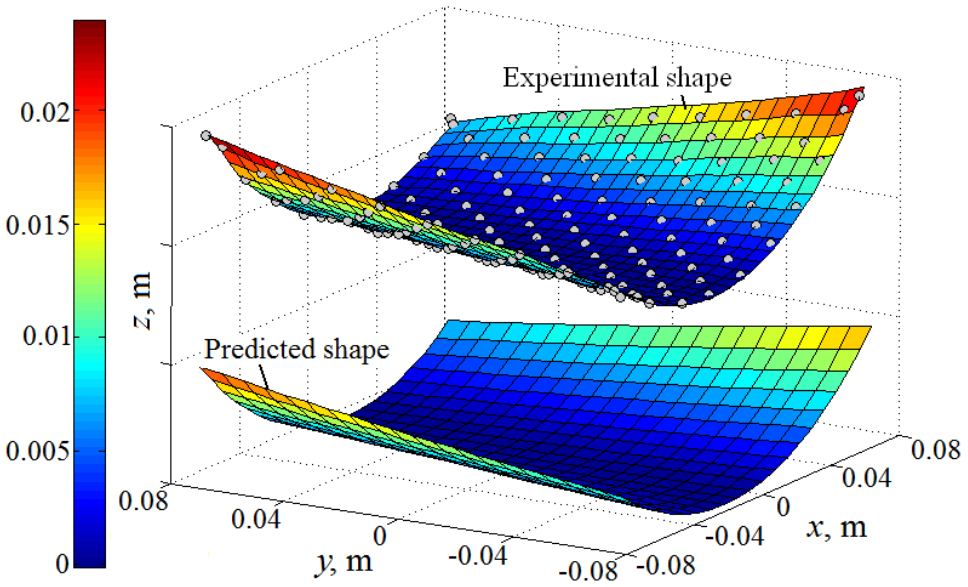

Figure 5.4: Predicted shapes and offset experimental data for state II shape for a square $[45/90]_{\mathrm{T}}$ laminate.

Figure 5.6 shows the curvature profile along the minor axis for the $[-45/45]_{\mathrm{T}}$ laminate. Here, the deflections for the analytical model show only a slight anticlastic curvature. The experimental data show near zero deflections in the non-boundary region but pronounced high curvatures near the boundaries. This clearly demonstrates that free edge characteristics around the boundaries affect just over 10% of the overall dimension. The existence of the free edge effects is well known [61] and this has not been included in the analytical model. The free edge effects are discussed further in Section 5.2.3.

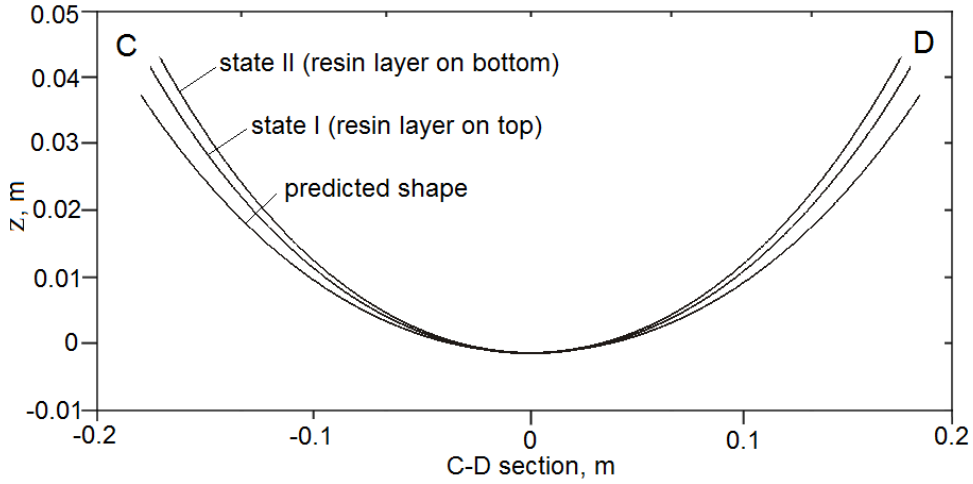

Figure 5.5: Cross-section profile of experimental and predicted shapes for a $[-45/45]_T$ laminate along line C-D.

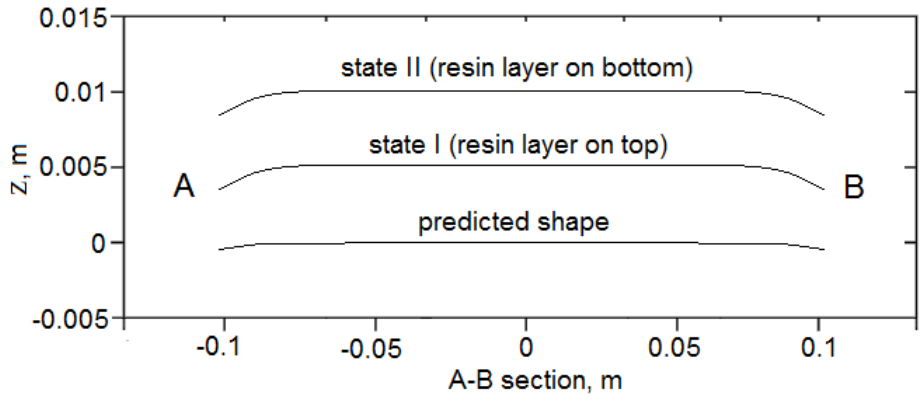

Figure 5.6: Cross-section profile of experimental and predicted shapes for a $[-45/45]_T$ laminate along line A-B.

The maximum errors at the corners for each of the ten laminate shapes at state I and state II are summarised in Table 5.2. As the analytical model predicts the same curvature for both states while each state has different curvature in practice, the difference between the two state curvatures (II-I) are also included in Table 5.2. This discrepancy is attributed to the thin resin layer. A layer with the properties of the cured resin [39] is added to the analytical model and discussed further in Section 5.2.1. The percentage error represents the predicted maximum out-of-plane displacement minus the measured displacement. The factors contributing to the errors are examined more closely in the following sections.

Table 5.2: Experimental and predicted maximum out-of-plane displacements for all tested laminates. II-I corresponds to the difference between states I and II.

Laminate	State	Maximum out-of-plane displacement (mm)			Error (%)	
		Predicted (ideal)	Predicted (resin)	Experimental	Ideal	Resin
[-45/45]	I	38.05	37.25	42.69	-10.9	-12.7
	II	38.05	37.99	43.39	-12.2	-12.4
	II-I	0.00	0.74	0.70	1.3	0.3
[-30/60]	I	35.51	34.76	38.14	-6.9	-8.9
	II	35.51	35.45	41.24	-13.9	-14.0
	II-I	0.00	0.69	3.10	7.0	5.1
[-15/75]	I	28.55	27.95	29.29	-2.5	-4.6
	II	28.55	28.50	31.67	-9.9	-10.0
	II-I	0.00	0.55	2.38	7.4	5.4
[45/90]	I	26.61	24.76	27.77	-4.2	-10.8
	II	19.03	19.29	22.85	-16.7	-15.6
	II-I	-7.58	-5.47	-4.92	12.5	4.8
[30/60]	I	14.63	12.56	12.77	14.6	-1.6
	II	14.63	15.94	15.09	-3.0	5.6
	II-I	0.00	3.38	2.32	17.6	7.2

5.2 Discussion of Sources of Modelling Uncertainty

A number of different sources are considered to contribute to the errors observed in this experimental investigation. These include issues with the manufacturing technique leading to an additional resin layer and uneven ply thicknesses, modelling limitations relating to free edge characteristics, dependency on temperature change, and uncertainy in material properties. All of these areas are discussed briefly in this section before forming a full sensitivity investigation.

5.2.1 Effects of an Additional Resin Layer

One distinct characteristic of these results is the consistent effect of the thin resin layer. All laminates of the $[0\pm\theta/90\pm\theta]_{\mathrm{T}}$ family were found to have larger out-of-plane displacement in state II than state I, with the rough resin layer on the convex surface, Fig. 5.2. As this layer is not included in the analytical model the two states are predicted to have equal magnitudes of maximum displacement. The laminate profile of Fig. 5.5 shows that the difference in shape is not negligible between state I and II as discussed earlier. The difference in maximum out-of-plane displacement between states for this family of laminates was found to vary by between 0.7 - 3.1mm leading to differences in errors between states of 1.3 - 17.6%.

A thin layer of cured epoxy resin is added to the analytical model to quantify its effect. This is achieved by using the analytical solution for the ideal modelling case as a close initial guess to the imperfect laminate with the additional resin layer. Equation 4.12 is then solved iteratively to obtain the imperfect shape. Images of the cross-section from optical microscopy of one example laminate are used to investigate the thickness of this additional layer [39]. It is found that far from having a uniform thickness the resin layer varies from negligible to 0.08mm across the entire surface. A mean thickness of 0.025mm is taken to be representative of this layer and this approach has been used in a FE model to achieve good accuracy [39].

The effect of modelling an additional resin layer is shown in Table 5.2. Where previously it had been predicted that state I and state II should have equal maximum out-of-plane displacements, the shapes with a resin layer show the differential curvatures as seen in the experimental results. The state with the largest displacement agrees with experimental results for all laminates. The differences in the predicted maximum out-of-plane displacement between states for the $[0\pm\theta/90\pm\theta]_{\mathrm{T}}$ family of laminates are found to vary by between 0.7 - 3.4mm, correlating well with experimental results. This additional layer in the model leads to differences in errors between states of 0.3 - 7.2%, a significant improvement over the ideal model. Improvements to the manufacturing process could greatly reduce this resin imperfection.

It is also noted that a thin layer of resin exists between the plies. This layer is observed to be of the order of one hundredth of a ply thickness so the effect on the overall laminate shape is small. Inclusion of a resin layer between plies in the analytical model showed that a layer of one twentieth of a ply thickness is required for a 1% variation in maximum displacement. This effect is clearly less than that of the surface resin layer, but could be significant for a different manufacturing process.

5.2.2 Effects of Ply Thickness

For the ideal modelling predictions of the laminate shapes it is also assumed plies are uniform both in terms of geometry and material properties. Hamamoto and Hyer [45] previously found that slight imperfections as little as 1% in the thickness of each layer of the laminate can cause the bifurcation behaviour to disappear and significantly affect the temperature-curvature relationship.

Figure 5.7 shows an image of a two ply laminate section. The microscopy measurements suggest it is reasonable to expect $\pm 2\%$ variation in the thicknesses of individual plies as a result of variability during manufacturing. The effect of these potential imperfections is investigated by modelling each of the laminates with a through-thickness profile of

[t+2%/t-2%], where t is the ideal single ply thickness. The analytical solution for the ideal modelling case is again used as a close approximation to the nonuniform case to obtain the imperfect laminate shapes. This imperfection is found to lead to changes in maximum out-of-plane displacement for the ten laminate shapes of up to ±4.6%. Given the magnitudes of the errors in Table 5.2 this thickness effect is significant and should be investigated further.

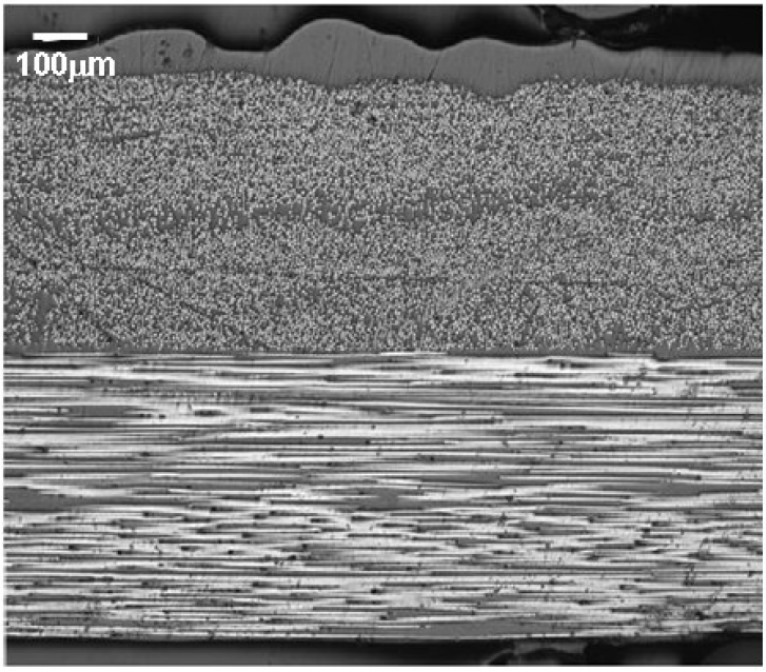

Figure 5.7: Microscopy image of a two-ply laminate section.

5.2.3 Free Edge Characteristics

Figure 5.6 shows the profiles of the predicted and experimental shapes along the minor curvature A-B (see Fig. 5.2) for the $[-45/45]_{\mathrm{T}}$ laminate. This trend was observed in all laminates tested where the out-of-plane displacement is small across the central region but increases significantly at the edges. It is well known that interlaminar stresses increase rapidly near free edges of laminates and this leads to the high out-of-plane displacement observed in Fig. 5.6 [61]. As the interlaminar stresses are not included in the analytical model, this high out-of-plane displacement is only observed in the experimental data.

In-plane stresses arises from the mismatch of thermal expansion coefficients between plies. In order to satisfy boundary conditions at the free edges, the overall in-plane direct stresses of the laminate must be zero. This leads to increased through-thickness stresses along the edges of the laminate, hence the high out-of-plane displacement [68].

It follows that the magnitude of the displacement is dependent on the ply orientations [71]. It has been suggested that the combination of two adjacent free edge effects further increases the displacement at the corners [68]. This free corner effect is observed in the sudden curvature change and the peak displacement in Fig. 5.6. However, the effect is localised and does not significantly alter the overall shape or bistable behaviour of the laminate.

Previous work to model bistable laminates using FEA [39] has shown that the free edge effects can be captured. Complex analytical models have also been developed to model this behaviour [71]. However, these modelling approaches are computationally expensive, typically require some prior knowledge of the solution, and are therefore not well suited to optimisation.

5.2.4 Dependency on the Operating Environment

The bistable configuration arises from the anisotropic thermal expansion of the composite materials, Table 5.1. As a result the dependency of the bistable laminate shapes on the cure and ambient temperatures must be quantified. The relationship between temperature and curvature is well documented [24] and the sensitivity can be easily investigated using the existing analytical model. Away from the bifurcation point the temperature-curvature relation is approximately linear. With reference to Eq. 4.1, the three displacement coefficients defining the out-of-plane displacement of the $[-45/45]_{\mathrm{T}}$ laminate, a, b and c, are modelled to vary with temperature as shown in Fig. 5.8.

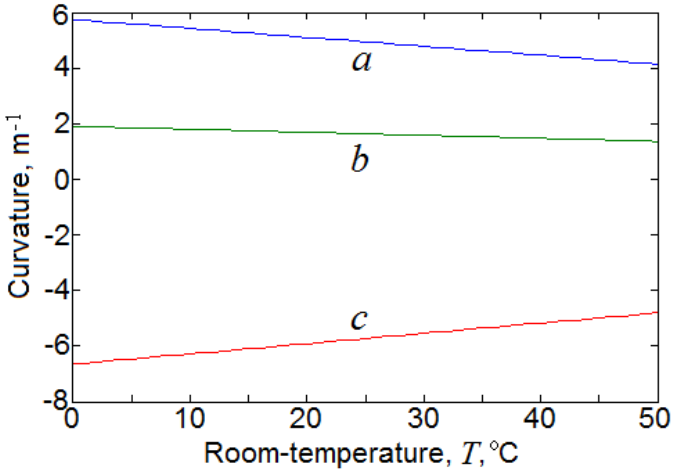

Figure 5.8: Variation in curvature with temperature for a $[-45/45]_{\mathrm{T}}$ laminate.

The predicted shapes of the laminates are generated using a standard room-temperature value of 21°C. Any variation in temperature when obtaining the experimental data will affect the measured curvatures. It is reasonable to assume that there is some variability

in the quoted cure temperature of 180°C. Equally, the room-temperature around the experimental test area cannot be guaranteed consistent. Using the relationships shown in Fig. 5.8, as little as 5°C difference in the temperature change corresponds to a change in maximum deflection of around 3% of the total deflection when compared with the quoted modelling values. A similar magnitude was observed for all laminates. Potential temperature dependent discrepancy is significant. This result highlights the sensitivity of the model to physical conditions.

Other environmental effects such as moisture content [34] may also be significant in the long term. It is widely known that epoxy resin systems typically used in the manufacture of composite laminates will absorb atmospheric moisture [101, 109]. This leads to an expansion of the material which is proportional to the moisture expansion coefficients [2, 14]. This moisture induced expansion relaxes the residual stresses caused by the thermal contraction from cure to ambient temperature [104] which leads to a reduction in the thermally induced deformations, and therefore a reduction in the energy input required for actuation.

Moisture absorption has been considered by Etches et al. [34] and Portela et al. [76] using both finite element and analytical modelling methods. Etches et al. [34] modelled the effect for a range of relative humidities and compared predictions with experimental results for multiple samples. It was shown that the change in curvature with moisture absorption is small for relative humidities of approximately 40% or less (corresponding to 0.6% moisture content) with the variation becoming more pronounced beyond this point. Given that the modelling formulation becomes disproportionately large to capture an effect which occurs in very restricted circumstances, the effect is omitted from the modelling in this work. However, it is acknowledged that this may affect where a bistable laminate could be deployed.

5.2.5 Material Properties and Manufacturing Accuracy

The final source of uncertainty considered is variability in prepreg material properties. These variations can arise for two reasons. Firstly, some material properties required for modelling are difficult to accurately measure, in particular the Poisson's ratio. Secondly, the prepreg material properties decay over time leading to variation between specimens. A typical sample of material will have a useful 'shelf life' of around 30 days at room temperature prior to curing. Unlike some of the previously discussed sources of uncertainty, this unknown element in the material characterisation cannot be controlled by improving the manufacturing process or measuring a manufactured sample. A more detailed investigation of the sensitivities of the modelling to material uncertainty is presented in the following section.

5.3 Sensitivity Analysis

The sources of uncertainty which cannot be reduced by improvements to the manufacturing process are the material properties, temperature dependency and ply thicknesses. The significance of each of these areas is investigated fully in this section where the matrix formulation (Eq. 4.67) of the analytical model is exploited to derive relationships linking each individual property with the associated change in total laminate strain energy. By this method the relative sensitivities of the model to each of the properties can be highlighted.

5.3.1 Longitudinal Young's Modulus

The first property considered is the longitudinal Young's modulus of the the prepreg material, E_{11}. In the matrix formulation of the total laminate strain energy equation (Eq. 4.67) only the stiffness matrix $\boldsymbol{Q}$, a component of the stiffness invariant matrix $\boldsymbol{U}$, is dependent on this property. To derive the total strain energy derivative with respect to E_{11} each term of $\boldsymbol{Q}$ is differentiated in turn as follows,

$$\frac{\partial Q_{11}}{\partial E_{11}} = \frac{E_{11}\left(E_{11} - 2\nu_{12}^2 E_{22}\right)}{\left(E_{11} - \nu_{12}^2 E_{22}\right)^2} \tag{5.1}$$

$$\frac{\partial Q_{22}}{\partial E_{11}} = \frac{-E_{22}^2 \nu_{12}^2}{\left(E_{11} - \nu_{12}^2 E_{22}\right)^2} \tag{5.2}$$

$$\frac{\partial Q_{12}}{\partial E_{11}} = \frac{-E_{22}^2 \nu_{12}^3}{\left(E_{11} - \nu_{12}^2 E_{22}\right)^2} \tag{5.3}$$

$$\frac{\partial Q_{66}}{\partial E_{11}} = 0 \tag{5.4}$$

Equations 5.1 - 5.4 are then gathered to define the partial derivative of $\boldsymbol{Q}$ with respect to E_{11}, denoted $\boldsymbol{Q}_{E_{11}}$.

$$[\boldsymbol{Q}_{E_{11}}] = \begin{bmatrix} \frac{\partial Q_{11}}{\partial E_{11}} & \frac{\partial Q_{22}}{\partial E_{11}} & \frac{\partial Q_{12}}{\partial E_{11}} & \frac{\partial Q_{66}}{\partial E_{11}} \end{bmatrix} \tag{5.5}$$

Equation 5.5 is then substituted into Eq. 4.21 to define the partial derivative of $\boldsymbol{U}$ with respect to E_{11}, denoted $\boldsymbol{U}_{E_{11}}$.

$$[\boldsymbol{U}_{E_{11}}] = [\boldsymbol{Q}_{E_{11}}][\boldsymbol{Q}_{coef}] \tag{5.6}$$

Finally, Eq. 5.6 is substituted into Eq. 4.67 to define the change in total strain energy with change in E_{11}.

$$\frac{\partial W}{\partial E_{11}} = [\boldsymbol{U}_{E_{11}}][\boldsymbol{Z}][\boldsymbol{K}][\boldsymbol{T}][\boldsymbol{X}][\boldsymbol{L}] \tag{5.7}$$

This expression can then be used to demonstrate the sensitivity of the analytical model to variation in E_{11}. To do this a single $[-30/60]_T$ laminate layup is selected from the experimental investigation and is modelled for values between 5% below and 5% above the expected value of E_{11}. This is repeated for a wide range of edge length to thickness ratios (L/t) from 0 to 250. For each laminate composition Eq. 5.7 is used to calculate the variation in total laminate strain energy from the benchmark value associated with the manufacturer stated value for E_{11}. Results are shown in Fig. 5.9.

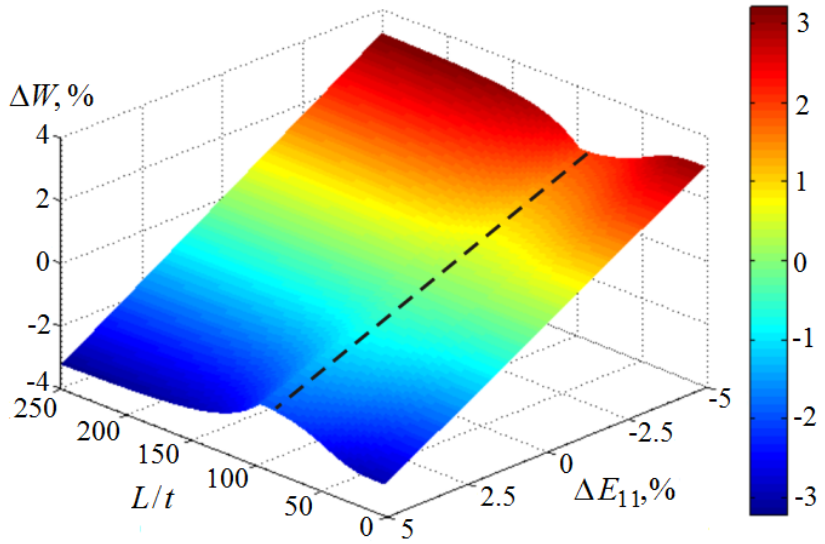

Figure 5.9: Percentage change in total strain energy with ±5% change in E_{11} for a $[-30/60]_T$ laminate. Dashed line denotes bifurcation point.

Figure 5.9 shows that the minimum change in strain energy for any given change in E_{11} occurs at the bifurcation point at approximately $L/t = 100$. Away from the bifurcation point the percentage change in strain energy approaches an upper limit of around ±3.2% for a ± 5% variation in E_{11}.

Variation in the observed relationship with change in laminate layup is considered by repeating this modelling process for four different cross-symmetric layups, $[0/90]_T$, $[-15/75]_T$, $[-30/60]_T$, and $[-45/45]_T$. The results are shown in Fig. 5.10 for a -5% change in E_{11}. It is found that for edge length to thickness ratios away from the bifurcation point the percentage change in total strain energy approaches the same limit of 3.2% for all tested layups. Around the bifurcation point some variation in the results is observed, due primarily to the variation in the location of the bifurcation point for each layup. In all cases, the largest percentage change in strain energy occurs as L/t becomes large.

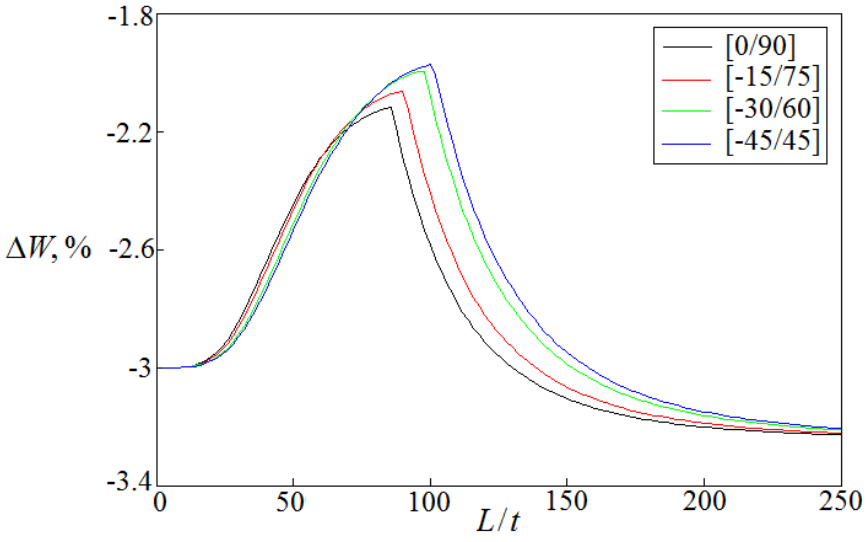

Figure 5.10: Percentage change in total strain energy with -5% change in E_{11} for four cross-symmetric layups.

5.3.2 Transverse Young's Modulus

The next variable considered is the transverse Young's modulus of the prepreg material, E_{22}. Following the same process as in the previous section, only the matrix $\boldsymbol{Q}$ of Eq. 4.67 varies with E_{22}. To find the derivative of the total strain energy with respect to E_{22} each term of $\boldsymbol{Q}$ is differentiated in turn.

$$\frac{\partial Q_{11}}{\partial E_{22}} = \frac{E_{11}^2 \nu_{12}^2}{\left(E_{11} - \nu_{12}^2 E_{22}\right)^2} \tag{5.8}$$

$$\frac{\partial Q_{22}}{\partial E_{22}} = \frac{E_{11}^2}{\left(E_{11} - \nu_{12}^2 E_{22}\right)^2} \tag{5.9}$$

$$\frac{\partial Q_{12}}{\partial E_{22}} = \frac{E_{11}^2 \nu_{12}}{\left(E_{11} - \nu_{12}^2 E_{22}\right)^2} \tag{5.10}$$

$$\frac{\partial Q_{66}}{\partial E_{22}} = 0 \tag{5.11}$$

Equations 5.8 - 5.11 are then gathered to form the partial derivative of $\boldsymbol{Q}$ with respect to E_{22}, denoted $\boldsymbol{Q}_{E_{22}}$.

$$[\boldsymbol{Q}_{E_{22}}] = \begin{bmatrix} \frac{\partial Q_{11}}{\partial E_{22}} & \frac{\partial Q_{22}}{\partial E_{22}} & \frac{\partial Q_{12}}{\partial E_{22}} & \frac{\partial Q_{66}}{\partial E_{22}} \end{bmatrix} \tag{5.12}$$

Equation 5.12 is then substituted into Eq. 4.21 to define the partial derivative of $\boldsymbol{U}$ with respect to E_{22}, denoted $\boldsymbol{U}_{E_{22}}$.

$$[\boldsymbol{U}_{E_{22}}] = [\boldsymbol{Q}_{E_{22}}][\boldsymbol{Q}_{coef}] \tag{5.13}$$

Finally, Eq. 5.13 is substituted into Eq. 4.67 to define the change in total strain energy with respect to E_{22}.

$$\frac{\partial W}{\partial E_{22}} = [\boldsymbol{U}_{E_{22}}][\boldsymbol{Z}][\boldsymbol{K}][\boldsymbol{T}][\boldsymbol{X}][\boldsymbol{L}] \tag{5.14}$$

This expression is then used to assess the sensitivity of the analytical model to variation in E_{22}. Figure 5.11 shows the surface plot of this relationship for the same $[\text{-}30/60]_{\text{T}}$ laminate, with the change in E_{22} from -5% to +5% and change in L/t from 0 to 250.

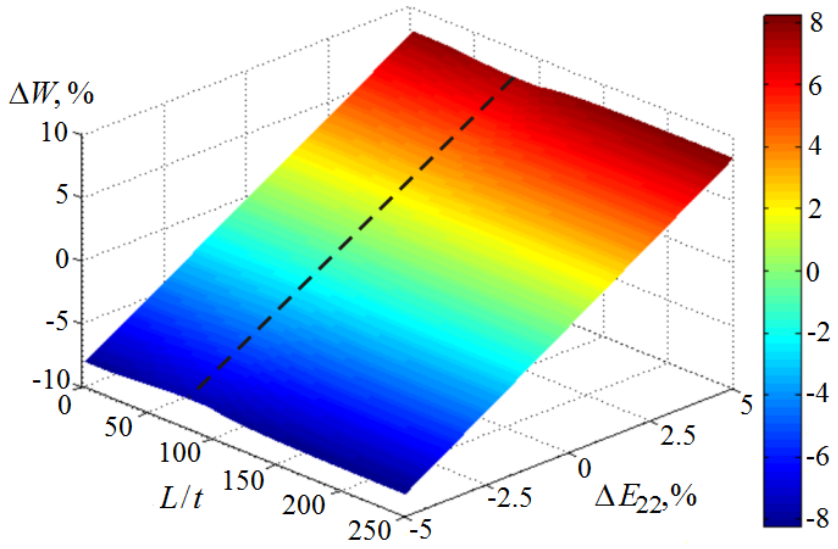

Figure 5.11: Percentage change in total strain energy with ±5% change in E_{22} for a $[\text{-}30/60]_{\text{T}}$ laminate. Dashed line denotes bifurcation point.

The basic pattern of results seen in Fig. 5.11 mirrors that for the longitudinal Young's modulus, Fig. 5.9. The smallest variation in strain energy for any given change in E_{22} is again observed to be at the bifurcation point ($L/t \approx 100$), with increasing variation for low or high geometric ratios. However, the absolute values are significantly higher than for E_{11}, with a maximum variation in strain energy of approximately 8.2%. This suggests that accurate estimation of the transverse Young's modulus is of higher significance than the longitudinal value.

This sensitivity analysis is again repeated for four example cross-symmetric layups. The pattern of results is seen to follow the same trend as for variation in E_{11}, with all layups tending to the same absolute variation in total strain energy for high ratios of L/t. Again, some variation in results is observed around the bifurcation point for each laminate layup.

5.3.3 Poisson's Ratio

The significance of the Poisson's ratio of the material ν_{12} is now considered. This property is particularly difficult to characterise experimentally for carbon fibre/epoxy laminates [49], as typical measurement methods are not suited to the small diameter, fibre-like material. Therefore, understanding the sensitivity of the model to this parameter is of particular importance. To derive this relationship, each term of the matrix $\boldsymbol{Q}$ is differentiated with respect to ν_{12},

$$\frac{\partial Q_{11}}{\partial \nu_{12}} = \frac{2E_{11}^2 E_{22}\nu_{12}}{\left(E_{11} - \nu_{12}^2 E_{22}\right)^2} \tag{5.15}$$

$$\frac{\partial Q_{22}}{\partial \nu_{12}} = \frac{2E_{11} E_{22}^2 \nu_{12}}{\left(E_{11} - \nu_{12}^2 E_{22}\right)^2} \tag{5.16}$$

$$\frac{\partial Q_{12}}{\partial \nu_{12}} = \frac{E_{11}E_{22}\left(E_{11} + \nu_{12}^2 E_{22}\right)}{\left(E_{11} - \nu_{12}^2 E_{22}\right)^2} \tag{5.17}$$

$$\frac{\partial Q_{66}}{\partial \nu_{12}} = 0 \tag{5.18}$$

which gives the following form for the partial derivative of $\boldsymbol{Q}$ with respect to ν_{12}, denoted $\boldsymbol{Q}_{\nu_{12}}$.

$$[\boldsymbol{Q}_{\nu_{12}}] = \begin{bmatrix} \frac{\partial Q_{11}}{\partial \nu_{12}} & \frac{\partial Q_{22}}{\partial \nu_{12}} & \frac{\partial Q_{12}}{\partial \nu_{12}} & \frac{\partial Q_{66}}{\partial \nu_{12}} \end{bmatrix} \tag{5.19}$$

Equation 5.19 is then substituted into Eq. 4.21 to define the partial derivative of $\boldsymbol{U}$, denoted $\boldsymbol{U}_{\nu_{12}}$.

$$[\boldsymbol{U}_{\nu_{12}}] = [\boldsymbol{Q}_{\nu_{12}}][\boldsymbol{Q}_{coef}] \tag{5.20}$$

which is finally substituted into Eq. 4.67 to define the change in total strain energy with respect to ν_{12}.

$$\frac{\partial W}{\partial \nu_{12}} = [\boldsymbol{U}_{\nu_{12}}][\boldsymbol{Z}][\boldsymbol{K}][\boldsymbol{T}][\boldsymbol{X}][\boldsymbol{L}] \tag{5.21}$$

This expression is then used to assess the sensitivity of the model to variation in ν_{12}. Figure 5.12 shows the surface plot of this relationship for the $[\text{-}30/60]_{\text{T}}$ laminate, with the change in ν_{12} from -5% to +5% from the manufacturer quoted value, and change in L/t from 0 to 250.

The pattern of results seen in Fig. 5.12 shows some distinctly different features than for the longitudinal and transverse Young's moduli. In this case the smallest variation in total strain energy is not observed to be at the bifurcation point, but rather for lower edge length to thickness ratios. This variation increases as the ratio tends towards the bifurcation point before slowly approaching a limit value for high values of L/t. More significantly however, this limiting value is considerably smaller than for the previously considered properties. For a $\pm$5% change in ν_{12} only a $\pm$0.6% variation

in total strain energy is observed. Having stated that the Poisson's ratio is particularly difficult to characterise experimentally, it is significant to note than large uncertainty in this property will not significantly affect the analytical model.

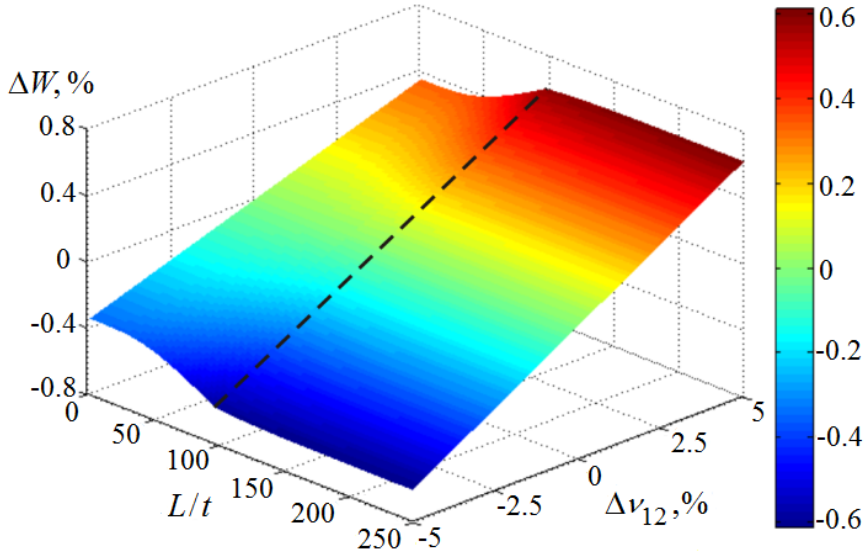

Figure 5.12: Percentage change in total strain energy with ±5% change in ν_{12} for a $[\text{-}30/60]_{\text{T}}$ laminate. Dashed line denotes bifurcation point.

As with the Young's modulus variation, the pattern of results is found to not vary significantly with layup for cross-symmetric stacking sequences. All laminates are found to tend towards to the same level of strain energy variation for high L/t, with small variation around the bifurcation point.

5.3.4 Shear Modulus

The shear modulus of the material G_{12} is the final property whose variation is limited to the matrix $\boldsymbol{Q}$. Furthermore, it only appears in a single term of the matrix $\boldsymbol{Q}$, leading to the following simple form of the partial derivatives with respect to G_{12}.

$$\frac{\partial Q_{11}}{\partial \nu_{12}} = 0 \tag{5.22}$$

$$\frac{\partial Q_{22}}{\partial \nu_{12}} = 0 \tag{5.23}$$

$$\frac{\partial Q_{12}}{\partial \nu_{12}} = 0 \tag{5.24}$$

$$\frac{\partial Q_{66}}{\partial \nu_{12}} = 1 \tag{5.25}$$

The partial derivative of $\boldsymbol{Q}$ with respect to G_{12} then takes the following form, and is denoted $\boldsymbol{Q}_{G_{12}}$.

$$[\boldsymbol{Q}_{G_{12}}] = \begin{bmatrix} \frac{\partial Q_{11}}{\partial G_{12}} & \frac{\partial Q_{22}}{\partial G_{12}} & \frac{\partial Q_{12}}{\partial G_{12}} & \frac{\partial Q_{66}}{\partial G_{12}} \end{bmatrix} \tag{5.26}$$

Equation 5.26 is then substituted into Eq. 4.21 to give the partial derivative of $\boldsymbol{U}$, denoted $\boldsymbol{U}_{G_{12}}$.

$$[\boldsymbol{U}_{G_{12}}] = [\boldsymbol{Q}_{G_{12}}][\boldsymbol{Q}_{coef}] \tag{5.27}$$

which is finally substituted into Eq. 4.67 to define the change in total strain energy with respect to G_{12}.

$$\frac{\partial W}{\partial G_{12}} = [\boldsymbol{U}_{G_{12}}][\boldsymbol{Z}][\boldsymbol{K}][\boldsymbol{T}][\boldsymbol{X}][\boldsymbol{L}] \tag{5.28}$$

This expression is then used to assess the sensitivity of the model to variation in G_{12}. Figure 5.13 shows the surface plot of this relationship for the [-30/60]$_\mathrm{T}$ laminate, with the change in G_{12} from -5% to +5% from the manufacturer quoted value, and change in L/t from 0 to 250.

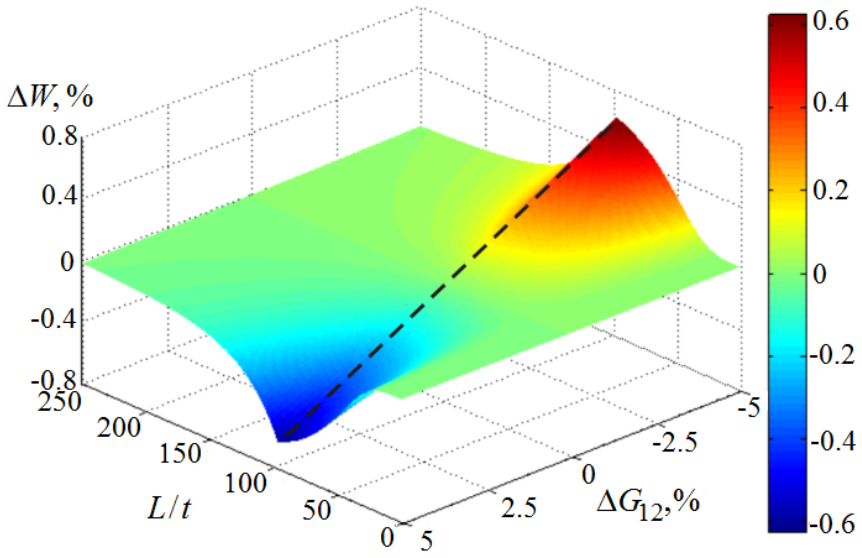

Figure 5.13: Percentage change in total strain energy with ±5% change in G_{12} for a [-30/60]$_\mathrm{T}$ laminate. Dashed line denotes bifurcation point.

The pattern of results seen in Fig. 5.13 is different to that seen for the previous material properties. As the ratio L/t tends to small or large values, the variation in total strain energy with G_{12} approaches zero. Only around the bifurcation point does the property have any significant effect on the analytical model. This suggests that for laminates which are comfortably within the bistable region, accurate estimation of the shear modulus is of little importance. However, when defining the boundary between monostable and bistable designs, the shear modulus becomes more significant. Even in this case, the variation in total strain energy with G_{12} is small. The maximum variation oberved for ±5% change in G_{12} is approximately ±0.6%, similar to that for

the Poisson's ratio and an order of magnitude smaller than the transverse Young's modulus.

When considering this relationship for different cross-symmetric laminates, some variation is observed. As with the $[\text{-}30/60]_{\text{T}}$ laminate, the variation in total strain energy with G_{12} is seen to tend towards zero for small and large values of L/t for all laminates. However, each laminate has a slightly different bifurcation point and a different maximum variation in strain energy is observed in each case. This value remains small for all stacking sequences, with the lowest variation observed for the $[0/90]_{\text{T}}$ laminate, increasing to a maximum for the $[\text{-}45/45]_{\text{T}}$ laminate.

5.3.5 Longitudinal Thermal Expansion Coefficient

The next property considered is the thermal expansion coefficient in the fibre direction, α_1. With reference to Eq. 4.67, the only component of the analytical model which varies with this property is the matrix $\boldsymbol{K}$. Therefore, the partial of derivative of $\boldsymbol{K}$ with respect to α_1 is taken, denoted $\boldsymbol{K}_{\alpha_1}$.

$$[\boldsymbol{K}_{\alpha_1}] = \begin{bmatrix} [0_{10\times10}] & & [0_{3\times10}] & \\ & \alpha_{A_1} & 0 & 0 \\ & \alpha_{B_1} & 0 & 0 \\ [0_{10\times6}] & 0 & \alpha_{A_1} & 0 \\ & 0 & \alpha_{B_1} & 0 \\ & 0 & 0 & \alpha_{A_1} \\ & 0 & 0 & \alpha_{B_1} \end{bmatrix} \tag{5.29}$$

where the factors α_{A_1} and α_{B_1} are defined as follows.

$$\alpha_{A_1} = \alpha_{B_1} = \frac{1}{2}\Delta T \tag{5.30}$$

Equation 5.29 is then substituted back into Eq. 4.67 to define the change in the total strain energy of the laminate with respect to change in α_1.

$$\frac{\partial W}{\partial \alpha_1} = [\boldsymbol{U}][\boldsymbol{Z}][\boldsymbol{K}_{\alpha_1}][\boldsymbol{T}][\boldsymbol{X}][\boldsymbol{L}] \tag{5.31}$$

This expression is then used to assess the sensitivity of the model to variation in α_1. Figure 5.14 shows the surface plot of this relationship for the $[\text{-}30/60]_{\text{T}}$ laminate, with change in α_1 from -5% to +5% from the manufacturer quoted value, and change in L/t from 0 to 250.

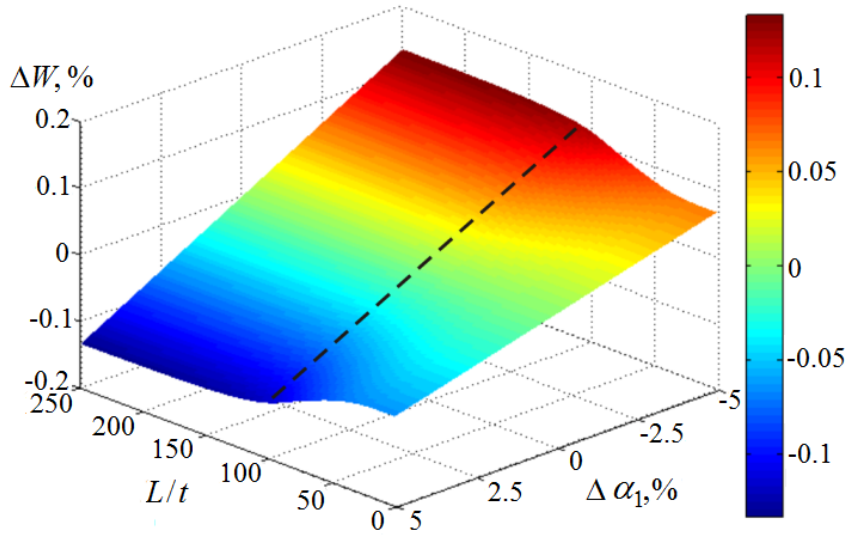

Figure 5.14: Percentage change in total strain energy with ±5% change in α_1 for a $[-30/60]_T$ laminate. Dashed line denotes bifurcation point.

Figure 5.14 shows that the variation in total strain energy with α_1 follows a very similar pattern to that for ν_{12}. The smallest variations are observed for low edge length to thickness ratio with a smooth increase through the bifurcation point. Beyond the bifurcation point the variation tends to an upper limit of around ±0.13% for a ±5% change in α_1. This represents the smallest variation observed for any of the design variables and suggests that accurate estimation of α_1 is of little importance. This pattern is observed for all cross-symmetric laminates. With reference to Table 5.1, α_1 is two orders of magnitude smaller than the corresponding transverse thermal expansion coefficient α_2. It is therefore unsurprising that this property does not significantly affect the analytical model.

5.3.6 Transverse Thermal Expansion Coefficient

Having shown that the longitudinal thermal expansion coefficient has little effect on the analytical model, the larger transverse coefficient α_2 is considered. Once again, only the matrix $\boldsymbol{K}$ varies with thermal properties so the partial derivative with respect to α_2, denoted $\boldsymbol{K}_{\alpha_2}$, is taken,

$$[\boldsymbol{K}_{\alpha_2}] = \begin{bmatrix} [0_{10\times10}] & & [0_{3\times10}] & \\ & \alpha_{A_2} & 0 & 0 \\ & \alpha_{B_2} & 0 & 0 \\ [0_{10\times6}] & 0 & \alpha_{A_2} & 0 \\ & 0 & \alpha_{B_2} & 0 \\ & 0 & 0 & \alpha_{A_2} \\ & 0 & 0 & \alpha_{B_2} \end{bmatrix} \tag{5.32}$$

where the factors α_{A_2} and α_{B_2} are defined as follows.

$$\alpha_{A_2} = \frac{1}{2}\Delta T, \quad \alpha_{B_2} = -\frac{1}{2}\Delta T \tag{5.33}$$

Equation 5.32 is then substituted back into Eq. 4.67 to define the change in the total strain energy of the laminate with respect to change in α_2.

$$\frac{\partial W}{\partial \alpha_2} = [\boldsymbol{U}][\boldsymbol{Z}][\boldsymbol{K}_{\alpha_2}][\boldsymbol{T}][\boldsymbol{X}][\boldsymbol{L}] \tag{5.34}$$

This expression is used to assess the sensitivity of the model to variation in α_2. Figure 5.15 shows the surface plot of this relationship for the $[\text{-}30/60]_\text{T}$ laminate, with the change in α_2 from -5% to +5% from the manufacturer quoted value, and change in L/t from 0 to 250.

The results in Fig. 5.15 show a distinctly different pattern than for α_1. The smallest variation in total strain energy is found at the bifurcation point with increases as the L/t tends to either small or large values. The largest variation is observed as L/t becomes large, with a maximum value of approximately $\pm 10.1\%$ for a $\pm 5\%$ change in α_2. This is the highest variation observed for any of the material properties, and is observed in all cross-symmetric laminates. However, the thermal expansion coefficients, and in particular the transverse coefficient, can be characterised experimentally to a high degree of accuracy [9]. Assuming that the material has not degraded prior to manufacture, errors in the quoted material property will be an order of magnitude smaller than the limit considered in this study. Of greater concern is variation in the ambient temperature, considered in the following section.

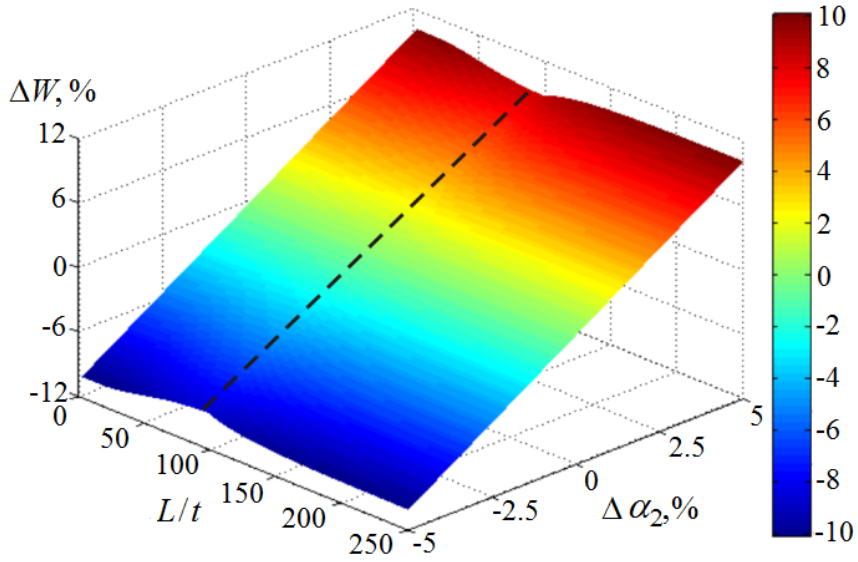

Figure 5.15: Percentage change in total strain energy with $\pm 5\%$ change in α_2 for a $[\text{-}30/60]_\text{T}$ laminate. Dashed line denotes bifurcation point.

5.3.7 Temperature Change from Cure

All design variables considered to this point have been material properties. These values are determined experimentally and the level of uncertainty in the model can be controlled by accurate characterisation of each property. In this section the change in temperature from cure to ambient ΔT is considered as a variable. Two aspects of consideration here are accurate measurement of the maximum temperature experienced during the cure cycle, and variation in the ambient temperature for different operation conditions. To determine the sensitivity of the model to temperature the partial derivative of the matrix $\boldsymbol{K}$, denoted $\boldsymbol{K}_{\alpha_T}$, is taken,

$$[\boldsymbol{K}_{\alpha_T}] = \begin{bmatrix} [0_{10\times10}] & & [0_{3\times10}] & \\ & \alpha_{A_{\Delta T}} & 0 & 0 \\ & \alpha_{B_{\Delta T}} & 0 & 0 \\ [0_{10\times6}] & 0 & \alpha_{A_{\Delta T}} & 0 \\ & 0 & \alpha_{B_{\Delta T}} & 0 \\ & 0 & 0 & \alpha_{A_{\Delta T}} \\ & 0 & 0 & \alpha_{B_{\Delta T}} \end{bmatrix} \tag{5.35}$$

where the factors $\alpha_{A_{\Delta T}}$ and $\alpha_{B_{\Delta T}}$ are defined as follows.

$$\alpha_{A_{\Delta T}} = \frac{1}{2}\left(\alpha_1 + \alpha_2\right), \quad \alpha_{B_{\Delta T}} = \frac{1}{2}\left(\alpha_1 - \alpha_2\right) \tag{5.36}$$

Equation 5.35 is then substituted back into Eq. 4.67 to define the change in the total strain energy of the laminate with respect to change in ΔT.

$$\frac{\partial W}{\partial \Delta T} = [\boldsymbol{U}][\boldsymbol{Z}][\boldsymbol{K}_{\Delta T}][\boldsymbol{T}][\boldsymbol{X}][\boldsymbol{L}] \tag{5.37}$$

This expression is used to assess the sensitivity of the model to variation in ΔT. Figure 5.16 shows the surface plot of this relationship for the $[-30/60]_{\mathrm{T}}$ laminate, with the change in α_2 from -5% to +5% from the manufacturer quoted value, and change in L/t from 0 to 250.

Figure 5.16 shows that the minimum variation in strain energy occurs around the bifurcation point, with maximum variation occurring for large edge length to thickness ratios. The maximum variation observed for a $\pm5\%$ change in ΔT is approximately $\pm10\%$, observed for all cross-symmetric laminates. This highlights that accurate values for the change in temperature are vital for accurate modelling of the laminate shapes. Given that the curvatures are entirely thermally induced, this result is expected.

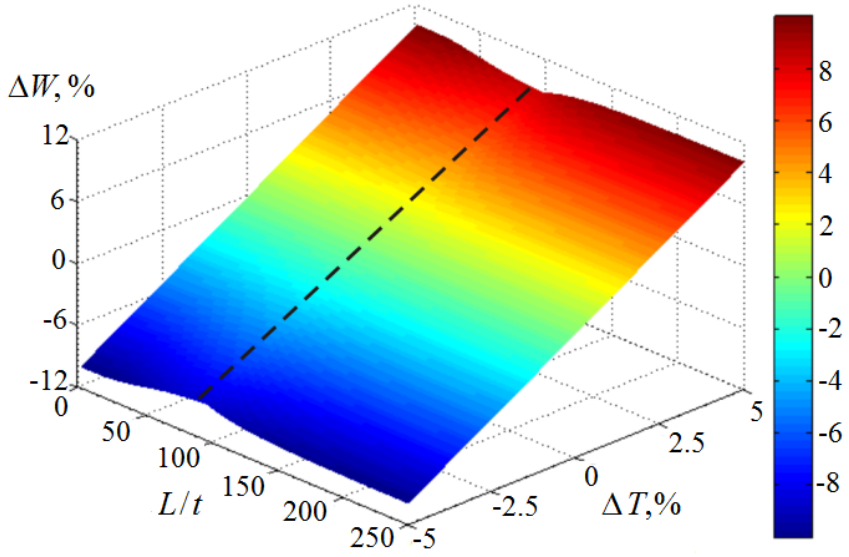

Figure 5.16: Percentage change in total strain energy with ±5% change in ΔT (cure to ambient) for a $[-30/60]_{\mathrm{T}}$ laminate. Dashed line denotes bifurcation point.

All modelling presented in this work assumes a cure temperature of 180°C as quoted by the manufacturer [47]. This value can be controlled to a high degree of accuracy in the manufacturing process so little variation is expected. Therefore the ambient temperature is the critical value. The worst case considered in this study (±5% error) corresponds to approximately an 8°C variation in temperature. While the ambient temperature can clearly be controlled well within this limit, this result does demonstrate that variation in operating conditions must be considered in the modelling.

5.3.8 Ply Thickness

The final property considered in this sensitivity analysis is the single ply thickness, t. This property only appears in the matrix $\boldsymbol{T}$ of Eq. 4.67. The partial derivative of $\boldsymbol{T}$ with respect to t, denoted $\boldsymbol{T}_t$, is therefore considered as follows.

$$[\boldsymbol{T}_t] = \mathrm{diag}\begin{bmatrix} 2 & 2 & 2 & 2 & -2t & -2t & 2t^2 & 2t^2 & 2t^2 & 2t^2 & 1 & t & t \end{bmatrix} \tag{5.38}$$

Equation 5.38 is then substituted into Eq. 4.67 to give the following expression for the change in total strain energy with variation in t.

$$\frac{\partial W}{\partial t} = [\boldsymbol{U}][\boldsymbol{Z}][\boldsymbol{K}][\boldsymbol{T}_t][\boldsymbol{X}][\boldsymbol{L}] \tag{5.39}$$

This expression is illustrated in Fig. 5.16 for the $[-30/60]_{\mathrm{T}}$ laminate, with variation in t of -5% to +5% from the manufacturer quoted value, and change in L/t from 0 to 250.

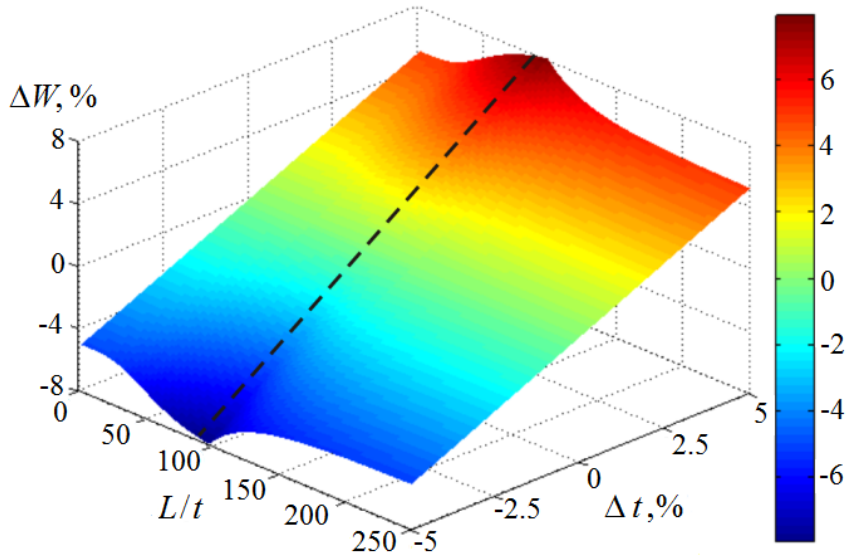

Figure 5.17: Percentage change in total strain energy with ±5% change in t for a $[\text{-}30/60]_{\text{T}}$ laminate. Dashed line denotes bifurcation point.

Figure 5.17 shows that the maximum variation in strain energy (±8%) is found at the bifurcation point, decreasing as L/t tends to a large value. This lower limit is observed to be approximately ±5% for all cross-symmetric laminates. Accurate characterisation of t depends on two factors. Firstly, the thickness of the material prior to manufacture, which can be obtained through microscopy techniques. Secondly, the effect of the layup process. Provided that this process is suitably repeatable, little variation is expected due to manufacturing. It is therefore expected that the relatively high variations seen in Fig. 5.17 can be negated by manufacturing quality control.

5.4 Concluding Remarks

This chapter has outlined a novel experimental study to characterise the shapes of a series of cross-symmetric layups. The results of this study have been compared to predictions made using the analytical model outlined in the previous chapter. Based on these results, a number of areas of uncertainty within the model have been identified, including edge effects, laminate geometry, material properties, manufacturing process and operating environment. These areas have been the focus of a sensitivity analysis to assess the suitability of the analytical model for defining the profiles of the deformed laminates shapes.

The experimental study aimed to characterise the room-temperature shapes of a series of laminates ($[-45/45]_T$, $[-30/60]_T$, $[-15/75]_T$, $[30/60]_T$ and $[45/90]_T$) through standard three-dimensional motion analysis techniques. The mean of the RMS error for all laminates was 0.2mm. The results of this study were used to compare cross-sectional profiles and maximum out-of-plane displacement values with modelling predictions, with up to 16.7% error in displacement values.

The experimental results identified a number of sources of uncertainty. Cross-sectional profiles highlighted that different magnitudes of curvature can be seen for two opposite stable shapes, where modelling predicts two equal and opposite shapes. This was attributed to a thin resin layer which occurs on the laminate surface during the manufacturing process. Inclusion of this layer in the analytical model reduced errors between states from 17.6% to 7.2%. Areas of localised deformation were also observed along the laminate edges, attributed to the well known edge effects.

The remaining discrepancies between the experimental results and modelling predictions are considered to be the result of inaccuracies in material properties and variation in the thermal conditions. A sensitivity analysis of the model with respect to each of these properties was conducted to highlight the importance of accurate estimation of each variable. The results of this study are summarised in Table 5.3 where the maximum variation in strain energy for $\pm 5\%$ change in design variable is stated for a $[-30/60]_T$ laminate. These results were found to be representative of all cross-symmetric laminates.

Of the material properties considered in this study the most significant variables in the model are clearly α_2, E_{22} and to a lesser extent E_{11}. Thermal properties can be characterised experimentally to a high degree of accuracy [9], while the Young's moduli are based on simple stress-strain behaviour. Therefore, little inaccuracy in these properties is expected and the high variations in the modelling should not be observed

in practice. Only negligible effects are observed for ν_{12}, G_{12} and α_1. Some variation in the quoted values of ν_{12} is expected as the property is difficlut to determine for carbon fiber/epoxy structures [49]. However, these results illustrate that this uncertainty will have little effect on modelling.

Table 5.3: Maximum change in total strain energy for ±5% change in design variable as L/t becomes large.

	Maximum change in W with ± 5% change in variable	
Variable	+5%	-5%
Longitudinal Young's modulus, E_{11}	-3.22	3.22
Transverse Young's modulus, E_{22}	8.24	-8.24
Poisson's ratio, ν_{12}	0.61	-0.61
Shear modulus, G_{12}	0*	0*
Longitudinal thermal expansion coefficient, α_1	-0.13	0.13
Transverse thermal expansion coefficient, α_2	10.07	-10.07
Temperature change from cure, ΔT	9.97	-9.97
Single ply thickness, t	5.05**	-5.05**

Note: A higher limit is seen for G_{12} near the bifurcation point of ± 0.63%. A higher limit is seet for t near the bifurcation point of ± 7.94%.

The model is observed to be sensitive to the additional design variables of temperature change and ply thickness. Both of these properties can be controlled by ensuring a good level of quality control within the manufacturing process. However, the results for temperature change do raise a secondary issue. While the cure temperature can be accurately quantified, it is reasonable to expect some variation in operating conditions for the laminate.

It is concluded that while the existing modelling techniques are successful in accurately predicting all stable states of cross-symmetric laminates, an accurate definition of the laminate structure, and in particular the operating environment, is essential. Provided that this definition is available, the model is considered suitable for design optimisation studies.

Chapter 6

Optimisation of Directional Properties of Bistable Laminates

This chapter presents an optimisation study for the design of bistable composite laminates enabled by the derivation of an analytical model for stable laminate shapes outlined in Chapter 4. The optimisation formulation addresses a well-known challenge of using bistable composite laminates for morphing applications where external operating loads must be prevented from inducing unwanted structural deformation. This motivation for the study is detailed in Section 6.1.

Section 6.2 introduces the optimisation problem formulation. The objective function is used to define the conflicting stiffness requirements of the laminate structure. A constraint is included to ensure bistability and a minimum deflection requirement is developed using the understanding of both stable states provided by the analytical modelling. The problem is solved using an iterative gradient based optimisation scheme.

Results obtained for a series of design examples are presented in Section 6.3. The design problem is found to have multiple local optima, with the global optimum not intuitively obvious from the problem definition, differing from the typical high deflection cross-ply solutions. Improvements in objective function are investigated by introducing variable geometry with nonuniform ply thicknesses.

Finally some concluding remarks discuss the feasibility of designing a bistable laminate requiring only a small actuation energy input while still providing a reasonable resistance to loads. Based on the results of this preliminary study, extension to include a method of actuation within the modelling is discussed.

6.1 Motivation for Optimisation

The optimisation formulation introduced in this chapter addresses a well-known challenge of using bistable composites for adaptive structures. To achieve large deformations and to allow low energy snap-through it is necessary to have low stiffness. However, low stiffness can also lead to unwanted structural deformation, meaning that normal operating loads (e.g. aerodynamic) have the potential to induce an unwanted state-change. The structural requirement to resist normal operating loads and a low energy requirement for actuation are therefore conflicting, leading to constrained optimisation of bistable laminate design.

The conflicting requirements for actuation loads and external operating loads is well evidenced by Diaconu et al. [31]. Using FEA, the design of a NACA 23012 airfoil was analysed with the rear section of the profile replaced with a bistable laminate combination, see Fig. 6.1. Designs consisting of 0°, 45° and 90° plies were assessed for actuation and displacement characteristics. Importantly the aerodynamic pressure that appears on the structure was ignored, while it was noted that in practice the structure should be designed not to be activated by ambient aerodynamic loading. Rather than incorporating the aerodynamic loading, requiring a dynamic analysis, it was proposed that an internal structure could be introduced to resist operating load deformations.

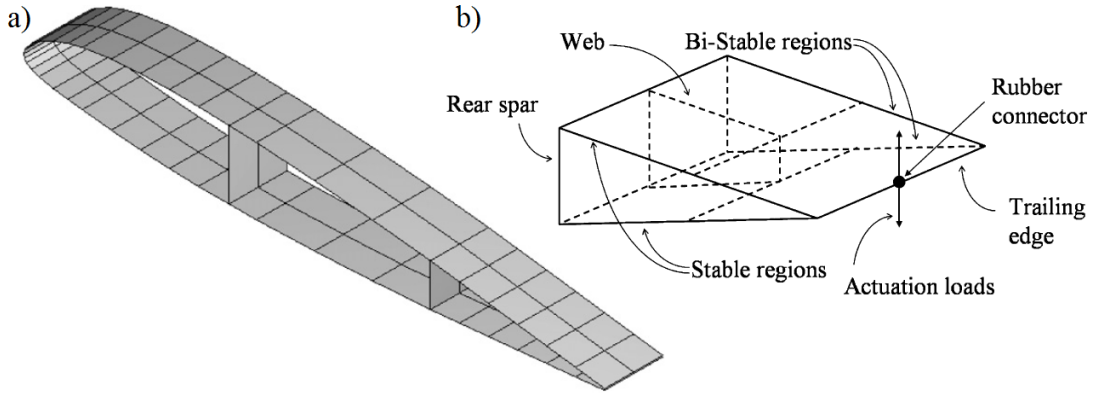

Figure 6.1: a) NACA 23012 airfoil and b) bistable trailing edge box, from [31].

In the work presented here an alternative approach is taken. The conflicting requirements are addressed by taking advantage of the directional stiffness properties of composite laminates. While the direction of aerodynamic loading may be dictated by other design constraints, the actuation direction can be considered a variable. Defining these two directions, ϕ_1 and ϕ_2 (see Fig. 6.2), the conflicting stiffnesses can be optimised.

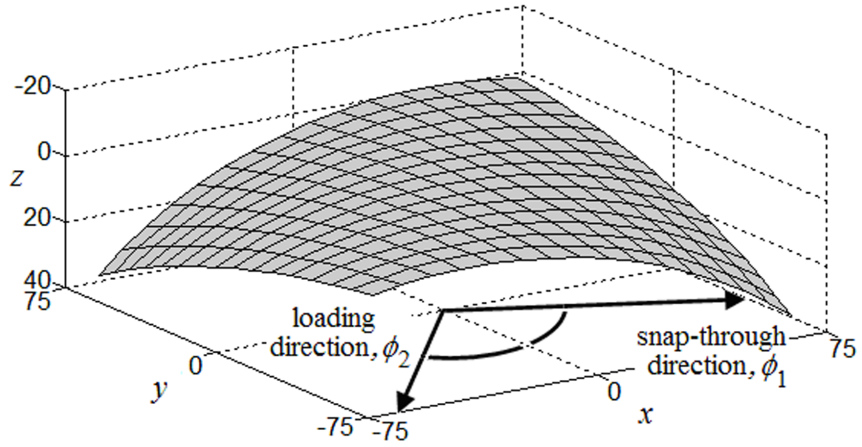

Figure 6.2: Ideal directional stiffness properties.

6.2 Optimisation Problem Formulation

In this section the optimisation formulation is introduced as follows:

Minimise:	Ratio of bending stiffnesses in two chosen directions, ϕ_1 and ϕ_2, Section 6.2.1.
Subject to:	The laminate must be bistable, Section 6.2.2.
	Deflection must be greater than a minimum value, Section 6.2.3.
	The four design rules outlined in Section 4.2.2
Variables:	Ply orientations θ_1 and θ_2.
	Ply thicknesses t_1 and t_2.
	Square laminate edge length L.

It is noted that this formulation is stated for the design of a four-ply laminate configuration (defined in terms of the top two plies according to Section 4.2.2) for ease of illustration. However, it is trivial to extend to any number of plies.

6.2.1 Objective Function

As discussed, the requirements for low stiffness in an actuation direction and high stiffness in the direction of an externally applied load are inherently conflicting. This issue is addressed by minimising the ratio of bending stiffness between two specified orientations, ϕ_1 and ϕ_2, Eq. 6.1. Thus the bending stiffness in ϕ_1, the direction of snap-through moment, is minimised while the bending stiffness in ϕ_2, the direction of the working load, is maximised, see Fig. 6.2. To characterise the bending stiffness at

ϕ, the change of major shape coefficient a_ϕ with respect to a moment applied in that direction, $M_{x\phi}$ is considered. The objective function which is to be minimised is then the ratio of this property in each of the two chosen directions.

$$\text{Objective function :} \quad \frac{\delta a_{\phi 2}}{\delta M_{x\phi 2}} / \frac{\delta a_{\phi 1}}{\delta M_{x\phi 1}} \tag{6.1}$$

This property is evaluated by considering the plate constitutive equations which relate externally applied forces and moments, N's and M's, to the plate curvatures, a, b and c, and midplane strains, ϵ^0's, using the $\boldsymbol{A}$, $\boldsymbol{B}$ and $\boldsymbol{D}$ matrices. Substituting Eq. 4.29 into the plate constitutive equations leads to Eq. 6.2.

$$\begin{bmatrix} N_x \\ N_y \\ N_{xy} \\ M_x \\ M_y \\ M_{xy} \end{bmatrix} = \begin{bmatrix} A_{11} & A_{12} & A_{16} & B_{11} & 0 & B_{16} \\ A_{12} & A_{11} & -A_{16} & 0 & -B_{11} & B_{16} \\ A_{16} & -A_{16} & A_{66} & B_{16} & B_{16} & 0 \\ B_{11} & 0 & B_{16} & D_{11} & D_{12} & D_{16} \\ 0 & -B_{11} & B_{16} & D_{12} & D_{11} & D_{16} \\ B_{16} & B_{16} & 0 & D_{16} & D_{16} & D_{66} \end{bmatrix} \begin{bmatrix} \epsilon_x^0 \\ \epsilon_y^0 \\ \epsilon_{xy}^0 \\ -a \\ -b \\ -c \end{bmatrix} \tag{6.2}$$

Equation 6.2 highlights that the relationship between the curvature a and an applied moment M_x is not dependent on a single property, but rather a complex combination of many properties. To develop this relationship Eq. 6.2 is first transformed to align with the direction of interest, ϕ_1 or ϕ_2, using the transformation matrix of Eq. 6.3, [100].

$$[\boldsymbol{T}_\phi] = \begin{bmatrix} m^4 & n^4 & 2m^2n^2 & 4m^2n^2 & -4m^3n & -4mn^3 \\ n^4 & m^4 & 2m^2n^2 & 4m^2n^2 & 4mn^3 & 4m^3n \\ m^2n^2 & m^2n^2 & m^4+n^4 & -4m^2n^2 & 2(m^3n-mn^3) & 2(mn^3-m^3n) \\ m^2n^2 & m^2n^2 & -2m^2n^2 & (m^2-n^2)^2 & 2(m^3n-mn^3) & 2(mn^3-m^3n) \\ m^3n & -mn^3 & mn^3-m^3n & 2(mn^3-m^3n) & m^4-3m^2n^2 & 3m^2n^2-n^4 \\ mn^3 & -m^3n & m^3n-mn^3 & 2(m^3n-mn^3) & 3m^2n^2-n^4 & m^4-3m^2n^2 \end{bmatrix} \tag{6.3}$$

where m and n are $\cos\phi$ and $\sin\phi$ of the angle of transformation. The transformed $\boldsymbol{A}$, $\boldsymbol{B}$ and $\boldsymbol{D}$ matrices, denoted by *, are then defined by the following expressions.

$$\begin{aligned} [\boldsymbol{A}^*] &= [\boldsymbol{T}_\phi]^{-1}[\boldsymbol{A}] \\ [\boldsymbol{B}^*] &= [\boldsymbol{T}_\phi]^{-1}[\boldsymbol{B}] \\ [\boldsymbol{D}^*] &= [\boldsymbol{T}_\phi]^{-1}[\boldsymbol{D}] \end{aligned} \tag{6.4}$$

The forces N_x, N_y and N_{xy}, and moments M_y and M_{xy} in the transformed direction are then set to zero and the remaining system is solved to give an expression for a in terms of $\boldsymbol{A}$, $\boldsymbol{B}$, $\boldsymbol{D}$, M_x and ϕ. This expression is obtained for each ϕ value using symbolic computing and is used to define the objective function of Eq. 6.1.

6.2.2 Bistability Constraint

Bistability is not guaranteed simply by the asymmetric nature of the stacking sequence. One stable state (saddle shape) exists for low edge length to thickness ratios (L/t) in all asymmetric layups [59], from point A to B in Fig. 6.3. Only beyond a critical edge to thickness ratio, point B, does the solution bifurcate to produce two stable solutions (approximately cylindrical states 1 and 2) and an unstable saddle solution (dotted line). This critical ratio is dependent on laminate geometry, stacking sequence, material properties and temperature change.

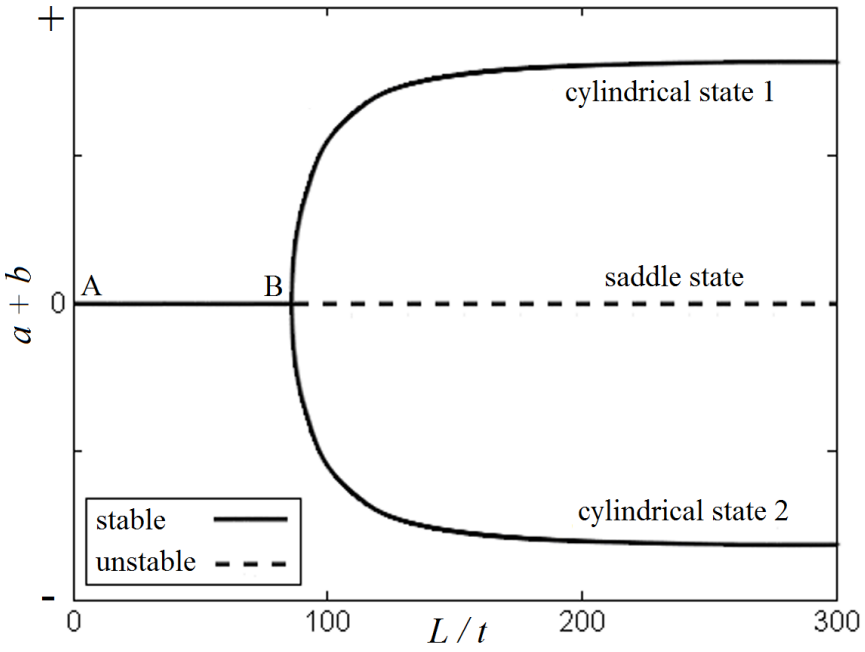

Figure 6.3: Example bistable constraint values.

To ensure that the design space for this optimisation problem is constrained to guarantee a bistable solution, a constraint is introduced using the shape coefficients: For the family of laminates considered here, the x- and y-curvatures have equal and opposite magnitude for the saddle shape, thus the sum of the curvatures a and b must always be zero. In contrast, the sum of the curvatures is either positive or negative for the two cylindrical shapes. Thus this property can be used to ensure that the design is bistable. Furthermore, by specifying either a positive or negative sum it is possible to determine which of the two shapes is being considered. In this work a positive value is used and the shape coefficients refer to cylindrical state 1 with large positive curvature in the x-direction.

$$\text{Bistability constraint}: \quad a + b > 0 \tag{6.5}$$

6.2.3 Deflection Constraint

It is noted that the bifurcation point is highly sensitive to uncertainties and imperfections such as material properties or manufacture [8]. As highlighted in Chapter 5 some level of uncertainty is expected near the bifurcation point. This can be accounted for by specifying a lower bound to move the constraint boundary away from the monostable region, considered to be a minimum deflection. For the deflection constraint the change in out-of-plane displacement at a corner of the laminate between states 1 and 2 is considered, see Fig. 6.4. The magnitude of the deflection between states at all four corners of this family of laminates are equal. Equation 4.1 defines the displacement for all points in the x-y plane. The corner deflection between states, w_{def}, at $x = y = L/2$ can therefore be expressed by Eq. 6.6, where the subscript denotes the associated stable state.

$$w_{def} = w_1 - w_2 = \frac{1}{8}\left(a_1 + b_1 + c_1\right) L^2 - \frac{1}{8}\left(a_2 + b_2 + c_2\right) L^2 \tag{6.6}$$

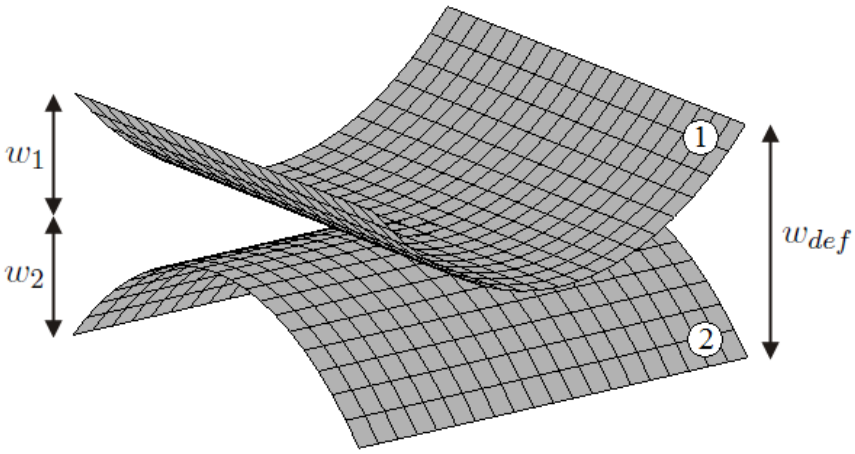

Figure 6.4: Deflection between two stable states for an example $[0/90]_{\mathrm{T}}$ laminate.

The curvatures a, b and c can be expressed in terms of the first state alone due to the two states having curvatures of equal and opposite magnitude, see Section 4.3.4. The x- and y-curvatures of the two states switch alignment and out-of-plane direction, while the x-y curvature remains unchanged between states. Equation 6.6 can therefore be rewritten in terms of only a_1 and b_1 (Eq. 6.7) and can be used to define the constraint on minimum deflection between states.

$$\text{Deflection constraint}: \quad w_{def} = \frac{1}{4}\left(a_1 + b_1\right) L^2 \tag{6.7}$$

It is noted that Eq. 6.7 also incorporates the bistability constraint $a + b$, making the bistability constraint inactive for this problem when a minimum deflection is stated.

6.2.4 Optimisation Algorithm

The optimisation algorithm used to solve the problem outlined in this chapter is a built in sequential quadratic programming (SQP) function in Matlab, `fmincon`. The SQP algorithm is an iterative method for nonlinear optimisation, suitable where the objective function and constraints are differentiable. With the explicit solution to modelling derived in Chapter 4, such an SQP routine is ideal for the objective function and constraints outlined in this chapter. Here, the algorithm performs a line search using a merit function similar to that proposed in [46, 78, 79]. The quadratic programming subproblem is solved using an active set strategy similar to that described in [41]. This method is used throughout the following chapters.

6.3 Numerical Results

This section presents a series of numerical optimisation results using the problem formulation of Section 6.2. All examples use M21/T800 material properties, Table 5.1.

6.3.1 Unconstrained Optimisation

This section presents the results for a design constrained only by the four design rules and no deflection or bistability constraints, intended to demonstrate the nature of the design space. For graphical illustration the problem is restricted to the two ply orientations as variables. The square laminate edge length is set to 0.15m, and a uniform single ply thickness set to 0.25mm. Figure 6.5 shows the design space for this problem where the direction of low stiffness ϕ_1 is set to 0° and the direction of high stiffness ϕ_2 is set to 45°. It should be noted that only the first two ply orientations are plotted for illustration. The red dots indicate the points where Eq. 6.1 is locally optimised while green dots indicate the global optima, detailed in Table 6.1.

The symmetry in the laminate geometry as defined by the design rules in Section 4.2.2 is mirrored in the symmetry of these results. Four local optima are found which can be grouped into two pairs. The first pair being the solutions at $[-45_2/45_2]_\mathrm{T}$ and $[45_2/-45_2]_\mathrm{T}$, points A and B respectively, which represent the same laminate design. Both of these solutions have 16.3mm deflection between states while achieving an objective function value of 0.319, meaning the chosen direction of high stiffness is approximately three times stiffer than the flexible direction. The second pair of solutions at $[\pm 45]_{2\mathrm{T}}$ and $[\mp 45]_{2\mathrm{T}}$, points C and D respectively, achieve a higher value of the

objective function, with the stiff direction (ϕ_2) being more than five times stiffer than the flexible direction (ϕ_1). However, without consideration of the deflection constraint the optimisation has settled on a monostable design at these points.

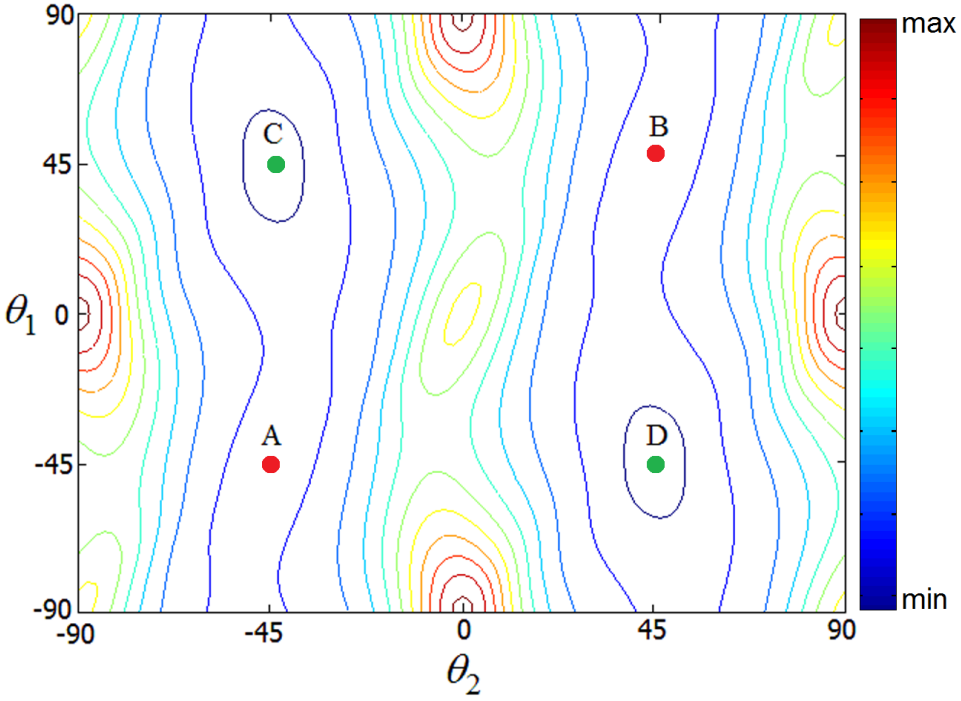

Figure 6.5: Unconstrained design space. Red dots mark local optima, green dots mark global optima, solutions detailed in Table 6.1.

Table 6.1: Optima for unconstrained optimisation.

	θ_1 (°)	θ_2 (°)	Deflection (mm)	Objective Function
A	-45.0	-45.0	16.3	0.319
B	45.0	45.0	16.3	0.319
C	45.0	-45.0	monostable	0.194
D	-45.0	45.0	monostable	0.194

One additional point of interest is the periodic nature of the design space. While the plot in Fig. 6.5 is constrained by $-90<\theta_1,\theta_2<90$, the optimisation routine has no bounds. Beyond these limits the pattern of results repeats, as illustrated by Fig. 6.6. Therefore the optimisation settles on solutions which are not shown in Table 6.1, but which can be redefined as equivalent to one of these four solutions. No limit is placed on the ply orientations to avoid finding meaningless local solutions along these boundaries.

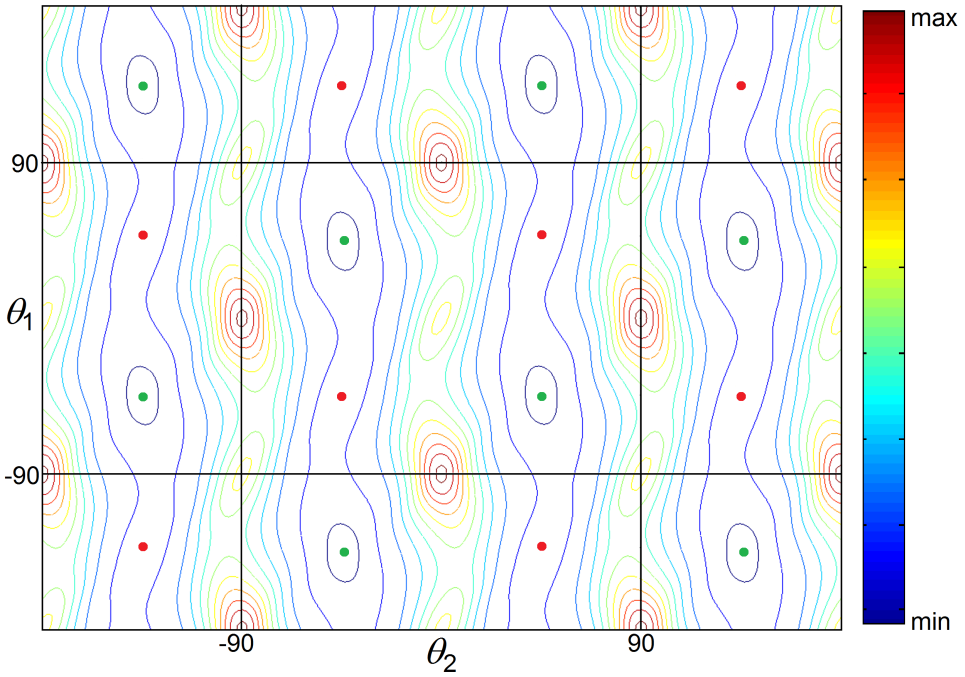

Figure 6.6: Periodic design space. Red dots mark local optima, green dots mark global optima.

6.3.2 Deflection Constrained Optimisation

The minimum deflection constraint is now introduced to the problem. The design variables are again restricted to the ply orientations for graphical illustration. The square laminate edge length is set to 0.15m, a uniform single ply thickness to 0.25mm, and the flexible direction chosen to be $\phi_1 = 0°$ and the stiff direction is chosen to be $\phi_2 = 45°$. The minimum deflection requirement is set to 10mm. Results obtained for this problem formulation are shown in Fig. 6.7. The red dots again represent local optima, and green dots the global optima. The grey areas denote the infeasible regions where the darker areas are the monostable regions and the lighter areas have deflection between states of less than the required 10mm.

This problem has six local optima, detailed in Table 6.2. As seen in the previous unconstrained optimisation, the two off-axis cross-ply solutions $[-45_2/45_2]_T$ and $[45_2/-45_2]_T$, points A and B, are unconstrained optima where the gradients are zero. The other four solutions, points C-F, are on the deflection constraint boundaries and are global optima. All four solutions achieve an equal objective function value of 0.285. While this value represents a solution where the direction of high stiffness is approximately 3.5 times stiffer than the flexible direction, this is significantly lower than for the unconstrained example. This highlights the compromise introduced by adding a minimum deflection requirement.

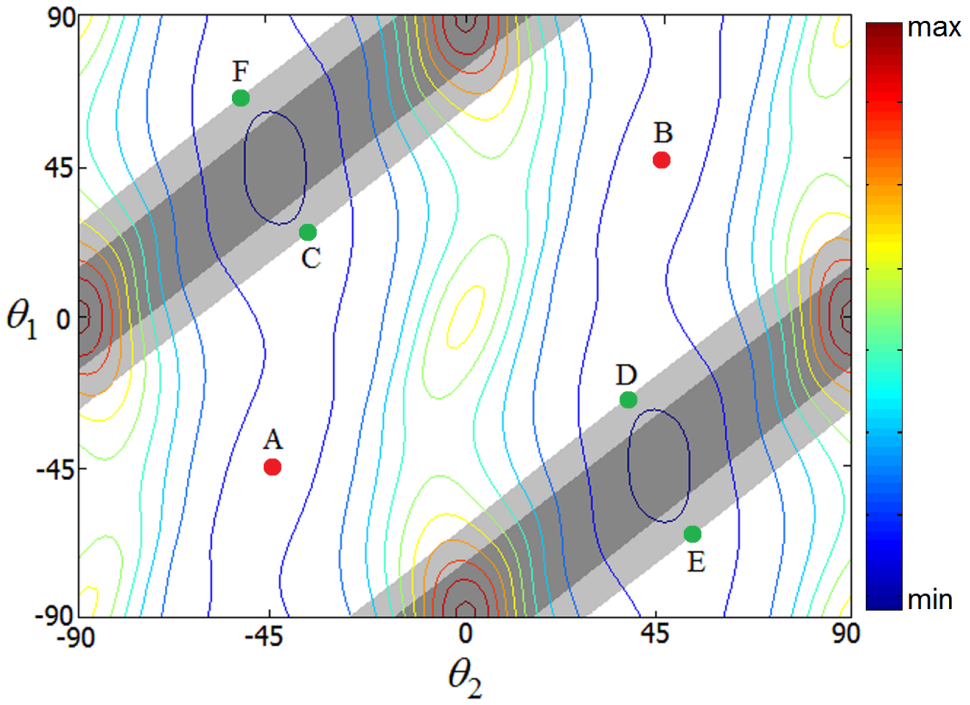

Figure 6.7: Deflection constrained design space. Red dots mark local optima, green dots mark global optima, dark grey regions are monostable and light grey regions have deflection less than 10mm. Solutions detailed in Table 6.2.

Table 6.2: Optima for deflection constrained optimisation.

	θ_1 (°)	θ_2 (°)	Deflection (mm)	Objective Function
A	-45.0	-45.0	16.3	0.319
B	45.0	45.0	16.3	0.319
C	23.1	-39.0	10.0	0.285
D	-23.1	39.0	10.0	0.285
E	-66.9	51.0	10.0	0.285
F	66.9	-51.0	10.0	0.285

6.3.3 Constrained Optimisation with Geometric Design Variables

In this final example the geometric design variables are included in addition to the ply orientations. They are the individual ply thicknesses t_1 and t_2, 0.05mm $< t_1, t_2 <$ 0.75mm; the half laminate thickness (t_1+t_2), 0.2mm $< (t_1+t_2) <$ 1.0mm; and the laminate edge length L, 0.15m $< L <$ 0.5m. The minimum required deflection is increased to 100mm due to the wider range of geometry which has been introduced. Once again the flexible and stiff directions are specified at $\phi_1 = 0°$ and $\phi_2 = 45°$ respectively.

Table 6.3 shows all eight optimum solutions found for this problem. As with both previous examples, the off-axis cross-ply designs of $[-45_2/45_2]_T$ and $[45_2/-45_2]_T$, A and B, are local optima. However, as the deflection constraint is inactive for a range of geometric variables at these ply orientations, there are many solutions achieving equal objective function values. The deflection between states for these solutions vary from 100mm to 515mm. The laminate edge length, which does not affect the objective function but only the deflection constraint, has a minimum value of 0.22m.

Table 6.3: Optima for deflection constrained optimisation with nonuniform variable ply thicknesses and edge length.

	θ_1 (°)	θ_2 (°)	t_1 (mm)	t_2 (mm)	L (m)	Deflection (mm)	Objective function
A	-45.0	-45.0	0.05-0.75	0.05-0.75	0.22-0.5	100-515	0.319
B	45.0	45.0	0.05-0.75	0.05-0.75	0.22-0.5	100-515	0.319
C	-49.9	52.8	0.05	0.15	0.5	100	0.220
D	49.9	-52.8	0.05	0.15	0.5	100	0.220
E	-40.1	37.2	0.05	0.15	0.5	100	0.220
F	40.1	-37.2	0.05	0.15	0.5	100	0.220
G	-45.0	45.0	0.094	0.106	0.5	100	0.191
H	45.0	-45.0	0.094	0.106	0.5	100	0.191

Four local optima are also found along the deflection constraint boundaries approaching the $[\pm 45]_{2T}$ and $[\mp 45]_{2T}$ layups. The geometric variables at these solutions all reach either the upper or lower bounds in order to maximise the laminate deflection. The resulting four solutions have $t_1 = 0.05$mm, $t_2 = 0.15$mm, $L = 0.5$m and ply orientations of $[-49.9/52.8/-37.2/40.1]_T$, $[49.9/-52.8/37.2/-40.1]_T$, $[-40.1/37.2/-52.8/49.9]_T$ and $[40.1/-37.2/52.8/-49.9]_T$, points C, D, E, and F in Table 6.3, all with an objective function value of 0.220. Despite the higher deflection requirement the introduction of a range of allowable values for the geometric variables has allowed a significant improvement on the results of the previous section.

Unlike the previous examples, there is a further pair of optima, G and H, with $t_1 = 0.094$mm as shown in Table 6.3. These solutions are $[\mp 45]_{2T}$ and $[\pm 45]_{2T}$ which have the lowest objective function value but violated the bistable and deflection constraints in the previous examples. However, with the addition of the geometric variables, there exists a solution with the ply angles $[\mp 45]_{2T}$ and $[\pm 45]_{2T}$ which satisfies the deflection constraint. The first of these solutions is illustrated in Fig. 6.8 which reveals that the objective function is nonlinear with respect to t_1 leading to an additional solution on the deflection constraint boundary. This solution is repeated at $[\pm 45]_{2T}$ where both solutions have equal objective function values of 0.191, meaning a ratio of greater than five between the stiff and flexible directions. These solutions are not seen in previ-

ous examples as the limits on the edge length and thicknesses do not allow sufficient deflection.

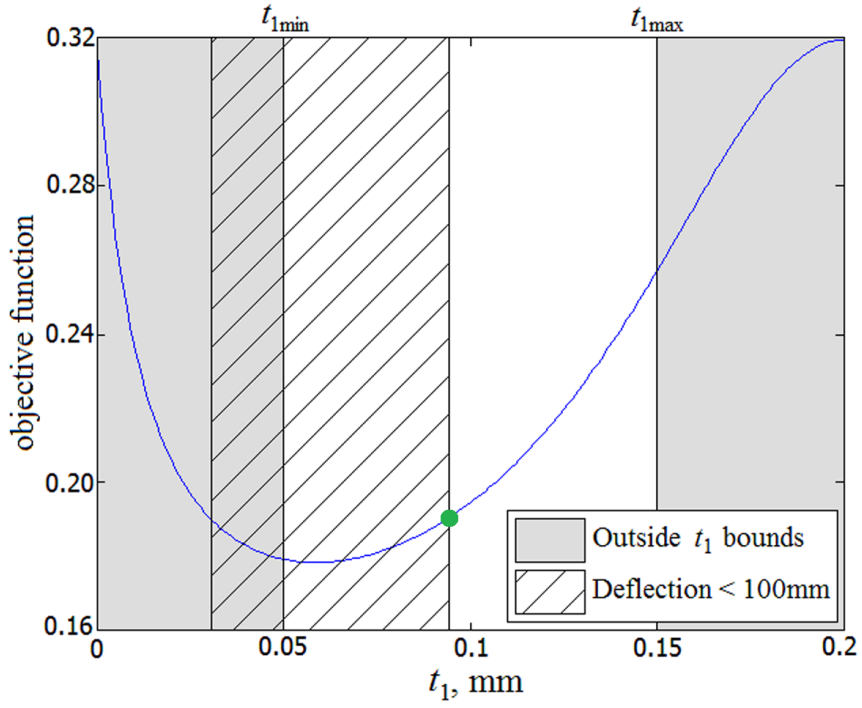

Figure 6.8: Variation in objective function with t_1 for a $[\mp 45]_{2T}$ laminate.

6.3.4 Changing the Stiff and Flexible Directions

All examples presented in this section have been based on stiff and flexible directions of 45° and 0° respectively. In examples where the bounds on the geometric variables allow sufficient deflection, the optimum stacking sequence is found to be $[\mp 45]_{2T}$ or $[\pm 45]_{2T}$. When the bounds are too constraining, pairs of optimum stacking sequences are found on the deflection constraint boundary, close to the unconstrained optimum. These interactions between the optima and the constraint boundaries are dependent on the relative values of the stiff and flexible directions.

Optimisation results have been examined for a range of pairs of stiff and flexible directions, with the difference between the stiff and flexible angles varying from 10° to 90° at 10° intervals. It is observed that a pattern of optimum solutions emerges. Figure 6.9 shows the design space for ply-variable optimisation where the stiff and flexible directions are $\phi_2 = 60°$ and $\phi_1 = 50°$ respectively. This problem is otherwise identical to that in Section 6.3.2. Local optima are marked by red dots, global optima marked by green dots and the six solutions are detailed in Table 6.4.

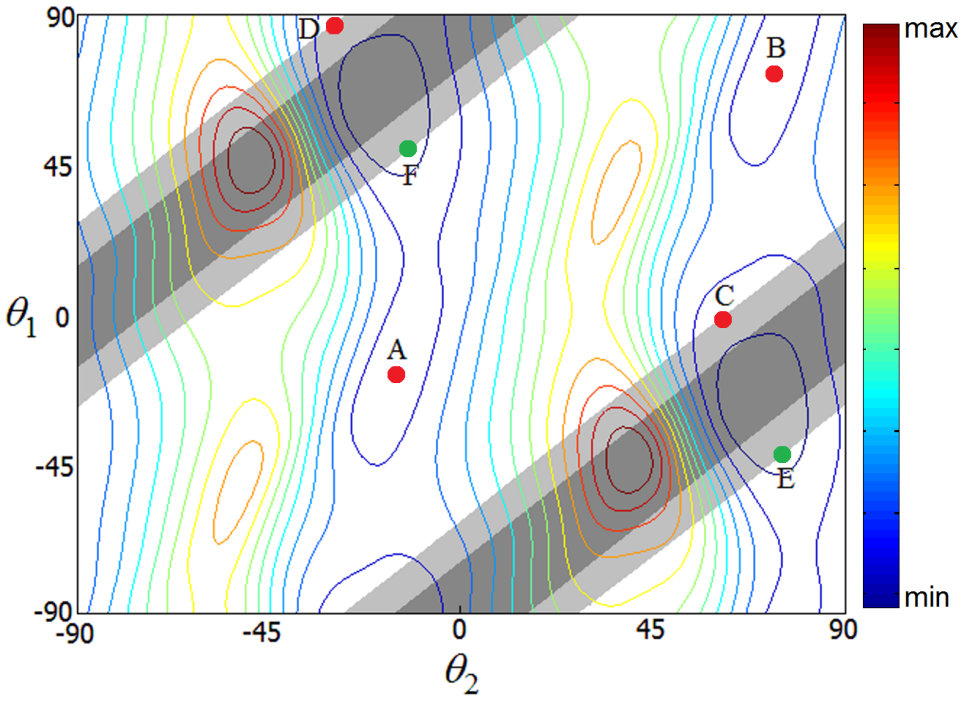

Figure 6.9: Design space for $\phi_1 = 50°$ and $\phi_2 = 60°$. Red dots mark local optima, green dots mark global optima, dark grey regions are monostable and light grey regions have deflection less than 10mm. Solutions detailed in Table 6.4.

With the angles so close together the maximum and minimum objective function values are seen to be much closer together than for the previous examples. Two off-axis cross-ply solutions are again observed at $[-20_2/70_2]_T$ and $[70_2/-20_2]_T$, points A and B respectively, with objective function value of 0.664. However, the four solutions along the boundary, C-F no longer have the same objective function value. A pair of solutions, C $[-4/62/-28/86]_T$ and D $[86/-28/62/-4]_T$, at the constraint boundary has a higher objective function value (0.675), thus can no longer be considered optimum. The other solutions at the constraint boundary, E $[-42/76/-14/48]_T$ and F $[48/-14/76/-42]_T$, have an objective function value of 0.607 and are the global optima. It is noted that when there is a smaller angle between the flexible and stiff directions the value of the objective function is significantly higher, as should be expected.

Table 6.4: Optima for deflection constrained optimisation, $\phi_1 = 50°$ and $\phi_2 = 60°$.

	θ_1 (°)	θ_2 (°)	Deflection (mm)	Objective Function
A	-20.0	-20.0	16.3	0.664
B	70.0	70.0	16.3	0.664
C	-4.0	62.0	10.0	0.675
D	86.0	-28.0	10.0	0.675
E	-42.0	76.0	10.0	0.607
F	48.0	-14.0	10.0	0.607

6.4 Concluding Remarks

In this chapter an optimisation study for arbitrary asymmetric laminates has been presented. The optimisation study considered design of bistable laminates through variation in ply orientations, non-uniform ply thicknesses and laminate edge length, enabled by the derivation of an analytical solution for stable laminate shapes outlined in Chapter 4.

The class of laminates considered in this study offer the maximum useful deflection between states whilst allowing the directional stiffness of the laminate to be tailored. The design space, constrained by bistability and minimum deflection constraints, is found to be multimodal with the number of local and global optima found to vary with the bounds on the design variables and the deflection constraint. This approach demonstrated that appreciable difference in bending stiffnesses could be achieved whilst ensuring that the specified deflection constraint is satisfied.

Off-axis cross-ply designs are found to represent a local optimum to this problem while the global optima are generally found on the deflection constraint boundary with ply orientations and ply thicknesses which are not intuitively obvious from the problem definition. The intuitive solutions for optimal stiffness have low deflections between states and are usually found to be infeasible. However, in some situations the intuituve layups are found to be feasible (and optimal) with nonuniform geometry allowing sufficient deflection to meet the constraint. This general pattern of results is observed for all combinations of stiff and flexbile directions. However, the level of objective function is dependent on the relative angles of these directions. In all cases where a deflection constraint is imposed, the bistability constraint is understandably inactive.

The numerical studies have shown examples where the stiffness in the loading direction can be as high as five times that of the snap-through direction. This demonstrates that it is feasible to design a bistable laminate with a low stiffness in an actuation direction while still providing a reasonable stiffness to resist operating loads.

Chapter 7

Analysis of Actuation Methods

The optimisation study presented in the previous chapter has demonstrated the feasibility of designing a bistable laminate with a low stiffness in an actuation direction whilst providing a reasonable resistance to external loads. How this actuation is achieved forms the focus of the work presented in this chapter. Three methods are considered in experimental studies and for extension of the existing modelling.

Section 7.1 presents a modelling extension to include a simple mechanical force applied in the out-of-plane direction. This modelling technique is used to determine the structural deformations and actuation force for an example laminate. This study is then extended to consider variation in the actuation configuration.

Section 7.2 outlines the inclusion of a piezoelectric actuator in the model as an additional anisotropic layer. This model is validated against experimental and FEA results for the prediction of both the actuation voltage and the static shape profiles. Finally, reversible actuation using two orthogonal piezoelectric layers is discussed.

The third actuation method considered is the use of shape memory alloy wires to induce high strain shape change, with a simple approach to modelling presented in Section 7.3. An experimental study is conducted to determine the actuation voltage for a bistable cantilever. This study is then extended to consider piezoelectric material combined with shape memory wires to achieve reversible actuation, Section 7.4

Finally, a discussion of the advantages and disadvantages of each of the above methods is presented with the aim of identifying the most suitable actuation technique to be incorporated in a subsequent optimisation study.

7.1 Simply Applied Mechanical Force

This section presents a brief overview of the existing modelling of the response to external forces, followed by a simplified approach which introduces the work done by an out-of-plane force into the existing energy minimisation model.

7.1.1 Existing Modelling Techniques

Existing work to predict the response of bistable laminates to mechanical force is limited. Dano and Hyer [23] considered the effect of mechanical force in a formulation designed to simulate the effects of shape memory alloy wires. For this reason, the formulation is constrained to applying the force in the in-plane direction. Due to the complexities which arise from applying the force in this way, detailed later in this section, Dano and Hyer [23] use a much simplified form of the energy minimisation problem, proposed by Hamamoto and Hyer [45]. This formulation is limited to modelling of laminates with 0° and 90° plies only, where the out-of-plane displacement can be approximated by the following quadratic.

$$w(x,y) = \frac{1}{2}\left(ax^2 + by^2\right) \tag{7.1}$$

The corresponding in-plane displacements are assumed to be of the following form,

$$\begin{aligned} u^0(x,y) &= cx - a^2\frac{x^3}{6} - ab\frac{xy^2}{4} \\ v^0(x,y) &= dy - b^2\frac{y^3}{6} - ab\frac{yx^2}{4} \end{aligned} \tag{7.2}$$

where c and d are in-plane coefficients and midplane shear strains are neglected. Using these relationships in the formulation outlined in Section 4.1, the total laminate strain energy W can be expressed as a function of the four displacement coefficients.

$$W = W\left(a,b,c,d\right) \tag{7.3}$$

Minimisation of Eq. 7.3 with respect to the coefficients results in prediction of the unloaded laminate shapes. The response to an applied force F is then considered by assuming the configuration shown in Fig. 7.1. A pair of supports are positioned at opposite edges of the laminate, perpendicular to the laminate surface. The supports are positioned at $x = \pm L_{xp}$ and $y = 0$, and have a length e.

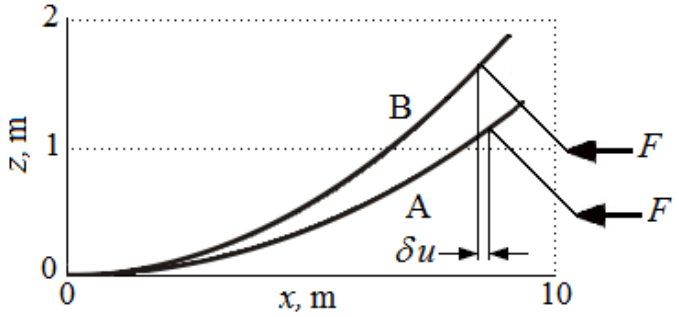

Figure 7.1: In-plane x-displacement under an applied force F, half-laminate shown.

The first variation of total energy of this system can be expressed as follows,

$$\delta W_T = \delta W - \delta W_F \tag{7.4}$$

where W_T is the total energy in the loaded system and W_F is the work done by the force. W_F is defined as the product of the force and the resulting displacement,

$$\delta W_F = -F\delta u \tag{7.5}$$

where δu is a function of both out-of-plane and in-plane displacement coefficients.

$$\delta u = L_{xp}\delta c - \frac{L_{xp}^3}{3}a\delta a + \left(e + \frac{H}{2}\right) L_{xp}\cos\left(aL_{xp}\right)\delta a \tag{7.6}$$

Substitution of Eqs. 7.5 and 7.6 into Eq. 7.4 results in the following form for the first variation of the total energy,

$$\begin{aligned}\delta W_T = {} & \delta W(a,b,c,d,\delta a,\delta b,\delta c,\delta d) \\ & + 2F\left(L_{xp}\delta c - \frac{L_{xp}^3}{3}a\delta a + \left(e + \frac{H}{2}\right) L_{xp}\cos\left(aL_{xp}\right)\delta a\right)\end{aligned} \tag{7.7}$$

where the factor 2 has been added to account for an equal force F applied to the opposite side of the laminate. Since equilibrium requires $\delta W_T = 0$, the loaded shapes are calculated by considering a system of the form of Eq. 7.8.

$$f_i\left(a,b,c,d,F\right) = 0; \quad i = 1,2,3,4 \tag{7.8}$$

Dano and Hyer [23] compared this model with experimental data and found good correlation. However, the formulation is overly restrictive in only considering cross-ply laminates. The complexity of Eq. 7.7 demonstrates the problem. By considering in-plane displacement the additional energy term becomes a function of both in-plane and out-of-plane coefficients. A simpler approach considering purely out-of-plane displacement is derived in the following section, applicable to laminates of arbitrary layup.

7.1.2 Simplified Modelling Approach

An alternative approach presented here, similar to that considered by Diaconu et al. [30] and Pirrera et al. [75], is to apply the force directly on the laminate surface in the z-direction. Figure 7.2 shows the geometry of this structure. A force $F/2$ is applied vertically downwards at $x = \pm L_x/2$ and $y = 0$. The $1/2$ factor is included for the force such that the problem may be considered equivalent to fixing the laminate corners and applying a force F at the geometric centre.

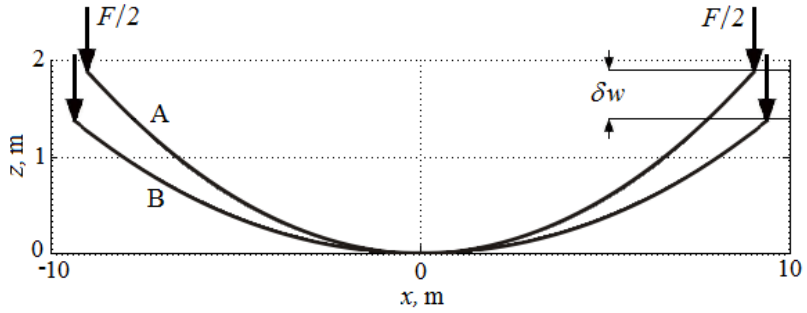

Figure 7.2: Displacement from profile A to B under applied force in the z-direction.

The work done in deforming the laminate is the product of the force and the displacement in the direction of the force, δw.

$$\delta W_F = -\frac{F}{2}\delta w \tag{7.9}$$

The displacement due to any pair of forces positioned symmetrically about the geometric centre ($x = \pm L_{xp}/2$, $y = \pm L_{yp}/2$) can be expressed without consideration of the in-plane shape coefficients. For laminates of arbitrary layup δw is defined as

$$\begin{aligned}\delta w &= w_A - w_B \\ &= \frac{1}{2}\Big(a\frac{L_{xp}^2}{4} - (a-\delta a)\frac{L_{xp}^2}{4} + b\frac{L_{yp}^2}{4} - (y-\delta y)\frac{L_{yp}^2}{4} + c\frac{L_{xp}L_{yp}}{4} - (c-\delta c)\frac{L_{xp}L_{yp}}{4}\Big) \\ &= \frac{1}{8}\left(\delta a L_{xp}^2 + \delta b L_{yp}^2 + \delta c L_{xp}L_{yp}\right)\end{aligned} \tag{7.10}$$

Substitution of Eq. 7.10 into Eq. 7.9 gives the work done by the force. Then substituting this into Eq. 7.4 for the modelling formulation of Section 4.1, the first variation of the total energy can be expressed as follows,

$$\delta W_T = \delta W(a, b, c, d_{1-11}, \delta a, \delta b, \delta c, \delta d_{1-11}) + \frac{F}{8}\left(\delta a L_{xp}^2 + \delta b L_{yp}^2 + \delta c L_{xp}L_{yp}\right) \tag{7.11}$$

where a factor 2 has been added to account for both forces. Minimisation of the total energy is then found by solving a system of equations of the form of Eq. 7.12.

$$f_i\left(a, b, c, d_{1-11}, F\right) = 0; \quad i = 1, 2, ..., 14 \tag{7.12}$$

The method for calculating static shapes outlined in Chapter 4 is based on stable shapes of equal and opposite curvature. With an external force applied to the laminate this assumption is no longer valid so Eq. 7.12 cannot be reduced to a smaller system of eleven equations in the same way as Eq. 4.69. However, for a laminate meeting these geometric constraints, the analytical solution does provide an exact solution for the initial unloaded shape. Equation 7.12 can then be solved efficiently by a Newton-Raphson technique for incremental changes in applied force.

7.1.3 Determination of an Actuation Force

In this section an example of the determination of an actuation force is presented. Figure 7.3 shows how the curvatures in the x- and y-directions of a $[0/90]_{\mathrm{T}}$ laminate vary with force applied as shown in Fig. 7.2. The initially unloaded shape at A has a large positive x-curvature, state 1. The shape coefficients are then calculated at increasing load levels and the x-curvature reduces. At point B a dramatic change is observed with x-curvature becoming very small and the y-curvature becoming large and negative, point C. This marks the transition from state 1 to state 2. As the load is then incrementally removed the laminate curvatures tend towards point D which represents the unloaded second state.

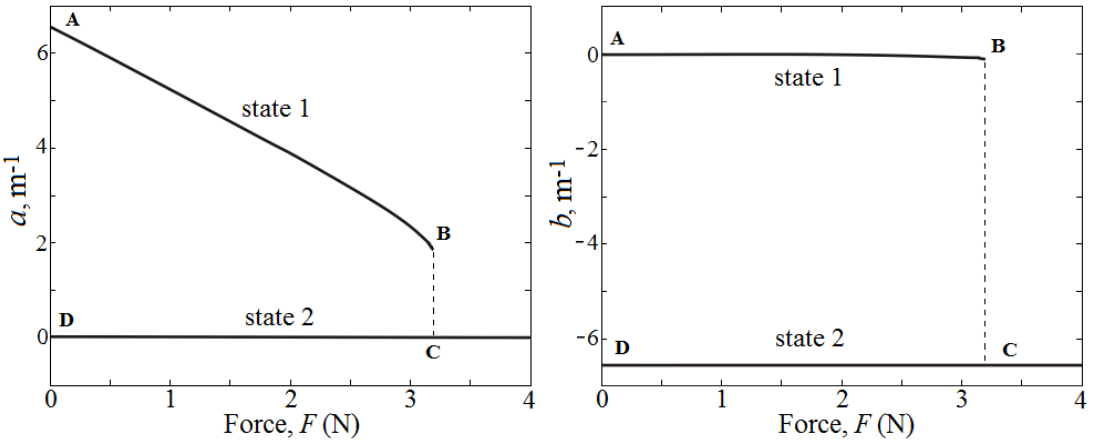

Figure 7.3: Actuation behaviour and changing x-direction (a) and y-direction (b) curvatures for a $[0/90]_{\mathrm{T}}$ laminate under an applied force.

In addition to allowing arbitrary layups this methodology allows consideration of forces applied at any location on the laminate surface. To demonstrate the variation in actuation force with location the geometry of Fig. 7.4 is considered. A force $F/2$ is applied at an angle ϕ to the y-axis for a 0.15×0.15m $[0/90]_{\mathrm{T}}$ laminate. A second force is applied at 180° to the first. The force required to actuate is calculated at 10° intervals 0.05m from the origin. Actuation forces ($F/2$+$F/2$) are shown in Fig. 7.5a.

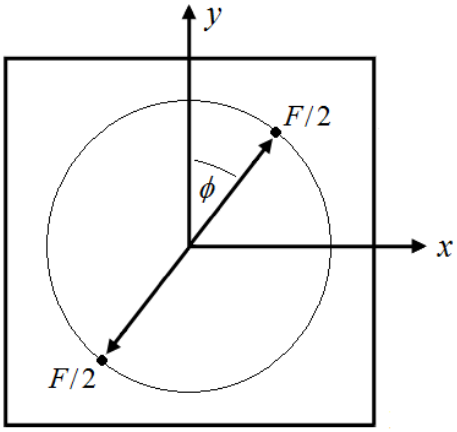

Figure 7.4: Location of applied force.

The maximum actuation force occurs when $\phi = 0°$. This represents a force aligned with the minor curvature b. The minimum force required occurs when $\phi = 90°$, or aligned with the major curvature a. A large variation from 6 to 79N is observed.

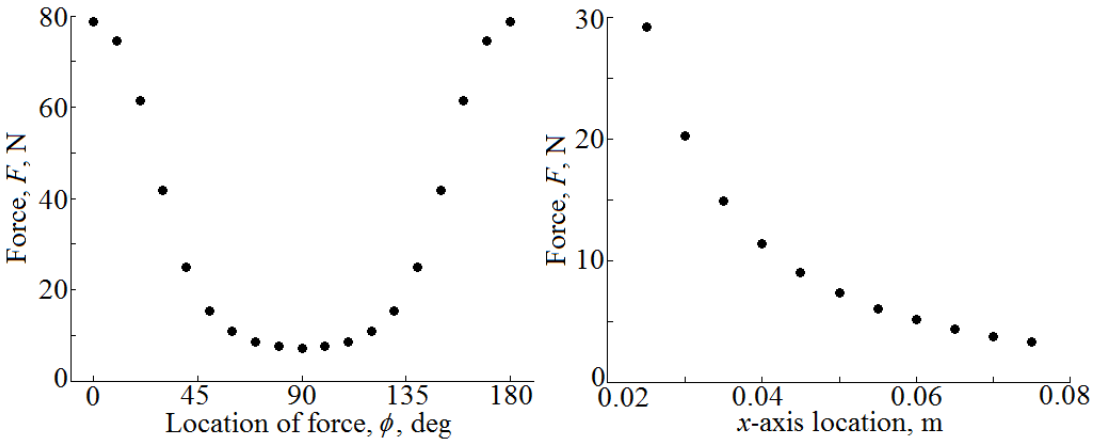

Figure 7.5: Actuation force F at a) varying angles ϕ and b) at varying x-axis locations.

All points in Fig. 7.5a are positioned at a fixed distance from the origin. Figure 7.5b demonstrates variation in actuation force with distance along the x-axis at $\phi = 90°$. The force is found to decrease with the square of the distance in the x-direction.

The simplicity of this modelling and the ease with which the location of the force can be varied are ideal for optimisation of actuated laminate design. However, while the system of supports used by Dano and Hyer [23] has been removed, the inconvenience of applying an external force remains. The potentially cumbersome mechanisms which may be required to actuate the laminate in this way may prove restrictive for many practical applications. An ideal solution would be an actuation mechanism incorporated within the laminate structure.

7.2 Macro-Fibre Composite Actuators

Macro-fibre composite actuators (MFC's) consist of piezoelectric fibres embedded in an epoxy resin, with copper interdigitated electrodes bonded to the surfaces. Typical commercially available MFC's [96] use fibres of lead zirconate titanate (PZT) as these fibres exhibit particularly high strain per unit electric field (piezoelectric coefficients). These properties are ideal for providing the strains required to deform a laminate.

In this section an extension to the analytical model to incorporate an MFC actuator, referred to more generally as a piezoelectric layer, is presented. Actuation voltages predicted by this model are compared with experimental values. The model is then further investigated by comparing the predicted shape profiles of laminates with and without MFC's with both experimental and FEA results. Finally, reversible actuation using two orthogonal piezoelectric layers is discussed.

7.2.1 Modelling Extension for Piezoelectric Layers

The modelling extension for a piezoelectric layer can conveniently be treated in much the same way as each individual layer of the laminate. However there are some differences in the way it must be modelled. Firstly, this additional layer is attached post-cure and therefore does not experience any temperature change. Secondly, the piezoelectric effect must be included in the model. To account for adding the piezoelectric layer post-cure the thermal expansion coefficients can be set to zero. In effect the model considers all layers to be cured together but that the piezoelectric layer is unaffected by this process. To allow for the piezoelectric effect an additional voltage dependent term is added to the strain energy density of Eq. 4.7, resulting in the following form,

$$\omega = \frac{1}{2} c_{ijkl}\epsilon_{ij}\epsilon_{kl} - \hat{\alpha}_{ij}\epsilon_{ij}\Delta T - \hat{\beta}_{ij}\epsilon_{ij}\Delta V \tag{7.13}$$

where $\hat{\beta}_{ij}$'s are constants relating to piezoelectric coefficients and ΔV is the voltage change. To allow different planform dimensions for the piezoelectric layer and laminate, the associated strain energies are considered separately. The total energy is then the sum of the laminate energy W_{lam} and the piezoelectric layer energy W_{MFC}.

$$W = W_{lam} + W_{MFC} \tag{7.14}$$

where W_{MFC} is found by integrating the strain energy density over the layer volume,

$$W_{MFC} = \int_{vol} (\omega)\, \mathrm{d}vol \tag{7.15}$$

which results in consideration of the piezoelectrically induced forces N_x^P, N_y^P and N_{xy}^P, and moments M_x^P, M_y^P and M_{xy}^P.

$$\begin{aligned}
[N_x^P, M_x^P] &= \int_{-H/2}^{H/2} (\bar{Q}_{11}\beta_x + \bar{Q}_{12}\beta_y + \bar{Q}_{16}\beta_{xy})\Delta V[1, z]\mathrm{d}z \\
[N_y^P, M_y^P] &= \int_{-H/2}^{H/2} (\bar{Q}_{12}\beta_x + \bar{Q}_{22}\beta_y + \bar{Q}_{26}\beta_{xy})\Delta V[1, z]\mathrm{d}z \\
[N_{xy}^P, M_{xy}^P] &= \int_{-H/2}^{H/2} (\bar{Q}_{16}\beta_x + \bar{Q}_{26}\beta_y + \bar{Q}_{66}\beta_{xy})\Delta T[1, z]\mathrm{d}z
\end{aligned} \tag{7.16}$$

where β's are piezoelectric coefficients. Equation 7.14 can then be substituted into Eq. 4.11 and solved to find the stable laminate shapes under piezoelectric loading. This extension to the modelling breaks the design rules outlined in Section 4.2.2, therefore the assumptions on which the analytical solution are based are no longer valid. It is therefore necessary to solve the energy minimisation using numerical techniques for incremental increases in the applied voltage, where the exact solution to the unloaded shapes can be used as an initial 'guess'.

7.2.2 Experimental MFC Actuation Study

In this section an experimental study is outlined to compare observed actuation voltages with modelling predictions for an arbitrary layup laminate.

Laminate Manufacture

The laminate used for the experimental study was a $[\text{-}30/60]_\text{T}$ laminate with ply thickness of 0.25mm. A square laminate of size 150mm was manufactured using the standard layup procedure using M21/T800 carbon fibre prepreg sheet (see Table 5.1 for properties). The manufacturing process involved a maximum cure temperature of 180°C and a pressure of 0.69MPa. The laminate was placed on a flat metallic surface during cure leading to a smooth surface on one side while the opposite side had a rough resin surface. The cylindrical state with this rough resin layer on the concave surface is referred to as state I, while the resin layer on the convex surface refers to as state II.

A piezoelectric MFC was attached to the laminate after the cure cycle with epoxy, creating a $[\text{-}30/60/0^\text{P}]_\text{T}$ laminate, where superscript P denotes a piezoelectric layer. The active area of the MFC was 85×57mm, with thickness of 0.3mm, and has a recommended operating range of -500V to 1500V. The material properties of the MFC are shown in Table 7.1. The two stable shapes resulting from this manufacturing process are shown in Fig. 7.6.

Table 7.1: M8557-P1 MFC properties [96].

Property	Value
Longitudinal Young's modulus, E_{11} (GPa)	30.3
Transverse Young's modulus, E_{22} (GPa)	15.9
Poisson's ratio, ν_{12}	0.31
Shear modulus, G_{12} (GPa)	5.5
Longitudinal piezoelectric coefficient, β_1 ($\times 10^{-12}$m/V)	467
Transverse piezoelectric coefficient, β_2 ($\times 10^{-12}$m/V)	-231

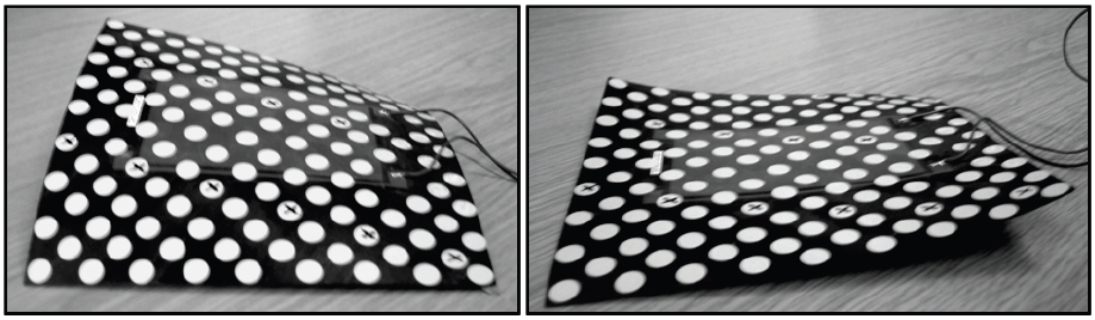

Figure 7.6: Two stable states of a $[-30/60/0^{\mathrm{P}}]_{\mathrm{T}}$ laminate.

Actuation Voltage

The response of the laminate outlined in the previous section to an applied voltage is modelled using the extended method of Section 7.2.1. Figure 7.7 illustrates the predicted variation in x- and y-curvature, a and b respectively where the subscript denotes the associated state, across the full operating range of the MFC. With the laminate initially in its unloaded state II shape, point A, the curvatures in both the x- and y-directions are positive. As the voltage is incrementally increased the curvatures shallow until reaching point B. At this point (995V) a dramatic change in curvature is observed as both the x- and y-curvatures become negative, point C. As the voltage is then removed the laminate returns to its unloaded state I shape at point D.

This actuation cycle is repeated experimentally and the observed actuation voltage is highlighted in Fig. 7.7. The general behaviour of the laminate is captured, with actuation occurring within the operating range of the MFC as predicted. However, the experimental value, found to be 700V consistently across a number of actuation cycles, varies significantly from the predicted value. The analytical model represents an over-estimation by 42%. This is largely attributed to the constant curvature assumption in the analytical model. By limiting the out-of-plane shape definition to three coefficients the degrees of freedom are restricted, effectively increasing the stiffness of the model.

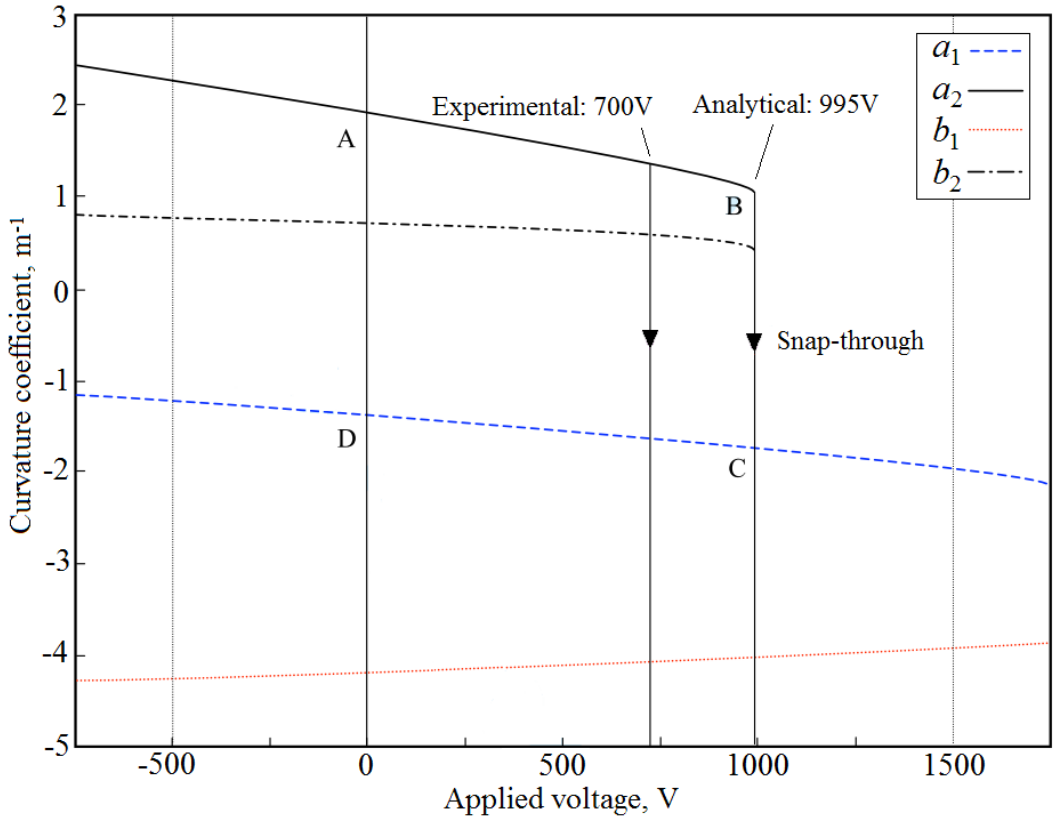

Figure 7.7: Modelling and experimental actuation of a $[-30/60/0^{P}]_{T}$ laminate.

Finite Element Predictions

To further validate the experimental actuation voltage the $[-30/60]_{T}$ laminate, with and without the MFC, was modelled using the FE software Ansys [10]. Twenty-node quadratic layered 3D solid elements (Solid186) were used to model the laminate while twenty-node coupled-field solid elements (Solid226) were used to capture piezoelectric behaviour of the MFC. The MFC was modelled by three-dimensional stiffness, piezoelectric and permittivity matrices, thereby representing the homogenised electromechanical properties.

Previous characterisation [38] of a cross-ply $[0^{P}/0/90]_{T}$ laminate demonstrated that ply thickness could vary by up to 6% from nominal values. One primary reason for this variation was a layer of resin seepage during curing which varied widely in thickness. This was seen to have a significant influence on the cured shapes of bistable composites. Representative ply thickness for the FE model was calculated by taking the mean value of the thickness distribution measured from optical microscopy, detailed in Table 7.2. This variation was accounted for by reducing the Young's modulus of the additional resin layer by 50%, and this value is used here.

Table 7.2: Average layer thicknesses used in FE modelling.

	Layer thickness (mm)	Standard deviation
60° ply	0.255	0.013
-30° ply	0.234	0.018
Resin layer	0.027	0.021
Total laminate	0.516	0.045

As in the analytical model, a change in temperature of ΔT = -159°C was applied to all nodes in the model to simulate cooling from a cure cycle of 180°C to a room temperature of 21°C. The laminate was simply supported at its geometric centre. Piezoelectric actuation was modelled by applying a drive voltage to nodes at one end of the MFC while constraining the voltage at the opposite end to zero. Due to the high curvatures of the laminate-MFC combination, nonlinear analysis was used.

The FE model, accounting for manufacturing imperfections and through-thickness effects, showed an excellent quantitative agreement with the experimental result with 702V for actuation. While the analytical model offered a good qualitative agreement with experiment this FE value captures the behaviour more accurately. Reasons for the discrepancy between the FE and analytical models are further analysed in the following section.

7.2.3 Shape Characterisation Incorporating Piezoelectric Material

The two cylindrical shapes of both the $[-30/60]_{\mathrm{T}}$ and $[-30/60/0^{\mathrm{P}}]_{\mathrm{T}}$ laminates were characterised experimentally using the three-dimensional motion analysis technique outlined in Section 5.1.2. Each laminate had 145 round coloured labels of 8mm diameter attached to one surface as shown in Fig. 7.6. Using a setup similar to Fig. 5.1, camera 1 was always positioned to view from a high position (the centre of the lens positioned 2.19m away from the origin of the experimental area at a height of 1.86m). The other two cameras were moved such that the best possible viewing angle was always achieved without compromising the umbrella configuration [70]. Cameras 2 and 3 had the centre of lens ranging from 1.63 to 2.71m away from the origin in different setups with the height ranging from 0.51 to 1.32m above the experimental area. The angle between the cameras ranged from 55 to 105° with a mean angle between the three cameras varying from 77 to 92° in different setups.

The laminate shapes captured using the motion analysis technique are shown in Fig. 7.8 (without the piezoelectric layer) and Fig. 7.9 (with the piezoelectric layer). Analytical modelling and FE predictions of the laminate shapes are also presented for comparison.

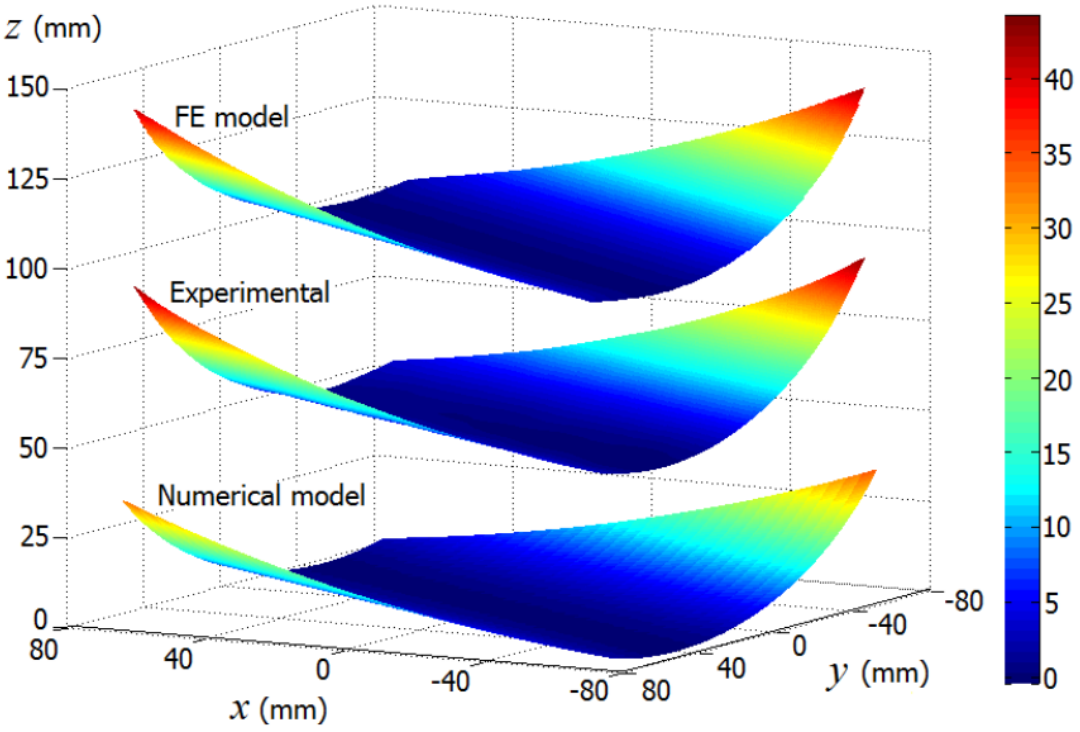

Figure 7.8: Experimental shapes with analytical modelling and FE predictions of state II for a $[-30/60]_T$ laminate. Data offset for illustration.

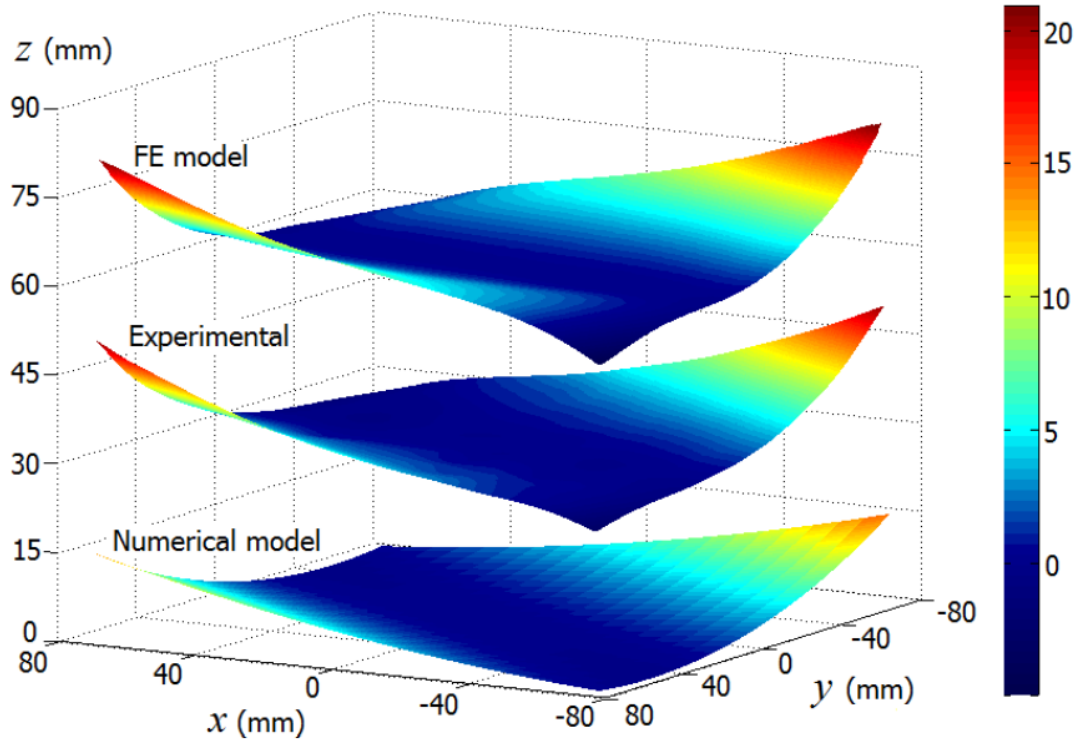

Figure 7.9: Experimental shapes with analytical modelling and FE predictions of state II for a $[-30/60/0^P]_T$ laminate. Data offset for illustration.

For the $[-30/60]_T$ laminate the curvatures of states I and II were predicted to be equal by the analytical model while the experimental results show that the state II deflection was greater than that of state I. This difference was captured by the FE model with the inclusion of a thin resin layer. FE modelling was also able to capture areas of locally reversed curvature near the laminate corners, barely visible in Fig. 7.8. Excellent agreement between experimental and FE results was seen for maximum out-of-plane deflection for state II (2.4%), with a larger error observed for the deflection in state I (12.2%), a comparable result to analytical prediction. Quantitative agreement in both states could be improved by using laminate specific composition in the analytical model rather than average values for typical laminates.

For the $[-30/60/0^P]_T$ laminate the experimentally observed maximum out-of-plane displacement reduced by approximately 50% with the addition of the MFC. This is due to the significantly reduced curvature in the central region where the MFC is attached.

The locally reversed curvature in the minor axis in Fig. 7.9 was prominent in both the experimental and FE results while this is not captured in the analytical model. This is attributed to the use of a quadratic polynomial in approximating the cylindrical shapes. These simplifications may explain the discrepancies found when comparing the analytical model to the experimentally measured actuation voltage.

Clearly the accuracy of the analytical model is sensitive to changes in stiffness across the laminate surface. However, these inaccuracies are localised and do not significantly affect the overall laminate shape. Accuracy would likely be improved by including an MFC which covers the entire laminate surface. Of a greater concern for the use of MFC actuators for bistable laminates is achieving reversible state-change. As Fig. 7.7 demonstrates, the full working voltage range of a single piezoelectric layer does not allow resetting of the laminate once a single actuation has occurred.

7.2.4 Reversible Actuation

MFC actuators are designed to provide in-plane strain in a single dominant direction. Some level of strain is achieved in the transverse direction ($\sim$40-50%) but this is insufficient to achieve bistable laminate actuation. The limitation of needing to align the MFC with the direction of major curvature (actuation direction) has been considered by Schultz et al. [93] who achieved a reversible state change by attaching two orthogonal piezoelectric layers to opposite laminate surfaces. In this way one piezoelectric effect is always aligned with the direction of actuation. However it is noted that Schultz et al. [93] required a voltage outside the recommended range of the piezoelectric actuator.

7.3 Shape Memory Alloy Actuation

An alternative material for 'smart' actuators is shape memory alloy (SMA) metal, typically in the form of thin wires. SMA has the property of 'remembering' its original configuration, returning to a pre-deformed state upon heating [102]. Using SMA wires, typically made from Nickel Titanium (NiTi), has a number of advantages over piezoelectrics [50]. The phase change upon heating from martensite to austenite induces high levels of strain of upto ∼7%, (∼2% for piezoelectric actuators), and high levels of stress of upto $7\times10^{8}\mathrm{Nm}^{-2}$. However, to achieve the large deformations required for actuation it is necessary to sufficiently deform the SMA prior to heating. In this section the proposed idea is to utilise the state change of a bistable laminate to deform SMA wires attached to the surface such that electrical heating of the SMA could return the bistable composite to the original shape.

7.3.1 Integration of SMA Wires

Incorporating SMA actuation into the existing model for stable laminate shapes presents a challenge as, unlike the piezoelectric material, it does not occur in the structure as an additional layer. As an approximation, an additional layer is considered consisiting of SMA wires embedded in epoxy resin attached to the top surface of the laminate. This approach requires a volume fraction method to combine the properties of the SMA and epoxy taken from [65]. The required layer properties are therefore defined as,

$$\begin{aligned} E_{11} &= E_f\psi_f + E_m\psi_m \\ E_{22} &= (E_fE_m)/(\psi_mE_f + \psi_fE_m) \\ \nu_{12} &= \nu_f\psi_f + \nu_m\psi_m \\ G_{12} &= (G_fG_m)/(\psi_mG_f + \psi_fG_m) \\ \alpha_1 &= \alpha_f\psi_f + \alpha_m\psi_m \\ \alpha_2 &= (\alpha_f\alpha_m)/(\psi_m\alpha_f + \psi_f\alpha_m) \end{aligned} \tag{7.17}$$

where E is Young's modulus, ν is Poisson's ratio, G is shear modulus, α is the thermal expansion coefficient and ψ is the volume fraction. The subscripts f and m refer to fibre (SMA) and matrix (epoxy) properties respectively and subscripts 1 and 2 refer to combined layer properties.

Unlike the laminate and piezoelectric material, SMA properties are not constant over the full working range of applied voltages. During the martensite to austenite transition the material properties vary approximately linearly. Figure 7.10 shows an example of the variation of the Young's modulus during the transition. At a temperature below

the transition start temperature A_{s0} the material has a fixed Young's modulus E_A. Beyond the transition end temperature A_{f0} the material has a higher fixed Young's modulus E_M. Between these two temperatures the Young's modulus varies approximately linearly based on the martensite volume fraction ζ.

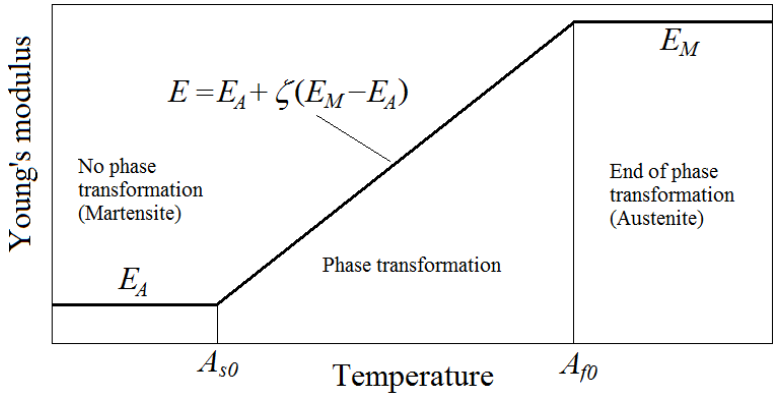

Figure 7.10: Young's modulus as a function of SMA wire temperature.

The material properties defined in Eq. 7.17 must therefore be calculated at each voltage interval for modelling. This provides an approximate method for incorporating the stiffness contribution of the SMA wires into the existing energy model, Chapter 4. Transition between states is then considered as a single event (no gradual shape change), defined by the transition voltage (or temperature) of the SMA, discussed later in this section.

7.3.2 Experimental SMA Actuation Study

This section outlines an experimental study of SMA actuation of a bistable laminate. A square laminate with $[0/90]_{\mathrm{T}}$ layup, side length of 150mm and ply thickness of 0.25mm was manufactured using M21/T800 prepreg sheet. The aim of this test was to demonstrate that this bistable laminate can be actuated by a NiTi SMA wire of 0.175mm diameter. The properties of the SMA wire used in this test are shown in Table 7.3, while the properties of the composite laminate are those of Table 5.1.

A simple rig was manufactured for the experiment as a method of approximating the attachment of the SMA wire to the laminate. The rig, shown in Fig. 7.11, consists of two sets of fixing points spaced 170mm apart. The SMA wire is stretched between these points and fixed at bolts positioned 30mm further back. These bolts can be tightened to pretension the wires and remove any slack. The laminate is then placed beneath the wire and a power supply is attached at either end of the tensioned wire.

Table 7.3: Mechanical properties of NiTi wire [66].

Property	Value
Purely austenitic Young's modulus, E_A (GPa)	75.0
Purely martensitic Young's modulus, E_M (GPa)	32.0
Poisson's ratio, ν	0.33
Shear modulus, G (GPa)	30.0
Purely austenitic thermal expansion coefficient, α_A ($\times 10^{-6}/°C$)	11.0
Purely martensitic thermal expansion coefficient, α_M ($\times 10^{-6}/°C$)	6.7
Transition start temperature, A_{s0} (°C)	50
Transition finish temperature, A_{f0} (°C)	65

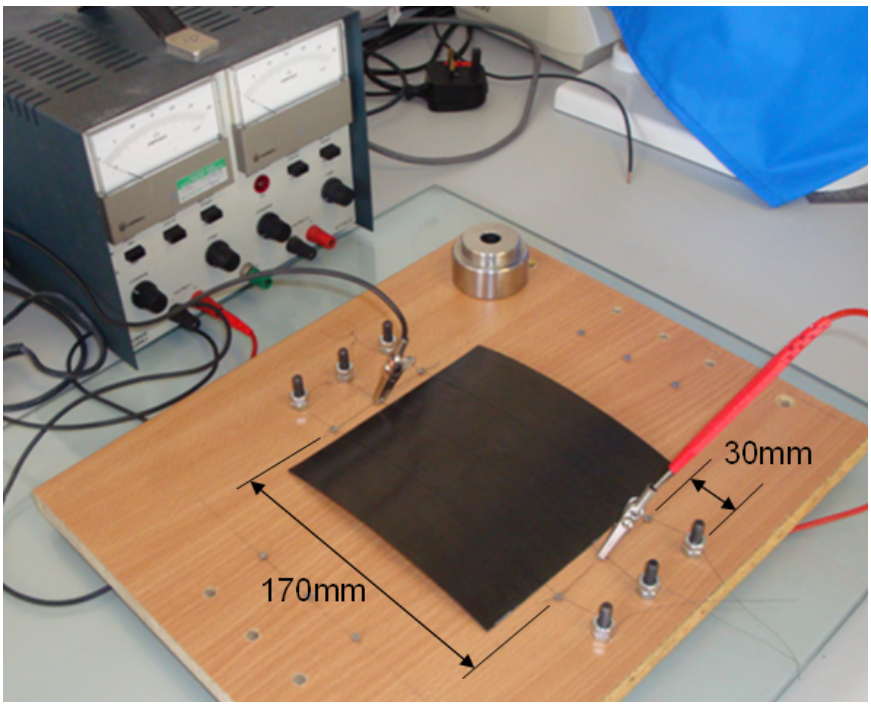

Figure 7.11: Experimental SMA test rig.

The first test used a single wire attached between the centre points and tightened so that the laminate had an initial maximum out-of-plane displacement of 10mm. When voltage was applied (∼9V), raising the temperature of the wire beyond the transformation point, the displacement reduced to 6mm but no snap occurred. Modelling predicts snap-through occurs at 5mm displacement. A second test added a second and third wire to the rig evenly spaced across the laminate as shown in Fig. 7.11 and the same voltage was applied. This induced the snap-through and the two stable configurations were observed as shown in Fig. 7.12. The state change was observed to be completely repeatable.

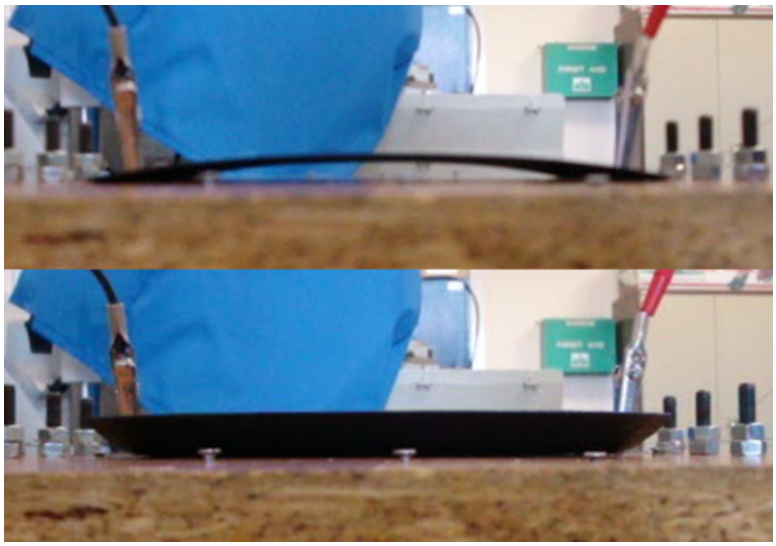

Figure 7.12: Snap-through of a $[0/90]_{\mathrm{T}}$ laminate under applied SMA load.

7.3.3 Experimental Comparison With Theory

The voltage required in the SMA to induce snap-through between stable states is investigated by considering the voltage-temperature relationship of the SMA material. Details from the manufacturer [66] state that the martensite to austenite transition occurs between 50°C and 65°C, where the transition temperature T_s is defined as,

$$T_s = \frac{V^2 A}{h_c S \rho l_w} + T_\infty \tag{7.18}$$

where V is the applied voltage, A is the cross-section area of the wire, h_c is the convection heat transfer coefficient, S is the surface area of the wire, ρ is the electrical resistivity, l_w is the total length of the wire and T_∞ is the zero-volt temperature. Applying the properties of Table 7.4 to Eq. 7.18 gives the voltage-temperature relationship of Fig. 7.13, where V_{s0} and V_{f0} are the start and finish transition voltages respectively.

Table 7.4: Transition properties of NiTi wire [66].

Property	Value
Wire cross-section area, A (10^{-8}m^2)	2.41
Convection heat transfer coefficient, h_c (Wm^{-2} °C^{-1})	160
Wire surface area, S (10^{-4}m^2)	3.63
Electrical resitivity, ρ ($10^{-7}\Omega$m)	11.0
Total wire length, l_w (m)	0.66
Zero-volt temperature, T_∞ (°C)	21

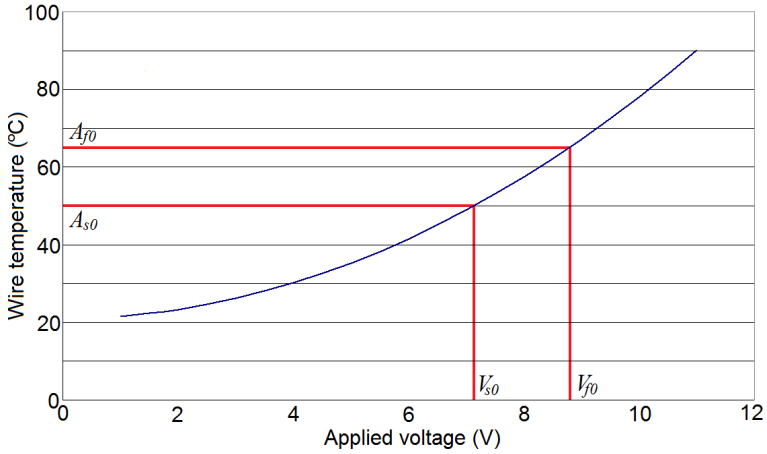

Figure 7.13: Wire temperature as a function of applied voltage.

Figure 7.13 shows that the transition should occur between 7.1V and 8.8V, which compares well with the experimental value of ∼9V found in the previous section. In fact the experiment showed that small displacements occur from around 6V and continue to at least 11V. This discrepancy is due to the simplistic nature of the numerical model, where in practice the strain actually follows a smooth curved profile either side of the transition region, shown in Fig. 7.14.

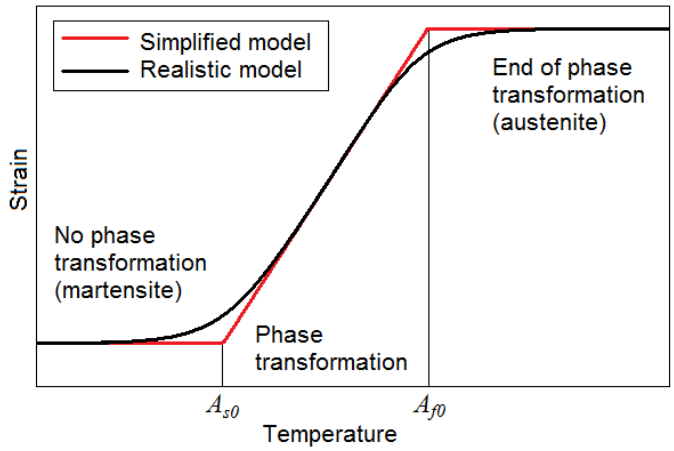

Figure 7.14: Simplified model of the SMA strain-temperature relationship.

It has been demonstrated that actuation of a bistable laminate can be achieved using SMA wires, and that the transition voltage can be accurately predicted. However, the issue of reversible actuation remains with the need for repeated deformation of the SMA wire. Furthermore, the slow response times (maximum operating frequencies are lower than 10Hz for SMA compared with over 10kHz for piezoelectric actuators) and lack of fine shape control using SMA actuation do not compare well with piezoelectric actuation [50]. A combination of the advantages of both methods is considered in the following section.

7.4 Reversible Actuation Using MFCs and SMA

This section outlines an experimental study of an actuation mechanism combining the advantages of the piezoelectric and SMA materials to achieve self-resetting bistable laminates, referred to here as Shape Memory Alloy - Piezoelectric Active Structures (SMAPAS). The approach uses piezoelectric actuation to provide rapid snap-through from state I to state II with a fine degree of control, and a relatively slow but high strain SMA actuation to reverse the state change, state II to state I. For reversible actuation the deflection induced by the piezoelectric actuation must be sufficiently high to deform (twin) the SMA material, thus enabling the shape memory effect to be utilised.

7.4.1 Manufacturing of SMAPAS Demonstrator

A thin composite cantilever beam of $[0/0/90/90]_T$ layup is used to demonstrate the two-way actuation. Figure 7.15 shows the cantilever beam setup, showing the rectangular cantilever and the location of both the MFC actuator and SMA wire. This is the same structural configuration used in a previous study which showed that two-way actuation was not achievable using only the piezoelectric actuation [12]. The dimensions of the cantilever beam are 300×60×0.52mm manufactured using HTA (12k) 913 prepreg sheet [12].

The MFC actuator (M2814-P1 [96]) has an operating range of -500V (contraction) to 1500V (extension). The dimensions are 37×17mm with an active area of 28×14mm and a thickness of 0.3mm. A two-part araldite epoxy was used to bond the MFC actuator where the direction of the main actuator strain (and its piezoelectric fibres) was aligned along the axis of curvature, Fig. 7.15. The surface of the carbon fibre composite was roughened to provide a better adhesion surface. The actuator and composite laminate were held flat under a weight to provide a good contact while the epoxy was allowed to cure for 24 hours. The amplifier used to apply an electric potential for piezoelectric actuation was a TREK PZD700 with a maximum unipolar voltage of 1.4kV, maximum current of 50mA and slew rate of 100V/s.

SMA actuation was achieved by application of a voltage to heat a NiTi SMA wire (0.175mm diameter) [66]. The four 20×20 mm corners removed from the composite allowed the SMA to be clamped to the cantilever beam. The SMA wire was electrically and thermally insulated by a series of ceramic thermocouple tubes and the wire was wrapped around the end tab of the cantilever beam and clamped at the opposite end. The two ends of the SMA wire were then fixed behind the clamping point to tighten and remove any slack.

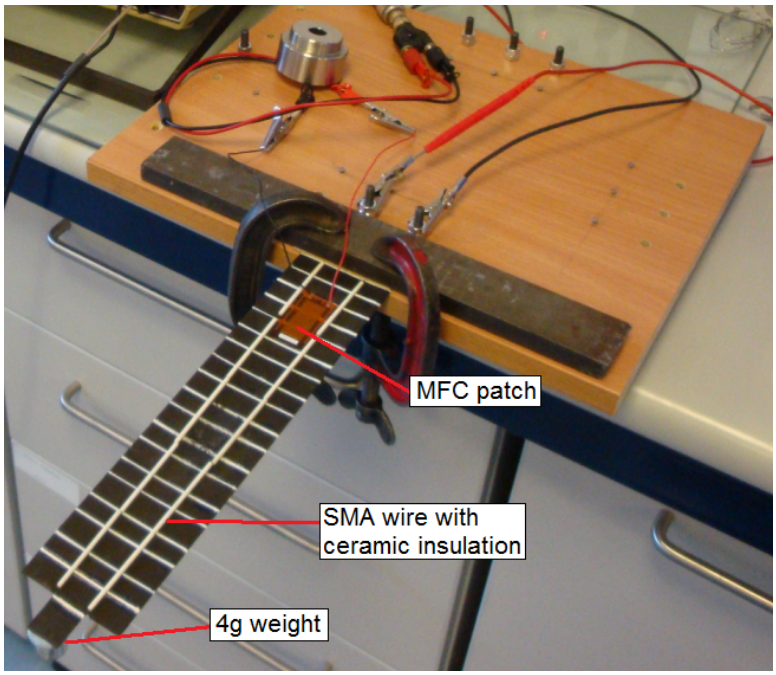

Figure 7.15: Experimental SMAPAS cantilever test rig.

A small mass was added to the cantilever to ensure sufficient deformation of the SMA from state I to II. Figure 7.16 shows the two stable states of the bistable cantilever.

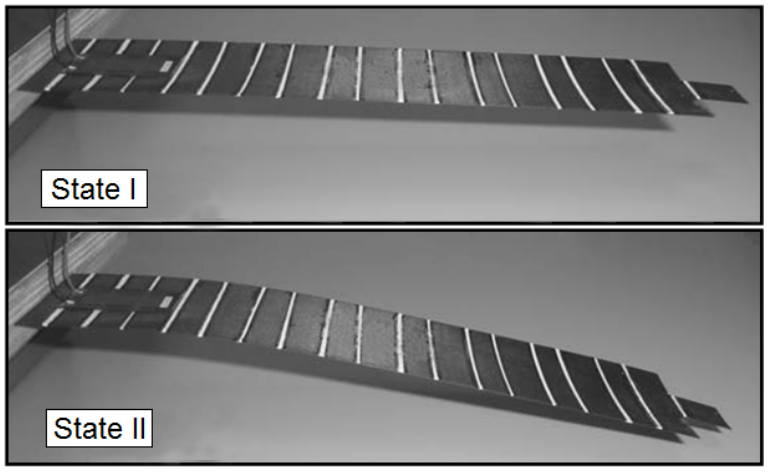

Figure 7.16: Two stable states of a SMAPAS bistable cantilever.

7.4.2 Characterisation of Actuation

Deflections and shape as a function of actuation were characterised using a motion analysis technique as in Bowen et al. [12]. A digital video camera recorder (Sony DCR-TRV 900E) was set up 4.80m from the cantilever with the lens axis perpendicular to the side plane of the sample. A rectangular calibration object of 346×262mm was

videotaped for scaling purposes before commencement of the experimental work. The cantilever beam was videotaped at each actuation voltage in steps of 100V for MFC actuation and 1V for SMA actuation. A time step of approximately two minutes was allowed between each measurement. The cantilever beam profile was manually digitised on Peak Motus (v8.5, Vicon, USA) by selecting 34 points approximately uniformly along the edge of the cantilever beam. The four corners of the calibration object were also manually digitised. The digitised area consisted of 1440×1152 pixels, hence an effective resolution of digitisation was ∼0.3mm in both horizontal and vertical directions. Following the scaling and reconstruction these 34 discrete coordinates were exported to Excel software and a fifth order polynomial least squares fit was used to recreate the profile of the cantilever in each condition.

7.4.3 Results and Discussion

The first part of the experiment was to examine the cantilever deflection due to piezoelectric actuation while no voltage was applied to the SMA. The cantilever beam was initially in its raised state (state I) at 0V. The shape of the cantilever beam profile was then recorded for the positive voltage range of the MFC actuator (maximum of 1500V). The results at 0, 300, 600, 900, 1200 and 1300V are presented in Fig. 7.17.

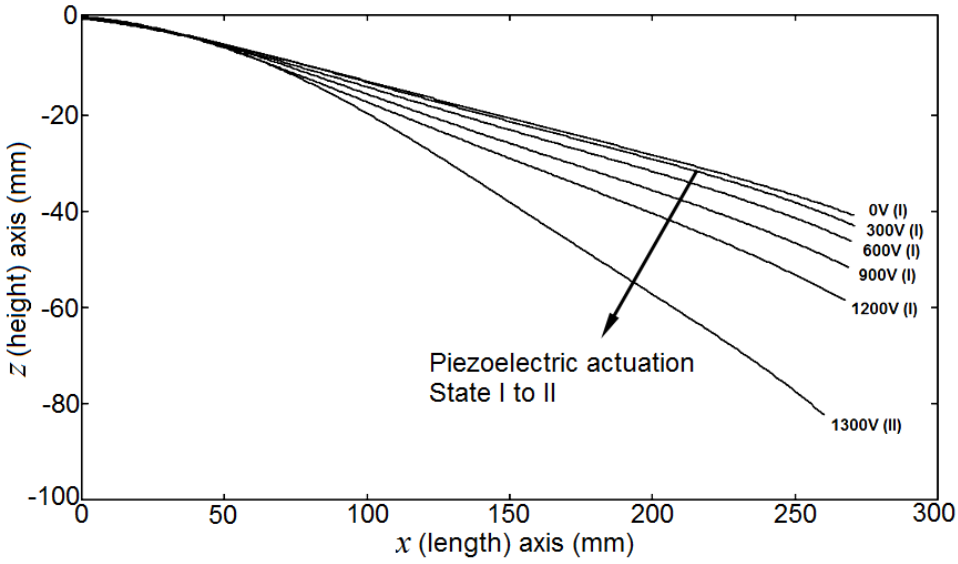

Figure 7.17: Cantilever shape profile during piezoelectric actuation. Associated state highlighted in brackets for each voltage.

It was observed that applying voltages between 0 and 1200V increased the deflection of the cantilever beam but the structure remained in state I. At 1300V there was a significant change in the deflection as a result of transition from state I to II. On re-

moval of the applied voltage a small reduction in the deflection was observed but the structure remained in state II. The cantilever could not be returned to state I using the MFC alone, consistent with the previous findings [12]. Comparing this result with that presented by Bowen et al. [12] the actuation voltage requirement of 1300V in this work was 300V higher due to the increased stiffness caused by the addition of the SMA wires to the upper surface of the cantilever beam.

The second part of the experiment examined the cantilever beam deflection in response to SMA actuation. After transition from state I to state II using the piezoelectric and removing the applied voltage, the input voltage to the SMA wire was increased from 0 to 11V at 1V intervals. The cantilever beam profiles at 0, 5, 6, 7, 8, 9, 10 and 11V are shown in Fig. 7.18.

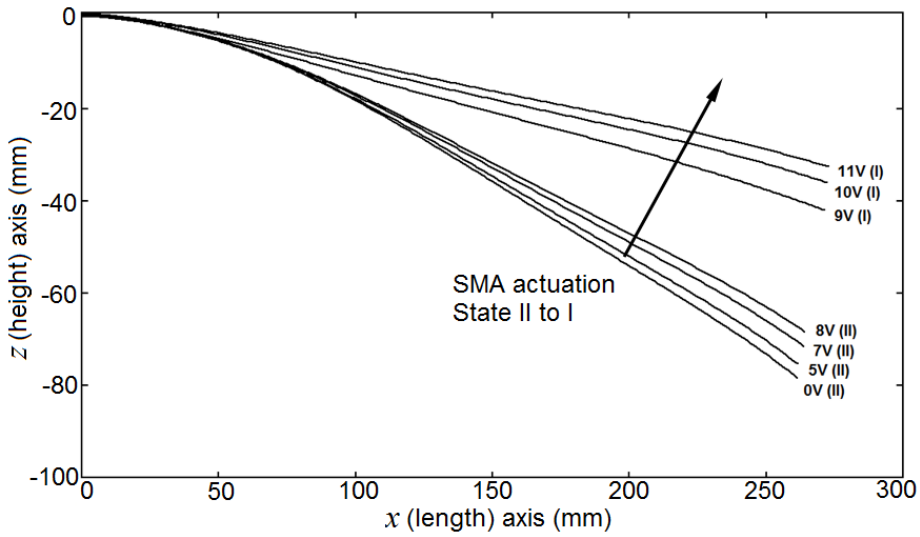

Figure 7.18: Cantilever shape profile during SMA actuation. Associated state highlighted in brackets for each voltage.

In this case the purpose of the applied voltage was to provide sufficient Joule (resistive) heating to achieve a martensite to austenite phase change in the SMA and induce a shape memory effect. Small deflection changes were seen between 0 and 5V as the temperature in the wire had not reached the transition temperature. There was a more marked change between 5V and 8V although the cantilever beam remained in state II. Transition from state II to I was observed at 9V. Upon removal of the voltage to the SMA the cantilever beam returned to its original (0V) state I profile as in Fig. 7.17. This reversible actuation was completely repeatable indicating that the piezoelectric actuation from state I to state II was sufficient to deform (twin) the SMA wire and enable fully reversible actuation using the SMA-piezoelectric combination. It is noted that repeated actuation of the structure over a longer time period may reduce the twinning effect and the resetting ability may be lost.

A comparison of Figs. 7.17 and 7.18 reveals the different power requirements of the two actuator materials. The piezoelectric requires a high voltage (>1000V) and electric field (∼1-2kV/mm) with low current (since the piezoelectric is a dielectric) while the SMA requires a much lower voltage (<15V) with high current (up to 1A). Since piezoelectric strain is proportional to electric field the voltage requirement could be lowered by reducing the interdigitated electrode spacing of the MFC. The piezoelectric is primarily a reactive (capacitive) load while the SMA is a resistive load, necessitating different levels of rectification and power. Based on the MFC capacitance [96] of 14nF, the time to attain a voltage of 1300V is 364ms. This equates to a peak power of 33J/s for piezoelectric actuation. A voltage of 15V and current of 1A for the SMA equates to a lower power of 15J/s, which is applied for longer periods to achieve Joule heating.

7.5 Concluding Remarks

This chapter has discussed a number of actuation methods which may be applicable to actuation of a bistable laminate. Combinations of mechanical force, MFC's and SMA wires have been modelled and considered in experimental studies to assess the feasibility of each technology. The advantages and disadvantages of each for application to a design study similar to that in Chapter 6 are summarised in Table 7.5.

Table 7.5: Summary of actuation methods for bistable laminates.

Actuation method	Advantages	Disadvantages
Mechanical force	Ease of modelling Fine shape control Variable actuation configuration No effect on static shape	Practical application of force External actuation required
MFC actuators	Ease of modelling Fine shape control Response time Range of operation	Two-way actuation requires two MFC's Reduces static laminate curvature
SMA wires	High strain Large in-plane force	Slow response time No fine shape control Integration into structure
SMAPAS	Reversible actuation Repeatable SMA effect	Fine control in one direction only Low frequency actuation

A simple extension to the analytical model for static laminate shapes to include a simple mechanical force has been presented. This modelling has been used to demonstrate the prediction of an actuation force applied in the out-of-plane direction at the laminate centre, with a fine degree of shape control achievable for lower forces. With

optimisation in mind a short study of variation in actuation force with applied location has been conducted showing a large variation in actuation behaviour. However, the practical implications of applying the out-of-plane force are severely limiting.

A second study considered incorporating a piezoelectric MFC actuator into the existing model. This 'layer-like' extension provides a simple method of predicting actuation voltages and displacements and has been validated experimentally. Observed discrepancies are attributed to differences between the manufactured laminate and the ideal modelling case. A shape characterisation study highlighted areas of locally reversed curvature around the MFC edges, not predicted by modelling. This may contribute to the observed errors but is not considered to significantly affect the overall curvature. To achieve reversible actuation two MFCs are required. This technique allows fast and repeatable two-way actuation with fine control in both directions.

SMA wires were considered due to the high level of strain which can be achieved. A volume fraction approach has been used to incorporate a layer of SMA wires embedded in epoxy resin. This technique does not significantly affect the static laminate shapes, thus not compromising the bistable behaviour. An experimental study was then conducted to demonstrate the feasibility of SMA actuation of a cross-ply laminate and to determine the required voltage. The observed voltage showed excellent agreement with modelling predictions but no intermediate shape change was considered. The difficulty in incorporating this complex mechanism into the existing model, and the lack of fine shape control are considered to be limiting factors.

A final study combining the advantages of both MFC actuators and SMA wires demonstrated reversible actuation of a bistable cantilever. Two-way actuation is achieved without the need for attaching two MFC actuators to the laminate, thus maintaining higher static curvatures. However, the issue of the slow response time remains. Furthermore, the twinning of the SMA wire may decay overtime resulting in the inability to reset the laminate.

Based on these studies, reversible actuation using two MFC actuators is considered to be both the most suitable method for bistable laminate actuation and the most applicable to the existing analytical model. By incorporating two orthogonal piezoelectric layers into the design formulation of Chapter 6 an optimisation study for the design of reversibly actuated bistable laminates can be conducted.

Chapter 8

Optimisation of Actuated Bistable Laminates

This chapter presents an optimisation study for the design of bistable laminates incorporating piezoelectric layers. This work builds on that presented in Chapter 6 to address the issues associated with the inherent flexibility of bistable laminates. The objective is to minimise unwanted structural deformation in a known loading direction subject to bistability, minimum deflection and available actuation energy constraints.

Section 8.1 outlines the extensions to the laminate geometry which are required for this problem, with two orthogonal piezoelectric layers on opposite laminate surfaces incorporated into the design rules of Section 4.2.2. The necessary extensions to the existing modelling to include the additional stiffness of the extra layers and the response to applied voltages are introduced, with an analytical example of the determination of an actuation voltage. This modelling then forms the basis of the optimisation problem formulation outlined in Section 8.2.

Results obtained for a series of examples are presented in Section 8.3. The problem is found to be multimodal with the multiple optima dependent on the loading and actuation directions and the constraint boundary interactions. Based on these results a secondary study is presented to reduce the total actuation voltage through the simultaneous use of the positive and negative working ranges of the two piezoelectric layers. Finally, the performance of the optimisation methodology is discussed.

8.1 Design Problem

In this section an extension to the laminate geometry of Fig. 4.2 is introduced for the incorporation of two orthogonal piezoelectric layers, as discussed in Chapter 7. The new laminate configuration is defined by the following design rules, and the n-ply geometry is illustrated in Fig. 8.1.

1. Two piezoelectric layers on the top and bottom surfaces of the laminate 90° apart.
2. Even number of plies, with pairs of plies about the laminate midplane 90° apart.
3. Square edge lengths L for both the piezoelectric layers and composite laminate.
4. Equal thicknesses t_p for both piezoelectric layers.
5. Equal ply thicknesses about the laminate midplane t_1, t_2, ... , t_n.
6. Each ply is made from the same material.

This laminate configuration is selected for two reasons. Firstly, the piezoelectric layers are positioned orthogonal to each other to align with the major curvatures of the two stable cylindrical states, Rule 1. Secondly, it allows for the maximum deflection between the two states while providing scope for tailoring the directional stiffness properties, Rule 2.

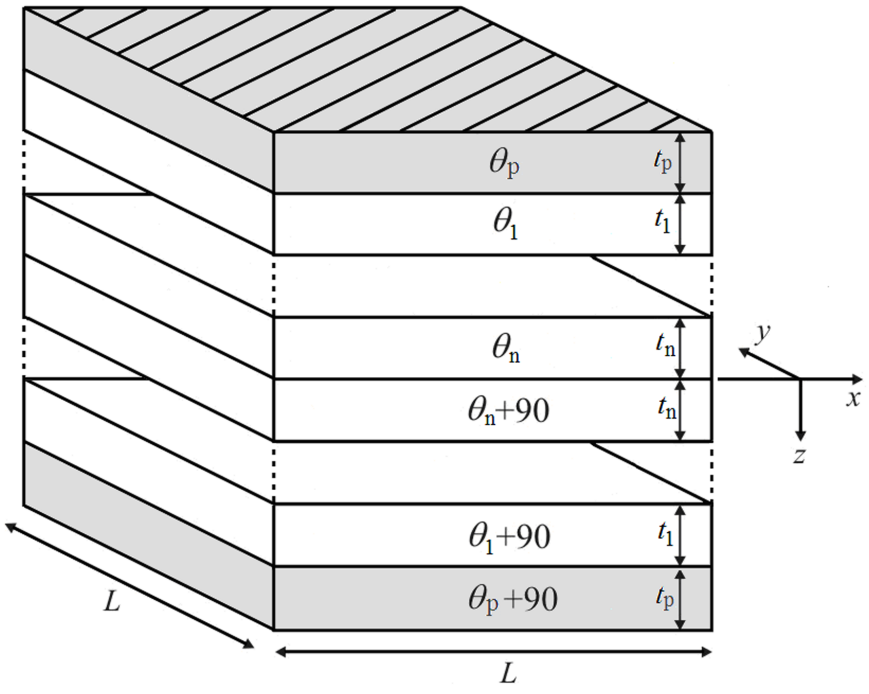

Figure 8.1: n-ply laminate (white) geometry with orthogonal piezoelectric layers (grey).

8.1.1 Modelling Extension

The existing analytical model is extended to account for the orthogonal piezoelectric layers. Firstly the piezoelectric stiffness is added to the laminate structure, and secondly the effect of a voltage applied to the piezoelectric material is included. The first of these is a simple extension to the matrix formulation of Chapter 4 where the piezoelectric layers are treated in the same way as a single ply. With reference to Eq. 4.67, the components of the energy formulation which must be modified to include the piezoelectric layers are $\boldsymbol{U}$, $\boldsymbol{Z}$, $\boldsymbol{K}$ and $\boldsymbol{T}$, which define the stiffness matrices and thermal force and moment terms as follows,

$$[\boldsymbol{S}] = [\boldsymbol{U}][\boldsymbol{Z}][\boldsymbol{K}][\boldsymbol{T}] = [A_{11}\ \ A_{12}\ \ A_{16}\ \ A_{66}\ \ B_{11}\ \ B_{16}\ \ D_{11}\ \ D_{12}\ \ D_{16}\ \ D_{66}\ \ N_x^T\ \ M_x^T\ \ M_{xy}^T] \tag{8.1}$$

Each property defined by Eq. 8.1 can be considered cumulative. The total contribution of the laminate and piezoelectric layers $\boldsymbol{S}_{tot}$ is therefore expressed as the following sum,

$$\begin{aligned}[\boldsymbol{S}_{tot}] &= [\boldsymbol{S}_{lam}] + [\boldsymbol{S}_p] \\ &= [\boldsymbol{U}][\boldsymbol{Z}][\boldsymbol{K}][\boldsymbol{T}] + [\boldsymbol{U}_p][\boldsymbol{Z}_p][\boldsymbol{K}_p][\boldsymbol{T}_p]\end{aligned} \tag{8.2}$$

where the subscript *lam* refers to laminate properties and p denotes a piezoelectric property. Terms are split into their constitutive parts in the same way as outlined in Chapter 4 defined as follows,

$$\begin{aligned}[\boldsymbol{U}_p] &= \text{Piezoelectric stiffness properties} \\ [\boldsymbol{Z}_p] &= \text{Piezoelectric layer orientations} \\ [\boldsymbol{K}_p] &= \text{Piezoelectric thermal expansion properties} \\ [\boldsymbol{T}_p] &= \text{Piezoelectric layer thickness terms}\end{aligned}$$

The matrix $\boldsymbol{U}_p$ is unchanged from the definition of Eq. 4.21 but is defined using the corresponding piezoelectric properties, see Table 7.1. As the piezoelectric layers are typically attached post-cure [84, 93] they do not produce any thermal forces or moments but do contribute to the $\boldsymbol{A}$, $\boldsymbol{B}$ and $\boldsymbol{D}$ terms. The matrix $\boldsymbol{K}_p$ is therefore modified from Eq. 4.51 to the following form to eliminate the temperature dependent terms.

$$[\boldsymbol{K}_p] = \begin{bmatrix}[I_{10\times10}] & [0_{3\times10}] \\ [0_{10\times6}] & [0_{3\times6}]\end{bmatrix} \tag{8.3}$$

For the matrices $\boldsymbol{Z}_p$ and $\boldsymbol{T}_p$ Eq. 4.54 is considered for the special case of a single pair of layers positioned on the outer laminate surfaces. Substituting the distance to the top ($E_i = (nt + t_p)/t$) and bottom ($E_{i+1} = (nt)/t$) surface of the top piezoelectric layer into Eq. 4.54, the following form is obtained for the piezoelectric layers alone,

$$\begin{aligned}
\boldsymbol{V}_p^A &= 2t_p \begin{bmatrix} 0 & \cos 4\theta_p & 0 & \sin 4\theta_p \end{bmatrix} \\
\boldsymbol{V}_p^B &= \left((nt)^2 - (nt+t_p)^2\right) \begin{bmatrix} \cos 2\theta_p & 0 & \sin 2\theta_p & 0 \end{bmatrix} \\
\boldsymbol{V}_p^D &= \frac{2}{3}\left((nt+t_p)^3 - (nt)^3\right) \begin{bmatrix} 0 & \cos 4\theta_p & 0 & \sin 4\theta_p \end{bmatrix}
\end{aligned} \tag{8.4}$$

where n is the number of plies above the midplane and θ_p is the orientation of the top piezoelectric layer. The layer orientation and thickness terms are then separated in the same way as Eq. 4.55 to give,

$$\boldsymbol{Z}_p^A = \frac{\boldsymbol{V}_p^A}{2t_p}, \quad \boldsymbol{Z}_p^B = \frac{\boldsymbol{V}_p^B}{(nt)^2 - (nt+t_p)^2}, \quad \boldsymbol{Z}_p^D = \frac{\boldsymbol{V}_p^D}{\frac{2}{3}\left((nt+t_p)^3 - (nt)^3\right)} \tag{8.5}$$

The matrix $\boldsymbol{Z}_p$ then has the same form as Eq. 4.52 but with the piezoelectric layer properties, and the matrix $\boldsymbol{T}_p$ contains the thickness dependent terms of Eq. 8.5 in the same form as Eq. 4.53. Finally, Eq. 8.2 is substituted into Eq. 4.69 to define the equilibrium equations to be solved to find the stable shapes of the unloaded laminate including the two orthogonal piezoelectric layers.

$$f_i = [\boldsymbol{S}_{tot}][\boldsymbol{X}]_i[\boldsymbol{L}] \tag{8.6}$$

Given the cumulative nature of the properties in Eq. 8.6, the full form of the equilibrium equations is identical to that for Eq. 4.69, only with different values for each of the $\boldsymbol{A}$, $\boldsymbol{B}$ and $\boldsymbol{D}$ matrix terms. The analytical solution derived in Chapter 4 and detailed in Appendix B.10 is therefore still valid with these new properties and provides a fast and robust method of calculating the static shapes.

8.1.2 Actuation Voltage

The second extension necessary to consider the addition of piezoelectric layers is the effect of applying a voltage to the material. When a voltage is applied to the piezoelectric layers to deform the laminate shape the assumptions on which the analytical solution to the existing model is based are invalid. Specifically, the reduced number of shape coefficients of Eq. 4.66 is not suitable for two deformed shapes of unequal curvature. Equation B.38 can therefore not be used to find the loaded shapes. However, the exact solution for the unloaded shape provides a very close initial guess to the shapes for a small applied voltage. Using the modelling extension outlined in Section 7.2.1 and the unloaded shape as an initial guess, the loaded shapes can be calculated iteratively using a Newton-Raphson technique for small increments of the applied voltage. Given the quality of the initial guess this method is found to be efficient and reliable for assessing the voltage induced shape change.

As an example of the determination of an actuation voltage, a $[0^{P}/0/90/90^{P}]_{T}$ laminate is considered where P denotes a piezoelectric layer. Figure 8.2 illustrates the change in major and minor out-of-plane displacement coefficients a and b where the subscript denotes the associated stable state, with applied voltage to the top layer. The exact zero-voltage shape at point A is calculated using Eq. B.38. As the applied voltage is incrementally increased the loaded shapes are computed using the Newton-Raphson method. At a critical voltage, point B, a switches to near-zero and the coefficient b jumps to a large negative value, point C. The voltage at this transition from point B to C is the actuation voltage. As the voltage is then incrementally removed, the curvatures approach the second unloaded shape at point D.

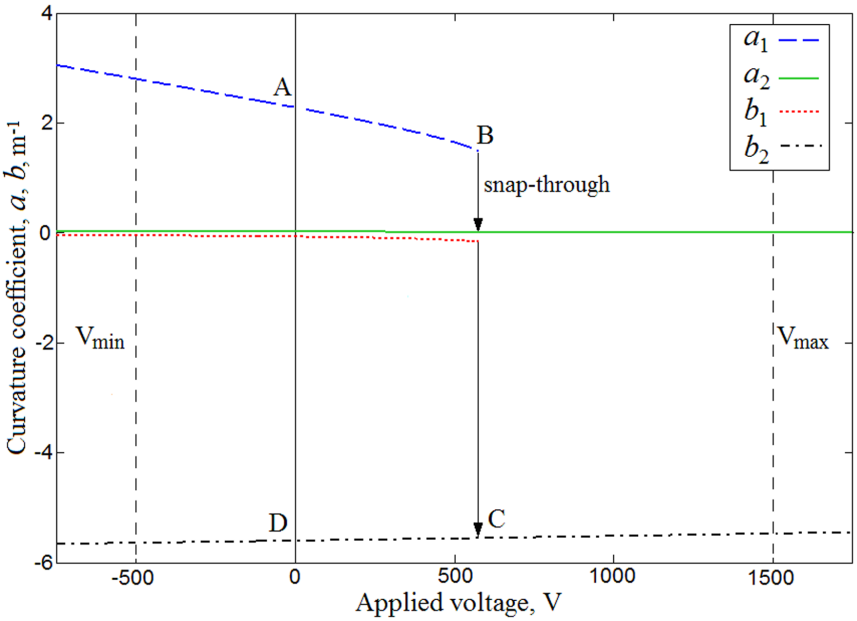

Figure 8.2: Actuation of a $[0^{P}/0/90/90^{P}]_{T}$ laminate. Subscript denotes the associated stable state.

For reversible actuation using the laminate definition of Fig. 8.1 the two voltages applied to the top and bottom piezoelectric layers are considered separately. Therefore the actuation scheme described above uses a single voltage to describe each shape transition.

8.2 Optimisation Problem Formulation

In this section the optimisation problem formulation for actuated bistable laminates is introduced. This formulation is an extension of that considered in Chapter 6 to include orthogonal piezoelectric layers. The problem is defined as follows,

Maximise:	Bending stiffness in a chosen direction ϕ_2 (see Fig. 6.2), Section 8.2.1.
Subject to:	The laminate must be bistable, Section 8.2.2.
	The deflection between states must be greater than a minimum value, enforcing a meaningful shape change, Section 8.2.2.
	Reversible snap-through must be within the working voltage limits of the piezoelectric layers, Section 8.2.3.
Variables:	Ply orientations θ_1 and θ_2 defining all four ply orientations.
	Piezoelectric fibre orientation θ_p.
	Ply thicknesses t_1 and t_2.
	Square edge length L common to the laminate and piezoelectrics.
	Snap-through direction ϕ_1 and loading direction ϕ_2.

It is noted that this formulation is stated for the design of a four-ply laminate configuration for ease of illustration. However, the method can be easily extended to any number of plies.

8.2.1 Objective Function

As discussed in Section 6.1, bistable laminates are inherently flexible to allow low energy state-change. However, this can lead to unwanted structural deformation due to external operating loads. Unlike the work presented in Chapter 6 these conflicting requirements are separated in this formulation. With a method of determining the actuation voltage, the actuation behaviour can be considered as a constraint, outlined later in this section. This leaves the behaviour in the loading direction as the objective function. To resist unwanted deformation in this direction the bending stiffness is maximised, characterised as minimising the change in curvature with applied moment in the loading direction. This property is calculated as described in Section 6.2.1.

$$\text{Objective function :} \quad \frac{\delta a_{\phi 2}}{\delta M_{x\phi 2}} \quad (\mathrm{N^{-1}m^{-2}}) \tag{8.7}$$

8.2.2 Bistability and Deflection Constraints

The addition of two orthogonal piezoelectric layers will inevitably reduce the laminate curvatures due to the added stiffness. Constraints to ensure bistability and subsequently a minimum deflection are therefore vital. Conveniently the changes to the modelling in this chapter do not affect the formulations for these constraints outlined in Sections 6.2.2 and 6.2.3. They therefore remain unchanged.

8.2.3 Actuation Constraint

A constraint is imposed to ensure that the laminate can be actuated within the working voltage limits of the piezoelectric layers. The applied voltage to the piezoelectric layers in the direction of actuation ϕ_1 is therefore constrained to be within these bounds. For the piezoelectric material used in this work (M8557-P1) the lower and upper bounds for applied voltage are -500V and 1500V respectively [96]. The maximum positive voltage of 1500V represents a limit to avoid dielectric breakdown of the piezoelectric and corresponds to a free strain of 1350μstrain. The -500V cannot be exceeded since it can lead to depolarisation of the piezoelectric and corresponds to a free strain of -450μstrain. This constraint is included using the technique outlined in Section 8.1.2.

8.3 Numerical Results

This section presents the results of numerical optimisation using the problem formulation of Section 8.2. The problem is solved using Matlab's sequential quadratic programming (SQP), `fmincon`. In order to find all local solutions, multiple starting points are used. All examples use M21/T800 material properties for the laminate (Table 5.1) and M8557-P1 properties for the piezoelectric layers (Table 7.1).

8.3.1 Maximisation of Bending Stiffness

To demonstrate the nature of the design space, optimum solutions constrained only by the cross-symmetric design rules of Fig. 8.1 and no bistability, deflection or snap-through constraints are imposed. The design variables are restricted to the ply orientations for illustrative purposes. The square laminate edge length L is set to 0.15m, and the uniform single ply thickness $t_1 = t_2$ set to 0.1mm. The piezoelectric layers are assumed to have the same edge length L with a thickness of 0.2mm. The snap-through

direction ϕ_1 is fixed to 90°. The pattern of results observed is dependent on the relative values of the snap-through direction and loading direction rather than the individual angles. Figure 8.3 shows the design space for this problem for changing values of the loading direction ϕ_2. The contours show the objective function value, the red dots are used to indicate points where Eq. 8.7 is locally optimal and green dots used to indicate global optima.

With the loading direction initially set to 0°, four distinct local solutions are found with $[0_2/90_2]_\mathrm{T}$, $[90_2/0_2]_\mathrm{T}$, $[0/90]_{2\mathrm{T}}$ and $[90/0]_{2\mathrm{T}}$ layups, Fig. 8.3a. Due to the periodic nature of the design space these solutions are repeated at equivalent positions along the boundaries. Each of these four solutions has a different value of the objective function, with the global optimum found at $[0/90]_{2\mathrm{T}}$ with a value of $0.737\mathrm{N}^{-1}\mathrm{m}^{-2}$. As the loading direction ϕ_2 is changed the pattern of four local solutions shifts away from 0° and 90° ply angles and the solutions no longer appear orthogonally to one another. When ϕ_2 approaches 20° one of the four solutions is lost. Of the remaining three solutions the global optimum is found at $[22/\text{-}58/32/\text{-}68]_\mathrm{T}$ with an objective function value of $0.811\mathrm{N}^{-1}\mathrm{m}^{-2}$, Fig. 8.3e. When $\phi_2 = 30°$ the number of local solutions reduces further to just two, Fig. 8.3g. As ϕ_2 tends towards 45° the two remaining solutions become closer to being orthogonal to one another until settling on $[44/\text{-}38/52/\text{-}46]_\mathrm{T}$ and $[\text{-}44/38/\text{-}52/46]_\mathrm{T}$ at $\phi_2 = 45°$, with both solutions exhibiting equal objective function value of $0.936\mathrm{N}^{-1}\mathrm{m}^{-2}$, Fig. 8.3j.

In addition to the changing number of optima, an increase in the global optimum objective function values with increasing ϕ_2 is observed. Figure 8.4 shows this relationship for the range of ϕ_2, shown as the blue line. The minimum solution is found when ϕ_2 is 0°. This design represents a laminate layup where the piezoelectric layer orientations are orthogonal to the chosen loading direction. This is expected as the laminate composition makes best use of the directional stiffnesses of anisotropic materials by having the two conflicting requirements as far apart as possible. For comparison, the optimum cross-ply solutions $[\theta_1/\theta_1/\theta_1{+}90/\theta_1{+}90]_\mathrm{T}$ are also shown in Fig. 8.4, shown as the red line. These cross-ply layups are the most common in bistable laminate design as they exhibit high deflection, generally with $\theta_1 = 0°$. Comparing these typical designs against the global optima reveals improvement in objective function from 12% to 29% is obtained by the use of ply orientations as defined by design rule 2 of Section 8.1.

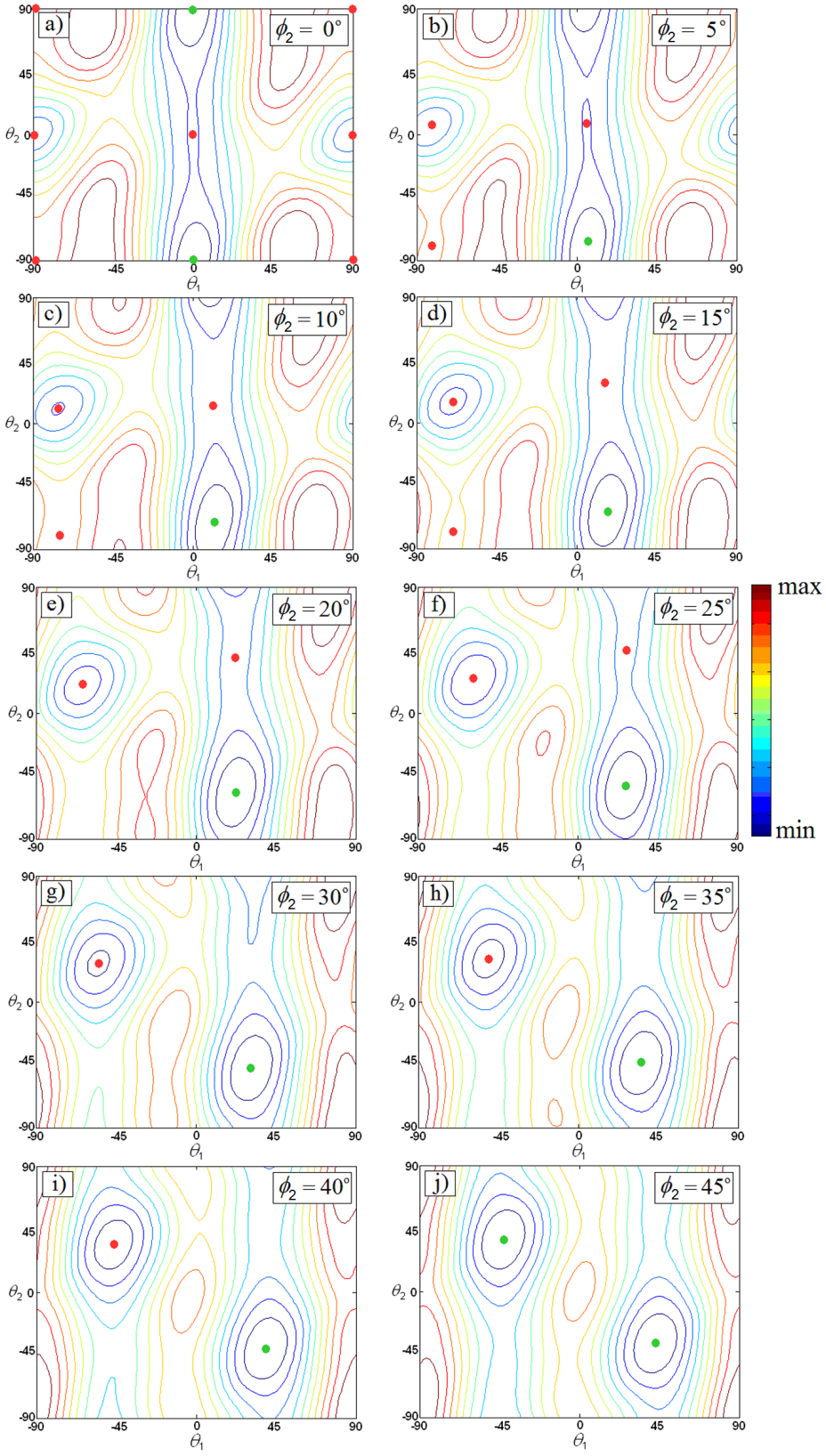

Figure 8.3: Variation in design space for a $[0^{\mathrm{P}}/\theta_1/\theta_2/\theta_2{+}90/\theta_1{+}90/90^{\mathrm{P}}]_{\mathrm{T}}$ laminate with change in loading direction ϕ_2. Contours represent the objective function, red dots mark local optima, while green dots denote global optima.

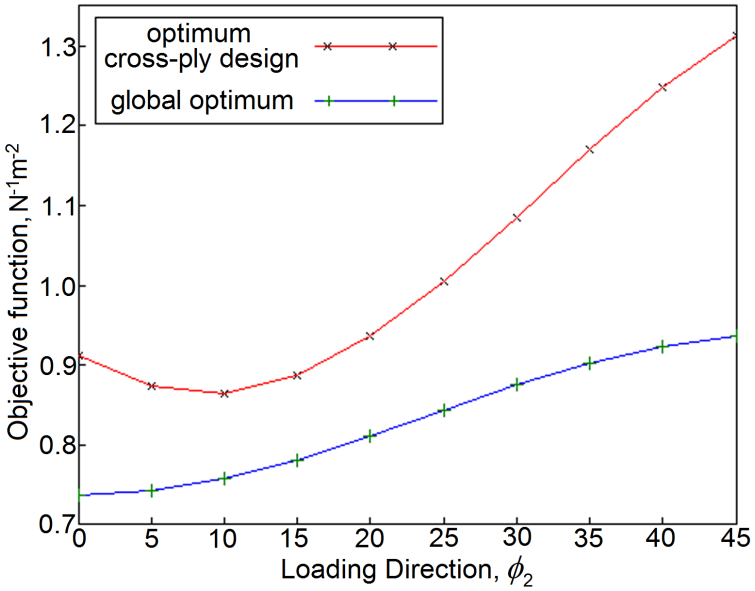

Figure 8.4: Variation in objective function with change in loading direction.

8.3.2 Addition of Deflection and Actuation Constraints

This section investigates how the optimum solutions are affected by the introduction of a minimum deflection and actuation voltage constraints. Figure 8.5 shows contours of the deflection between two states for the geometry of Section 8.3.1, where the edge length L is 0.15m, ply thickness t is 0.1mm and the piezoelectric layers are oriented at 0° and 90°. This composite laminate geometry is bistable for all ply orientations considered as the edge length to thickness ratio is sufficiently high. In the unconstrained examples it was observed that the global optimum stiffness solutions tend to sit in the regions marked by the black dotted lines in Fig. 8.5, while the highest deflection designs are observed in the region marked by the red line. This conflict demonstrates the need for constrained optimisation to tailor the design.

The deflection and actuation constraints are now introduced to the problem in Section 8.3.1 for a range of loading directions (0° to 45° at 5° intervals) and a fixed snap-through direction (90°) as in the unconstrained examples. The design variables are extended to include the nonuniform ply thicknesses t_1 and t_2 and laminate edge length L as well as the ply orientations. However, all locally optimal designs for this problem are found at the upper or lower bounds of the geometric variables. Therefore results are presented with the square laminate edge length set to 0.15m, and the uniform single ply thickness set to 0.1mm, noting that an increase in edge length or a decrease in ply thickness will increase the achievable deflection but not affect the general pattern of results observed.

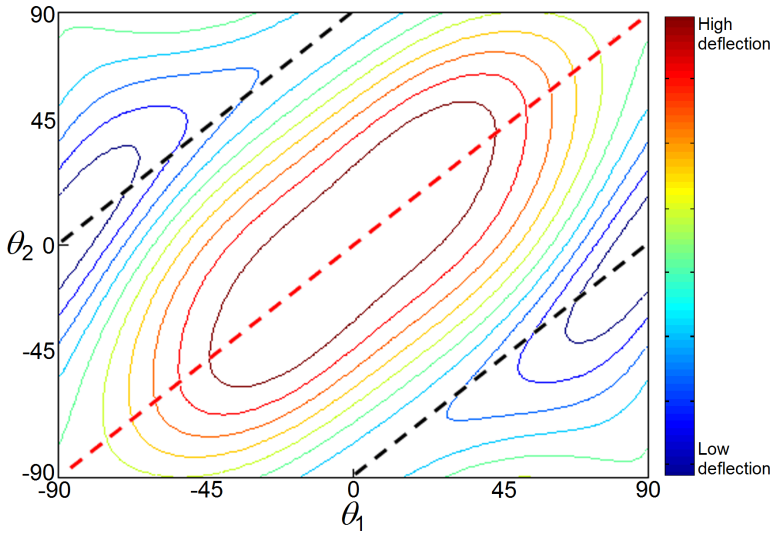

Figure 8.5: Deflection between states for a $[0^{P}/\theta_1/\theta_2/\theta_2{+}90/\theta_1{+}90/90^{P}]_{T}$ laminate. Black lines mark optimum stiffness regions, red line marks high deflection region.

Figure 8.6 shows the constrained design space for three example loading directions, 0°, 20°, and 45°, chosen to show the behaviour across the range shown in Fig. 8.3. For each loading direction results are presented for the actuation voltage constrained by the upper limit of the working range (1500V) where the infeasible region is marked in light grey. Each example is repeated for a range of deflection constraint values (30-70mm at 10mm intervals, 30, 50 and 70mm shown in Fig. 8.6), with the infeasible regions marked in dark grey. The local solutions are marked with red dots and the global solutions marked with green dots.

The optimum solutions are summarised in Table 8.1. It can be seen in Fig. 8.6a that the global optimum solution for 0° loading direction and the deflection constraint of 30mm is not affected by the constraints. Some local solutions are found to be infeasible, but $[0/90]_{2T}$ is still the global optimum with an objective function value of $0.737\text{N}^{-1}\text{m}^{-2}$. As the deflection constraint is increased to 50mm this solution becomes infeasible and a new global optimum is found on the deflection constraint boundary at $[2/76/\text{-}14/\text{-}88]_{T}$ with an increased objective function value of $0.754\text{N}^{-1}\text{m}^{-2}$, Fig. 8.6b. Increasing the deflection constraint further to 70mm continues to move the solution away from the unconstrained optimum. The actuation constraint (light grey region) remains inactive for all deflection values in Figs. 8.6a-c.

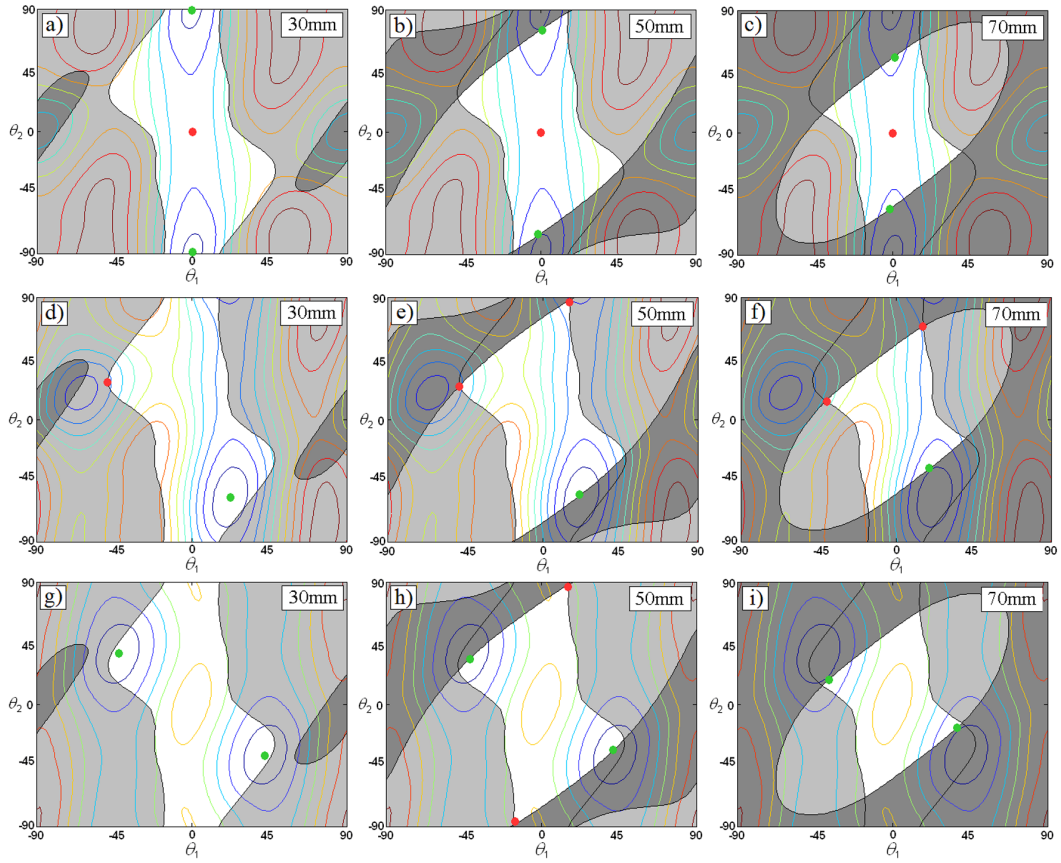

Figure 8.6: Constrained design space for loading directions a-c) $\phi_2 = 0°$, d-f) $\phi_2 = 20°$ and g-i) $\phi_2 = 45°$, for different deflection constraint values of 30, 50, and 70mm. Light grey regions infeasible due to voltage constraint, dark grey regions infeasble due to deflection constraint, red dots mark local optima and green dots mark global optima.

Table 8.1: Constrained global optimum solutions.

Loading direction ($\phi°$)	Deflection constraint (mm)	θ_1 (°)	θ_2 (°)	Actual deflection (mm)	Objective Function ($N^{-1}m^{-2}$)
0	30	0	90	43.3	0.737
	40	0	90	43.3	0.737
	50	2	76	50.0	0.754
	60	4	68	60.0	0.773
	70	2	56	70.0	0.787
20	30	22	-59	46.7	0.811
	40	22	-59	46.7	0.811
	50	21	-56	50.0	0.813
	60	21	-44	60.0	0.832
	70	20	-36	70.0	0.854
45	30	43	-38	44.2	0.936
	40	43	-38	44.2	0.936
	50	41	-33	50.0	0.943
	60	39	-35	60.0	0.972
	70	36	-19	70.0	1.014

For the solutions with loading direction of 20° a similar pattern is observed (Figs. 8.6d-f). For the low deflection constraint of 30mm the global optimum is unchanged, $[22/-59/31/-68]_T$ with an objective function value of $0.811 N^{-1}m^{-2}$, Fig. 8.6d. An additional local solution is found where the actuation constraint is active. As the deflection requirement is increased from 30mm to 50mm the global solution is shifted by the deflection constraint boundary to $[21/-56/34/-69]_T$ with an objective function value of $0.813 N^{-1}m^{-2}$ and an additional local solution constrained by the actuation requirement appears, Fig. 8.6e.

For the loading direction at 45° a slight change in the pattern of the results is observed (Figs. 8.6g-i). Due to the symmetry of this particular problem we find two solutions of equal objective value. For the 30mm deflection problem these solutions are unconstrained and are found at $[43/-38/52/-47]_T$ and $[-43/38/-52/47]_T$ with an objective function value of $0.936 N^{-1}m^{-2}$, Fig. 8.6g. As the deflection constraint is increased these two solutions move simultaneously to points on the constraint boundary, still with equal but higher objective value (Figs. 8.6h-i). In all cases the light grey actuation constraint remains inactive for the global optima.

These examples demonstrate that actuation through the use of two orthogonal piezoelectric layers is achievable for this family of laminates. Furthermore the state-change is achievable while maintaining a useful deflection between states and a reasonable improvement on the typical high deflection cross-ply designs, as shown in Fig. 8.4.

In all examples examined in this section the actuation voltage constraint was not the constraining factor for the global optima. This problem formulation also makes use of only one of the piezoelectric layers at any one time with the second piezoelectric layer used for the reverse actuation. Given that the full capacity of the actuation is not used and the potential of the second layer to contract under the application of a negative bias is neglected there is scope for a reduction in the total voltage requirement.

8.3.3 Combined Use of Two Piezoelectric Layers

The piezoelectric layers modelled in this work have a working range of -500V to 1500V. However, frequent use at these high voltage levels can lead to degradation of the piezoelectric and a reduced lifespan [48, 80]. Furthermore the use of drive voltages in excess of 1000V may limit application of the technology due to safety concerns or the need to rectify local power sources. Having considered only the positive range of one layer so far, and having observed that this constraint is inactive at the global optima for all cases, it is investigated whether the voltage requirement can be reduced by simultaneously utilising the negative voltage range of the layer on the opposite surface.

The voltage requirement for each optimum stiffness solution shown in Table 8.1 is analysed by the numerical method discussed in Section 8.1.2. Figure 8.7 shows the variation in the total voltage requirement (top layer voltage + bottom layer voltage) for each loading direction for the 50mm deflection problem. The green dots indicate the lowest combination of voltages for each example. For the 45° loading direction the optimum solution is found when the bottom layer voltage is 0V. Therefore no improvement in the voltage requirement is found. For the 20° loading direction the optimum solution is again found to be to use only the positive range of the top layer. However, the increase in combined voltage with increase in negative voltage is more gradual. For the 0° loading direction this pattern is reversed, with the optimum combination found at the negative voltage limit, -500V. This is combined with a small positive voltage of 30V for the opposite layer. The combined requirement of 530V represents a 23.7% reduction in the total applied voltage using only one piezoelectric layer. Results for all cases are shown in Table 8.2.

It is found that a reduction in the total voltage requirement is achievable for the 0° loading direction with up to 33.8% reduction from the corresponding single layer actuation solutions. In the case of a 40mm deflection constraint, $[0^{\mathrm{P}}/0/90/0/90/90^{\mathrm{P}}]_{\mathrm{T}}$, it is seen that using a negative voltage on the bottom layer alone requires less total voltage input. For the 20° loading direction there is a clear switching point where the use of the bottom layer no longer aids actuation. This is also the case for all 45° loading direction cases. Whether the bottom layer actuation is effective is dependent on the orientation of the piezoelectric layers relative to the laminate major curvature.

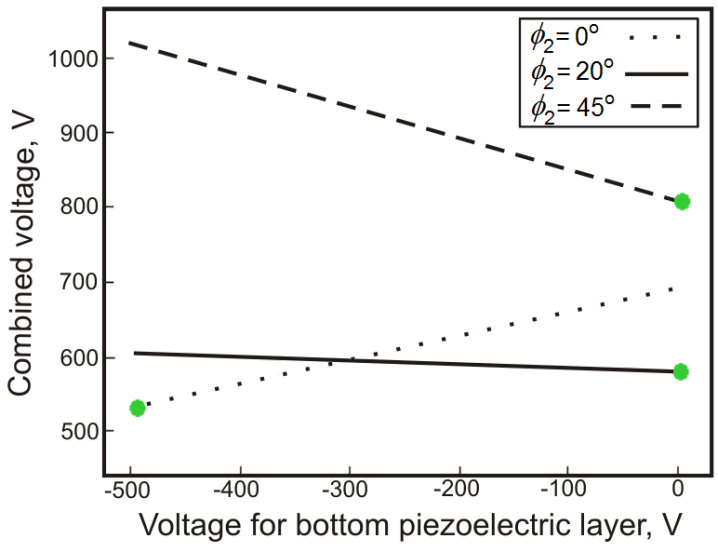

Figure 8.7: Combined voltage requirements for 50mm deflection.

Table 8.2: Voltage requirements using both piezoelectric layers simultaneously.

Loading direction ($\phi°$)	Deflection constraint (mm)	Top layer (V)	Bottom layer (V)	Combined voltage (V)	Reduction (%)
0	40	0	-410	410	33.8
	50	30	-500	530	23.7
	60	215	-500	715	11.7
	70	355	-500	855	1.7
20	40	75	-500	575	2.5
	50	590	0	590	0
	60	675	0	675	0
	70	775	0	775	0
45	40	865	0	865	0
	50	815	0	815	0
	60	940	0	940	0
	70	1085	0	1085	0

This study only considered orthogonal piezoelectric layers and showed that the use of both layers simultaneously can reduce the total voltage requirement. This suggests that there is scope for further improvement by relaxing the constraint on the piezoelectric layer orientations and making use of the full working range of the layers.

8.4 Concluding Remarks

This chapter has detailed an optimisation study for the design of reversibly actuated bistable laminates of cross-symmetric layup. This class of laminates have been chosen to allow tailoring of the laminate's directional stiffness whilst offering maximum useful deflection between states. The optimisation study has been enabled by the incorporation of two orthogonal piezoelectric layers into the analytical solution of Chapter 4 for the shapes of bistable laminates.

The optimisation study addresses the challenge of providing resistance to external loads in a known direction whilst maintaining useful bistable characteristics. The objective function is used to maximise the bending stiffness of the laminates in a chosen loading direction, while an actuation constraint is imposed by considering the operating range of the piezoelectric layers. Two additional constraints to ensure bistability and a minimum deflection are also included.

With the ply orientations and laminate geometry as variables the optimisation problem has been found to be multimodal, with the interactions of the multiple local optima with the constraint boundaries dependent on the chosen loading and actuation direc-

tions and the values of the constraints. Given the complex and multimodal nature of the actuated bistable laminate design space, multiple starting points are required to capture all optima.

As a secondary study the optimisation tool has been used to investigate the total voltage requirements for actuation. Through the combined use of the positive and negative applied voltages to the top and bottom piezoelectric layers, it is found that a reduction in the total actuation voltage of up to 33.8% is achievable in some cases. This indicates that there is scope to investigate simultaneous optimisation of stiffness requirements and actuation energy for bistable laminates.

Chapter 9

Bistable Laminates for Piezoelectric Energy Harvesting

In this chapter many of the methods developed in this work are combined in a study of a piezoelectric energy harvester to convert mechanical motion into electrical energy. Section 9.1 provides a brief outline of existing literature on the topic of energy harvesting using piezoelectric composite laminates. This background review highlights an existing experimental study of a bistable cross-ply laminate for energy harvesting, presented by Arrieta et al. [5]. The experimental study focuses on a laminate structure similar to that considered in Chapter 8. Due to the complex nature of existing modelling techniques optimisation of the design of the laminate has not been considered in the existing literature.

Section 9.2 outlines an optimisation problem formulation for the design of a similar structure to that presented experimentally in [5]. The objective of this study is to maximise the electrical energy generated between two stable states of a cross-symmetric laminate. This objective function is introduced by considering the curvature-induced deformations in piezoelectric material due to the alternating laminate curvatures. A number of modelling extensions are introduced including a variable configuration of piezoelectric layers and inclusion of variable laminate aspect ratio.

The results of the optimisation study are presented in Section 9.3 and the problem is found to have multiple local optima. These multiple solutions are then investigated in more detail in a series of design parameter studies. These studies are intended to demonstrate the dependence of solutions on the ply thickness, stacking sequence, aspect ratio and overall laminate geometry. Variation in the optimum piezoelectric configuration is observed depending on the problem definition.

Finally, some concluding remarks discuss the optimisation results in the context of practical applications. Large scope for improvement in the design of piezoelectric energy harvesters is identified, with a number of areas for future research suggested.

9.1 Background

In recent years there has been a steady rise in the use of wireless sensor networks and electronics requiring a portable energy source [4]. These systems typically rely on electrochemical batteries. However, while the electronics have become more sophisticated and require larger power supply over longer time periods, battery technology is the limiting factor. To address this issue research is focused on ways of harvesting electrical energy from ambient mechanical vibrations to provide the necessary power.

There are a number of ways of achieving mechanical energy to electrical energy conversions, such as electrostatic generation [67], electromagnetic induction [42] and the piezoelectric effect. Results presented by Priya [81] have shown that piezoelectric materials have a number of advantages, including ease of integration within a system, higher strain energy densities and the simplicity of the conversion from strain energy to useful electrical energy. Later work by Priya [82] aimed to evaluate a range of piezoelectric compositions to identify the most suitable for energy harvesting applications. A simple figure of merit (FOM) was derived to assess the electrical energy available under an alternating stress excitation in the off-resonance condition. Notably, this work presented a method to quantify the electrical energy in a purely static analysis, outlined further later in this chapter.

Piezoelectric material has been incorporated into structures to harvest energy from ambient vibrations. These devices are often tuned to operate near resonance to maximise their power generation [4]. However, resonant devices are not easily scalable and their performance falls significantly when operated outside their resonant frequency range [33]. Thus typical linear resonant systems are unsuitable for random ambient vibrations. More recently work has focused on exploiting nonlinearity for broadband energy harvesting. Encouraging results [32, 98, 99] have been obtained using nonlinear cantilevered beams. Stanton et al. [98] modelled and experimentally validated a nonlinear energy harvester using a piezoelectric cantilever. An end magnet on the cantilever excited by an electromagnetic shaker interacts with oppositely poled, stationary magnets. This technique was shown to outperform linear systems when excited by varying frequencies. However, such systems would require an obtrusive arrangement of external magnets, rendering them unsuitable for a number of applications.

An alternative method is to use asymmetric bistable composites to induce large amplitude oscillations [5], exploiting the rich nonlinear dynamics of such a structure [6]. The inherent structural bistability means an asymmetric laminate system can be designed to occupy a smaller space and is potentially more convenient and portable. Arrieta et al. [5] presented an experimental study of a 200 $\times$ 200mm $[0_2/90_2]_\mathrm{T}$ laminate with four piezoelectric layers attached to the top surface. Results demonstrated high levels of power extraction over a wide range of frequencies when compared to resonant systems.

Given the complex nature of existing modelling techniques, optimisation of bistable energy harvesters is not presented in existing literature. The modelling formulation presented in Chapter 4 is ideally suited to this problem, enabling the wide scope for tailoring of the design to be exploited. In this chapter a problem formulation is proposed based on this analytical model to optimise the electrical energy output of a bistable piezoelectric laminate, considering the alternating stress excitation due to actuation between two static states.

9.2 Optimisation Problem Formulation

In this section the optimisation problem formulation for maximum piezoelectric energy harvesting capability is introduced. The problem is defined as follows:

Maximise:	Piezoelectrically induced electrical energy, Section 9.2.3.
Subject to:	The laminate must be bistable, Section 9.2.5.
	Piezoelectric strain must be below a maximum value, Section 9.2.5.
	The laminate must meet the design rules, Section 9.2.1.
Variables:	Ply and piezoelectric layer orientations, θ and θ_p respectively.
	Single ply thickness, t.
	Aspect ratio of the laminate, L_x/L_y.
	Piezoelectric surface area, % of total area.

The problem is solved using MATLAB's sequential quadratic programming function, `fmincon`. In order to find all optimum solutions multiple starting points are used positioned randomly throughout the design space.

9.2.1 Laminate Structure

The laminate configuration considered for this study follows the same basic set of design rules as outlined in Section 8.1 and illustrated in Fig. 8.1. However, two extensions to this modelling formulation are introduced. The first of these is to allow variable aspect ratio for the laminate using the method discussed in Section 9.2.4. Figure 9.1 shows two $[0/90]_T$ laminates with aspect ratios of 1 (a) and 5 (b). For an aspect ratio of 5 it can be seen that one cylindrical shape has significantly larger displacements than the opposite cylindrical shape. The potential trade-off between the magnitudes of electrical energy produced in each state will be investigated later in this chapter.

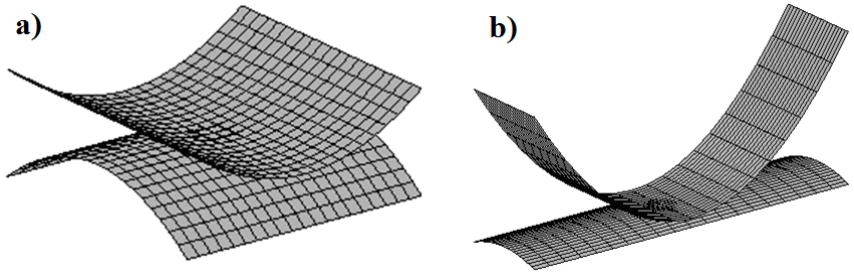

Figure 9.1: Two stable states of a $[0/90]_T$ laminate with aspect ratio of a) 1 and b) 5.

The second extension is to allow variation in the configuration of the piezoelectric layers. All studies in this work so far have considered piezoelectric layers which cover the entire laminate surface. However, for the energy harvesting application this may not be the optimal solution. Firstly, the large size of the piezoelectric layer reduces the curvature of the laminate and can reduce the harvestable energy. Secondly, with vibration-based actuation in mind there is a concern that the natural oscillations may be suppressed by the additional stiffness [5]. In this study the piezoelectric material is split into four sections, each positioned at the centre of one quarter of the laminate surface as considered by Arrieta et al. [5]. Unlike in [5] this pattern is mirrored on the opposite surface by piezoelectric layers oriented perpendicularly as defined by the design rules of Section 8.1. Figure 9.2 shows an example of this configuration for varying piezoelectric sizes.

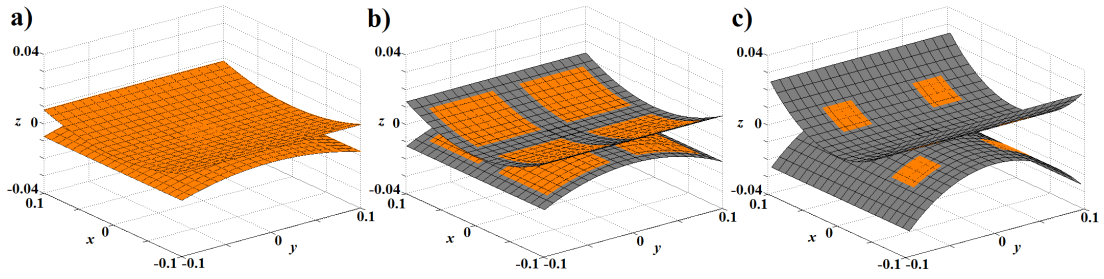

Figure 9.2: Stable laminate shapes for a square $[0/90]_T$ laminate with a) 100%, b) 50% and c) 10% piezoelectric surface area, piezoelectric layers shown in orange.

When the four layers occupy the entire laminate surface, Fig. 9.2a, the configuration is equivalent to a single layer. As the layer sizes are reduced, Figs. 9.2b (50% coverage) and 9.2c (10% coverage), the curvature of the laminate increases. This trade-off between the available curvature (proportional to piezoelectric strain) and the useful piezoelectric area is one of the key points investigated in this study.

It is noted that variation in piezoelectric layer size does highlight a limitation of the analytical model. Given the form of the assumed out-of-plane displacement (Eq. 4.1) localised deformation caused by the change in stiffness at the bounds of the piezoelectric material is not captured by the model. Rather a continuous reduction in the overall curvature due to the addition of the extra layers is predicted. This point has been demonstrated experimentally and discussed in Section 7.2.3. However, the simplification is not anticipated to affect the pattern of results for this optimisation study.

9.2.2 Actuation Configuration

The laminate is held at all four corners (zero z-displacement) and a mechanical actuator is attached to the centre point of the laminate surface such that displacement applied in the z-direction (out-of-plane) induces a state-change, simulating the ambient mechanical motion. This arrangement is illustrated in Fig. 9.3.

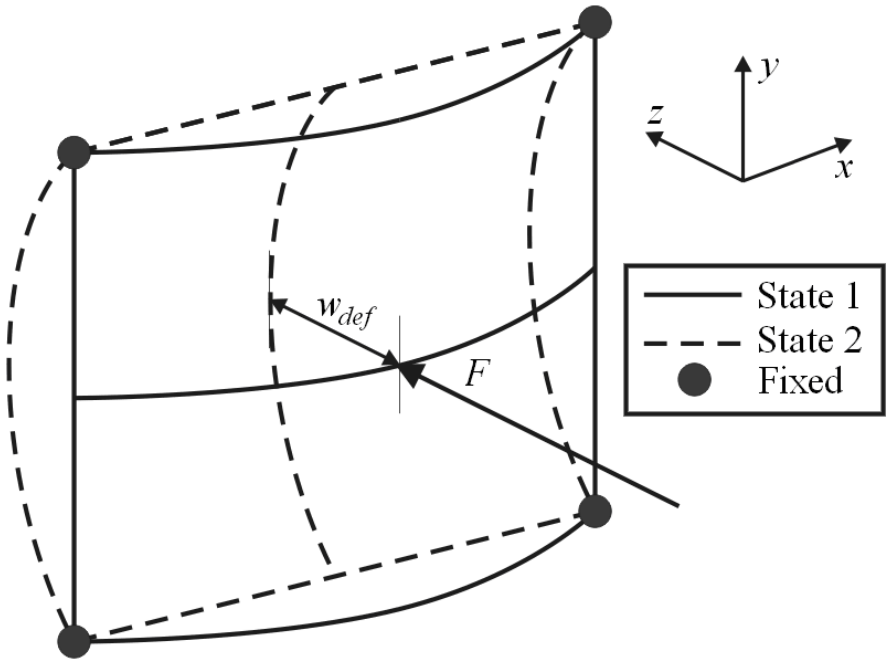

Figure 9.3: Actuation arrangement for a rectangular cross-ply laminate by a force F.

This configuration can be modelled in much the same way as the method outlined in Section 7.1. A force $F/4$ is applied at each corner while the geometric centre is held and displacements are defined with reference to the centre. This simple extension to the modelling can be applied to laminates of arbitrary layup to predict the force required for actuation. However, for off-axis ply orientations the experimental arrangement would need to be modified. The configuration in Fig. 9.3 requires all four corners of the laminate to experience the same displacement, i.e. $[0/90]_{\mathrm{T}}$ laminates. For arbitrary stacking sequences it may be preferable to hold the laminate at two opposite corners.

It is noted that the force required for actuation is not considered to be a constraint in this formulation. The potential influence of including force constraints is discussed in Section 9.3.1.

9.2.3 Objective Function

The objective of this study is to maximise the electrical energy generated by a bistable piezoelectric composite laminate. At off-resonance frequencies a piezoelectric layer can be assumed to behave like a parallel plate capacitor. Therefore the problem is modelled based on the static states of the system. The objective function is thus the electrical energy U induced in the piezoelectric material under the alternating stress excitation due to transition between two stable states [82],

$$U = \frac{1}{2}CV^2 \tag{9.1}$$

where C is the capacitance and V is the open circuit output voltage, as defined by the following equations,

$$C = \frac{Q}{V} = \frac{d_{ij}\sigma A}{V} \tag{9.2}$$

$$V = Et_p = -g_{ij}\sigma t_p \tag{9.3}$$

where d_{ij} is the effective piezoelectric strain constant (charge Q per unit force), σ is the stress, g_{ij} is the effective piezoelectric voltage constant (electric field E per unit stress), A is the surface area of the layer, and t_p is the thickness of the layer. Substituting Eqs. 9.2 and 9.3 into Eq. 9.1 gives

$$U = \frac{1}{2}(d_{ij}g_{ij})\sigma^2(At_p) \tag{9.4}$$

where the terms have been split into the fixed properties of the piezoelectric material (d_{ij} and g_{ij}), the stress in the material which is a function of the laminate curvatures, and the material geometry (A and t_p). The piezoelectric material, poled in the longitudinal direction in this work, is strained in both the longitudinal direction (referred

to as the 33 direction) and the transverse direction (31 direction) due to the anticlastic nature of the curvatures. The contributions of both components in both stable states are therefore considered, each with the associated 33 and 31 material properties as illustrated in Fig. 9.4.

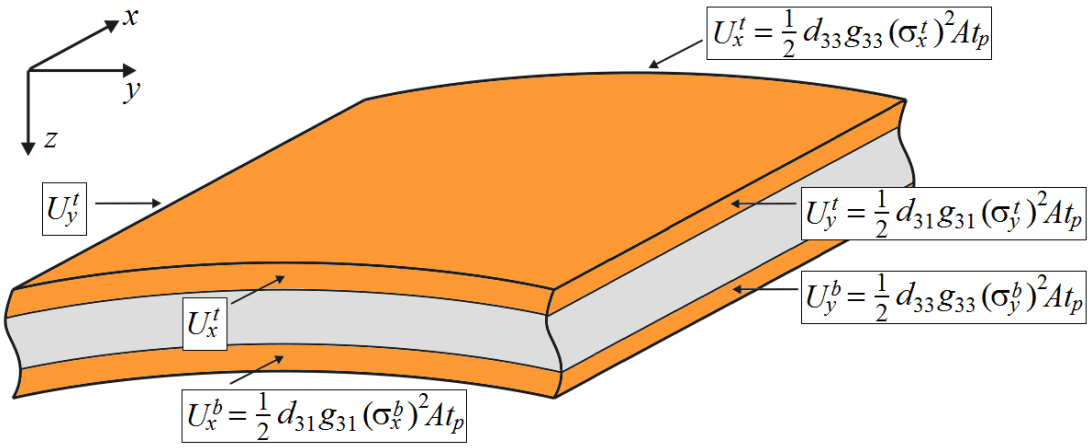

Figure 9.4: Longitudinal and transverse components of the total electrical energy U. Note: subscript denotes the associated direction, superscript denotes the top (t) and bottom (b) piezoelectric layer.

When attached to the surface of a curved laminate the stress in the piezoelectric material varies across the volume as a function of the strains induced by the mismatched thermal properties. The electrical energy is therefore expressed in the following integral form for piezoelectric layers positioned at 0° (top surface) and 90° (bottom surface),

$$U = 4 \sum_{m=1}^{2} \left[\frac{1}{2} \int_{v_t} \left(d_{33} g_{33} \sigma_x^2 + d_{31} g_{31} \sigma_y^2 \right) \mathrm{d}v_t + \frac{1}{2} \int_{v_b} \left(d_{33} g_{33} \sigma_y^2 + d_{31} g_{31} \sigma_x^2 \right) \mathrm{d}v_b \right] \quad (9.5)$$

where the factor 4 accounts for all piezoelectric layers on one surface, m defines the associated stable state, v_t and v_b are the volumes of two layers on the top and bottom laminate surfaces and the stresses in the x- and y-directions are defined by the following equations,

$$\begin{aligned} \sigma_x &= \bar{Q}_{11} \epsilon_x + \bar{Q}_{12} \epsilon_y + \bar{Q}_{16} \epsilon_{xy} \\ \sigma_y &= \bar{Q}_{12} \epsilon_x + \bar{Q}_{22} \epsilon_y + \bar{Q}_{26} \epsilon_{xy} \end{aligned} \quad (9.6)$$

where the $\bar{Q}$'s are transformed stiffness terms dependent on the material orientations and ϵ's are the in-plane strains. Equation 9.5 is used to define the objective function which is to be maximised. The material properties d_{ij} and g_{ij} are considered fixed in this chapter as their optimisation has been considered by Priya [82]. A is considered continuously variable while t_p is considered fixed for practical reasons.

9.2.4 Modelling Extensions

The modelling formulation outlined in Chapter 4 and Section 8.1.1 has two major limitations for the problem formulation presented in this chapter. Firstly, the design is limited to square laminates, and secondly, the piezoelectric layer configuration is limited to a single layer on each surface of the same dimensions as the laminate. This section discusses the methodology to overcome these limitations.

The primary issue with optimisation based on existing modelling techniques [24] is the need for a good initial guess of each laminate shape to capture the multiple solutions at each design iteration. The exact solution for a square laminate of cross-symmetric layup derived in Eq. B.38 provides a close initial guess for a rectangular laminate of otherwise identical composition. Similarly, a close approximation to the shapes of a laminate with piezoelectric material covering 80% of the surface area can be obtained by considering the exact solution for 100% coverage. Experience shows that the solution is reliably converged typically in 5 iterations. Figure 9.5 shows a flow chart of the process used to find the stable shapes of laminates defined in Section 9.2.1 and steps 1 to 6 below give details of the solution procedure.

1. $\boldsymbol{A}$, $\boldsymbol{B}$ and $\boldsymbol{D}$ matrix terms and thermal loads and moments are calculated for a square laminate using the modelling formulation outlined in Chapter 4 and Section 8.1.1. To model the smaller piezoelectric layers, these properties are calculated with and without the piezoelectric material for use in step 6.

2. The first cylindrical shape (defined as having large positive x-direction curvature) is calculated using Eq. B.38.

3. The bistability condition defined in Section 6.2.2 is used to check the solution.

4. The second cylindrical shape can be found using only the first cylindrical shape as shown in Section 4.3.4.

5. The two solutions for the square laminate provide very close initial guesses for a laminate with a different aspect ratio. An iterative method is used to solve Eq. 4.12 for the rectangular laminate. Variation in the aspect ratio will affect the location of the bifurcation point so a second check on the bistability condition is performed.

6. The size and number of the piezoelectric layers can be varied using the method outlined in Section 7.2.1, where the bounds on the integral of Eq. 7.15 are changed for each individual piezoelectric area. The properties calculated in step 1 above are used for each bounded area. Including the contributions of all piezoelectric layers Eq. 4.12 can then be solved iteratively using the rectangular shapes as a close initial guess. As stiffness is being removed from the structure by reducing the size of the piezoelectric layers bistability does not need to be checked again.

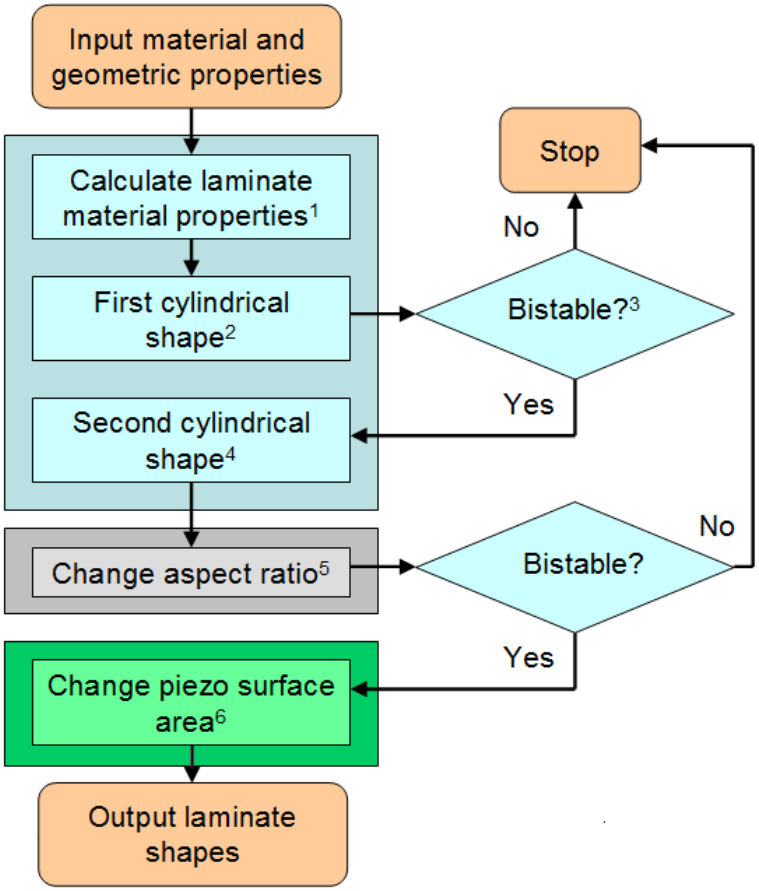

Figure 9.5: Work flow for calculating the stable shapes of laminates for an energy harvesting configuration.

9.2.5 Design Constraints

The constraint defined in Section 6.2.2 is used in this problem formulation to ensure a bistable solution.

$$\text{Bistability constraint: } a + b > X_s \tag{9.7}$$

The factor X_s has been introduced to move the solution away from the bifurcation point. This is necessary due to the introduction of variable aspect ratio in this problem. Saddle shape solutions close to the bifurcation point exhibit a small variation from the relationship $a + b = 0$ with larger curvature in one direction than the other. This variation decreases as the geometry tends away from the bifurcation point [59]. Variation is observed to be small and a factor of around 0.1 is suitable to ensure that feasible solutions are always bistable.

The variation in the piezoelectric configuration does not not affect the bistability condition as the individual layers are positioned symmetrically about both the x and y axis.

In this energy harvesting study zero voltage is applied to the piezoelectric material with the electrical energy being removed as it is generated. The limiting factor is therefore dependent on the fracture strain of the material. A representative value of 2000μstrain is taken from [44].

9.3 Numerical Results

The results of two example design problems using the energy harvesting optimisation formulation are presented in this section. The stacking sequence of the laminate is limited to a two-ply layup of the family $[\theta/\theta + 90]_{\mathrm{T}}$, with variable ply thickness used to model additional layers. In each example the fibre orientation of the piezoelectric material is limited to 0° and 90° by practical manufacturing constraints.

Based on the results of these optimisation problems a series of design parameter studies are then presented to illustrate the pattern of results around the optimum solutions. The dependence of the solutions on the ply thickness, stacking sequence, aspect ratio and overall laminate geometry are illustrated, including discussion of the presence of a local solution.

All examples presented in this section use M21/T800 prepreg material properties (Table 5.1) and M8557-P1 piezoelectric properties (Table 7.1).

9.3.1 Optimisation Results

The first problem is defined as follows where an additional constraint to fix the laminate surface area is added to allow direct comparison between optimum solutions:

Maximise:	Electrical energy generated in two sets of four piezoelectric layers.
Subject to:	The laminate must be bistable, $a + b > 0.1$.
	Piezoelectric strain must be below 2000μstrain.
	The laminate must meet the design rules of Section 9.2.1.
	Fixed laminate surface area, $L_x \times L_y = 0.04\mathrm{m}^2$.
Variables:	Ply orientation θ for a $[0^{\mathrm{P}}/\theta/\theta + 90/90^{\mathrm{P}}]_{\mathrm{T}}$ laminate.
	Single ply thickness, $0.125 < t < 0.25$mm.
	Aspect ratio of the laminate, $1 < L_x/L_y < 5$.
	Piezoelectric surface area, $0 <$ % of total area < 100.

Bounds on the ply thickness are chosen based on typical single ply values. In order to capture all optima 20 random start points are considered in the SQP routine. Table 9.1 details the two solutions found for this problem. One represents a local solution with stacking sequence $[0^{\mathrm{P}}/90/0/90^{\mathrm{P}}]_{\mathrm{T}}$ and objective function value 11.45mJ, and the other is the global optimum with stacking sequence $[0^{\mathrm{P}}/0/90/90^{\mathrm{P}}]_{\mathrm{T}}$ and objective function value 17.87mJ.

Table 9.1: Optimum solutions with t bounded from 0.125mm to 0.25mm.

	Global Optimum	Local Optimum
Stacking sequence, $[0^{\mathrm{P}}/\theta/\theta+90/90^{\mathrm{P}}]_{\mathrm{T}}$	$[0^{\mathrm{P}}/0/90/90^{\mathrm{P}}]_{\mathrm{T}}$	$[0^{\mathrm{P}}/90/0/90^{\mathrm{P}}]_{\mathrm{T}}$
Single ply thickness, t (mm)	0.25	0.25
Piezoelectric area, %	32.07	19.45
Aspect ratio, L_x/L_y	1	1
Maximum piezoelectric strain (μstrain)	1201	1170
Electrical energy, U (mJ)	17.87	11.45
Actuation force, F (N)	2.40	2.33

The bistability and maximum strain constraints are inactive for this problem, with maximum predicted strains of 1170 and 1201μstrain for the local and global solutions respectively. Both solutions have a square aspect ratio and are on the upper bound of ply thickness, 0.25mm. This suggests improvement may be found by introducing more plies. This is not an intuitively obvious result as the curvatures will be suppressed by the additional stiffness. Interestingly, a different optimum piezoelectric area is observed for each solution suggesting a balance between useful piezoelectric area and the reduced curvatures.

A second set of results is now presented for a modified problem. Based on the results of the first problem the bounds on the ply thickness are removed. The limit on the total thickness of the laminate is therefore bounded only by the bistability constraint. The problem is otherwise unchanged and results are detailed in Table 9.2.

Table 9.2: Optimum solutions with unconstrained t.

	Global Optimum	Local Optimum
Stacking sequence, $[0^{\mathrm{P}}/\theta/\theta+90/90^{\mathrm{P}}]_{\mathrm{T}}$	$[0^{\mathrm{P}}/0/90/90^{\mathrm{P}}]_{\mathrm{T}}$	$[0^{\mathrm{P}}/90/0/90^{\mathrm{P}}]_{\mathrm{T}}$
Single ply thickness, t (mm)	0.626	0.619
Piezoelectric area, %	72.43	42.40
Aspect ratio, L_x/L_y	1	1
Maximum piezoelectric strain (μstrain)	1097	1113
Electrical energy, U (mJ)	33.74	20.39
Actuation force, F (N)	3.41	3.39

Two solutions are again found, but with significantly higher electrical energy than the constrained example of 33.74 and 20.39mJ for the global and local solutions respectively. These have the same stacking sequences, $[0^{\mathrm{P}}/0/90/90^{\mathrm{P}}]_{\mathrm{T}}$ and $[0^{\mathrm{P}}/90/0/90^{\mathrm{P}}]_{\mathrm{T}}$, as the previous example but the geometry has changed. The unconstrained single ply thickness is now found to be 0.619mm for the local solution and 0.626mm for the global solution. Conveniently this global optimum is almost exactly 5 plies of 0.125mm meaning the solution could be redefined as $[0^{\mathrm{P}}/0_5/90_5/90^{\mathrm{P}}]_{\mathrm{T}}$. Interestingly the bistability constraint is again inactive. The optimum thickness is therefore not on any boundary, a property which will be investigated further in the following sections. The maximum strain constraint is also inactive and a square aspect ratio is again found to be optimal.

Actuation Force

For both optima in Table 9.2 the actuation forces are determined analytically as outlined in Section 7.1. Little variation is observed between the global and local solutions, 3.41 and 3.39N respectively, as the compositions are similar in both layup and overall thickness. While a limit on the force has not been imposed as a constraint in this work this property represents an important consideration. Where actuation relies on ambient vibration, larger or stiffer designs may suppress modes of vibration, thus limiting the practical application. It also important to note that this highlights the significance of accurate estimation of the actuation force. As discussed in Section 7.2.2, the constant curvature assumption of the analytical model has the effect of overpredicting the stiffness of the laminate. Therefore, the predicted actuation forces represent an overestimate. A close examination reveals that the optimum solutions are in fact, highly sensitive to the allowable actuation force, i.e. if the allowable force is less than 3.39N this will change the optimum ply thickness and piezoelectric area. Intuitively, to reduce the required force the stiffness of the overall structure must be reduced. This can be achieved through variation in layup or through reduction of the total thickness. These points are investigated in more depth in the following section.

9.3.2 Design Parameter Studies

In this section the results of the optimisation problem are investigated further in a series of design parameter studies. The aim of these studies is to gain a better understanding of the complex interactions of the physical constraints and requirements, and to illustrate the pattern of results around the optimum solutions.

Ply Thickness

The first study considers the effect of ply thickness on the problem. Figure 9.6 shows the objective function values for differing number of plies (1 to 6) for the full range of piezoelectric areas. All results correspond to $[0^{\mathrm{P}}/0_n/90_n/90^{\mathrm{P}}]_{\mathrm{T}}$ laminates of 0.2m square edge length. For each different number of plies the optimum solution with respect to piezoelectric area is highlighted by points A to F, detailed in Table 9.3. It is noted that point E approximately corresponds to the unconstrained optimum found in the previous section.

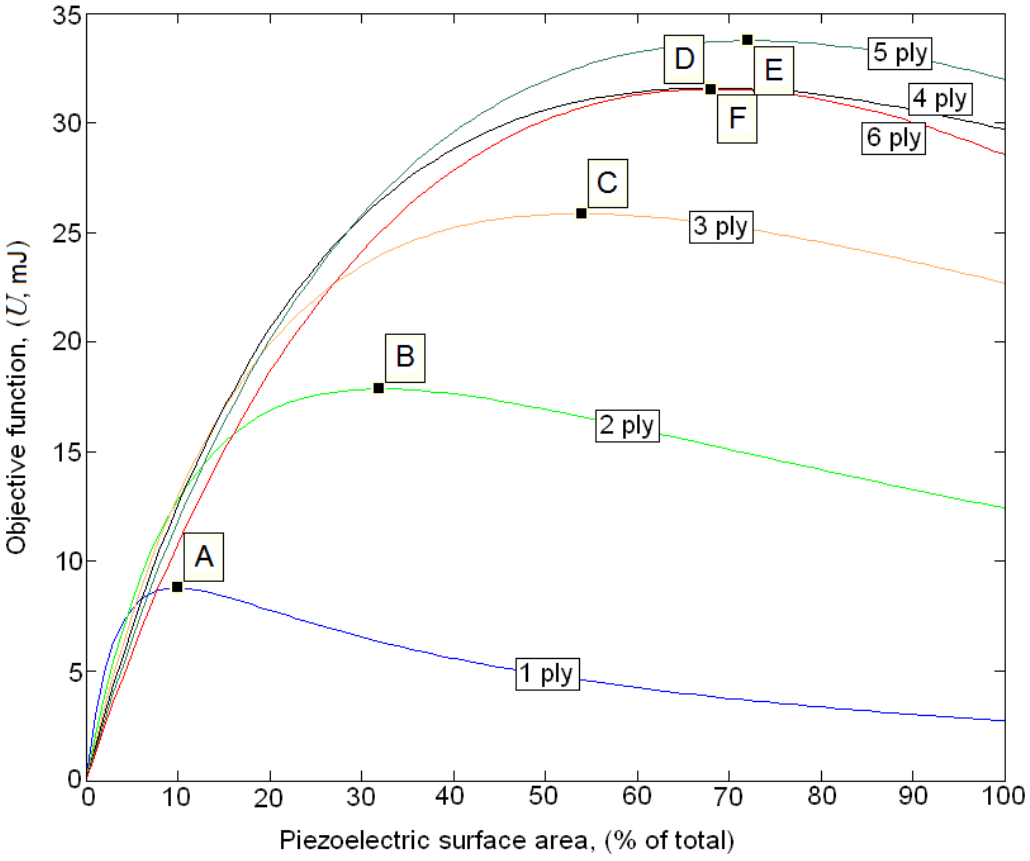

Figure 9.6: Variation in electrical energy with number of 0.125mm plies (shown on each line) and piezoelectric surface area. Points A to F are detailed in Table 9.3.

Table 9.3: Optimum solutions for varying number of plies for $[0^{\mathrm{P}}/0_n/90_n/90^{\mathrm{P}}]_{\mathrm{T}}$.

	A	B	C	D	E	F
No. plies, ($t = 0.125$mm)	1	2	3	4	5	6
Piezoelectric area, (%)	9.84	32.07	53.72	67.90	72.43	68.24
Electrical energy, (U, mJ)	8.81	17.93	25.90	31.61	33.74	31.52

A consistent pattern of results is observed for ply numbers from 1 to 5. For zero piezoelectric area the electrical energy generated is of course zero. The electrical energy then

increases with additional piezoelectric area to an optimum value. This optimum area is larger for each additional number of plies up to 72.43% for 5 plies. However, beyond 5 plies this pattern changes with both the optimum area and the maximum electrical energy decreasing for thicker laminates. This is a result of approaching the bifurcation point (between 6 and 7 plies depending on the piezoelectric surface area), resulting in decreasing curvature until the bistable behaviour is lost. This pattern confirms the finding that the bistability constraint is inactive at the global optimum.

With reference to the required actuation force, if a lower force limit was imposed as a constraint the total thickness would need to be reduced. From Fig. 9.6 it is clear that any reduction in thickness will compromise the optimum solution.

Laminate Stacking Sequence

The next study considers the change in objective function with laminate stacking sequence. Figure 9.7 shows the objective function values for differing values of θ for laminates of $[0^{\mathrm{P}}/\theta/\theta+90/90^{\mathrm{P}}]_{\mathrm{T}}$ layup, 0.2m square edge length and 0.25mm ply thickness. Different piezoelectric orientations are not considered as only the angles relative to ply orientations are of interest. The optimum solution for each different θ is highlighted by points A to G and detailed in Table 9.4.

The optimum solutions for each different θ form a parabolic shape which helps to understand the presence of the local solution to the optimisation problem. Point A confirms that the optimum value of θ is 0° and corresponds to the global solution to the constrained optimisation in the previous section. As θ increases the electrical energy output decreases, as does the optimum piezoelectric area, until reaching approximately 60°. Beyond this value the electrical energy begins to increase again until reaching the limit of 90°, point G. This corresponds to the local solution to the constrained optimisation. Negative values of θ are not considered as they represent rotations of designs already considered.

The reason for this parabolic shape can be understood by considering how the major curvature, and therefore the highest strains, are oriented relative to the piezoelectric effect. For the 0° solution the major curvature is aligned with the longitudinal piezoelectric effect (d_{33}) and electrical energy is maximum. For the 90° solution the major curvature is aligned with the transverse piezoelectric effect (d_{31}) and a lesser electrical energy is produced. Between these two values the major curvature is not aligned with either direction with the worst case being a θ value of around 60°, point E. Considering the optimisation method used to solve this problem, an initial guess of θ above 60° is likely to result in the optimisation settling on the local solution.

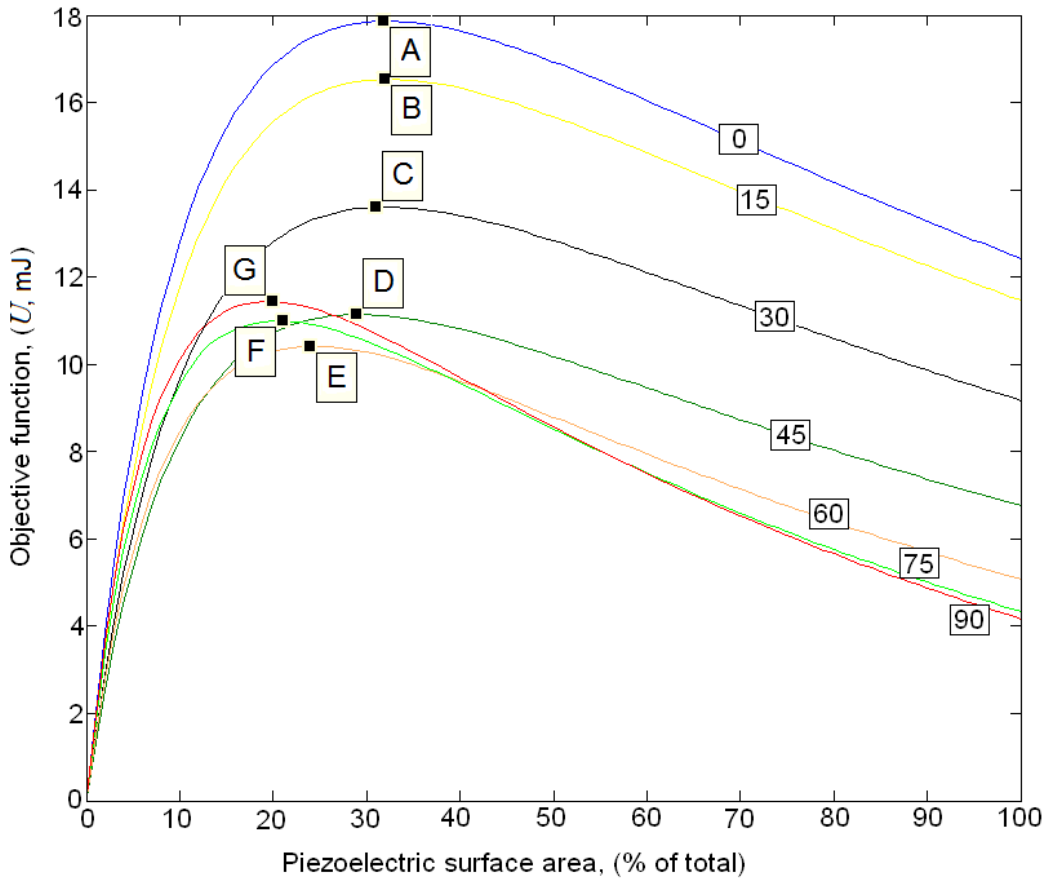

Figure 9.7: Variation in electrical energy with θ (shown on each line) and piezoelectric surface area for $[0^{\mathrm{P}}/\theta/\theta+90/90^{\mathrm{P}}]_{\mathrm{T}}$ laminates. Points A to G are detailed in Table 9.4.

Table 9.4: Optimum solutions for stacking sequences $[0^{\mathrm{P}}/\theta/\theta+90/90^{\mathrm{P}}]_{\mathrm{T}}$.

	A	B	C	D	E	F	G
θ, (°)	0	15	30	45	60	75	90
Piezoelectric area, (%)	32.07	32.28	31.96	29.08	24.17	20.59	19.45
Electrical energy, (U, mJ)	17.92	16.53	13.58	11.13	10.39	11.01	11.45

Laminate Aspect Ratio

The effect of the aspect ratio of the laminate on the objective function is now investigated. The optimum solutions in the previous section are all found to converge on a square aspect ratio of 1. Figure 9.8 shows how the objective function varies as the aspect ratio is increased from 1 to 5 for laminates of $[0^{\mathrm{P}}/0_2/90_2/90^{\mathrm{P}}]_{\mathrm{T}}$ layup, 0.04m^2 surface area and 0.25mm ply thickness. The optimum solutions for each different aspect ratio are highlighted by points A to E and are detailed in Table 9.5.

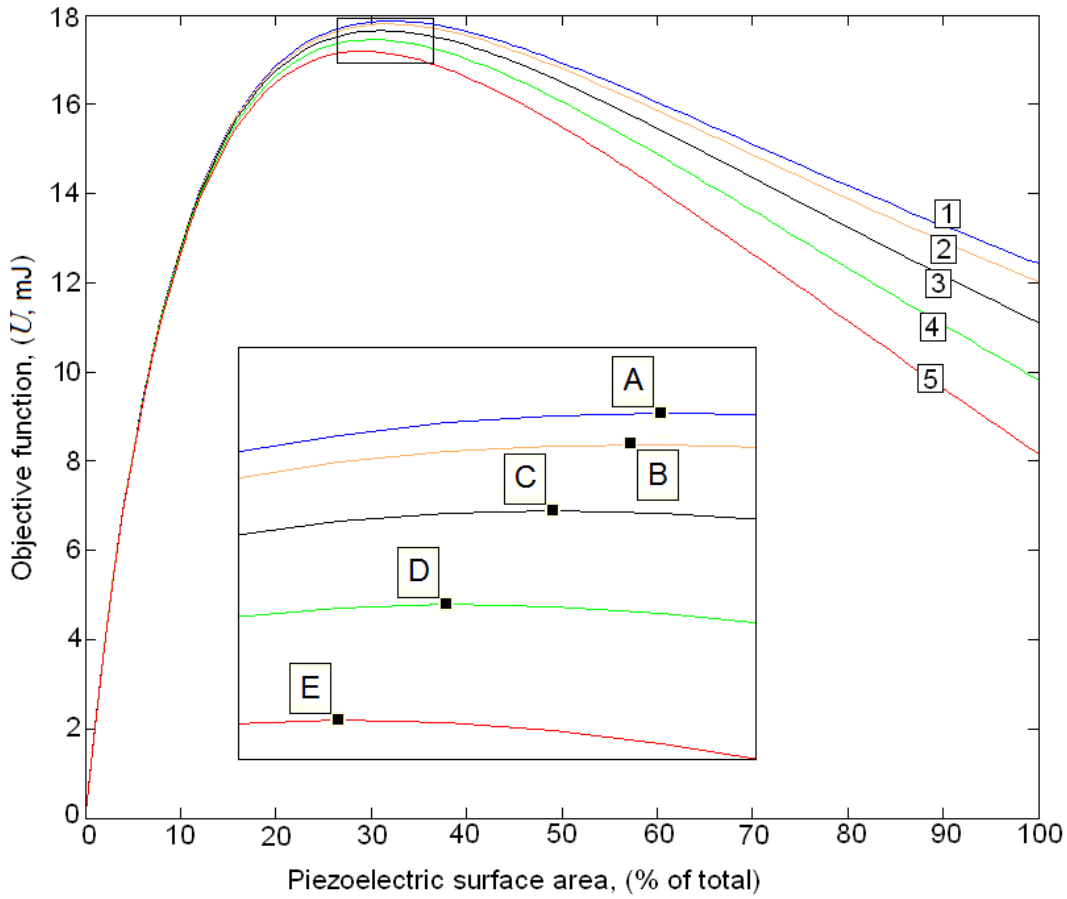

Figure 9.8: Variation in electrical energy with aspect ratio (shown on each line) and piezoelectric surface area. Points A to E are detailed in Table 9.5.

Table 9.5: Optimum solutions for varying aspect ratio for $[0^{\mathrm{P}}/0_2/90_2/90^{\mathrm{P}}]_{\mathrm{T}}$.

	A	B	C	D	E
Aspect ratio, L_x/L_y	1	2	3	4	5
Piezoelectric area, (%)	32.07	31.73	31.04	30.13	29.08
Electrical energy, (U, mJ)	17.87	17.79	17.65	17.40	17.18

The results demonstrate that while a square aspect ratio does represent the optimum solution the variation in electrical energy with aspect ratio is small. The objective function is found to vary from 17.18 to 17.87mJ in the range of aspect ratio from 1 to 5. These solutions are all found to have piezoelectric area of between 29.08 and 32.07%, far smaller variation than for the thickness or layup.

Jun and Hong [59] have previously investigated the influence of aspect ratio on the stable laminate shapes. They found that away from the bifurcation point the curvatures of square and rectangular laminates will tend towards the same limiting values. The stress in the piezoelectric σ is directly related to the curvatures of the laminate,

and the laminate surface area has remained unchanged for each example. It is therefore unsurprising that little variation is observed in the objective function. Furthermore, Jun and Hong [59] highlighted that the bifurcation point varies with aspect ratio and so some divergence in curvatures is observed in this region. This explains the divergence of results in Fig. 9.8 as the piezoelectric area, and thus the stiffness of the laminate, increases.

Pirrera et al. [75] further investigated this phenomenon by considering the bifurcation behaviour of laminates with varying aspect ratio. Any loss of symmetry in the laminate design will result in a limit point at the loss of bistability (see Fig. 3.2), referred to as broken pitchfork behaviour. When the percentage of 0° and 90° plies are different Hyer's model [24] correctly predicts this imperfect bifurcation behaviour. However, for non-square laminates the perfect bifurcation behaviour is incorrectly maintained. Pirrera et al. [75] modelled the variation of aspect ratio using various orders of polynomials to approximate the displacements. They confirmed that for the order of Hyer's model the bifurcation point is a pitchfork. However, for all higher order polynomials the correct broken bifurcation behaviour was captured. These results, confirmed by FEA, suggest that great care should be taken when considering variable aspect ratio close to the loss of bistability.

Laminate Surface Area

In this final study the effect of increasing the total laminate surface area is considered. This property was fixed for the optimisation examples and is anticipated to be a design constraint for any practical applications where the space occupied by the energy harvester is limited. Figure 9.9 shows how the objective function varies as the square edge length is increased from 0.12 to 0.35m for laminates of $[0^{\mathrm{P}}/0/90/90^{\mathrm{P}}]_{\mathrm{T}}$ layup and 0.25mm ply thickness. The optimum solutions for each different edge length are highlighted by points A to F and detailed in Table 9.6.

It is well known that as the edge length of the laminate relative to the thickness increases the major and minor curvatures converge to limiting values [53]. With reference to Eq. 9.6 the stress component of the objective function must also converge to a limiting value. The design then becomes scalable with laminate size. This is confirmed by the results of Fig. 9.9. For low edge lengths close to the bifurcation point the relationship between the laminate size and objective function is nonlinear as there is variation in the curvatures. As results tend towards larger laminates (0.25 to 0.35m) the relationship becomes approximately linear. The scalable nature of the problem is further confirmed by the results tending towards a consistent optimum piezoelectric area as the size is increased ($\sim$32.8%).

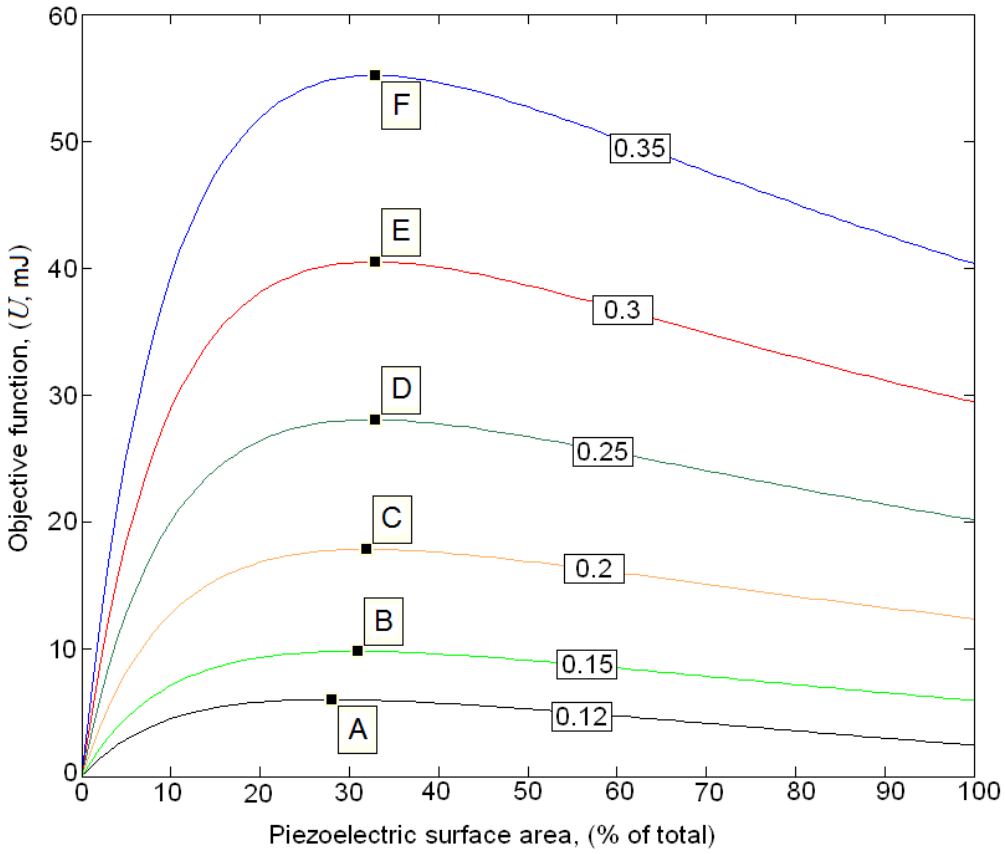

Figure 9.9: Variation in electrical energy with laminate edge length (value in m shown) and piezoelectric surface area. Points A to F are detailed in Table 9.6.

Table 9.6: Optimum solutions for varying edge length for $[0^{\mathrm{P}}/0_2/90_2/90^{\mathrm{P}}]_{\mathrm{T}}$.

	A	B	C	D	E	F
Edge length, L_x=L_y (m)	0.12	0.15	0.20	0.25	0.30	0.35
Piezoelectric area, (%)	27.87	30.50	32.07	32.54	32.71	32.78
Electrical energy, (U, mJ)	6.02	9.83	17.87	28.13	40.52	55.18

9.4 Concluding Remarks

In this chapter many of the modelling and optimisation techniques developed in this work have been combined to investigate optimisation of the design of a developing technology. This study has considered optimisation of a piezoelectric bistable laminate as a nonlinear device for broadband energy harvesting, converting ambient mechanical motion into useful electrical energy. Due to the complex nature of existing modelling techniques optimisation of the design of such devices has not been considered in existing literature.

This study has been identified as an emerging application for bistable laminates. Combined with the complex mechanical-electrical coupling due to the application of piezoelectric layers this problem has been considered in experimental studies only, with the scope for tailoring the design identified but not explored. With the novel techniques developed in this work this problem has been approached.

Extensions to the design rules outlined in Chapter 4 have been achieved to model the more complex structure required for energy harvesting, including extension to variable aspect ratio and more varied piezoelectric configurations with multiple patches on each laminate surface. The existing analytical solution to the square cross-symmetric design has been used as an initial guess to the more complex structure, enabling solutions to be found in a fast and reliable manner.

The optimisation study presented in this chapter has investigated maximising the electrical energy output due to the alternating stress excitation induced by repeated mechanical actuation. Constraints have been imposed to ensure bistability and to limit the strain in the piezoelectric material to below failure strain. Through variation in laminate geometry, arbitrary stacking sequences and piezoelectric configurations, optimum solutions have been found which differ from those considered experimentally.

It is found that laminates with major curvatures aligned with the direct piezoelectric effect d_{33} represent a global optimum, but that a local optimum exists for laminates with a major curvature aligned with the d_{31} effect. The optimum ply thicknesses are found not to be on a constraint boundary, with thicker laminates being more optimal than high deflection designs. This pattern reverses as the geometry approaches the bifurcation point. Similarly, increased piezoelectric size with increased laminate thickness is found to be optimal, with the pattern reversing near the loss of bistability.

Although not imposed as a constraint the mechanical actuation forces for each optimal design have been determined analytically. Where actuation relies on ambient vibration stiffer designs may suppress modes of vibration, thus limiting practical application. More detailed parameter studies have demonstrated that if a force constraint was imposed it could compromise the optimal solutions. This is primarily due to the reduced thickness which would be required to meet a lower actuation force requirement.

It is concluded that there is large scope for improving the design of piezoelectric bistable laminates for energy harvesting applications. It is proposed that further experimental studies should consider the geometries determined in this chapter. Future analytical studies may look to include dynamics and a consideration of the vibrational modes.

Chapter 10

Conclusions and Future Work

10.1 Conclusions

Chapter 4 - Modelling of Bistable Laminate Shapes
Chapter 4 presents the derivation of explicit expressions defining the stable shapes of bistable laminates. This formulation provides fast and robust analysis of the shapes of laminates with off-axis cross-symmetric layup and differing ply thicknesses. This novel solution method is enabled by considering a simplified geometry, selected to encourage bistable behaviour. For more general cases such as rectangular profiles and laminates incorporating actuation the simplified modelling work provides a close approximation to the more complex case.

Chapter 5 - Experimental Shape Characterisation
Chapter 5 presents the results of an experimental study aimed at validating the model derived in the previous chapter, and to highlight areas of uncertainty. The experimental study used a three-dimensional motion analysis technique to map the surface profiles of a series of arbitrary layup laminates. These profiles were compared to modelling predictions. It was found that the overall shape of the laminates was accurately predicted by the model. However, some discrepancies were identified. Well-known edge effects were observed at the corners of the laminates with regions of localised deformation not captured by modelling. Additional errors due to manufacturing uncertainties, most notably a thin resin layer on one laminate surface, were identified. By modifying the modelling to include imperfections, improvements in the predicted shapes over the ideal case were achieved highlighting the importance of accurate characterisation of the laminate composition.

Based on the experimental study a sensitivity analysis was performed to identify the material and geometric properties which provide the highest level of uncertainty in the predicted shapes. The most significant material properties were found to be E_{22}, α_2 and to a lesser extent E_{11}, all of which can be characterised experimentally to a high degree of accuracy. More significantly the dependence on ambient temperature was quantified, highlighting the significant nature of the operating environment for bistable laminates.

Chapter 6 - Optimisation of Bistable Laminates

Chapter 6 presents an optimisation study to maximise the ratio of bending stiffnesses between a loading direction and an actuation direction, enabled by the modelling derived in Chapter 4. This study addressed the inherent flexibility in a bistable laminate structure. Through variation in ply orientations, non-uniform ply thicknesses and laminate edge length, optimum solutions were obtained constrained by bistability and minimum deflection constraints.

The problem was found to be multimodal with the number of local and global optima found to vary with the bounds on the design variables and the deflection constraint. Intuitive solutions for optimal directional stiffness properties were observed to have low deflections between states and generally found to be infeasible. Optimum solutions are therefore not obvious from the problem definition. The numerical studies show examples where the stiffness in the loading direction can be as high as five times that of the actuation direction. This demonstrates the feasibility of designing a bistable laminate with low stiffness in a direction of actuation and high stiffness in the direction of externally applied operating loads.

Chapter 7 - Analysis of Actuation Methods

Chapter 7 presents a series of experimental and analytical studies of a number of actuation methods which may be applicable to actuation of a bistable laminate. Combinations of mechanical force, MFCs and SMA wires were considered to assess the feasibility of each technology.

It was concluded that reversible actuation using two orthogonal MFC actuators is the most suitable method for bistable laminate actuation and the most applicable to the existing analytical model. This approach allows fine shape control of the laminate over a wide range of applied voltages and enables reversible actuation with quick response time. Incorporation of this technology was identified as a key step in enabling optimisation studies for the design of reversibly actuated bistable laminates.

Chapter 8 - Optimisation of Actuated Bistable Laminates

Extension to the existing modelling to include the effect of two orthogonal MFCs is outlined in Chapter 8. The 'layer-like' structure of MFCs allows a simple extension which maintains the closed-form manner of the unloaded model. When modelling laminate shapes with an applied voltage, the analytical model is found to provide a close initial guess for a numerical solver for efficient determination of actuation voltages.

The extended modelling has been applied to an optimisation study where the objective function maximises the bending stiffness of a laminate in a chosen loading direction, while an actuation constraint is imposed by considering the operating range of the piezoelectric layers. Additional constraints to ensure bistability and a minimum deflection are also included. Given the complex nature of the design space it is found that multiple starting points are required to capture all local optima in an SQP routine.

A secondary study has been presented to investigate the total voltage requirements for actuation. Through the combined use of the positive and negative applied voltages to the top and bottom piezoelectric layers it was found that a reduction in the total actuation voltage of up to 33.8% is achievable in some cases.

Chapter 9 - Optimisation for Piezoelectric Energy Harvesting

In Chapter 9 many of the modelling and optimisation techniques developed in this work were combined to investigate optimisation of the design of a developing technology. An optimisation study of piezoelectric bistable laminates has been considered for electrical energy harvesting from ambient mechanical vibrations. Due to the complex nature of existing modelling techniques optimisation of the design of such devices is a novel result.

Extension to the modelling to include variable aspect ratio and variation in the size of multiple MFCs has been presented and is found to maintain the robust and efficient characteristics of the simpler modelling in the earlier chapters. Optimum designs have been presented with variable laminate geometry, arbitrary stacking sequences and piezoelectric configurations. This formulation includes constraints to ensure bistability and to limit the strain in the piezoelectric material to below failure strain.

It was found that laminates with major curvatures aligned with the direct piezoelectric effect d_{33} represent a global optimum, but that a local optimum exists for laminates with a major curvature aligned with the d_{31} effect. The optimum ply thicknesses are found not to be on a constraint boundary, with thicker laminates being more optimal than high deflection designs. This pattern reverses as the geometry approaches the bifurcation point. Similarly, increased piezoelectric size with increased laminate thickness is found to be optimal, with the pattern reversing near the loss of bistability. These results represent a significant deviation from designs considered in existing literature.

10.2 Future Work

Investigation of Tristable Results

Vidoli and Maurini [103] recently presented the possibility of tristability for orthotropic shells with zero bending-extension coupling. In the short study presented in Appendix A asymmetric stacking sequences with zero bending-extension coupling have been identified for a minimum of six plies. Identification of uncoupled asymmetric stacking sequences which exhibit bistability could lead to a comparative study to investigate the possibility of tristable composite laminates. However, the presence of bistable solutions is not guaranteed within this data set. Assuming a bistable layup can be found within this data the dimensions of the laminate may be prohibitively large due to the relative thickness of a six-ply laminate.

Multi-Objective Optimisation Studies

The optimisation formulation considered in Chapter 8 was split into two distinct phases. Initially the directional stiffness properties of the laminate were optimised to provide resistance to external loads within the operating range of the MFCs. These optimum stiffness designs were then considered in a secondary study to optimise the combination of positive and negative voltages applied to MFCs on opposite surfaces. It is suggested that further improvements may be achievable in a multi-objective formulation which considers the combined voltage and stiffness requirements simultaneously. Furthermore, the full operating range of the piezoelectric material has been allowed here without consideration for the effects of high-field behaviour or degradation due to repeated high voltages. Any future multi-objective formulation should consider the optimum solutions with practical applications in mind, specifically the need to rectify a local power supply.

Experimental Studies

While the model used in this work is presented in an original formulation, the underlying equations have been extensively validated against both FEA results and experimental results. The work presented in Chapter 5 has further validated this formulation and advanced the understanding of the modelling limitations. However, future experimental studies should involve manufacture of the optimum designs for comparison with what may be considered intuitive solutions. In particular, experimental comparison with the optimum energy harvesting designs of Chapter 9 would add confidence to the finding of increased electrical energy output.

Dynamic Analysis

The work presented in this thesis has considered the behaviour of bistable laminates in static analysis only. This is ideal in the presented studies where the focus has been

on stiffness properties and the overall deformation between two states, with no concern for the behaviour during actuation. While the results have not been directly applied to practical morphing applications, in future studies where this is likely to be the case a dynamic understanding of the laminate behaviour is essential. For example, in aerospace applications the unstable transition between states could be a critical consideration.

Dynamic analysis of designs for electrical energy harvesting is another suggestion for future investigation. The formulation for optimum electrical energy generation presented in Chapter 9 was specifically formulated using static analysis without considering optimisation close to resonance in order to provide broadband energy harvesting. However, while this has been achieved, there is concern that the thicker designs found in this study may suppress modes of vibration which are intended to be captured.

Energy Harvesting

The energy harvesting studies presented in this work have served to highlight the wide scope for improving this emerging technology. Further development of this investigation is proposed to consider many additional aspects of the piezo-laminate design. By including dynamic analysis of the laminate the highly nonlinear coupled behaviour between electrical and mechanical components could be better exploited. At a mechanical level this is suggested to include consideration of the driving ambient forces, frequency of vibrations, and topological optimisation of the bistable laminate shape. At an electrical level the design of the MFC can be considered an optimisation study, with piezoelectric material and electrode spacing included as additional variables. Finally, operation of the harvesting device presents additional questions such as the optimum time to remove the electrical energy within each cycle, and time-dependent harvesting patterns.

Appendix A

Formulation for Zero Bending-Extension Coupling

In general when composite plies are stacked with orientations of arbitrary alignment the resulting laminate will be fully anisotropic, exhibiting coupled behaviour both in-plane and out-of-plane. However, many applications require uncoupled behaviour. Furthermore, some existing modelling approaches [94, 95, 103] for the static shapes of asymmetric laminates include assumptions of zero bending-extension coupling, requiring an understanding of laminates to which such assumptions are applicable. Typically, uncoupled behaviour is obtained by imposing symmetric constraints on the stacking sequence. In the case of bistable laminates this is not an option so asymmetric stacking sequences exhibiting uncoupled behaviour are sought.

The short study presented in this appendix aims to identify uncoupled asymmetric laminates of differing numbers of plies. The problem is restricted to searching for stacking sequences with zero bending-extension coupling i.e. the $\boldsymbol{B}$ matrix is null, for laminates with plies of uniform thickness. To satisfy this condition the following set of full expressions for the terms of the $\boldsymbol{B}$ matrix must be zero.

$$B_{11} = \frac{1}{2}\sum_{j=1}^{p}\left[Q_{11}m_j^4 + 2(Q_{12}+2Q_{66})n_j^2m_j^2 + Q_{22}n_j^4\right]\left(h_j^2 - h_{j-1}^2\right) \tag{A.1}$$

$$B_{22} = \frac{1}{2}\sum_{j=1}^{p}\left[Q_{11}n_j^4 + 2(Q_{12}+2Q_{66})n_j^2m_j^2 + Q_{22}m_j^4\right]\left(h_j^2 - h_{j-1}^2\right) \tag{A.2}$$

$$B_{12} = \frac{1}{2}\sum_{j=1}^{p}\left[(Q_{11}+Q_{22}-4Q_{66})n_j^2m_j^2 + Q_{12}(m_j^4+n_j^4)\right]\left(h_j^2 - h_{j-1}^2\right) \tag{A.3}$$

$$B_{66} = \frac{1}{2}\sum_{j=1}^{p}\left[(Q_{11}+Q_{22}-2Q_{12}-2Q_{66})n_j^2 m_j^2 + Q_{66}(m_j^4+n_j^4)\right]\left(h_j^2-h_{j-1}^2\right) \tag{A.4}$$

$$B_{16} = \frac{1}{2}\sum_{j=1}^{p}\left[(Q_{11}-Q_{12}-2Q_{66})n_j m_j^3 + (Q_{12}-Q_{22}+2Q_{66})n_j^3 m_j\right]\left(h_j^2-h_{j-1}^2\right) \tag{A.5}$$

$$B_{26} = \frac{1}{2}\sum_{j=1}^{p}\left[(Q_{11}-Q_{12}-2Q_{66})n_j^3 m_j + (Q_{12}-Q_{22}+2Q_{66})n_j m_j^3\right]\left(h_j^2-h_{j-1}^2\right) \tag{A.6}$$

where h_j is the distance from the laminate midplane to the top surface of the j-th ply, h_{j-1} is the distance from the laminate midplane to the bottom surface of the j-th ply, m and n are $\sin\theta$ and $\cos\theta$ of the ply orientation, Q's are stiffness matrix terms as defined by Eq. 4.16 and p is the total number of plies. For uniform ply thicknesses this problem can be greatly reduced by using lamination parameters. With reference to Eq. 4.26, the set of equations A.1 - A.6 are equal to zero if the following set of lamination parameters V_{1-4}^B are equal to zero.

$$\begin{aligned} V_1^B &= \int_{-H/2}^{H/2}\cos 2\theta z \mathrm{d}z = 0 \\ V_2^B &= \int_{-H/2}^{H/2}\cos 4\theta z \mathrm{d}z = 0 \\ V_3^B &= \int_{-H/2}^{H/2}\sin 2\theta z \mathrm{d}z = 0 \\ V_4^B &= \int_{-H/2}^{H/2}\sin 4\theta z \mathrm{d}z = 0 \end{aligned} \tag{A.7}$$

Despite this simplified form a general solution to this system cannot be found analytically. For the case of a two-ply stacking sequence the entire set of possible layups can be assessed and illustrated very easily. Figure A.1 shows a series of surface plots for each term of the $\boldsymbol{B}$ matrix where the axes are the two ply orientations θ_1 and θ_2. A blue region denotes a negative value, red denotes a positive value and green indicates a near zero value. Locations of exactly zero are highlighted by black lines.

Some interesting patterns emerge for this simple example. B_{11} and B_{22}, relating in-plane direct forces to plate curvatures and bending moments to in-plane direct strains, are zero for symmetric laminates $[\theta_1/\theta_1]_\mathrm{T}$ and angle-ply laminates $[\theta_1/-\theta_1]_\mathrm{T}$ only. B_{12} and B_{66}, equal to each other for this family of laminates (see Eq. 4.26), are zero for symmetric, angle-ply, and $[\theta_1/\pm\theta_1\pm 90]_\mathrm{T}$ laminates. B_{16} and B_{26}, relating in-plane direct forces to plate twisting and torque to in-plane direct strains, are zero for symmetric laminates and additional more complex relationships. However, as a null $\boldsymbol{B}$ matrix is sought only symmetric laminates will satisfy these conditions fully.

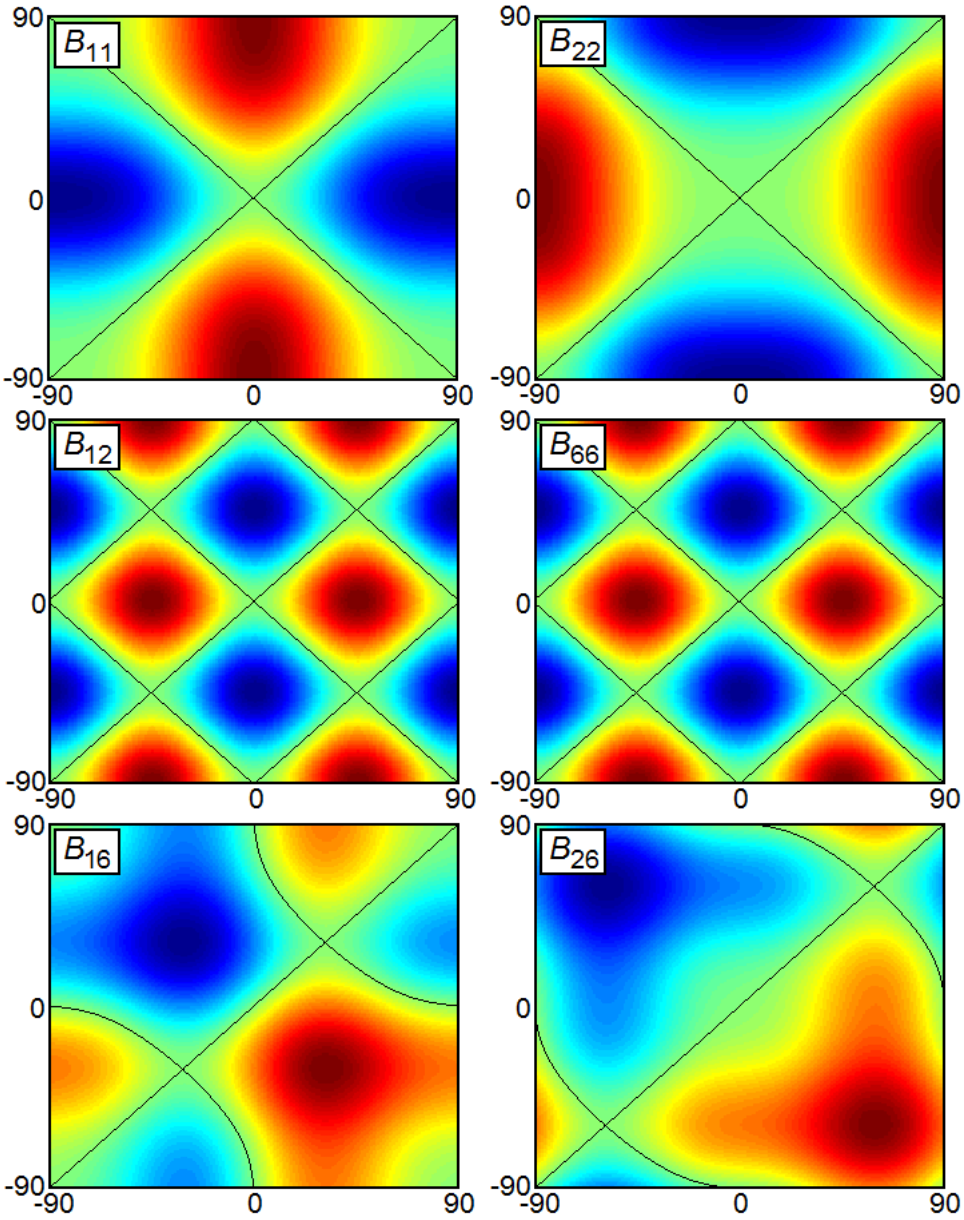

Figure A.1: $\boldsymbol{B}$ matrix values for all two-ply combinations. Blue shows a negative value, red a positive value, and black lines indicate a zero $\boldsymbol{B}$ matrix value.

For larger numbers of plies the exhaustive method is inefficient and illustration of the results becomes more difficult. As an analytical solution to Eq. A.7 is not possible a numerical search method (Matlab's built in function `fsolve` for solving a system of nonlinear equations) is used to obtain fully general stacking sequences which exhibit zero $\boldsymbol{B}$ matrix behaviour.

For numbers of plies from two to five only symmetric stacking sequences are found to satisfy $\boldsymbol{B} = 0$. However, for six plies or more there exist asymmetric stacking sequences which satisfy Eq. A.7. To demonstrate this a six-ply problem is outlined in more detail. Using 1000 initial guesses for the `fsolve` function 1000 distinct six-ply

stacking sequences are obtained. Many of these are symmetric as with the two to five ply laminates, but many asymmetric layups are also found. To show the distribution of these solutions in the full design space the first three ply angles (θ_1, θ_2, θ_3) for each solution are considered. Fig. A.2 shows how these three ply angles are distributed in the θ_1-θ_2 plane. The full set of solutions has been split into two separate plots for ease of illustration of the various different patterns which are observed. The full set of symmetric solutions which also satisfy Eq. A.7 are omitted.

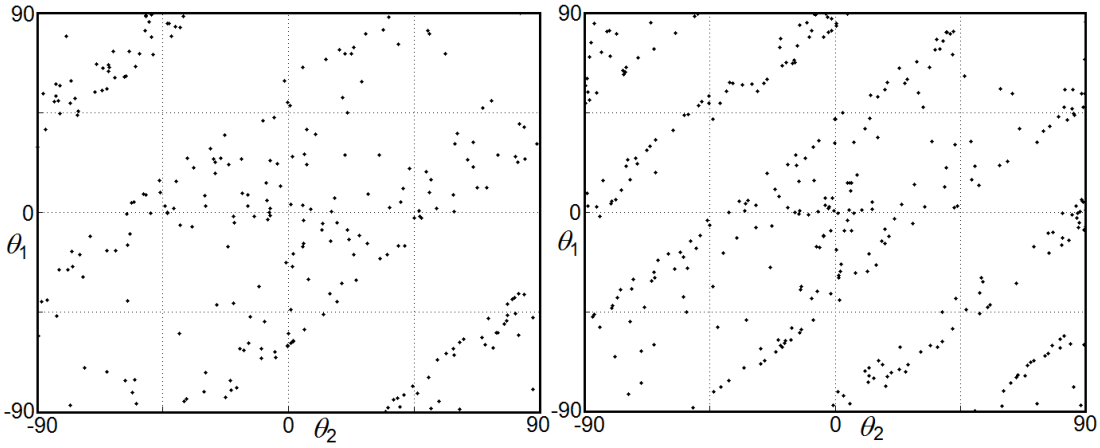

Figure A.2: Zero $\boldsymbol{B}$ matrix six-ply solutions, first three ply angles plotted in the θ_1-θ_2 plane. Solutions split into two plots to illustrate the different patterns of solutions.

Figure A.2 shows that zero $\boldsymbol{B}$ matrix laminates occur in discrete regions of the full design space. Within these discrete bands of data points there are clear areas of more concentrated solutions. Closer examination of this design space reveals that complex relationships exist within the data. Figure A.3 shows the same set of data rotated to a specific isometric view clearly highlighting highly nonlinear patterns.

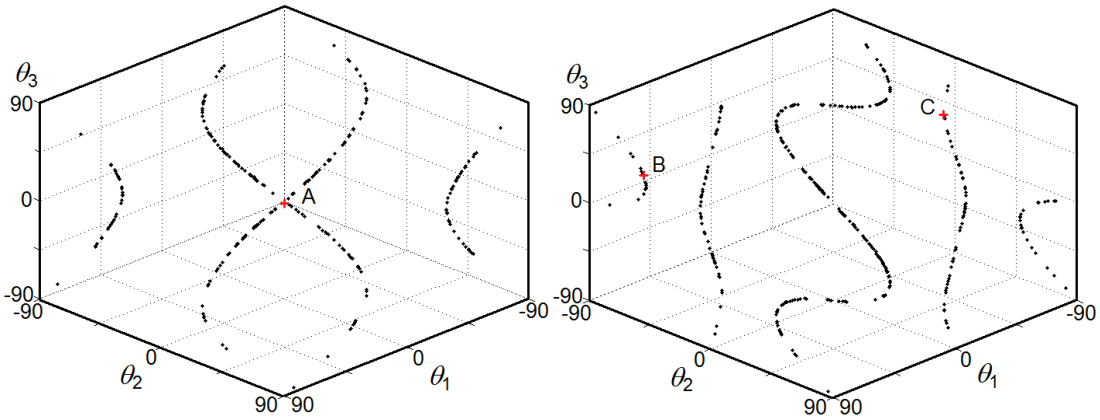

Figure A.3: Zero $\boldsymbol{B}$ matrix six-ply solutions, first three ply angles plotted in an isometric view. Points A-C discussed in the text.

The commonly considered asymmetric layup for bistable laminates is a simple on-axis cross-ply stacking sequence, $[0_n/90_n]_\mathrm{T}$. The point corresponding to 0_3 for the first three ply angles is highlighted as point A in Fig. A.3, and can be seen to be on one of the lines relating to zero $\boldsymbol{B}$ matrix values. However, when we examine the corresponding three angles for the bottom half of this laminate (θ_4, θ_5, θ_6) it is found that the solution is not cross-ply. Figure A.4 shows the corresponding data for every solution for θ_4, θ_5 and θ_6 with point A again highlighted. This solution is in fact symmetric $[0_6]_\mathrm{T}$, and is a point where the symmetric solution set, omitted here, intercepts with the asymmetric data. The same result is found for all general cross plies, $[\theta_n/\theta + 90_n]_\mathrm{T}$.

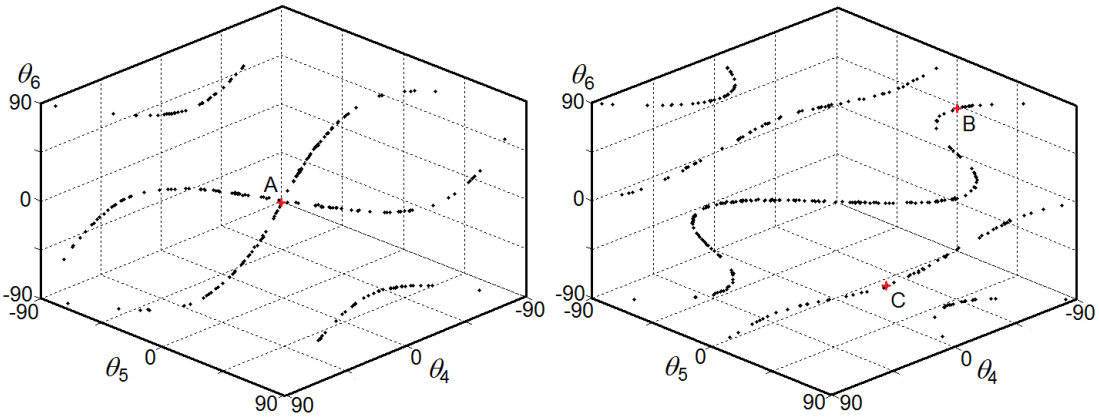

Figure A.4: Zero $\boldsymbol{B}$ matrix six-ply solutions, bottom three ply angles plotted in an isometric view. Points A-C discussed in the text.

However, there are clearly many asymmetric solutions to this problem, with numerous distinct patterns. Points B and C in Figs. A.3 - A.4, $[64.9/-74.8/20.2/-50.8/44.2/84.5]_\mathrm{T}$ and $[-64.5/17.8/56.6/-8.6/30.3/-67.4]_\mathrm{T}$ respectively, represent two examples of these many patterns. These representative solutions do not exhibit bistability due to the mix of ply angles through-thickness. A more thorough investigation would be required if specific patterns for bistability are to be identified. However, this simple study does highlight the very limited nature of the zero $\boldsymbol{B}$ matrix set, continued for higher numbers of plies. Modelling of the warped shapes of asymmetric laminates omitting $\boldsymbol{B}$ matrix terms therefore has rather limited application.

Vidoli and Maurini [103] recently presented the possibility of tristability for orthotropic shells with zero bending-extension coupling. Given the results shown in Fig. A.4, identification of uncoupled asymmetric stacking sequences which exhibit bistability could lead to a comparative study to investigate the possibility of tristable composite laminates.

Aside from considering bistability, future studies in this area may consider this simple numerical approach for more in-depth coupling analysis. For example fully orthotropic laminates with special orthotropy in the extensional matrix $\boldsymbol{A}$ and the flexural matrix

$\boldsymbol{D}$, i.e. $A_{16} = A_{26} = 0$ and $D_{16} = D_{26} = 0$, could be assessed by including four additional equations equal to zero,

$$A_{16} = \sum_{j=1}^{p} \left[(Q_{11} - Q_{12} - 2Q_{66}) n_j m_j^3 + (Q_{12} - Q_{22} + 2Q_{66}) n_j^3 m_j \right] (h_j - h_{j-1}) \tag{A.8}$$

$$A_{26} = \sum_{j=1}^{p} \left[(Q_{11} - Q_{12} - 2Q_{66}) n_j^3 m_j + (Q_{12} - Q_{22} + 2Q_{66}) n_j m_j^3 \right] (h_j - h_{j-1}) \tag{A.9}$$

$$D_{16} = \frac{1}{3} \sum_{j=1}^{p} \left[(Q_{11} - Q_{12} - 2Q_{66}) n_j m_j^3 + (Q_{12} - Q_{22} + 2Q_{66}) n_j^3 m_j \right] \left(h_j^3 - h_{j-1}^3 \right) \tag{A.10}$$

$$D_{26} = \frac{1}{3} \sum_{j=1}^{p} \left[(Q_{11} - Q_{12} - 2Q_{66}) n_j^3 m_j + (Q_{12} - Q_{22} + 2Q_{66}) n_j m_j^3 \right] \left(h_j^3 - h_{j-1}^3 \right) \tag{A.11}$$

With reference to Eq. 4.26 this set of equations can again be reduced to considering four lamination parameters equal to zero (Eq. A.12) in addition to the lamination parameters of Eq. A.7. This study for fully general stacking sequences could form an interesting area for future work.

$$\begin{aligned} V_3^A &= \int_{-H/2}^{H/2} \sin 2\theta \mathrm{d}z = 0 \\ V_4^A &= \int_{-H/2}^{H/2} \sin 4\theta \mathrm{d}z = 0 \\ V_3^D &= \int_{-H/2}^{H/2} \sin 2\theta z^2 \mathrm{d}z = 0 \\ V_4^D &= \int_{-H/2}^{H/2} \sin 4\theta z^2 \mathrm{d}z = 0 \end{aligned} \tag{A.12}$$

Appendix B

Laminate Modelling Formulation

This appendix presents full derivations of important steps in the modelling work outlined in Chapter 4. Relevant sections in the main body are referenced.

B.1 Stiffness Invariants for Transformed Stiffness Terms

The transformed stiffness terms are redefined using multiple angle rules, resulting in the following forms in terms of the newly introduced stiffness invariants, U_i. See Eq. 4.19.

$$\begin{aligned}
\bar{Q}_{11} &= m^4 Q_{11} + n^4 Q_{22} + 2m^2 n^2 (Q_{12} + 2Q_{66}) \\
&= \frac{1}{8}(3 + 4\cos 2\theta + \cos 4\theta) Q_{11} + \frac{1}{8}(3 - 4\cos 2\theta + \cos 4\theta) Q_{22} \\
&\quad + \frac{1}{4}(1 - \cos 4\theta)(Q_{12} + 2Q_{66}) \\
&= \frac{1}{8}(3Q_{11} + 3Q_{22} + 2Q_{12} + 4Q_{66}) + \frac{1}{2}(Q_{11} - Q_{22}) \cos 2\theta \\
&\quad + \frac{1}{8}(Q_{11} + Q_{22} - 2Q_{12} - 4Q_{66}) \cos 4\theta \\
&= U_1 + U_2 \cos 2\theta + U_3 \cos 4\theta
\end{aligned} \tag{B.1}$$

$$\begin{aligned}
\bar{Q}_{22} &= n^4 Q_{11} + m^4 Q_{22} + 2m^2 n^2 (Q_{12} + 2Q_{66}) \\
&= \frac{1}{8}(3 - 4\cos 2\theta + \cos 4\theta) Q_{11} + \frac{1}{8}(3 + 4\cos 2\theta + \cos 4\theta) Q_{22} \\
&\quad + \frac{1}{4}(1 - \cos 4\theta)(Q_{12} + 2Q_{66}) \\
&= \frac{1}{8}(3Q_{11} + 3Q_{22} + 2Q_{12} + 4Q_{66}) - \frac{1}{2}(Q_{11} - Q_{22}) \cos 2\theta \\
&\quad + \frac{1}{8}(Q_{11} + Q_{22} - 2Q_{12} - 4Q_{66}) \cos 4\theta \\
&= U_1 - U_2 \cos 2\theta + U_3 \cos 4\theta
\end{aligned} \tag{B.2}$$

$$\begin{aligned}\bar{Q}_{12} &= m^2n^2(Q_{11}+Q_{22}-4Q_{66})+(m^4+n^4)Q_{12}\\ &= \frac{1}{8}(1-\cos 4\theta)(Q_{11}+Q_{22}-4Q_{66})+\frac{1}{8}(6+2\cos 4\theta)Q_{12}\\ &= \frac{1}{8}(Q_{11}+Q_{22}+6Q_{12}-4Q_{66})-\frac{1}{8}(Q_{11}+Q_{22}-2Q_{12}-4Q_{66})\cos 4\theta\\ &= U_4-U_3\cos 4\theta\end{aligned} \tag{B.3}$$

$$\begin{aligned}\bar{Q}_{66} &= n^2m^2(Q_{11}+Q_{22}-2Q_{12}-2Q_{66})+(m^4+n^4)Q_{66}\\ &= \frac{1}{8}(1-\cos 4\theta)(Q_{11}+Q_{22}-2Q_{12}-2Q_{66})+\frac{1}{8}(6+2\cos 4\theta)Q_{66}\\ &= \frac{1}{8}(Q_{11}+Q_{22}-2Q_{12}+4Q_{66})-\frac{1}{8}(Q_{11}+Q_{22}-2Q_{12}-4Q_{66})\cos 4\theta\\ &= U_5-U_3\cos 4\theta\end{aligned} \tag{B.4}$$

$$\begin{aligned}\bar{Q}_{16} &= nm^3(Q_{11}-Q_{12}-2Q_{66})+n^3m(Q_{12}-Q_{22}+2Q_{66})\\ &= \frac{1}{8}(2\sin 2\theta+\sin 4\theta)(Q_{11}-Q_{12}-2Q_{66})+\frac{1}{8}(2\sin 2\theta-\sin 4\theta)(Q_{12}-Q_{22}+2Q_{66})\\ &= \frac{1}{8}(2Q_{11}-2Q_{22})\sin 2\theta+\frac{1}{8}(Q_{11}+Q_{22}-2Q_{12}-4Q_{66})\sin 4\theta\\ &= \frac{1}{2}U_2\sin 2\theta+U_3\sin 4\theta\end{aligned} \tag{B.5}$$

$$\begin{aligned}\bar{Q}_{26} &= n^3m(Q_{11}-Q_{12}-2Q_{66})+nm^3(Q_{12}-Q_{22}+2Q_{66})\\ &= \frac{1}{8}(2\sin 2\theta-\sin 4\theta)(Q_{11}-Q_{12}-2Q_{66})+\frac{1}{8}(2\sin 2\theta+\sin 4\theta)(Q_{12}-Q_{22}+2Q_{66})\\ &= \frac{1}{8}(2Q_{11}-2Q_{22})\sin 2\theta-\frac{1}{8}(Q_{11}+Q_{22}-2Q_{12}-4Q_{66})\sin 4\theta\\ &= \frac{1}{2}U_2\sin 2\theta-U_3\sin 4\theta\end{aligned} \tag{B.6}$$

B.2 Simplified $\boldsymbol{A}$, $\boldsymbol{B}$, and $\boldsymbol{D}$ Matrix Terms

Introduction of the simplified form of the transformed stiffness terms of Appendix B.1 into the $\boldsymbol{A}$, $\boldsymbol{B}$ and $\boldsymbol{D}$ matrices results in the following integral evaluations. See Eq. 4.24.

$$\begin{aligned}[A_{11},B_{11},D_{11}] &= \int_{-H/2}^{H/2}\bar{Q}_{11}\left[1,z,z^2\right]\mathrm{d}z\\ &= \int_{-H/2}^{H/2}(U_1+U_2\cos 2\theta+U_3\cos 4\theta)\left[1,z,z^2\right]\mathrm{d}z\\ &= U_1\int_{-H/2}^{H/2}\left[1,z,z^2\right]\mathrm{d}z+U_2\int_{-H/2}^{H/2}\cos 2\theta\left[1,z,z^2\right]\mathrm{d}z\\ &\quad+U_3\int_{-H/2}^{H/2}\cos 4\theta\left[1,z,z^2\right]\mathrm{d}z\end{aligned} \tag{B.7}$$

$$
\begin{aligned}
[A_{22}, B_{22}, D_{22}] &= \int_{-H/2}^{H/2} \bar{Q}_{22} \left[1, z, z^2\right] \mathrm{d}z \\
&= \int_{-H/2}^{H/2} (U_1 - U_2 \cos 2\theta + U_3 \cos 4\theta) \left[1, z, z^2\right] \mathrm{d}z \\
&= U_1 \int_{-H/2}^{H/2} \left[1, z, z^2\right] \mathrm{d}z - U_2 \int_{-H/2}^{H/2} \cos 2\theta \left[1, z, z^2\right] \mathrm{d}z \\
&\quad + U_3 \int_{-H/2}^{H/2} \cos 4\theta \left[1, z, z^2\right] \mathrm{d}z
\end{aligned} \tag{B.8}
$$

$$
\begin{aligned}
[A_{12}, B_{12}, D_{12}] &= \int_{-H/2}^{H/2} \bar{Q}_{12} \left[1, z, z^2\right] \mathrm{d}z \\
&= \int_{-H/2}^{H/2} (U_4 - U_3 \cos 4\theta) \left[1, z, z^2\right] \mathrm{d}z \\
&= U_4 \int_{-H/2}^{H/2} \left[1, z, z^2\right] \mathrm{d}z - U_3 \int_{-H/2}^{H/2} \cos 4\theta \left[1, z, z^2\right] \mathrm{d}z
\end{aligned} \tag{B.9}
$$

$$
\begin{aligned}
[A_{66}, B_{66}, D_{66}] &= \int_{-H/2}^{H/2} \bar{Q}_{66} \left[1, z, z^2\right] \mathrm{d}z \\
&= \int_{-H/2}^{H/2} (U_5 - U_3 \cos 4\theta) \left[1, z, z^2\right] \mathrm{d}z \\
&= U_5 \int_{-H/2}^{H/2} \left[1, z, z^2\right] \mathrm{d}z - U_3 \int_{-H/2}^{H/2} \cos 4\theta \left[1, z, z^2\right] \mathrm{d}z
\end{aligned} \tag{B.10}
$$

$$
\begin{aligned}
[A_{16}, B_{16}, D_{16}] &= \int_{-H/2}^{H/2} \bar{Q}_{16} \left[1, z, z^2\right] \mathrm{d}z \\
&= \int_{-H/2}^{H/2} (\frac{1}{2} U_2 \sin 2\theta + U_3 \sin 4\theta) \left[1, z, z^2\right] \mathrm{d}z \\
&= \frac{1}{2} U_2 \int_{-H/2}^{H/2} \sin 2\theta \left[1, z, z^2\right] \mathrm{d}z + U_3 \int_{-H/2}^{H/2} \sin 4\theta \left[1, z, z^2\right] \mathrm{d}z
\end{aligned} \tag{B.11}
$$

$$
\begin{aligned}
[A_{26}, B_{26}, D_{26}] &= \int_{-H/2}^{H/2} \bar{Q}_{26} \left[1, z, z^2\right] \mathrm{d}z \\
&= \int_{-H/2}^{H/2} (\frac{1}{2} U_2 \sin 2\theta - U_3 \sin 4\theta) \left[1, z, z^2\right] \mathrm{d}z \\
&= \frac{1}{2} U_2 \int_{-H/2}^{H/2} \sin 2\theta \left[1, z, z^2\right] \mathrm{d}z - U_3 \int_{-H/2}^{H/2} \sin 4\theta \left[1, z, z^2\right] \mathrm{d}z
\end{aligned} \tag{B.12}
$$

B.3 Lamination Parameters for a Two-ply Laminate

The lamination parameters for a simplified laminate geometry with two orthogonal plies of equal thickness are evaluated as follows. See Eq. 4.27.

$$V_1^A = \int_{-H/2}^{H/2} \cos 2\theta \mathrm{d}z = t\cos 2\theta_1 + t\cos 2(\theta_1 + 90) = 0 \tag{B.13}$$

$$V_2^A = \int_{-H/2}^{H/2} \cos 4\theta \mathrm{d}z = t\cos 4\theta_1 + t\cos 4(\theta_1 + 90) = 2t\cos 4\theta_1 \tag{B.14}$$

$$V_3^A = \int_{-H/2}^{H/2} \sin 2\theta \mathrm{d}z = t\sin 2\theta_1 + t\sin 2(\theta_1 + 90) = 0 \tag{B.15}$$

$$V_4^A = \int_{-H/2}^{H/2} \sin 4\theta \mathrm{d}z = t\sin 4\theta_1 + t\sin 4(\theta_1 + 90) = 2t\sin 4\theta_1 \tag{B.16}$$

$$V_1^B = \int_{-H/2}^{H/2} \cos 2\theta z \mathrm{d}z = -\frac{t^2}{2}\cos 2\theta_1 + \frac{t^2}{2}\cos 2(\theta_1 + 90) = -t^2\cos 2\theta_1 \tag{B.17}$$

$$V_2^B = \int_{-H/2}^{H/2} \cos 4\theta z \mathrm{d}z = -\frac{t^2}{2}\cos 4\theta_1 + \frac{t^2}{2}\cos 4(\theta_1 + 90) = 0 \tag{B.18}$$

$$V_3^B = \int_{-H/2}^{H/2} \sin 2\theta z \mathrm{d}z = -\frac{t^2}{2}\sin 2\theta_1 + \frac{t^2}{2}\sin 2(\theta_1 + 90) = -t^2\sin 2\theta_1 \tag{B.19}$$

$$V_4^B = \int_{-H/2}^{H/2} \sin 4\theta z \mathrm{d}z = -\frac{t^2}{2}\sin 4\theta_1 + \frac{t^2}{2}\sin 4(\theta_1 + 90) = 0 \tag{B.20}$$

$$V_1^D = \int_{-H/2}^{H/2} \cos 2\theta z^2 \mathrm{d}z = \frac{t^3}{3}\cos 2\theta_1 + \frac{t^3}{3}\cos 2(\theta_1 + 90) = 0 \tag{B.21}$$

$$V_2^D = \int_{-H/2}^{H/2} \cos 4\theta z^2 \mathrm{d}z = \frac{t^3}{3}\cos 4\theta_1 + \frac{t^3}{3}\cos 4(\theta_1 + 90) = \frac{2t^3}{3}\cos 4\theta_1 \tag{B.22}$$

$$V_3^D = \int_{-H/2}^{H/2} \sin 2\theta z^2 \mathrm{d}z = \frac{t^3}{3}\sin 2\theta_1 + \frac{t^3}{3}\sin 2(\theta_1 + 90) = 0 \tag{B.23}$$

$$V_4^D = \int_{-H/2}^{H/2} \sin 4\theta z^2 \mathrm{d}z = \frac{t^3}{3}\sin 4\theta_1 + \frac{t^3}{3}\sin 4(\theta_1 + 90) = \frac{2t^3}{3}\sin 4\theta_1 \tag{B.24}$$

B.4 Lamination Parameters for an n-ply Laminate

The lamination parameters for an extended laminate geometry with n pairs of orthogonal plies with unequal thickness are evaluated as follows. See Eq. 4.54.

$$\begin{aligned} V_2^A &= \int_{-H/2}^{H/2} \cos 4\theta \mathrm{d}z \\ &= 2\left((E_1 - E_2)t\cos 4\theta_1 + (E_2 - E_3)t\cos 4\theta_2 + ... + (E_n - E_{n+1})t\cos 4\theta_n\right) \\ &= 2t\sum_{i=1}^{n}(E_i - E_{i+1})\cos 4\theta_i \end{aligned} \tag{B.25}$$

$$\begin{aligned} V_4^A &= \int_{-H/2}^{H/2} \sin 4\theta \mathrm{d}z \\ &= 2\left((E_1 - E_2)t\sin 4\theta_1 + (E_2 - E_3)t\sin 4\theta_2 + ... + (E_n - E_{n+1})t\sin 4\theta_n\right) \\ &= 2t\sum_{i=1}^{n}(E_i - E_{i+1})\sin 4\theta_i \end{aligned} \tag{B.26}$$

$$\begin{aligned} V_1^B &= \int_{-H/2}^{H/2} \cos 2\theta z \mathrm{d}z \\ &= 2\left(\frac{t^2}{2}(E_2^2 - E_1^2)\cos 2\theta_1 + \frac{t^2}{2}(E_3^2 - E_2^2)\cos 2\theta_2 + ... + \frac{t^2}{2}(E_{n+1}^2 - E_n^2)\cos 2\theta_n\right) \\ &= -t^2\sum_{i=1}^{n}(E_i^2 - E_{i+1}^2)\cos 2\theta_i \end{aligned} \tag{B.27}$$

$$\begin{aligned} V_3^B &= \int_{-H/2}^{H/2} \sin 2\theta z \mathrm{d}z \\ &= 2\left(\frac{t^2}{2}(E_2^2 - E_1^2)\sin 2\theta_1 + \frac{t^2}{2}(E_3^2 - E_2^2)\sin 2\theta_2 + ... + \frac{t^2}{2}(E_{n+1}^2 - E_n^2)\sin 2\theta_n\right) \\ &= -t^2\sum_{i=1}^{n}(E_i^2 - E_{i+1}^2)\sin 2\theta_i \end{aligned} \tag{B.28}$$

$$\begin{aligned} V_2^D &= \int_{-H/2}^{H/2} \cos 4\theta z^2 \mathrm{d}z \\ &= 2\left(\frac{t^3}{3}(E_1^3 - E_2^3)\cos 4\theta_1 + \frac{t^3}{3}(E_2^3 - E_3^3)\cos 4\theta_2 + ... + \frac{t^3}{3}(E_n^3 - E_{n+1}^3)\cos 4\theta_n\right) \\ &= \frac{2t^3}{3}\sum_{i=1}^{n}(E_i^3 - E_{i+1}^3)\cos 4\theta_i \end{aligned} \tag{B.29}$$

$$
\begin{aligned}
V_4^D &= \int_{-H/2}^{H/2} \sin 4\theta z^2 \mathrm{d}z \\
&= 2\left(\frac{t^3}{3}(E_1^3 - E_2^3)\sin 4\theta_1 + \frac{t^3}{3}(E_2^3 - E_3^3)\sin 4\theta_2 + ... + \frac{t^3}{3}(E_n^3 - E_{n+1}^3)\sin 4\theta_n\right) \\
&= \frac{2t^3}{3}\sum_{i=1}^{n}(E_i^3 - E_{i+1}^3)\sin 4\theta_i
\end{aligned}
\tag{B.30}
$$

B.5 Simplified Total Laminate Strain Energy Equation

The simplified form of the total strain energy equation is presented in this section. This includes simplifications to the $\boldsymbol{A}$, $\boldsymbol{B}$ and $\boldsymbol{D}$ matrices, thermal force and moment terms, and the set of shape coefficients outlined in Chapter 4. Note: the reduced number of in-plane displacement coefficients, $d_{1,2,3,4,5,9,10,11}$, have been renumbered as e_{1-8} for convenience. See page 64.

$$
\begin{aligned}
W =& \Bigg(\frac{1}{12}L^2(e_1e_2 + e_1e_4 + e_4e_5 + e_2e_5) + \frac{1}{80}L^4(e_2^2 + e_4^2) + \frac{1}{144}L^4(e_3^2 + 2e_2e_4) \\
&+ \frac{1}{2}(e_1^2 + e_5^2)\Bigg)L^2A_{11} + \Bigg(\frac{1}{12}L^2(e_1e_2 + e_1e_4 + e_4e_5 + e_2e_5) + \frac{1}{144}L^4(e_2^2 - e_3^2 + e_4^2) \\
&+ \frac{1}{40}L^4e_2e_4 + e_1e_5\Bigg)L^2A_{12} + \Bigg(\frac{1}{12}L^2(e_1e_7 + e_1e_8 - e_5e_7 - e_5e_8) - \frac{1}{288}c^2e_3L^4 \\
&+ \frac{1}{720}L^4(ace_2 + bce_4 - ace_4 - bce_2) + \frac{1}{180}L^4(e_2e_3 + e_2e_7 + e_4e_8 - e_2e_8 - e_4e_7) \\
&+ \frac{1}{48}L^2(ace_1 + bce_1 - ace_5 - bce_5) + 2e_6(e_1 - e_5) + \frac{1}{72}abe_3L^4 + \frac{1}{20}e_3e_4L^4\Bigg)L^2A_{16} \\
&+ \Bigg(\frac{1}{320}L^4(ace_7 + bce_8 + 2e_7^2 + 2e_8^2) + \frac{1}{24}L^2(ace_6 + bce_6 + 4e_6e_7 + 4e_6e_8) \\
&+ \frac{1}{1440}L^4(ace_3 - bce_3 + 2e_3^2 + 4e_3e_7 - 4e_3e_8) + \frac{1}{576}L^4(ace_8 + bce_7 + 2a^2b^2 \\
&+ 4e_7e_8 - 4c^2e_4 + 16abe_4 + 32e_4^2) + \frac{1}{2560}L^4(a^2c^2 + b^2c^2) + \frac{1}{4608}c^4L^4 + 2e_6^2 \\
&- \frac{1}{768}abc^2L^4\Bigg)L^2A_{66} + \Bigg(\frac{1}{12}L^2(be_4 - ae_4 + be_2 - ae_2) - ae_1 + be_5\Bigg)L^2B_{11} \\
&- \Bigg(\frac{1}{48}L^4\left((a^2 + b^2 + 2ab)c + 4(a + b)(e_7 + e_8) + 8c(e_2 + e_4)\right) \\
&+ (2ae_6 + 2be_6 + ce_1 + ce_5)\Bigg)L^2B_{16} + \frac{1}{2}\Bigg(a^2 + b^2\Bigg)L^2D_{11} + abL^2D_{12} \\
&+ \Bigg(ac - bc\Bigg)L^2D_{16} + \frac{1}{2}c^2L^2D_{66} - \Bigg(e_1 + e_5 + \frac{1}{6}L^2(e_2 + e_4)\Bigg)L^2N_x^T \\
&+ \Bigg(a - b\Bigg)L^2M_x^T + cL^2M_{xy}^T
\end{aligned}
\tag{B.31}
$$

B.6 Matrix $\boldsymbol{X}$ Containing Shape Coefficient Terms

The matrix $\boldsymbol{X}$, containing all of the shape coefficient dependent terms of Eq. 4.67, is defined as follows,

$$[\boldsymbol{X}] = \begin{bmatrix} \frac{1}{2}(e_1^2+e_5^2) & \frac{1}{12}(e_1+e_5)(e_2+e_4) & \frac{1}{72}e_2e_4+\frac{1}{144}e_3^2+\frac{1}{80}(e_2^2+e_4^2) \\ e_1e_5 & \frac{1}{12}(e_1+e_5)(e_2+e_4) & \frac{1}{40}e_2e_4+\frac{1}{144}(e_2^2-e_3^2+e_4^2) \\ 2e_6(e_1-e_5) & X_1 & X_2 \\ 2e_6^2 & X_3 & X_4 \\ be_5-ae_1 & X_5 & 0 \\ -2e_6(a+b)-c(e_1+e_5) & X_6 & 0 \\ \frac{1}{2}(a^2+b^2) & 0 & 0 \\ ab & 0 & 0 \\ c(a-b) & 0 & 0 \\ \frac{1}{2}c^2 & 0 & 0 \\ -e_1-e_5 & -\frac{1}{6}(e_2+e_4) & 0 \\ a-b & 0 & 0 \\ c & 0 & 0 \end{bmatrix} \tag{B.32}$$

where

$$\begin{aligned}
X_1 &= \frac{1}{12}(e_1-e_5)(e_7+e_8)+\frac{1}{48}(e_1-e_5)(a+b)c \\
X_2 &= \frac{1}{180}(e_2-e_4)(e_7-e_8)+\frac{1}{720}(a-b)(e_2-e_4)c+\frac{1}{180}(e_2+9e_4)e_3-\frac{1}{288}(c^2-4ab)e_3 \\
X_3 &= \frac{1}{24}(a+b)ce_6+\frac{1}{6}(e_7+e_8)e_6 \\
X_4 &= \frac{1}{160}(e_7^2+e_8^2)+\frac{1}{1440}(a-b)ce_3+\frac{1}{320}(be_8+ae_7)c+\frac{1}{576}(ae_8+be_7)c+\frac{1}{2560}(a^2+b^2)c^2 \\
&\quad +\frac{1}{360}(e_7-e_8)e_3+\frac{1}{144}e_7e_8+\frac{1}{36}(ab+2e_4)e_4+\frac{1}{4608}(c^2-6ab-32e_4)c^2+\frac{1}{288}a^2b^2 \\
&\quad +\frac{1}{720}e_3^2 \\
X_5 &= \frac{1}{12}(b-a)e_4+\frac{1}{12}(b-a)e_2 \\
X_6 &= -\frac{1}{12}(a+b)(e_7+e_8)-\frac{1}{48}(a^2+b^2+2ab+8e_2+8e_4)c
\end{aligned}$$

B.7 Simplified System of Equilibrium Equations

The set of energy equilibrium equations obtained by differentiating Eq. B.31 with respect to the laminate shape are defined in full as follows. See Eq. 4.69.

$$
\begin{aligned}
f_1 = &\left(\frac{1}{36}L^4be_4 + \frac{1}{1440}L^4ce_3 + \frac{1}{576}L^4ce_8 + \frac{1}{24}L^2ce_6 - \frac{1}{768}L^4bc^2 + \frac{1}{320}L^4ce_7\right.\\
&\left. + \frac{1}{144}L^4ab^2 + \frac{1}{1280}L^4ac^2\right)A_{66} - \left(\frac{1}{12}L^2e_2 + \frac{1}{12}L^2e_4 + L^2e_1\right)B_{11}\\
&+ \left(\frac{1}{48}L^2ce_1 + \frac{1}{72}L^4be_3 - \frac{1}{48}L^2ce_5 + \frac{1}{720}L^4ce_2 - \frac{1}{720}L^4ce_4\right)A_{16} + M_x^T\\
&- \left(\frac{1}{12}L^2e_7 + \frac{1}{24}L^2ac + \frac{1}{24}L^2bc + \frac{1}{12}L^2e_8 + 2e_6\right)B_{16} + D_{11}a + D_{16}c + D_{12}b\\
f_2 = &\left(\frac{1}{36}L^4ae_4 - \frac{1}{1440}L^4ce_3 + \frac{1}{576}L^4ce_7 + \frac{1}{24}L^2ce_6 - \frac{1}{768}L^4ac^2 + \frac{1}{320}L^4ce_8\right.\\
&\left. + \frac{1}{144}L^4a^2b + \frac{1}{1280}L^4bc^2\right)A_{66} + \left(\frac{1}{12}L^2e_2 + \frac{1}{12}L^2e_4 + L^2e_5\right)B_{11}\\
&+ \left(\frac{1}{48}L^2ce_1 + \frac{1}{72}L^4ae_3 - \frac{1}{48}L^2ce_5 - \frac{1}{720}L^4ce_2 + \frac{1}{720}L^4ce_4\right)A_{16} - M_x^T\\
&- \left(\frac{1}{12}L^2e_7 + \frac{1}{24}L^2ac + \frac{1}{24}L^2bc + \frac{1}{12}L^2e_8 + 2e_6\right)B_{16} + D_{11}b - D_{16}c + D_{12}a\\
f_3 = &\,(a-b)\,D_{16} - \left(e_1 + e_5 + \frac{1}{6}L^2e_2 + \frac{1}{6}L^2e_4 + \frac{1}{48}L^2a^2 + \frac{1}{24}L^2ab + \frac{1}{48}L^2b^2\right)B_{16}\\
&+ \left(\frac{1}{48}L^2ae_1 - \frac{1}{144}L^4ce_3 - \frac{1}{720}L^4be_2 - \frac{1}{48}L^2ae_5 + \frac{1}{720}L^4ae_2 - \frac{1}{720}L^4ae_2\right.\\
&\left. - \frac{1}{720}L^4ae_4 - \frac{1}{48}L^2be_5 + \frac{1}{48}L^2be_1\right)A_{16} + \left(\frac{1}{1152}L^4c^2 + \frac{1}{1440}L^4ae_3 + \frac{1}{576}L^4\right.\\
&ae_8 + \frac{1}{24}L^2ae_6 + \frac{1}{576}L^4be_7 - \frac{1}{384}L^4abc + \frac{1}{320}L^4be_8 + \frac{1}{320}L^4ae_7 + \frac{1}{24}L^2be_6\\
&\left. - \frac{1}{1440}L^4be_3 + \frac{1}{1280}L^4b^2c + \frac{1}{1280}L^4a^2c - \frac{1}{72}L^4ce_4\right)A_{66} + D_{66}c + M_{xy}^T\\
f_4 = &\left(e_5 + \frac{1}{12}L^2e_4 + \frac{1}{12}L^2e_2\right)A_{12} + \left(e_1 + \frac{1}{12}e_2 + \frac{1}{12}e_4\right)A_{11}\\
&+ \left(\frac{1}{48}L^2ac + \frac{1}{12}L^2e_7 + \frac{1}{48}L^2bc + \frac{1}{12}L^2e_8 + 2e_6\right)A_{16} - B_{11}a - B_{16}c - N_x^T\\
f_5 = &\left(\frac{1}{12}b - \frac{1}{12}a\right)B_{11} + \left(\frac{1}{12}e_5 + \frac{1}{12}e_1 + \frac{1}{72}L^2e_2 + \frac{1}{40}L^2e_4\right)A_{12}\\
&+ \left(\frac{1}{40}L^2e_2 + \frac{1}{12}e_1 + \frac{1}{72}L^2e_4 + \frac{1}{12}e_5\right)A_{11}\\
&+ \left(\frac{1}{180}L^2e_7 - \frac{1}{180}L^2e_8\frac{1}{180}L^2e_3 - \frac{1}{720}L^2bc + \frac{1}{720}L^2ac\right)A_{16} - \frac{1}{6}B_{16}c - \frac{1}{6}N_x^T
\end{aligned}
\tag{B.33}
$$

$$
\begin{aligned}
f_6 &= \frac{1}{72}A_{11}e_3 - \frac{1}{72}A_{12}e_3 + \left(\frac{1}{72}ab + \frac{1}{20}e_4 + \frac{1}{180}e_2 - \frac{1}{288}c^2 + \right) A_{16} \\
&\quad + \left(\frac{1}{1440}ac - \frac{1}{1440}bc + \frac{1}{360}e_7 + \frac{1}{360}e_3 - \frac{1}{360}e_8 + \right) A_{66} \\
f_7 &= \left(\frac{1}{9}L^2e_4 + \frac{1}{36}L^2ab - \frac{1}{144}L^2c^2\right) A_{66} + \left(\frac{1}{12}e_5 + \frac{1}{12}e_1 + \frac{1}{72}L^2e_4 + \frac{1}{40}L^2e_2\right) A_{12} \\
&\quad + \left(\frac{1}{12}b - \frac{1}{12}a\right) B_{11} + \left(\frac{1}{40}L^2e_4 + \frac{1}{12}e_1 + \frac{1}{72}L^2e_2 + \frac{1}{12}e_5\right) A_{11} \\
&\quad + \left(\frac{1}{180}L^2e_8 - \frac{1}{180}L^2e_7\frac{1}{20}L^2e_3 - \frac{1}{720}L^2ac + \frac{1}{720}L^2bc\right) A_{16} - \frac{1}{6}B_{16}c - \frac{1}{6}N_x^T \\
f_8 &= \left(\frac{1}{12}L^2e_2 + \frac{1}{12}L^2e_4 + e_1\right) A_{12} + \left(\frac{1}{12}L^2e_2 + \frac{1}{12}L^2e_4 + e_5\right) A_{11} \\
&\quad - \left(\frac{1}{12}L^2e_7 + \frac{1}{12}L^2e_8 + \frac{1}{48}L^2ac + \frac{1}{48}L^2bc - 2e_6\right) A_{16} + B_{11}b - B_{16}c - N_x^T \\
f_9 &= \left(4e_6 + \frac{1}{24}L^2ac + \frac{1}{24}L^2bc + \frac{1}{6}L^2e_7 + \frac{1}{6}L^2e_8\right) A_{66} \\
&\quad + (2e_1 - 2e_5)\, A_{16} - (2a + 2b)\, B_{16} \\
f_{10} &= \left(\frac{1}{80}L^2e_7 + \frac{1}{576}L^2bc + \frac{1}{320}L^2ac + \frac{1}{6}e_6 + \frac{1}{360}L^2e_3 + \frac{1}{144}L^2e_8\right) A_{66} \\
&\quad - \left(\frac{1}{12}a + \frac{1}{12}b\right) B_{16} + \left(\frac{1}{180}L^2e_2 + \frac{1}{12}e_1 - \frac{1}{180}L^2e_4 - \frac{1}{12}e_5\right) A_{16} \\
f_{11} &= \left(\frac{1}{80}L^2e_8 + \frac{1}{576}L^2ac + \frac{1}{320}L^2bc + \frac{1}{6}e_6 - \frac{1}{360}L^2e_3 + \frac{1}{144}L^2e_7\right) A_{66} \\
&\quad - \left(\frac{1}{12}a + \frac{1}{12}b\right) B_{16} + \left(\frac{1}{180}L^2e_4 + \frac{1}{12}e_1 - \frac{1}{180}L^2e_2 - \frac{1}{12}e_5\right) A_{16}
\end{aligned}
$$

B.8 Reduced Form of Equilibrium Equations

Having performed Gaussian elimination on the set of equations shown in Appendix B.7, the following reduced form is obtained.

$$
\begin{aligned}
f_1 &= \left(\frac{1}{6}L^2(e_2 + e_4) + e_1 + e_5\right)(A_{11} + A_{12}) + (b - a)B_{11} - 2B_{16}c - 2N_x^T \\
f_2 &= (A_{12} - A_{11})(e_1 - e_5) + (a + b)B_{11} - \left(\frac{1}{6}L^2(e_7 + e_8) + \frac{1}{24}L^2c(a + b) + 4e_6\right) A_{16} \\
f_3 &= \frac{1}{90}(e_2 - e_4)A_{16} + \frac{1}{720}c(a - b)A_{66} + \frac{1}{180}(e_3 + e_7 - e_8)A_{66} \\
f_4 &= \left(4e_6 + \frac{1}{6}(e_7 + e_8) + \frac{1}{24}c(a + b)\right) A_{66} + 2(e_1 - e_5)A_{16} - 2(a + b)B_{66} \\
f_5 &= \left(\frac{7}{1440}L^2c(a + b) + \frac{7}{360}L^2(e_7 + e_8) + \frac{1}{3}e_6\right) A_{66} + \frac{1}{6}(e_1 - e_5)A_{16} - \frac{1}{6}(a + b)B_{16}
\end{aligned}
\tag{B.34}
$$

$$
\begin{aligned}
f_6 &= \left(\frac{1}{180}(e_7 - e_8) + \frac{1}{720}c(a-b) - \frac{1}{45}e_3\right)A_{16} + \left(\frac{1}{288}c^2 - \frac{1}{18}e_4 - \frac{1}{72}ab\right)A_{66} \\
&\quad + \frac{1}{180}(e_2 - e_4)(A_{11} - A_{12}) \\
f_7 &= \left(\frac{1}{3}e_6 + \frac{1}{36}e_3 + \frac{7}{360}L^2(e_7 + e_8) + \frac{7}{1440}L^2c(a+b)\right)A_{16} + \frac{1}{6}(e_1A_{11} + e_5A_{12}) \\
&\quad - \frac{1}{6}(aB_{11} + cB_{16} + N_x^T) + \frac{7}{360}L^2(e_2 + e_4)(A_{11} + A_{12}) \\
&\quad + \left(\frac{1}{18}L^2e_4 - \frac{1}{288}L^2c^2 + \frac{1}{72}L^2ab\right)A_{66} \\
f_8 &= \left(\frac{1}{720}L^4c(e_3 - e_8 + e_7) + \frac{1}{36}L^4e_4(b-a) + \frac{1}{144}L^4ab(b-a)\right. \\
&\quad \left. + \frac{1}{480}L^4c^2(a-b)\right)A_{66} + \left(\frac{1}{72}L^4e_3(b-a) - \frac{1}{360}c(e_4 - e_2)\right)A_{16} \\
&\quad - \left(e_1 + e_5 + \frac{1}{6}L^2(e_2 + e_4)\right)B_{11} + (a-b)(D_{11} - D_{12}) + 2cD_{16} + 2M_x^T \\
f_9 &= \left(\frac{1}{12}L^2ce_6 + \frac{7}{1440}L^4c(e_7 + e_8) + \frac{1}{36}L^4e_4(a+b) - \frac{1}{1920}L^4c^2(a+b)\right. \\
&\quad \left. + \frac{1}{144}ab(a+b)\right)A_{66} + \left(\frac{1}{24}c(e_1 - e_5) + \frac{1}{72}e_3(a+b)\right)A_{16} + (e_5 - e_1)B_{11} \\
&\quad - \left(\frac{1}{6}L^2(e_7 + e_8) + \frac{1}{12}L^2c(a+b) + 4e_6\right)B_{16} + (a+b)(D_{11} + D_{12}) \\
f_{10} &= \left(\frac{1}{24}(e_1 - e_5) + \frac{1}{360}L^2e_2 + \frac{1}{40}L^2e_4 + \frac{1}{144}L^2ab - \frac{1}{576}c^2\right)A_{16} \\
&\quad + \left(\frac{1}{12}e_6 + \frac{1}{720}L^2e_3 + \frac{1}{160}L^2e_7 + \frac{1}{288}L^2e_8 + \frac{1}{5760}L^2c(9a+5b)\right)A_{66} \\
&\quad + \frac{1}{144}L^2e_3(A_{11} - A_{12}) - \frac{1}{24}(a+b)B_{16} \\
f_{11} &= (a-b)D_{16} + cD_{66} + M_{xy}^T - \left(e_1 + e_5 + \frac{1}{6}L^2(e_2 + e_4) + \frac{1}{48}L^2(a+b)^2\right)B_{16} \\
&\quad + \left(\frac{1}{48}L^2(a+b)(e_1 - e_5) + \frac{1}{720}L^4(a-b)(e_2 - e_4) - \frac{1}{144}L^4ce_3\right)A_{16} \\
&\quad + \left(\frac{1}{24}L^2e_6(a+b) + \frac{1}{1280}L^4(4(ae_7 + be_8) + 2e_3(a-b) + c(a^2 + b^2))\right. \\
&\quad \left. + \frac{1}{1152}L^4(e_3(b-a) + c^3 + 2(be_7 + ae_8) - 3abc - 16ce_4)\right)A_{66}
\end{aligned}
$$

B.9 Final Three Equilibrium Equations

The final three energy equilibrium equations in the derivation of the analytical solution for stable laminate shapes are given in this section. These equations are in terms of the out-of-plane displacement coefficients, a, b and c only. See page 65.

$$f_a = Y_1 c^2 + Y_2 c + Y_3 = 0$$

where

$$\begin{aligned}
Y_1 &= \frac{5}{8}\frac{-A_{12}A_{66} - A_{16}^2}{A_{11}^2 + 10A_{11}A_{66} - 10A_{16}^2 - A_{12}^2} - \frac{1}{16} \\
Y_2 &= \frac{-72(A_{11} - A_{12} + 10A_{66})(D_{16}(A_{11} + A_{12}) - B_{11}B_{16})}{L^4(a-b)(A_{11} + A_{12})(A_{11}A_{66} - A_{12}A_{66} - 2A_{16}^2)} \\
Y_3 &= \frac{5}{8}\frac{4A_{12}A_{66}ab + 4A_{16}^2 ab}{A_{11}^2 + 10A_{11}A_{66} - 10A_{16}^2 - A_{12}^2} + \frac{1}{4}ab \\
&\quad - \frac{1}{L^4(a+b)(A_{11} + A_{12})(A_{11}A_{66} - A_{12}A_{66} - 2A_{16}^2)}\Big(36(A_{11} - A_{12} + 10A_{66})((A_{11} \\
&\quad + A_{12})(D_{11} - D_{12})(a-b) - B_{11}^2(a-b) + 2(M_x^T(A_{11} + A_{12}) - B_{11}N_x^T))\Big)
\end{aligned} \tag{B.35}$$

$$f_b = Y_4 c^2 + Y_5 c + Y_6 = 0$$

where

$$\begin{aligned}
Y_4 &= \frac{5}{8}\frac{-A_{12}A_{66} - A_{16}^2}{A_{11}^2 + 10A_{11}A_{66} - 10A_{16}^2 - A_{12}^2} - \frac{1}{16} \\
Y_5 &= 0 \\
Y_6 &= \frac{5}{8}\frac{4A_{12}A_{66}ab + 4A_{16}^2 ab}{A_{11}^2 + 10A_{11}A_{66} - 10A_{16}^2 - A_{12}^2} \\
&\quad + \frac{1}{16}\frac{1}{L^4(A_{11}A_{66} - A_{12}A_{66} - 2A_{16}^2)^2}\Big(5760A_{11}A_{66}^2B_{12} + 1152A_{12}A_{16}^2D_{11} \\
&\quad + 11520A_{12}A_{66}B_{16}^2 + 1152A_{12}A_{16}^2D_{12} - 1152A_{11}^2B_{16}^2 + 2304A_{11}A_{12}B_{16}^2 \\
&\quad - 5760A_{12}A_{66}D_{12} + 576A_{12}^2A_{66}D_{12} + 576A_{11}^2A_{66}D_{11} - 5760A_{66}^2B_{11}^2 \\
&\quad + 576A_{12}^2A_{66}D_{11} - 11520A_{11}A_{66}B_{16}^2 - 1152A_{12}^2B_{16}^2 + 2304A_{11}A_{16}B_{11}B_{16} \\
&\quad + 5760A_{11}A_{66}^2D_{11} - 1152A_{11}A_{12}A_{66}D_{12} + 23040A_{16}A_{66}B_{11}B_{16} \\
&\quad - 1152A_{11}A_{12}A_{66}D_{11} - 2304A_{12}A_{16}B_{11}B_{16} - 11520A_{16}^2A_{66}D_{12} \\
&\quad - 5760A_{12}A_{66}^2D_{11} - 1152A_{11}A_{16}^2D_{12} + 576A_{12}A_{66}B_{11}^2 - 11520A_{16}^2A_{66}D_{11} \\
&\quad + 576A_{11}^2A_{66}D_{12} - 576A_{11}A_{66}B_{11}^2 - 1152A_{11}A_{16}^2D_{11} + L^4ab(16A_{16}^4 \\
&\quad + 16A_{12}A_{16}^2A_{66} - 16A_{11}A_{16}^2A_{66} + 4A_{12}^2A_{66}^2 + 4A_{11}^2A_{66}^2 - 8A_{11}A_{12}A_{66}^2)\Big)
\end{aligned} \tag{B.36}$$

$$
\begin{aligned}
f_c = \frac{5}{8}\frac{4A_{12}A_{66}ab + 4A_{16}^2ab - A_{12}A_{66}c^2 - A_{16}^2c^2}{A_{11}^2 + 10A_{11}A_{66} - 10A_{16}^2 - A_{12}^2} \\
- \frac{1}{16}\frac{1}{L^4(A_{11}A_{66} - A_{12}A_{66} - 2A_{16}^2)(A_{11} + A_{12})}\Big(1152A_{11}^2D_{66}c - 2304A_{11}B_{16}^2c \\
+ 2304A_{12}B_{16}N_x^T + 1152A_{11}^2M_{xy}^T - 1152A_{12}^2M_{xy}^T + 11520A_{66}B_{11}B_{16}b \\
- 1152A_{11}B_{11}B_{16}a + 1152A_{11}B_{11}B_{16}b + 11520A_{12}A_{66}M_{xy}^T + 11520A_{11}A_{66}D_{66}c \\
+ 11520A_{12}A_{66}D_{66}c - 11520A_{66}B_{11}B_{16}a - 1152A_{12}^2D_{66}c + 2304A_{12}B_{16}^2c \\
- 11520A_{12}A_{66}D_{16}b - 11520A_{11}A_{66}D_{16}b - 1152A_{12}^2D_{16}a - 1152A_{12}^2D_{16}b \\
+ 11520A_{11}A_{66}D_{16}a + 11520A_{12}A_{66}D_{16}a + 1152A_{11}^2D_{16}a + 1152A_{11}^2D_{16}a \\
- 1152A_{12}B_{11}B_{16}b + 1152A_{12}B_{11}B_{16}a - 1152A_{11}^2D_{16}b - 2304A_{66}B_{16}N_x^T \\
+ 11520A_{11}A_{66}M_{xy}^T - 23040A_{66}B_{16}N_x^T - 23040A_{66}B_{16}^2c \\
+ L^4(8A_{12}A_{16}^2abc + 8A_{11}A_{16}^2abc - 2A_{11}A_{16}^2c^3 - 2A_{12}A_{16}^2c^3 \\
- 4A_{12}^2A_{66}abc - 4A_{12}^2A_{66}abc - A_{12}^2A_{66}c^3 + A_{11}^2A_{66}c^3)\Big) = 0
\end{aligned}
\tag{B.37}
$$

B.10 Out-of-plane Displacement Coefficients

The explicit expressions for the shape coefficients a, b, and c are defined as follows. See page 65.

$$
\begin{aligned}
a &= \frac{-\gamma_{12}}{4\gamma_{11}} \pm \frac{\gamma_{20} \mp \sqrt{-(3\gamma_{15} + 2\gamma_{19} \pm 2\gamma_{16}/\gamma_{20})}}{2} \\
b &= \frac{\gamma_4 - \gamma_5 a \pm \sqrt{(\gamma_5^2 - 4\gamma_3^2)a^2 - (4\gamma_3\gamma_4 + 2\gamma_4\gamma_5)a + (\gamma_4^2 - 4\gamma_3\gamma_6)}}{2\gamma_3} \\
c &= \pm 2\sqrt{(ab + \beta_6/\beta_2)}
\end{aligned}
\tag{B.38}
$$

where the β's and γ's are factors used for simplification and are defined as follows,

$$
\begin{aligned}
\beta_1 &= 72(A_{11} - A_{12} + 10A_{66})/(L^4(A_{11} + A_{12})(A_{11}A_{66} - A_{12}A_{66} - 2A_{16}^2)) \\
\beta_2 &= (5/2)((A_{12}A_{66} + A_{16}^2)/(A_{11}^2 + 10A_{11}A_{66} - 10A_{16}^2 - A_{12}^2)) + 1/4 \\
\beta_3 &= D_{16}(A_{11} + A_{12}) - B_{11}B_{16} \\
\beta_4 &= (D_{11} - D_{12})(A_{11} + A_{12}) - B_{11}^2 \\
\beta_5 &= 2(M_x^T(A_{11} + A_{12}) - B_{11}N_x^T) \\
\beta_6 &= (10A_{66} + A_{11} - A_{12})(36(D_{11} + D_{12})(A_{66}(A_{11} - A_{12}) - 2A_{16}^2) - 72B_{16}^2(A_{11} - A_{12}) \\
&\quad + 144A_{16}B_{11}B_{16} - 36A_{66}B_{11}^2)/(L^4(A_{11}A_{66} - A_{12}A_{66} - 2A_{16}^2)^2) \\
\beta_7 &= D_{66}(A_{11} + A_{12}) - 2B_{16}^2 \\
\beta_8 &= (A_{11} + A_{12})M_{xy}^T - 2B_{16}N_x^T
\end{aligned}
$$

where the A_{ij}, B_{ij} and D_{ij} terms are stiffness matrix values, N_x^T, M_x^T and M_{xy}^T are thermal forces and moments and L is the square laminate edge length.

$$
\begin{aligned}
\gamma_1 &= 2\beta_1^2\beta_2^2\beta_3\beta_8 \\
\gamma_2 &= -2\beta_1^2\beta_2^2\beta_3^2 - 8\beta_2^2(\beta_6 + \beta_1\beta_7)^2 \\
\gamma_3 &= (\beta_2\beta_6 + \beta_1\beta_2\beta_4/2)^2 \\
\gamma_4 &= \beta_1\beta_2^2\beta_5(\beta_6 + \beta_1\beta_4/2) \\
\gamma_5 &= -2(\beta_2\beta_6 + \beta_1\beta_2\beta_4/2)^2 - 4\beta_1^2\beta_2^2\beta_3^2 \\
\gamma_6 &= \beta_1^2\beta_2^2\beta_5^2/4 - 4\beta_1^2\beta_2\beta_3^2\beta_6 \\
\gamma_7 &= \gamma_1 + (\gamma_1\gamma_5 + \gamma_2\gamma_4)/2\gamma_3 - \beta_1^2\beta_2^2\beta_3^2\gamma_4(\gamma_3 + \gamma_5)/\gamma_3^2 \\
\gamma_8 &= \beta_1^2\beta_2^2\beta_8^2 - 4\beta_2\beta_6(\beta_6 + \beta_1\beta_7)^2 + (\beta_1^2\beta_2^2\beta_3^2(\gamma_4^2 - 2\gamma_3\gamma_6) - \gamma_1\gamma_3\gamma_4)/2\gamma_3^2 \\
\gamma_9 &= \beta_1^2\beta_2^2\beta_3^2\gamma_5/2\gamma_3^2 - \gamma_2/2\gamma_3 \\
\gamma_{10} &= -\beta_1^2\beta_2^2\beta_3^2\gamma_4/2\gamma_3^2 + \gamma_1/2\gamma_3 \\
\gamma_{11} &= \gamma_9^2(\gamma_5^2 - 4\gamma_3^2) - ((\beta_1^2\beta_2^2\beta_3^2\gamma_5^2 - \gamma_2\gamma_3\gamma_5)/2\gamma_3^2)^2 \\
\gamma_{12} &= -2\gamma_9^2\gamma_4\gamma_5 - 4\gamma_9^2\gamma_3\gamma_4 + 2\gamma_5^2\gamma_9\gamma_{10} - 8\gamma_3^2\gamma_9\gamma_{10} + 2\gamma_7(\beta_1^2\beta_2^2\beta_3^2\gamma_5^2 - \gamma_2\gamma_3\gamma_5)/2\gamma_3^2 \\
\gamma_{13} &= \gamma_{10}^2(\gamma_5^2 - 4\gamma_3^2) + \gamma_9^2(\gamma_4^2 - 4\gamma_3\gamma_6) - 4\gamma_4\gamma_9\gamma_{10}(2\gamma_3 + \gamma_5) - \gamma_7^2 \\
&\quad - 2\gamma_8(\beta_1^2\beta_2^2\beta_3^2\gamma_5^2 - \gamma_2\gamma_3\gamma_5)/2\gamma_3^2 \\
\gamma_{14} &= 2\gamma_9\gamma_{10}(\gamma_4^2 - 8\gamma_3\gamma_6) - 2\gamma_4\gamma_{10}^2(\gamma_5 + 2\gamma_3) - 2\gamma_7\gamma_8 \\
\gamma_{15} &= \gamma_{13}/\gamma_{11} - 3\gamma_{12}^2/8\gamma_{11}^2 \\
\gamma_{16} &= \gamma_{12}^3/8\gamma_{11}^3 - \gamma_{12}\gamma_{13}/2\gamma_{11}^2 + \gamma_{14}/\gamma_{11} \\
\gamma_{17} &= \gamma_{12}^2\gamma_{13}/16\gamma_{11}^3 - 3\gamma_{12}^4/256\gamma_{11}^4 - \gamma_{12}\gamma_{14}/4\gamma_{11}^2 + (\gamma_{10}^2(\gamma_4^2 - 4\gamma_3\gamma_6) - \gamma_8^2)/\gamma_{11} \\
\gamma_{18} &= (((\gamma_{15}\gamma_{17}/6 - \gamma_{15}^3/216 - \gamma_{16}^2/16)^2 + (-\gamma_{15}^2/36 - \gamma_{17}/3)^3)^{1/2} \\
&\quad - (\gamma_{15}\gamma_{17}/6 - \gamma_{15}^3/216 - \gamma_{16}^2/16))^{1/3} \\
\gamma_{19} &= \gamma_{18} - 5\gamma_{15}/6 - (-\gamma_{17} - \gamma_{15}^2/12)/3\gamma_{18} \\
\gamma_{20} &= (\gamma_{15} + 2\gamma_{19})^{1/2}
\end{aligned}
$$

References

[1] YI Abdel-Aziz and HM Karara. Direct linear transformation from comparator coordinates into object space coordinates in close-range photography. In *Proceedings of the ASP/IU Symposium on Close-Range Photogrammetry*, pages 1–18, 1971.

[2] MJ Adamson. Thermal expansion and swelling of cured epoxy resin used in graphite/epoxy composite materials. *Journal of Materials Science*, 15:1736–1745, 1980.

[3] BD Agarwal and LJ Broutman. *Analysis and Performance of Fiber Composites*. John Wiley and Sons, New York, USA, 1980.

[4] SR Anton and HA Sodano. A review of power harvesting using piezoelectric materials (2003 to 2006). *Smart Materials and Structures*, 16:1–21, 2007.

[5] AF Arrieta, P Hagedorn, A Erturk, and DJ Inman. A piezoelectric bistable plate for nonlinear broadband energy harvesting. *Applied Physics Letters*, 97:1–3, 2010.

[6] AF Arrieta, SA Neild, and DJ Wagg. Nonlinear dynamic response and modeling of a bi-stable composite plate for applications to adaptive structures. *Nonlinear Dynamics*, 58:259–272, 2009.

[7] T Bein, H Hanselka, and E Breitbach. An adaptive spoiler to control the transonic shock. *Smart Materials and Structures*, 9:141–148, 2000.

[8] DN Betts, AIT Salo, CR Bowen, and HA Kim. Characterisation and modelling of the cured shapes of arbitrary layup bistable composite laminates. *Composite Structures*, 92:1694–1700, 2010.

[9] F De Bona and A Soma. Thermal expansion measurement of composites with optical heterodyne interferometry. *Experimental Mechanics*, 37:21–25, 1997.

[10] CR Bowen, DN Betts, PF Giddings, AIT Salo, and HA Kim. A study of bistable laminates of generic lay-up for adaptive structures. *Strain*, Accepted, 2011.

[11] CR Bowen, A Bowles, S Drake, N Johnson, and S Mahon. Fabrication and finite element modelling of interdigitated electrodes. *Ferroelectrics*, 228:257–269, 1999.

[12] CR Bowen, R Butler, R Jervis, HA Kim, and AIT Salo. Morphing and shape control using unsymmetrical composites. *Journal of Intelligent Material Systems and Structures*, 18:89–98, 2007.

[13] CR Bowen, LJ Nelson, R Stevens, MG Cain, and M Stewart. Optimisation of interdigitated electrodes for piezoelectric actuators and active fibre composites. *Journal of Electroceramics*, 16:263–269, 2006.

[14] DS Cairns and DF Adams. Moisture and thermal expansion properties of unidirectional composite materials and the epoxy matrix. *Journal of Reinforced Plastics and Composites*, 2:239–255, 1983.

[15] CR Calladine. *Theory of Shell Structures*. Cambridge University Press, Cambridge, UK, 1989.

[16] M Cerami and PM Weaver. Characterization of unsymmetric cross-ply laminate deflections using orthogonal polynomials. In *Proceedings of the 49th AIAA/ASME/ASCE/AHS/ASC Structures, Structural Dynamics, and Materials Conference, IL USA*, 2008.

[17] M Cho and HY Roh. Non-linear analysis of the curved shapes of unsymmetric laminates accounting for slippage effects. *Composites Science and Technology*, 63:2265–2275, 2003.

[18] I Chopra. Review of state of art of smart structures and integrated systems. *AIAA Journal*, 40:2145–2187, 2002.

[19] VMF Correia, MAA Gomes, A Suleman, CMM Soares, and CAM Soares. Modelling and design of adaptive composite structures. *Computer Methods in Applied Mechanics and Engineering*, 185:325–346, 2000.

[20] VMF Correia, CMM Soares, and CAM Soares. Refined models for the optimal design of adaptive structures using simulated annealing. *Composite Structures*, 54:161–167, 2001.

[21] VMF Correia, CMM Soares, and CAM Soares. Buckling optimization of composite laminated adaptive structures. *Composite Structures*, 62:315–321, 2003.

[22] J Dang and Y Tang. Calculation of the room-temperature shapes of unsymmetric laminates. In *Proceedings of the International Symposium on Composite Materials and Structures, China*, pages 201–206, 1986.

[23] M-L Dano and MW Hyer. The response of unsymmetric laminates to simple applied forces. *Mechanics of Composite Materials and Structures*, 3:65–80, 1996.

[24] M-L Dano and MW Hyer. Thermally-induced deformation behaviour of unsymmetric laminates. *International Journal of Solids and Structures*, 35:2101–2120, 1998.

[25] M-L Dano and MW Hyer. Snap-through of unsymmetric fiber-reinforced composite laminates. *International Journal of Solids and Structures*, 39:175–198, 2002.

[26] M-L Dano and MW Hyer. SMA-induced snap-through of unsymmetric fiber-reinforced composite laminates. *International Journal of Solids and Structures*, 40:5949–5972, 2003.

[27] A Deraemaeker, H Nasser, A Benjeddou, and A Preumont. Mixing rules for the piezoelectric properties of macro fiber composites. *Journal of Intelligent Material Systems and Structures*, 20:1475–1482, 2009.

[28] CG Diaconu and H Sekine. Flexural characteristics and layup optimization of laminated composite plates under hygrothermal conditions using lamination parameters. *Journal of Thermal Stresses*, 26:905–922, 2003.

[29] CG Diaconu and H Sekine. Erratum on Flexural characteristics and layup optimization of laminated composite plates under hygrothermal conditions using lamination parameters. *Journal of Thermal Stresses*, 27:1213–1216, 2004.

[30] CG Diaconu, PM Weaver, and AF Arrieta. Dynamic analysis of bi-stable composite plates. *Journal of Sound and Vibration*, 322:987–1004, 2009.

[31] CG Diaconu, PM Weaver, and F Mattioni. Concepts for morphing airfoil sections using bi-stable laminated composite structures. *Thin-Walled Structures*, 46:689–701, 2008.

[32] A Erturk, J Hoffman, and DJ Inman. A piezomagnetoelastic structure for broadband vibration energy harvesting. *Applied Physics Letters*, 94:1–3, 2009.

[33] A Erturk and DJ Inman. An experimentally validated bimorph cantilever model for piezoelectric energy harvesting from base excitations. *Smart Materials and Structures*, 18:1–18, 2009.

[34] J Etches, K Potter, P Weaver, and I Bond. Environmental effects on thermally induced multistability in unsymmetric composite laminates. *Composites Part A - Applied Science and Manufacturing*, 40:1240–1247, 2009.

[35] DA Galletly and SD Guest. Bistable composite slit tubes I. A beam model. *International Journal of Solids and Structures*, 41:4517–4533, 2004.

[36] DA Galletly and SD Guest. Bistable composite slit tubes II. A shell model. *International Journal of Solids and Structures*, 41:4503–4516, 2004.

[37] PF Giddings. *Bistable composite laminates for structural morphing.* PhD Thesis, Department of Mechanical Engineering, University of Bath, UK, 2010.

[38] PF Giddings, CR Bowen, R Butler, and HA Kim. Characterisation of actuation properties of piezoelectric bi-stable carbon-fibre laminates. *Composites Part A: Applied Science and Manufacturing*, 39:697–703, 2008.

[39] PF Giddings, CR Bowen, AIT Salo, HA Kim, and A Ive. Bistable composite laminates: Effects of laminate composition on cured shape and response to thermal load. *Composite Structures*, 92:2220–2225, 2010.

[40] M Gigliotti, MR Wisnom, and KD Potter. Loss of bifurcation and multiple shapes of thin [0/90] unsymmetric composite plates subject to thermal stress. *Composites Science and Technology*, 64:109–128, 2004.

[41] PE Gill, W Murray, and MH Wright. *Practical Optimization*. Academic Press, London, UK, 1981.

[42] P Glynne-Jones, MJ Tudor, SP Beeby, and NM White. An electromagnetic, vibration-powered generator for intelligent sensor systems. *Sensors and Actuators A: Physical*, 110:344–349, 2004.

[43] SD Guest and S Pellegrino. Analytical models for bistable cylindrical shells. *Proceedings of the Royal Society: Mathematical, Physical and Engineering Sciences*, 462:839–854, 2006.

[44] O Guillon, F Thiebaud, and D Perreux. Tensile fracture of soft and hard PZT. *International Journal of Fracture*, 117:235–246, 2002.

[45] A Hamamoto and MW Hyer. Nonlinear temperature-curvature relationships for unsymmetric graphite-epoxy laminates. *International Journal of Solids and Structures*, 23:919–935, 1987.

[46] SP Han. A globally convergent method for nonlinear programming. *Journal of Optimization Theory and Applications*, 22:297–309, 1977.

[47] Hexcel. Hexcel Corp. prepreg selector tool. `http://www.hexcel.com`.

[48] S Hooker, J Mueller, C Kostelecky, and K Womer. Fatigue resistant miniature piezoceramic actuators. *Journal of Intelligent Material Systems and Structures*, 18:153–157, 2007.

[49] Z Hu, H Xie, T Hua, and Z Wang. Advanced intensity correlation method for evaluating Poisson's ratio of fiberlike material. *Review of Scientific Instruments*, 80:1–5, 2009.

[50] JE Huber, NA Fleck, and MF Ashby. The selection of mechanical actuators based on performance indices. *Proceedings of the Royal Society London A: Mathematical, Physical and Engineering Sciences*, 453:2185–2205, 1997.

[51] W Hufenbach and M Gude. Analysis and optimisation of multistable composites under residual stresses. *Composite Structures*, 55:319–327, 2002.

[52] W Hufenbach, M Gude, L Kroll, A Sokolowski, and B Werdermann. Adjustment of residual stresses in unsymmetric fiber-reinforced composites using genetic algorithms. *Mechanics of Composite Materials*, 37:71–78, 2001.

[53] MW Hyer. Calculations of the room-temperature shapes of unsymmetric laminates. *Journal of Composite Materials*, 15:296–310, 1981.

[54] MW Hyer. Some observations on the cured shape of thin unsymmetric laminates. *Journal of Composite Materials*, 15:175–194, 1981.

[55] MW Hyer. The room-temperature shapes of 4-layer unsymmetric cross-ply laminates. *Journal of Composite Materials*, 16:318–340, 1982.

[56] K Iqbal and S Pellegrino. Bi-stable composite shells. In *Proceedings of the 41st AIAA/ASME/ASCE/AHS/ASC Structures, Structural Dynamics, and Material Conference, GA, USA*, 2000.

[57] K Iqbal, S Pellegrino, and A Daton-Lovett. Bistable composite slit tubes. In *Proceedings of the IUTAM-IASS Symposium on Deployable Structures, Cambridge, UK*, 1998.

[58] WJ Jun and CS Hong. Warping analysis of unsymmetric laminated composites. *Transactions of the Korean Society of Mechanical Engineers*, 7:404–409, 1983.

[59] WJ Jun and CS Hong. Effect of residual shear strain on the cured shape of unsymmetric cross-ply thin laminates. *Composite Science and Technology*, 38:55–67, 1990.

[60] WJ Jun and CS Hong. Cured shape of unsymmetric laminates with arbitrary lay-up angles. *Journal of Reinforced Plastics and Composites*, 11:1352–1366, 1992.

[61] T Kant and K Swaminathan. Estimation of transverse/interlaminar stresses in laminated composites - A selective review and survey of current developments. *Composite Structures*, 49:65–75, 2000.

[62] E Kebadze, SD Guest, and S Pellegrino. Bistable prestressed shell structures. *International Journal of Solids and Structures*, 41:2801–2820, 2004.

[63] JM Lloyd, RB Williams, DJ Inman, and WK Wilkie. An analytical model of the mechanical properties of the single crystal macro-fiber composite actuator. *Smart Structures and Materials 2004: Active Materials Behavior and Mechanics*, 5387:37–46, 2004.

[64] EH Mansfield. Large-deflection torsion and flexure of initially curved strips. *Proceedings of the Royal Society London, A*, 334:279–298, 1973.

[65] FL Matthews and RD Rawlings. *Stiffness of unidirectional composites and laminates. In: Composite Materials: Engineering and Science.* Chapman and Hall, London, UK, 1994.

[66] Memory Metalle. Nickel titanium memory metalle wire product overview. `http://www.memory-metalle.de`.

[67] PD Mitcheson, P Miao, BH Stark, EM Yeatman, AS Holmes, and TC Green. MEMS electrostatic micropower generator for low frequency operation. *Sensors and Actuators A: Physical*, 115:523–529, 2004.

[68] C Mittelstedt and W Becker. Interlaminar stress concentrations in layered structures: Part I - A selective literature survey on free-edge effect since 1967. *Journal of Composite Materials*, 38:1037–1062, 2004.

[69] T Murphey and S Pellegrino. A novel actuated composite tape-spring for deployable structures. In *Proceedings of the 45th AIAA/ASME/ASCE/AHS/ASC Structures, Structural Dynamics, and Material Conference, CA, USA*, 2004.

[70] BM Nigg, GK Cole, and IC Wright. *Biomechanics of the musculo-skeletal system.* John Wiley and Sons, Chichester, UK, 2001.

[71] A Nosier and M Maleki. Free-edge stresses in general composite laminates. *International Journal of Mechanical Sciences*, 50:1435–1447, 2008.

[72] AS Panesar and PM Weaver. Optimisation of blended bistable laminate for morphing flap. In *Proceedings of the 51st AIAA/ASME/ASCE/AHS/ASC Structures, Structural Dynamics, and Material Conference, FL, USA*, 2010.

[73] R Paradies and B Schlaepfer. Finite element modeling of piezoelectric elements with complex electrode configuration. *Smart Materials and Structures*, 18:1–13, 2009.

[74] LJB Peeters, PC Powell, and L Warnet. Thermally-induced shapes of unsymmetric laminates. *Journal of Composite Materials*, 30:603–626, 1996.

[75] A Pirrera, D Avitabile, and PM Weaver. Bistable plates for morphing structures: A refined analytical approach with high-order polynomials. *International Journal of Solids and Structures*, 47:3412–3425, 2010.

[76] P Portela, P Camanho, P Weaver, and I Bond. Analysis of morphing, multi stable structures actuated by piezoelectric patches. *Computers and Structures*, 86:347–356, 2008.

[77] K Potter, P Weaver, AA Seman, and S Shah. Phenomena in the bifurcation of unsymmetric composite plates. *Composites Part A: Applied Science and Manufacturing*, 38:100–106, 2007.

[78] MJD Powell. A fast algorithm for nonlinearly constrained optimization calculations. *Numerical Analysis*, 630:144–157, 1978.

[79] MJD Powell. *Nonlinear Programming: The convergence of variable metric methods for nonlinearly constrained optimization calculations.* Academic Press, London, UK, 1978.

[80] J Pritchard, CR Bowen, and F Lowrie. Multilayer actuators: Review. *British Ceramic Transactions*, 100:265–273, 2001.

[81] S Priya. Advances in energy harvesting using low profile piezoelectric transducers. *Journal of Electroceramics*, 19:167–184, 2007.

[82] S Priya. Criterion for material selection in design of bulk piezoelectric energy harvesters. *IEEE Transaction on Ultrasonics, Ferroelectrics and Frequency Control*, 57:2610–2612, 2010.

[83] L Ren. Theoretical study on shape control of thin cross-ply laminates using piezoelectric actuators. *Composite Structures*, 80:451–460, 2007.

[84] L Ren. A theoretical study on shape control of arbitrary lay-up laminates using piezoelectric actuators. *Composite Structures*, 83:110–118, 2008.

[85] L Ren and A Parvizi-Majidi. A model for shape control of cross-ply laminated shells using a piezoelectric actuator. *Journal of Composite Materials*, 40:1271–1285, 2006.

[86] L Ren, A Parvizi-Majidi, and Z Li. Cured shape of cross-ply composite thin shells. *Journal of Composite Materials*, 37:1801–1820, 2003.

[87] J Ryu, J Lee, M Cho, S-W Kim, J-S Koh, and K-J Cho. Snap-through behavior of bi-stable composite structure using SMA spring actuator. In *Proceedings of the 52nd AIAA/ASME/ASCE/AHS/ASC Structures, Structural Dynamics, and Material Conference, CO, USA*, 2011.

[88] DT Sandwell. Biharmonic spline interpolation of GEOS-3 and SEASAT altimeter data. *Geophysical Research Letters*, 14:139–142, 1987.

[89] M Schlecht and K Schulte. Advanced calculation of the room-temperature shapes of unsymmetric laminates. *Journal of Composite Materials*, 33:1472–1490, 1999.

[90] M Schlecht, K Schulte, and MW Hyer. Advanced calculation of the room-temperature shapes of thin unsymmetric composite laminates. *Composite Structures*, 32:627–633, 1995.

[91] MR Schultz and MW Hyer. Snap-through of unsymmetric cross-ply laminates using piezoceramic actuators. *Journal of Intelligent Material Systems and Structures*, 14:795–814, 2003.

[92] MR Schultz and MW Hyer. A morphing concept based on unsymmetric composite laminates and piezoceramic MFC actuators. In *Proceedings of the 45th AIAA/ASME/ASCE/AHS/ASC Structures, Structural Dynamics, and Material Conference, CA, USA*, 2004.

[93] MR Schultz, WK Wilkie, and RG Bryant. Investigation of self-resetting active multistable laminates. *Journal of Aircraft*, 44:1069–1076, 2007.

[94] KA Seffen. Morphing bistable orthotropic elliptical shallow shells. *Proceedings of the Royal Society*, 463:67–83, 2007.

[95] KA Seffen. *Multistable anisotropic shells: Governing equations of deformation.* CUED/D-STRUCT/TR 225, University of Cambridge, 2008.

[96] Smart Material Corp. Selector. Smart material macro fiber composite actuators and sensors. `http://www.smartmaterial.com`.

[97] CMM Soares, CAM Soares, and VMF Correia. Optimal design of piezolaminated structures. *Composite Structures*, 47:625–634, 1999.

[98] SC Stanton, CC McGehee, and BP Mann. Reversible hysteresis for broadband magnetopiezoeleastic energy harvesting. *Applied Physics Letters*, 95:1–3, 2009.

[99] SC Stanton, CC McGehee, and BP Mann. Nonlinear dynamics for broadband energy harvesting: Investigation of a bistable piezoelectric inertial generator. *Physica D: Nonlinear Phenomena*, 239:640–653, 2010.

[100] SW Tsai and HT Hahn. *Introduction to composite materials.* Technomic Publishing Company, Westport, Connecticut, USA.

[101] MR Vanlandingham, RF Eduljee, and JW Gillespie. Moisture diffusion in epoxy systems. *Journal of Applied Polymer Science*, 71:787–798, 1999.

[102] GS Venison. A practical look at shape memory alloys' potential as a thermal actuator. *Materials and Design*, 7:143–146, 1986.

[103] S Vidoli and C Maurini. Tristability of thin orthotropic shells with uniform initial curvature. *Proceedings of the Royal Society*, 464:2949–2966, 2008.

[104] SR White and HT Hahn. Process modeling of composite materials: Residual stress development during cure. Part II. Experimenal validation. *Journal of Composite Materials*, 26:2423–2453, 1992.

[105] JM Whitney. Shear correction factors for orthotropic laminates under static load. *Journal of Applied Mechanics*, 40:302–304, 1973.

[106] JM Whitney and NJ Pagano. Shear deformation in heterogeneous anisotropic plates. *Journal of Applied Mechanics*, 37:1031–1036, 1970.

[107] SA Wilson, RPJ Jourdain, Q Zhang, RA Dorey, CR Bowen, M Willander, QUI Wahab, M Willander, SM Al-Hilli, O Nur, E Quandt, C Johansson, E Pagounis, M Kohl, J Matovic, B Samel, W van der Wijngaart, EWH Jager, D Carlsson, Z Djinovic, M Wegener, C Moldovan, R Iosub, E Abad, M Wendlandt, C Rusu, and K Persson. New materials for micro-scale sensors and actuators: An engineering review. *Materials Science and Engineering*, 56:1–129, 2007.

[108] CB York. Characterization of nonsymmetric forms of fully orthotropic laminates. *Journal of Aircraft*, 46:1114–1124, 2009.

[109] JM Zhou and JP Lucas. Hygrothermal effects of epoxy resin. Part I: the nature of water in epoxy. *Polymer*, 40:5505–5512, 1999.